



**University of
Nottingham**

UK | CHINA | MALAYSIA

**Characterisation of the modulation of
immune response to polymer implants
using established and novel methods**

Waraporn Suvannapruk

Thesis submitted to the University of Nottingham
for the degree of Doctor of Philosophy

January 2023

Abstract

As understanding of host immune responses towards implanted biomaterials has grown, macrophages have been identified as critical predictors of inflammatory consequences following implantation. Depending on the phenotype they adopt in response to biomaterials *in vivo*, different macrophage phenotypes can either perpetuate chronic inflammation (via M1) or promote tissue healing (via M2). In the setting of tissue repair, a prompt shift in macrophage polarisation from a pro-inflammatory (M1 macrophages) to an anti-inflammatory (M2 macrophages) favours enhanced healing. In some cases, patients suffer adverse immune reactions to implanted devices leading to chronic inflammation, pain, and on occasion, implant failure. Therefore, it is beneficial to have an in-depth understanding of the metabolomics of different macrophage phenotypes, as this would help understand and improve the response of the human body to biomaterials.

Characterization of the small molecule signature, the metabolome of macrophage subsets within individual cells (*in vitro*) and tissue sections (*ex vivo*) offers great potential to understand the response of the human immune system to implanted biomaterials. As a first *in vitro* step I investigate the possibility of using 3D OrbiSIMS to characterise the metabolic profile of single cells after cytokine differentiation into naïve (non-polarised), M1 and M2. I identify key characteristic metabolites for each macrophage subset (Chapter 4). In the second step, I used of methacrylate monomers to synthesise copolymers via a thermal polymerization method and subsequently coat coverslips. Moreover, I found the coated polymers to impact on macrophage polarisation in terms of their behaviour and phenotype of macrophages (Chapter 5). In the third step *in vivo*, I investigate explanted as purchased and polymer coated silicon catheter coated sections as a model medical device in a subcutaneous rodent

model of foreign body response (Chapter 6). Here, I identified the bio-instructive polymer coatings to induce macrophage pro/anti-inflammatory responses *in vivo* by examining the tissue surrounding the foreign body site from mice using immunohistochemistry, staining and using the 3D OrbiSIMS specifically employing a gas cluster ion beam (GCIB) and an Orbitrap analyser.

In summary, findings from this study show the potential of metabolomic analysis by 3D OrbiSIMS to achieve unbiased insight into cellular phenotype at the resolution of a single cell in culture. Also, this is possible on explanted devices in order to their response to various biomaterials.

Acknowledgement

I am deeply thankful to my principal supervisor, Professor Morgan Alexander, firstly, for accepting me as his student, for support, helpful advice, and guidance throughout this research project. He has taught me how to professionally do research all his time which he has given me at Nottingham. I would also like to specially thank Professor Amir Ghaemmaghami has contributed immensely to my development as a researcher. I am very grateful to him for presenting me this platform. My sincere thanks also go to my supervisor, Dr Dong-hyun Kim, for his invaluable advice and insightful suggestions, which positively impacted the completion of this work. I would also like to express thanks to my supervisor Dr. David Scurr for his endless support and guidance throughout the course of this work. It was an incredible discussion and suggestion regarding the technical contents of my research during the four years of my PhD.

I also thank Dr. Max Edney and Dr. Anna Kotowska for their encouragement and huge help in my work. I would also like to thanks my colleagues in Immuno-bioengineering group, Life Sciences, for their help and advice throughout the year. I would specially like to thank Dr. Chidimma Mbadugha, Dr. Lisa Kammerling, Dr. Leanne Fisher and Karen Lawler in particular for training me on a variety of biological techniques and for never hesitating to apply their expertise and knowledge in helping me think through research problems. I would like to say a big thank you to Dr. Laurence Burroughs and Dr. Adam Dundas from the Advance Materials and Healthcare Technologies, School of Pharmacy, for training me on several chemistry and surface analysis techniques.

I would like to acknowledge The Royal Thai Government Scholarship provided by the National Metal and Materials Technology Centre (MTEC), the National Science and

Technology Development Agency (NSTDA), Thailand for a four-year scholarship which made it possible to pursue my PhD study.

I also need to express my gratitude to my parents, Mum and Dad, and brothers for their endless love and relentless efforts and sacrifices all my life. During my first year of PhD, I lost my mum and losing all family members can be unbearably difficult; however, wherever you are, you will always be in my heart. I have to say this, I love you so.

Publications

1. **W. Suvannapruk**, M. K. Edney, D. H. Kim, D. J. Scurr, A. M. Ghaemmaghami and M. R. Alexander. (2022) “Single cell metabolic profiling of macrophages using 3D OrbiSIMS: correlations with phenotype” **Anal. Chem** **2022**, 94, 9389-9398. (Chapter 4)

Manuscripts submitted

2. **W. Suvannapruk**, Max K. Edney, Leanne E Fisher, Jeni C Lockett, D. H. Kim, D. J. Scurr, A. M. Ghaemmaghami and M. R. Alexander. Label-free chemical characterisation of polarised immune cell in vitro and host response to implanted bio-instructive polymers *in vivo* using 3D OrbiSIMS. *Bio-protocol Journal*. (Chapter 3)

Manuscripts in preparation

3. **W. Suvannapruk**, Max K. Edney, Leanne E Fisher, Jeni C Lockett, D. H. Kim, D. J. Scurr, A. M. Ghaemmaghami and M. R. Alexander. “Host metabolite response to subcutaneous implantation of novel immune-instructive polymers in a mouse model using the 3D OrbiSIMS” (Chapter 6)

Conference Presentations

1. Single cell metabolic profiling of macrophages using 3D OrbiSIMS: correlations with phenotype. UK Surface Analysis Forum (July 2022) - oral Young Surface Analyst prize finalist
2. Single cell metabolic profiling of macrophages using 3D OrbiSIMS: correlations with phenotype UK Surface Analysis Forum (July 2022) - poster presentation
3. Single Cell Metabolomic Profiling of Activated Macrophages using 3D OrbiSIMS. 22nd International Conference on Secondary Ion Mass Spectrometry, Kyoto, 20-25 October 2019 - poster

Table of Contents

Chapter 1	19
1. General introduction.....	19
1.1. Biomaterials and medical device	19
1.1.1.The use of biomaterials for medical applications.....	19
1.1.2.Biocompatibility of implants and medical device	22
1.1.3.Foreign body reaction to implanted biomaterials.....	22
1.2. Macrophages as innate immune cells	24
1.2.1. Origin and functional of macrophages	24
1.2.2. Macrophage classification	25
1.3. Host response to biomaterials and medical device	27
1.3.1. Immune response towards biomaterial insertion.....	27
1.3.2. Role of macrophages in immune responses	28
1.4. The biological responses to biomaterial and medical devices: strategies for controlling their surface	29
1.4.1. Modification of biomaterial physical and structure properties.....	29
1.4.2. Modulation of macrophage phenotype and function by material physical and chemical properties	30
1.5. Metabolomics analysis for immune cell characterisation.....	31
1.5.1. Metabolic approaches.....	32
1.5.2. Metabolomics technologies and applications.....	33
1.5.2.1. Mass spectrometry (MS).....	33
1.5.2.2. Secondary ion mass spectrometry (SIMS).....	35
1.5.2.3. ToF analyser.....	39
1.5.2.4. Orbitrap analyser.....	39
1.5.2.5. Quantitative SIMS analysis.....	41
1.5.3. Metabolomics of macrophage	42
1.6. The scope of this thesis.....	43
Chapter 2	44
2. General methods.....	44

2.1. Cellular and molecular technique	44
2.1.1. Monocyte Isolation	44
2.1.2. The polarization of macrophages	44
2.1.3. Enzyme linked immunosorbent assay (ELISA)	45
2.1.4. Immunofluorescence staining.....	46
2.2. Polymer synthesis	47
2.2.1. Thermal polymerisation	47
2.2.2. Nuclear magnetic resonance spectroscopy (NMR)	49
2.2.3. Gel permeation chromatography (GPC).....	50
2.3. Surface characterisation techniques.....	51
2.3.1. Time of flight – secondary ion mass spectrometry (ToF-SIMS)	51
2.3.2. 3D OrbiSIMS	53
Chapter 3	57
3. Label-free chemical characterisation of polarised immune cell <i>in vitro</i> and host response to implanted bio-instructive polymers <i>in vivo</i> using 3D OrbiSIMS	57
3.1 Abstract	59
3.2. Introduction.....	60
3.3. Materials and Reagents	62
3.3.1. Cell culture	62
3.3.2. Animal study	63
3.3.3. Equipment	63
3.3.4. Software.....	64
3.4. Consideration before starting.....	64
3.4.1. Peripheral blood monocyctic cells (PBMCs) isolation	64
3.4.2. Macrophage polarisation	64
3.4.3. Implant sample preparation for <i>in vivo</i> studies.....	65
3.4.4. <i>Ex vivo</i> tissue sample preparation for 3D OrbiSIMS	65
3.5. Procedure	65
3.5.1. Preparation of PBMC isolation	65
3.5.2. Macrophage polarisation	68

3.5.3. Implant sample preparation for <i>in vivo</i> studies.....	69
3.5.4. <i>In vivo</i> study	70
3.5.5. <i>Ex vivo</i> tissue sample preparation for 3D OrbiSIMS	71
3.5.6. 3D OrbiSIMS analysis.....	72
3.5.7. Data analysis.....	74
3.6. Conclusion	76
Chapter 4	77
4. Single-Cell Metabolic Profiling of Macrophages Using 3D OrbiSIMS: Correlations with Phenotype	77
4.1. Abstract.....	79
4.2. Introduction.....	79
4.3. Methods	82
4.3.1. Sample preparation.....	82
4.3.2. Analysis of macrophages surface phenotype	83
4.3.3. Cytokine Quantification	83
4.3.4. 3D OrbiSIMS analysis.....	83
4.3.5. Principal component analysis (PCA)	84
4.3.6. Data processing and metabolites identification.....	85
4.4. Results and Discussion	85
4.4.1. Characterization of macrophage marker expression and cytokines analysis.	85
4.4.2. Targeted lipid analysis.....	86
4.4.3. Untargeted analysis approaches	90
4.4.4. Amino acid assignments.....	92
4.4.5. Metabolite identification	93
4.5. Conclusions.....	95
Chapter 5	96
5. Polymer synthesis for cell instructive coatings.....	96
5.1. Introduction.....	96
5.2. Materials and methods	99
5.2.1. Synthesis of copolymers.....	99

5.2.2. Characterization of the copolymers.....	100
5.2.2.1. Nuclear magnetic resonance spectroscopy (NMR).....	101
5.2.2.2. Gel permeation chromatography (GPC)	101
5.2.3. Sample preparation and characterisation of chemical copolymer surface	102
5.2.3.1. Preparation of copolymer coated on glass substrates.....	102
5.2.3.2. Time-of-flight secondary ion mass spectrometry	102
5.2.4. <i>In vitro</i> study	102
5.2.4.1. Cell culture	102
5.2.4.2. Cytotoxicity assay	103
5.2.4.3. Immunostaining for M1 and M2 surface markers	103
5.2.4.4. Image analysis.....	104
5.2.4.5. Cytokines production	104
5.3. Results.....	105
5.3.1. Characterisation of copolymer	105
5.3.1.1. NMR.....	105
5.3.1.2. GPC	106
5.3.1.3. ToF-SIMS characterisation of chemical copolymer surface.....	108
5.3.1.4. Evaluation of macrophages viability on polymer surface.....	114
5.3.1.5. Expression of surface markers on polymer coated	115
5.3.1.6. Cytokines analysis.....	117
5.4. Discussion.....	118
Chapter 6	121
6. Modulation of local host metabolite response to subcutaneous implantation by novel immune-instructive polymers in a mouse model using the 3D OrbiSIMS	121
6.1. Abstract.....	122
6.2. Introduction.....	122
6.3. Experimental.....	125
6.3.1. Implant sample preparation	125
6.3.2. <i>In vivo</i> models	126
6.3.3. Histological Analysis	127

6.3.4. Macrophage phenotype analysis.....	127
6.3.5. 3D OrbiSIMS analysis.....	128
6.3.6. Principal component analysis (PCA)	129
6.4. Results and discussions.....	130
6.4.1. Pro- and anti-inflammatory macrophage polymers influence immune cell infiltration and collagen deposition	130
6.4.2. Characterisation of local metabolite changes to implants	130
6.4.3. M1 polymer significantly increased lipids in close proximity to the implant	132
6.4.4. Imaging of lipids in the tissue	136
6.4.5. Amino acid ion intensities are higher for M2 polymer implants	138
6.4.6. Other small molecules	140
6.5. Conclusions.....	142
Chapter 7	143
7.1. Summary	143
References	147
Appendix	166

List of Figures

<i>Figure 1.1. Examples of biomaterial applications used to repair or replace dysfunctional tissues and for the treatment of various disorders.</i>	20
<i>Figure 1.2. Foreign body reaction against biomaterials.</i>	23
<i>Figure 1.3. Distribution of macrophages in tissues.</i>	25
<i>Figure 1.4. M1 and M2 macrophages classification.</i>	27
<i>Figure 1.5. The principle of secondary-ion mass spectrometry.</i>	37
<i>Figure 1.6. Molecular dynamics simulations of 15 keV Ga⁺, Au₃⁺, C₆₀⁺, and Ar₈₇₂⁺ primary ions bombarding an Ag (111) substrate.¹¹⁰</i>	38
<i>Figure 2.1. Schematic representation of the antigen detection using sandwich ELISA.</i>	46
<i>Figure 2.2. Illustration of different immunofluorescence staining between direct and indirect. Image source.¹⁴⁰</i>	47
<i>Figure 2.3. Schematic state of free radical polymerization.</i>	48
<i>Figure 2.4. Simplified representation of the NMR.</i>	49
<i>Figure 2.5. Distribution of molecular weights in a typical polymer sample.</i>	50
<i>Figure 2.6. Schematic representation of a ToF-SIMS instrument.</i>	52
<i>Figure 2.7. Definitions of resolution shows the “full width of the peak at half maximal height (FWHM) or 50% of peak height” definition.</i>	53
<i>Figure 2.8. The 3D OrbiSIMS spectrometer and mode of operation.</i>	54
<i>Figure 2.9. MS imaging of individual macrophage cell in rat alveolar, images showing the cell marker of phosphocholine at 184 m/z (gray), nuclear at 157 m/z (pink), and amiodarone [M+H]⁺ at 646 m/z (green). Image was adapted from Passarelli et al., Nature Methods (2017).¹⁵⁵</i>	55
<i>Figure 3.1. Schematic workflow of experiment.</i>	59
<i>Figure 3.2. Processing of PBMC isolation.</i>	67
<i>Figure 3.3. Schematic workflow of a catheter coated with copolymer for in vivo study. A. Clinical-grade silicone catheter. B. The catheters were cut to a length of 5 mm. C. Coating of catheter segments in immune instructive chemistries using dip</i>	

<i>coating. D. Catheter coated sample. E. Coated catheter segments are implanted in mice for 28 days.</i>	70
<i>Figure 3.4. Schematic workflow of fresh tissue section preparation for 3D OrbiSIMS.</i>	72
<i>Figure 3.5. Transfer sample to the stage.</i>	73
<i>Figure 3.6. Identification of phospholipid in single macrophages and tissue section samples.</i>	75
<i>Figure 4.1. Schematic workflow of single cell metabolomic profiling using 3D OrbiSIMS.</i>	85
<i>Figure 4.2. Lipid on single cell by 3D OrbiSIMS analysis.</i>	88
<i>Figure 4.3. a) Schematic of the membrane lipid components. b) Normalized intensity of lipids in three separate cells for each macrophage polarization with comparison of each phenotype in positive polarity $C_5H_{14}NO^+$ (sphingolipids, SP, m/z 104.1070), c) $C_2H_6PO_4^+$ (phosphocholines, PC, m/z 124.9998) and d) $C_5H_{15}NPO_4^+$ (phosphocholines, PC, m/z 184.0739).</i>	90
<i>Figure 4.4. Principal component analysis (scores and loadings) for different macrophage subsets results.</i>	91
<i>Figure 4.5. Characteristic amino acid fragments were detected in macrophage polarization in positive ion mode.</i>	93
<i>Figure 4.6. Metabolites significantly affected by macrophage polarization toward the M1 and M2.</i>	94
<i>Figure 5.1. Schematic of the high-throughput screening approach used to identify pro- or anti-inflammatory hit polymers in vitro and in vivo.</i>	98
<i>Figure 5.2. Schematic of the characterization of the copolymers.</i>	101
<i>Figure 5.3. 1H NMR spectrum of synthesis copolymers.</i>	106
<i>Figure 5.4. ToF-SIMS spectra and ion image of copolymers; CHMA-co-HDFDMA.</i>	109
<i>Figure 5.5. ToF-SIMS spectra and ion image of copolymers; CHMA-co-DMAEMA.</i>	110
<i>Figure 5.6. ToF-SIMS spectra and ion image of copolymers; tBCHMA.</i>	111
<i>Figure 5.7. ToF-SIMS spectra and ion image of copolymers; CHMA-co-iDMA</i>	112
<i>Figure 5.8. ToF-SIMS spectra and ion image of copolymers; PhMA-co-iDMA</i>	113

<i>Figure 5.9. Assessment of toxicity on polymer surfaces by ToxiLight assay. Fluorescence measured each polymer condition normalised to live cell maximum baseline, suggesting high cell viability on the five polymers surface.</i>	<i>114</i>
<i>Figure 5.10. Expression of surface phenotypic markers in M1 and M2.....</i>	<i>116</i>
<i>Figure 6.1. Schematic of the in vivo studies experimental.....</i>	<i>126</i>
<i>Figure 6.2. Principal component analysis (scores and loadings) for different tissue samples.....</i>	<i>130</i>
<i>Figure 6.3. Quantification of characteristic lipid fragments intensity were detected by OrbiSIMS in positive and negative ion mode.....</i>	<i>130</i>
<i>Figure 6.4. Chemical imaging of tissue sample.....</i>	<i>133</i>
<i>Figure 6.5. Characteristic amino acid fragments were detected in tissue section in positive ion mode.....</i>	<i>135</i>
<i>Figure 6.6. Metabolites detected in tissue significantly affected by M2-polymer... </i>	<i>137</i>

List of Tables

Table 1.1. Biomedical applications of biomaterials.....	21
Table 1.2. provides a brief overview of the advantages and disadvantages of both TOF-SIMS and MALDI-TOF.....	35
Table 5.1. Monomers name and chemical structures and reaction parameters.....	100
Table 5.2. Molecular weights and molecular weight distribution.....	107

List of Abbreviations

Ar	Argon
Bi	Bismuth
BMDMs	Bone marrow derived macrophages
BSA	Bovine serum albumin
CHMA	Cyclohexyl methacrylate
DAPI	4',6-Diamidino-2-Phenylindole
DMAEMA	Dimethylamino-ethyl methacrylate
EGDMA	Ethylene glycol dimethacrylate
ELISA	Enzyme linked immunosorbent assay
FBGCs	Foreign body giant cells
FBR	Foreign body responses
FBS	Fetal bovine serum
DESI	Desorption electrospray ionization
GCIB	Gas cluster ion beam
GLs	Glycerophospholipids
GM-CSF	Granulocyte/Macrophage – colony stimulating factor
GPC Gel	Permeation chromatography
GS	Goat serum
HDFDMA	Heptadecafluorodecyl methacrylate
IFN- γ	Interferon gamma
IL	Interleukin
lysoGLs	lysophospholipids

iDMA	Isodecyl methacrylate
LC-MS	Liquid chromatography mass spectrometry
LPS	Lipopolysaccharide
M1	Pro – inflammatory macrophages
M2	Anti – inflammatory macrophages
MACS	Magnetic cell separation
MALDI	Matrix-assisted laser desorption/ionization
M-CSF	Macrophage – colony stimulating factor
MDMs	Monocyte-derived macrophages
MFI	Mean fluorescence intensity
MR	Mannose receptor
MSCs	Mesenchymal stem cells
M _i	Molecular weight of molecules i
NMR	Nuclear magnetic resonance spectroscopy
n _i	Number of molecules with molecular weight i
O ₂	Oxygen
PBMC	Peripheral blood mononuclear cells
PBS	Phosphate buffered saline
PC	Principal component
PCA	Principal component analysis
PDMS	Poly – dimethyl siloxane
pHEMA	Poly (2 – hydroxyethyl methacrylate)
PhMA	Phenyl methacrylate
ppm	Parts per million

RAW 264.7	Murine macrophage cell line
SD	Standard deviation
SIMS	Secondary ion mass spectrometry
SM	Sphingomyelin
tBCHMA	Tertbutylcyclohexyl methacrylate
Tc	T – cytotoxic cells
TCP	Tissue culture polystyrene
TNF- α	Tumour necrosis factor – alpha
ToF-SIMS	Time of flight – secondary ion mass spectrometry
Wi	Mass of molecules with molecular weight i
3D OrbiSIMS	A Time of Flight Secondary Ion Mass Spectrometer (ToF-SIMS) with hybrid OrbiTrap TM

Chapter 1

1. General introduction

1.1. Biomaterials and medical device

Biomaterials are natural or synthetic materials and can be used in making medical devices.¹ These medical devices are used to replace, repair and support any part of the human body tissue which has been damaged or disordered by e.g., dental diseases, cardiovascular disorders, coronary stents, catheters, hip and knee replacements and even the everyday contact lens (Figure 1.1.).²⁻⁵ Moreover, biomaterials are utilised in various advanced medical technologies, including drug delivery devices, tissue engineering and other biomedical implants.⁶ Medical devices are materials that are used inside the human body or come in direct contact with tissues in the human body such as bone, cartilage or soft tissue. Medical devices and biomaterials should be non-toxic, biocompatible, and depending on their use sometimes biodegradable.

1.1.1. The use of biomaterials for medical applications

Medical devices and biomaterials should be made from natural or synthetic sources that are non-toxic and biocompatible to avoid adverse cellular (e.g. cell death) or immunological (e.g. excessive inflammation) reactions. Researchers are interested in developing biomaterials with favourable properties, which would decrease negative biologic responses. This would enable patients to have a recovery to a great quality of life after implantation surgery. Materials used for the development of medical devices are generally categorised into four groups, namely metals, ceramics, polymers and composite materials.^{1, 7} Table 1.1. shows some examples of medically relevant materials and their applications.

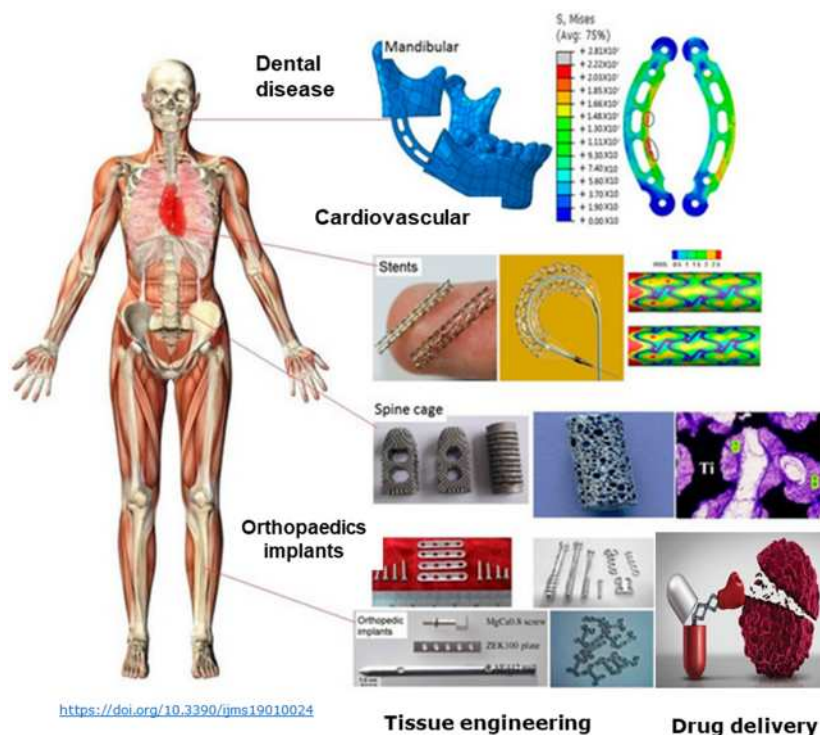


Figure 1.1. Examples of biomaterial applications used to repair or replace dysfunctional tissues and for the treatment of various disorders.

Adapted from Yang et al., *Int J Mol Sci* (2018).⁸

A group of synthetic polymers of polyacrylates has been found relevant in biomedical applications. They are synthesised by polymerisation from a wide array of acrylate monomers such as ethylene glycol dimethacrylate, heptadecafluorodecyl methacrylate, cyclohexyl methacrylate, dimethylamino-ethyl methacrylate and isodecyl methacrylate. These polymers are well-known for their good mechanical properties, transparency and biocompatibility.^{9, 10} Acrylate polymers are commonly used in many other biomedical applications^{11, 12}, including dental materials, bone cement for fixing prosthetic devices, hard or soft contact lenses as shown in Table 1.1. Recently, a group of acrylate polymers have been reported to be resistant to bacterial attachment.¹³ This capability illustrates the great potential of polyacrylate for the discovery of novel biomaterials.

Table 1.1. Biomedical applications of biomaterials.

Types	Materials	Applications
Metals	Stainless steel	Used as dental and surgical instruments such as fracture fixation, stents, screws ^{14, 15}
	Titanium	Used in maxillofacial surgery, cardiovascular surgery, joint replacement, orthopaedic ^{16, 17}
Ceramics	Calcium phosphate	Used for joint replacement as coating on metal, bone implants, bone graft ^{18, 19}
	Zirconia	Joint replacement ²⁰
Polymer	Polyethylene	Cardiovascular treatments, craniofacial reconstruction ²¹
	Poly (methyl methacrylate)	Bone cement lenses, bone substitutes, drug delivery systems ^{22, 23}
	Poly(vinyl alcohol)	Hydrogel formation nucleus pulposus, vitreous body replacement ^{24, 25}
	Poly (dimethylsiloxane)	Silicones are used as catheters, intraocular, lenses, drainage devices, ^{22, 26}
	Poly(ethylene glycol)	Hydrogels for the controlled release ²⁷
Composite	HA/alumina	Bone replacement materials ²⁸
	Cellulose /graphene	Bone tissue regeneration ²⁹

1.1.2. Biocompatibility of implants and medical device

Historically, the goal was to find biomaterials that were ‘inert’, with the ability to not induce any immune response. At present, new requirements in regenerative medicine mandate that biomaterials should be biocompatible. Biocompatibility is broadly defined as “*the ability of a material to perform its desired functions with respect to a medical therapy, to induce an appropriate host response in a specific application and to interact with living systems without having any risk of injury, toxicity, or rejection by the immune system and undesirable or inappropriate local or systemic effects*”.³⁰

General concepts of biocompatibility highlight the following³:

- Nontoxicity
- Cytotoxicity
- Osseointegration
- Non-combustible

The designed materials for biomaterials and medical devices should be capable of functioning *in vitro* and *in vivo* without exhibiting any undesirable local or systemic effects, such as immune responses, allergic, inflammatory, and carcinogenic responses surrounding the implant. Immune responses can lead to excessive inflammation, fibrotic healing of implants, fibrotic encapsulation, tissue destruction, and rejection of medical devices. Thus, this requires a deep understanding of the material or biology in order to develop technology that aims to reduce chronic inflammation and fibrotic capsule formation around implants. Therefore, it is beneficial to redefine biocompatibility that would also include promoting wound healing, reconstruction, and tissue integration.

1.1.3. Foreign body reaction to implanted biomaterials

When a material is implanted into the body, implantation often leads to a foreign body reaction induced by the immune system. Following implantation, proteins from blood and interstitial fluids adsorb onto the biomaterial surfaces. During this, acute phase of the inflammatory response, neutrophils and monocytes are recruited to the site of implantation and most of the recruited monocyte differentiate into macrophages, which heightens inflammation as shown in Figure 1.2.⁶ Within a few days of

implantation, macrophages release pro-inflammatory actors such as interleukin 6 (IL-6) and tumor necrosis factor alpha (TNF- α) in acute inflammation.³¹ This begins an acute inflammatory response that develops into foreign body response (FBR). In the chronic inflammatory stage, M2 macrophages reduce inflammatory activity by releasing anti-inflammatory cytokines such as interleukin 10 (IL10) and transforming growth factor beta (TGF- β) which promote pro-healing capacities^{32, 33} and, as well as their ability fuse to form foreign body giant cells (FBGCs) in order to increase the phagocytic ability. Over a period of weeks to months this inflammatory process develops into a chronic inflammation M2 macrophages release IL-10, TGF- β and IL-4 cytokines. These cytokines promote the fusion of fibroblast adhesion/proliferation, collagen deposition, and ultimately the formation of a largely avascular fibrotic capsule. Additionally, fibrotic capsule formation can separate an implanted medical device from the host tissue, thus avoiding device-tissue integration, which can cause device failure.

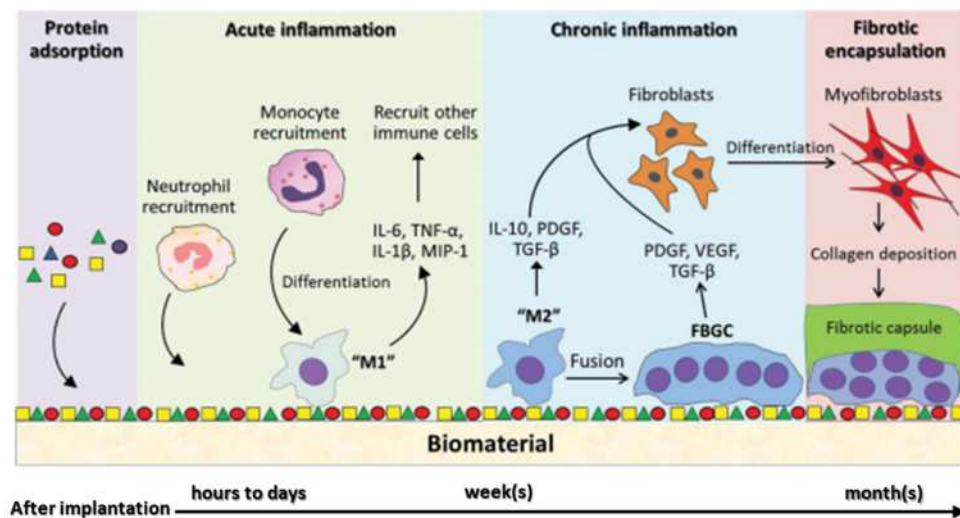


Figure 1.2. Foreign body reaction against biomaterials.

This shows the series of events leading to macrophage response to biomaterials. Adapted from Guoying and Thomas, *Macromol Biosci* (2018).⁶

1.2. Macrophages as innate immune cells

1.2.1. Origin and functional of macrophages

Macrophages are innate immune cells found in most tissues in the body. Tissue macrophages are often distributed in various body, organs such as the alveoli, liver, spleen, lymph nodes, lungs, bone marrow, bone tissue and central nervous system see Figure 1.3.³⁴ Macrophages differentiate from white blood cells which are called monocytes.^{35 36} Monocytes migrate from the blood to various tissues, where they differentiate into macrophages, adding to the pool of specialised macrophages in the tissues.^{37, 38} Macrophages play a variety of important immune-surveillance functions. Macrophages are immune system cells that provide protection against a wide range of diseases. They are critical mediators of the inflammatory process. On recognizing threats (e.g. pathogen/damage associated molecular patterns or foreign bodies), macrophages become activated; this enables them to release reactive oxygen and nitrogen species, which contributes to the killing of invading threats.³⁹ They also release pro-inflammatory cytokines which attract other immune cells to the site of injury or infection, where they all contribute to the inflammatory condition. Macrophages have been suggested to be the most important cell type that influences immune responses to biomaterials and medical devices.

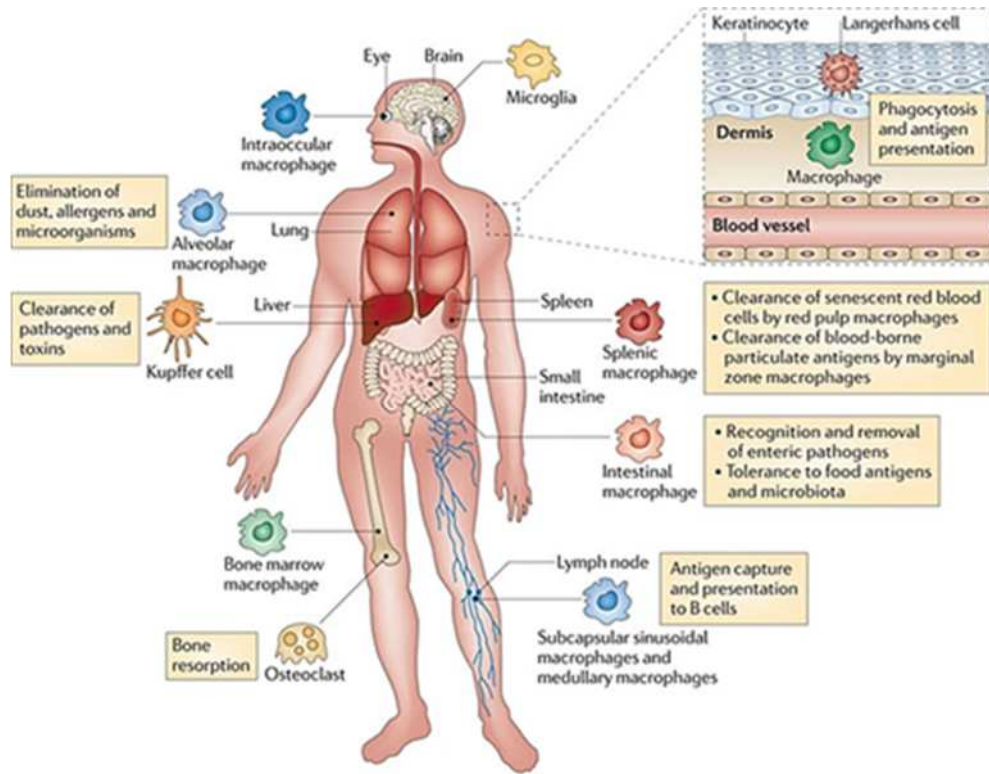


Figure 1.3. Distribution of macrophages in tissues.

Various populations of mature tissue macrophages are strategically located all over the body and conduct critical immune surveillance functions such as phagocytosis, antigen presentation, and immunological suppression. Adapted from Murray and Wynn, *Nature Reviews Immunology* (2011).³⁸

1.2.2. Macrophage classification

Macrophages have been broadly classified into two categories based on their functions, expressed phenotypic markers, expression of different transcription factors and cytokines namely, pro-inflammatory (M1) and anti-inflammatory (M2) macrophages.^{40, 41} M1 macrophages (classical activation) can be generated *in vitro* from monocytes and activated by the cytokines interferon gamma (IFN- γ)⁴² and/or lipopolysaccharide (LPS).⁴³⁻⁴⁵ M1 macrophages activated granulocyte macrophage colony-stimulating factor (GM-CSF), which increased pro-inflammatory activity.⁴⁵ M2 macrophages are different from the classical activation by anti-inflammatory and post-inflammatory wound healing responses⁴⁶ and can be generated *in vitro* from

monocyte by interleukin (IL-4).⁴⁷ Macrophages generated by colony-stimulating factor (M-CSF) have been proposed for M2 macrophages, causing the production of large amounts of the anti-inflammatory cytokine IL-10.⁴⁸ M1 and M2 macrophages classification as shown in Figure 1.4.

Classically activated macrophages

The term classically activated (M1) has been used to designate the effector macrophages which are produced during cell-mediated immune responses. The M1 macrophage is identified by the production of high levels of pro-inflammatory mediators, high production of reactive oxygen and nitrogen radicals.⁴⁹ Despite their usefulness in providing host defence against infections, this macrophage subset's unregulated activity can inflict massive damage to host tissues.^{40, 50} Additionally, GM-CSF can promote the differentiation of M1 macrophages and causes the production of higher levels of pro-inflammatory mediators.⁴⁵ The combination of two cytokines, granulocyte macrophage colony-stimulating factor (GM-CSF) and interferon gamma (IFN- γ) resulted in a macrophage phenotype that produced high levels of pro-inflammatory mediators such as IL-6 and TNF- α .⁵¹ Vogel *et al.* (2014) also demonstrated that IFN- γ /LPS activated macrophages produce more TNF- α and IL-6 than unactivated macrophages.⁴⁹ M1 macrophages produce nitric oxide or reactive oxygen intermediates (ROI) to protect against bacteria and viruses.

Alternatively activated macrophages

Alternatively activated macrophages (M2) can develop in response to innate or adaptive signals. In general, M2 macrophages are involved in the repair of damaged tissues and tissue remodelling during wound healing.⁵² They are thought to help keep tissues in a state of homeostasis by reducing their pro-inflammatory activity. Moreover, M2 macrophages are identified by production of high levels of anti-inflammatory and wound healing mediators when stimulated by interleukin 4 (IL-4) or interleukin 13 (IL-13) and macrophage colony-stimulating factor (M-CSF). Characterisation of activation has been widely investigated.⁵³ Vogel *et al.* (2014) recently reported that M2 macrophages activated with IL-4 had high expression of mannose receptor (MR, CD206) and produced the cytokine IL-10 which led to reduced

secretion of pro-inflammatory cytokines.^{53, 54} M2 macrophages produce ornithine and polyamines through the arginase pathway.⁵⁵

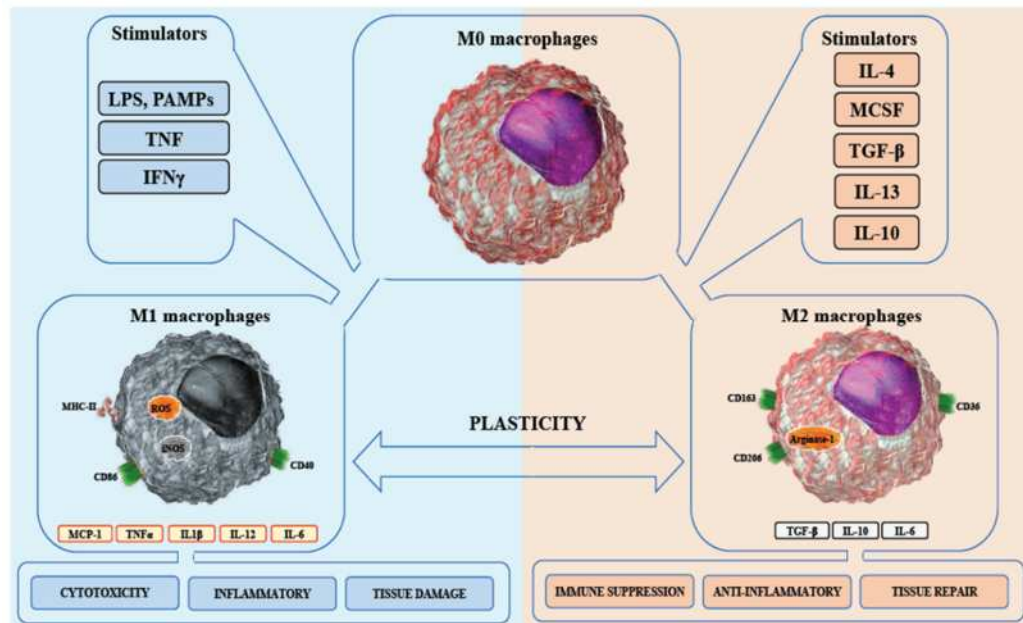


Figure 1.4. M1 and M2 macrophages classification.

Schematic illustrating the polarising stimuli, phenotypic markers, and functional characteristics of M1 and M2 macrophage subsets. Adapted from Ahmed and Ismail, J Cell Immunol (2020).⁵⁶

1.3. Host response to biomaterials and medical device

1.3.1. Immune response towards biomaterial insertion

When implants are inserted into body tissues, they are almost always recognised as foreign by the immune system, which then causes immunological reactions.^{57, 58} During implant insertion, vascularized tissues sustain localised damage; implants come into contact with blood, resulting in the formation of a blood-based provisional matrix around the implant surface.^{59, 60} This elicits responses from innate immune system cellular and non-cellular components, as well as the coagulation system. Complement and platelet activation, activation of tissue resident macrophages, and recruitment of neutrophils, monocytes, and mast cells are some of these reactions.⁶¹ During the acute phase of inflammation, several processes occur to stop bleeding and

eliminate harmful chemicals from injured tissues. Neutrophils and macrophages release reactive oxygen species (ROS), acid hydrolases, and inflammation cytokines and chemokines in response to the damage, while mast cells release histamine and other chemotactic factors. Collectively, these mediators promote the destruction of invading microorganisms and initiate the reparative processes that result in tissue regeneration.^{62, 63} Importantly, the duration of acute inflammation relies on the extent of tissue injury, the implant's placement, and the formation of a temporary matrix around the implant.⁶⁰ When acute inflammation caused by biomaterial implantation fails to be resolved, the inflammation becomes chronic (as it would in an implant-free tissue). As a result of the implant's constant activation of immune cells, chronic inflammation develops.⁶⁴ This level of inflammation is defined by the presence of mononuclear cells at the implant site, including inflammatory monocytes, macrophages, and lymphocytes. It has been demonstrated that macrophages are the primary drivers of implant-associated inflammation, which frequently results in implant failure.^{65, 66}

1.3.2. Role of macrophages in immune responses

As previously noted, inflammation is a key aspect of the host reaction to biomaterial implants. Macrophages adhere to plasma and ECM proteins adsorbed at the implant site via adsorption molecules known as integrins.^{59, 60} Macrophages recognise foreign ligands on implants, triggering the continual production of inflammatory mediators.^{60, 67} In an effort to eliminate the persistent foreign body, macrophages attempt to phagocytose the implant, a procedure that is frequently unsuccessful. If macrophages are unable to engulf and clear the foreign body, they enter a state called 'frustrated phagocytosis' and release large amounts of pro-inflammatory chemicals (such as cytokines and chemokines). When macrophages are in this state, they release parts of their lysosomes and digestive vacuoles into the surrounding tissues.⁶⁸ Still attempting to ingest the implant, macrophages fuse, generating foreign body giant cells (FBGCs); a defining trait of FBR. In FBR against implants, macrophages and FBGCs release ROS, which can lead to destruction of implanted biomaterials or devices.⁶⁶ Successful tissue repair processes necessitate a fast transition from M1 to M2 responses. A developing FBR, however, promotes a defective tissue healing process. Although the

mechanism is poorly understood, it is believed that macrophages and FBGCs produce substances that excessively increase the activities of (myo)fibroblasts and other tissue repair cells.⁶⁹ This is demonstrated by the excessive deposition of ECM proteins by myofibroblasts, the abnormal proliferation of cells, and the creation of granulomatous tissues around implants. Implants become encapsulated by these fibrous structures, isolating them from host tissues and so impairing their functioning. Biosensor devices, drug delivery devices, and electrical devices are examples of medical devices that are particularly sensitive to granulation tissue.^{57, 68}

1.4. The biological responses to biomaterial and medical devices: strategies for controlling their surface

1.4.1. Modification of biomaterial physical and structure properties

The discovery that related material properties influence biological reactions established a reasonable basis for developing synthetic materials that can influence biological responses positively. Various biomaterials have been developed to control biological processes such as adhesion, proliferation, migration, differentiation, and biomolecule production. In addition, biomaterials have been specifically designed to promote tissue growth which offer unique physical properties. Since the beginning, the main question that has driven biomedical researchers has been how to design and control the properties of materials to get a certain biological response.⁷⁰ Many different plastic types have been used in common tissue culture plastic. Untreated tissue culture plastic surfaces are more resistant to water absorption (hydrophobic) than treated tissue culture plastic surfaces, and treated tissue culture plastic surfaces promote the highest levels of cell attachment. Plasma etching has been frequently applied to modify the surface of polystyrene tissue culture and these plasma treatments are used to alter PS surfaces to improve cell growth.⁷¹ Moreover, surface chemistry modification has been used to alter the functional and phenotypic characteristics of several cell types.^{72, 73}

Champion *et al*, report the use of polystyrene to fabricate various sizes and shapes that must be created to initiate phagocytosis by macrophages.⁷⁴ Biomaterial surface topography has been demonstrated to selectively influence cell attachment. Several studies have found that nanoscale surface roughness increases extracellular matrix

(ECM) protein adsorption, which promotes osteoblast attachment.^{75, 76} Faia-Torres et al. demonstrated that nano/micro scale surface features promote mesenchymal stem cells osteogenic differentiation when compared to a smooth surface.⁷⁷ Numerous current materials have excellent physical and chemical properties, providing them desirable candidates for a wide range of biomedical applications. However, the clinical use can be limited by undesired side effects induced by uncontrolled inflammatory. The following section discusses strategies that have been employed for the modulation of macrophage responses by material physical and structural properties.

1.4.2. Modulation of macrophage phenotype and function by material physical and chemical properties

The modulation of macrophage phenotypes by various biomaterials and surface topographies has been extensively investigated. To manipulate macrophage responses, research has focused on the modification of biomaterial design principles to create microenvironmental circumstances that increase desired cell-material interactions. Immunomodulation is significantly influenced by topography, material physical properties such as porosity, and size/geometry. The wettability of a material's properties can also influence macrophage polarisation. Rostam et al. discovered that human monocytes cultured for 6 days on untreated hydrophobic polystyrene surfaces displayed an M2-like phenotype by expressing a higher level of mannose receptor (MR), IL-10, and CCL-18 than cells cultured on hydrophilic oxygen plasma-etched polystyrene surfaces.⁷² The TopoChip platform creates 2176 unique, randomly designed surface topographies using an algorithm.⁷⁸ These discoveries showed the importance of the pattern area of micropillars in identifying topographies that promote both the human macrophages attachment and phenotypes. Furthermore, Rostam et al. identified a variety of acrylates and methacrylates that encouraged macrophage attachment and differentiation towards pro or anti-inflammatory phenotypes *in vitro* and that were successfully translated into a mouse *in vivo* model with polymer-coated catheters.⁷⁹

1.5. Metabolomics analysis for immune cell characterisation

One of the challenges of systems biology and functional omics is to integrate genomics, transcriptomic, proteomic, and metabolomic information to have an in depth understanding of complex molecular interactions in biological systems.^{80, 81} Genomics is the study of the information in DNA and genetic in cells. Transcriptomics is the study of RNA and differences in mRNA expression using high-throughput technologies such as microarrays and high-throughput sequencing. However, due to the high costs of transcriptomics, only few studies include the high levels of replication necessary to satisfy adequate rigorous statistical standards.⁸² Proteomics is the large-scale study of proteomes which are sets of proteins produced in biological context. Metabolomics is a member of the omics family of system biology technologies that is primarily focused on the identification and characterisation of small molecules in a biological system (be it cells, tissues, organs, biological fluids or organisms).⁸³ This can be extended to dynamic temporal measurements as an organism's environment changes. The limitations of these approaches show that genomic, transcriptomic and proteomic studies, cannot alone serve as techniques that aid in the full understanding of various responses of biological systems to genetic and environmental changes, as well as metabolic stresses. As a result, metabolomics has been developed to investigate metabolic states and provide functional readouts in biological systems in order to provide a cellular state function readout. Metabolomics is an emerging technology, that involves quantitative and qualitative metabolite assessments. Metabolomics has recently been used to study the metabolic profile and expression of small molecules in biological systems.⁸⁴ Metabolomics has been applied to provide insights into immunomodulation. To date, the main focus of the field has been on using this information to identify biomarkers not previously known to be relevant to immune responses. Targeted metabolite assays, such as those for inflammatory cytokines, arginine, and citrulline, are currently used in clinical settings due to metabolite associations with immune regulatory pathways⁸⁵ and metabolic disorders.^{86, 87}

1.5.1. Metabolic approaches

The goal of metabolomics is to examine and analyse the metabolic complement of the target organism. However, this is currently unachievable since there are many metabolites across a broad chemical spectrum in organisms and a lack of a single acceptable analytical technique for the simultaneous qualitative and quantitative identification of all metabolites. To address specific concerns pertaining to biological systems, various metabolic techniques have been created based on a variety of analytic objectives. The following are definitions of the various metabolomics techniques proposed by Fiehn.^{82, 88}

Metabolite Target Analysis

Metabolite Target Analysis is an approach in which analysis is restricted to a particular chemical class of metabolites, metabolite pathway, or the direct detection of an individual metabolite created by a specific enzyme system. To prevent interferences from main metabolite components, it is common practise to perform significant sample purification processes to increase the sensitivity and precision of quantification. This technique is ideal for monitoring individual molecules in exceedingly complicated matrices, such as phytohormones.^{89, 90}

Metabolite

To understand the metabolome, it may not be necessary to identify every disturbance that occurs in each branch of metabolism. Consequently, this approach might be centred on the identification and quantification of a limited number of predefined metabolic pathways or metabolites with similar chemistry. This is mostly determined by the selected metabolomics platform. Typically, sample preparation is untargeted, allowing for the detection and quantification of a broad variety of metabolites; sample complexity is decreased by applying chromatographic separations prior to detection with mass spectrometry. This metabolite profiling technique is widely applied in all fields of biological (plants, fungi, animals, and environmental) metabolomics and in the clinical setting of drug research for biomarker discovery in biomedicine and drug development by tracing the metabolic fate of an administered drug.

Metabolomics

The impact of a mutation caused by a single genetic alteration may be directed to changes in metabolite levels from seemingly unrelated biochemical pathways because of pleiotropic effects. A comprehensive quantitative study of all metabolites in a biological system at a certain time and under certain conditions is required to elucidate these types of events. Metabolomics is a term for such a strategy. Well-established non-targeted sample preparation procedures and analytical techniques must be used to prevent omitting any metabolite of a biological system. To improve the resolving power of the analytical method utilised in metabolomics, high sensitivity, selectivity, matrix independence, and universality must be ensured. Since metabolomic data sets are complex due to the number of metabolites found in biological samples, appropriate informatics tools are needed to store, normalise, compare, and evaluate the obtained data to understand genetic interactions and reactions in biological systems.

1.5.2. Metabolomics technologies and applications

There are a wide range of techniques for the analysis of metabolic data from a cell or organism. Metabolomics studies typically use Fourier transform infrared (FT-IR) spectroscopy and mass spectrometry (MS) techniques because of their specificity and quantitative reproducibility.⁹¹ However, there are many analytical methods available for measuring the number of metabolites. Metabolomics are driven by a specific chemical class of metabolites and metabolite pathways. Increased understanding of this process will drive the advancement of the field of metabolomics. In this study, we will focus on mass spectrometry (MS).

1.5.2.1. Mass spectrometry (MS)

Mass spectrometry has been widely utilised in the field of metabolomics to profile a variety of metabolites in plants, microorganisms, and mammalian cells because MS-based techniques can provide sensitive, selective, and rapid quantitative and qualitative analyses. Mass spectrometry refers to the instrument used to detect the mass-to-charge ratio (m/z) and intensity of the various ionised analytes generated by

ionisation. Although all types of MS are composed of various elements, they combine three key components: an ionisation source, a mass analyser, and a detector. Mass analyser components are operated under vacuum to offer the best environment for ion transmission to the analyser and detector. Mass spectrometry (MS) analysis methods include liquid chromatography mass spectrometry (LC-MS), liquid extraction surface analysis mass spectrometry (LESA-MS), matrix-assisted laser desorption/ionization (MALDI), desorption electrospray ionization (DESI) and secondary ion mass spectrometry (SIMS). Liquid chromatography mass spectrometry (LC-MS)-based metabolomics is an effective approach for quantifying metabolites and identifying both known and unknown compounds in biological samples.⁹² Moreover, chromatography MS-based, techniques have a high sensitivity and thus a high potential for discovering new biomarkers for disease diagnosis and disease progression.⁹³ Metabolites can also be discovered using a combination of matching retention duration or retention index, mass spectral interpretation or comparison matching to pure compound mass spectra obtained under the same conditions in library databases. Typically, extraction of metabolites from biological samples is the first step in LC-MS-based metabolite studies. However, the technical limitations of LC-MS, especially in terms of its lack of reproducibility and using conventional LC-MS protocols typically require an average amount of 6 million cells to identify metabolic profiling in macrophages.⁹⁴ MALDI analysis involves the use of a matrix that is used to absorb the power from the laser, allowing the material desorption and ionisation and therefore sample modification, which is most commonly used in tissue or cells.⁹⁵ MALDI is a highly sensitive technique with different sample preparation procedures, e.g. matrices for ionisation of different analytes. It has been successfully applied as an identification method in clinical microbiology and is extensively utilised in routine laboratory practise due to its economic viability and diagnostic value.⁹⁶ MALDI-TOF provides the ability to identify and visualise in 2D high molecular weight compounds covering a broad range of molecules with a spatial resolution that ranges 5- 100 μm , a mass accuracy up to 40,000, it is advantageously applicable due to the existence of large databases for large molecules, including lipids and proteins.⁹⁷ For the work included MALDI might offer benefit for lipid detection, but it has poor sensitivities for molecules with molecular weights less than 200 (m/z). However,

SIMS does not require an application of matrix and so along with its high spatial resolution at submicron scale (200–400 nm) was preferred for this study.

Desorption electrospray ionisation (DESI) is an ambient ionization technique. DESI analysis is conducted in the sample's native environment, at atmospheric pressure, and with minimal sample preparation.⁹⁸ The main advantage of DESI is that it does not necessitate substantial sample preparation, as matrix fixation does in MALDI⁹⁹ However, its spatial resolution is also limited to about 250 μm , which is lower than that of MALDI (5 μm –200 μm) or SIMS (100 nm).^{100, 101}

Table 1.2 provides a brief overview of the advantages and disadvantages of both TOF-SIMS and MALDI-TOF.

Advantages		Limitations
MALDI (Laser beam)	<ul style="list-style-type: none"> ▪ 2D visualization ▪ Spatial resolution (10-50 μm) ▪ High molecular weight detection ▪ Mass resolution up to 40,000 ▪ Existence of large database (lipids, proteins ...) 	<ul style="list-style-type: none"> ▪ Require matrix spray ▪ Low sensitivity for low molecular weight ($m/z < 200$) ▪ Existence of analytes with high vapor pressure ▪ Some fluorescent analytes can absorb the laser beam ▪ No depth information
SIMS (Ion beam)	<ul style="list-style-type: none"> ▪ 2D and 3D chemical imaging and mapping ▪ Submicron scale (200-400 nm) ▪ Elemental and molecular analysis ▪ Identification of inorganics and organics components ▪ No labeling process ▪ High sensitivity for trace elements (ppm to ppb) ▪ Cold transfer option 	<ul style="list-style-type: none"> ▪ Impossible quantitative data ▪ Limited to small and medium-size molecules ▪ The presence of salts is a significant disadvantage

1.5.2.2. Secondary ion mass spectrometry (SIMS)

Secondary ion mass spectrometry generates ions for analysis using a primary ion beam of energetic particles (including Bi_n^+ , Ga^+ , Au_n^+ , C_{60}^+ and Ar_n^+) to cause secondary ion emission and ionisation from a solid surface.¹⁰² The selection of the primary ion source is determined by the objective of the study and the sample being analysed. Each beam has a unique overall performance and application suitability, including depth profiling, high spatial resolution imaging, and high sensitivity. SIMS technique provides detailed surface chemical information, including chemical group, element, and molecular details. In SIMS, a primary ion beam accelerates charged particles to the surface of a sample, causing surface molecules to be sputtered and a small fraction are ionised to form secondary ions, making them amenable to identification by a mass analyser as shown in Figure 1.5a. Traditionally, SIMS used monatomic ion sources such as O^+ ,

Ga^+ , Cs^+ , or Bi^+ . The monatomic ions penetrate deeply into the sample, causing damage (Figure 1.5b). Next, the development of polyatomic ion sources, such as C_{60}^+ , Au_3^+ , or Bi_3^+ , which are more suited for biological samples and low damage cross section.¹⁰³⁻¹⁰⁶

A clustered source with the same energy as a monoatomic source will have significantly less energy per atom as it impacts the surface and breaks up, their low kinetic energy per atom impact on the surface causes reduced fragmentation and enhance the secondary ion yield of larger ion fragments.^{103, 107} Mass spectra derived from GCIBs result in less fragmentation than those derived from smaller projectiles, allowing for the detection of molecular ions of a wider range of biomolecules with higher sensitivity. Consequently, it is reasonable to presume that the GCIB will be a valuable modality for bioimaging applications in which the sample consists of a complex array of fragile molecules.¹⁰⁸ Its disadvantage over mono atomic beams is its poorer focus.

Recent developments in gas cluster ion beams (GCIB) which can have varying cluster sizes are promising tools for SIMS applications because they reduce surface damage and increase intact molecular ion yield in comparison to C_{60}^+ ion sources.¹⁰⁹ The gas cluster source was first introduced in the SIMS study by Matsuo et al.¹¹⁰ The GCIB source generates electrically charged cluster ions composed of several hundred to tens of thousands of atoms.

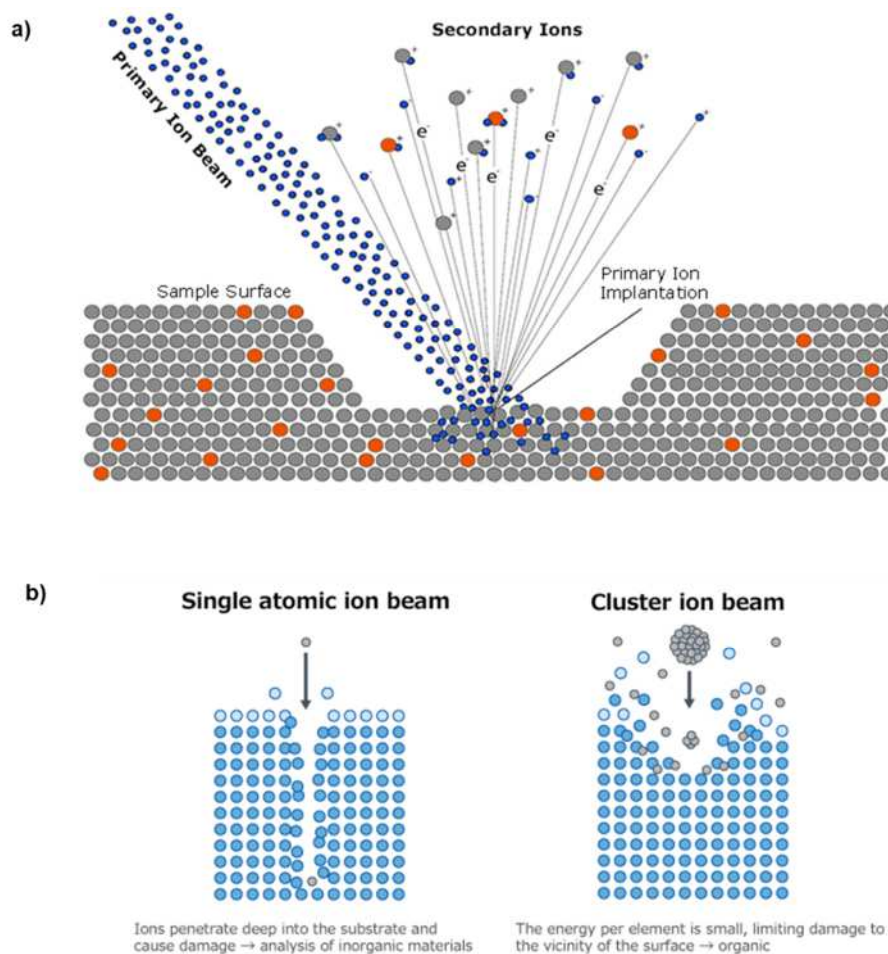


Figure 1.5. The principle of secondary-ion mass spectrometry.

a) The SMS process, the primary ion beam hits on the surface, image adapted from¹¹¹
 b) Comparison of the characteristics of ion beams of single atom ion beam and cluster ion beams. Adapted from¹¹²

Molecular dynamic (MD) simulations are computational sputtering experiments that reveal the interaction between the energetic primary ion and the targeted atomic of the sample surface. A MD simulation examination of the bombardment of Ag (111) was conducted with atomic, polyatomic and cluster ions (Figure 1.6).¹¹³ In the case of four primary ions bombarding on Ag (111) substrate, both Ga and Au₃⁺ ions penetrate deeply into the sample and causing damage with the mixing of the atomic layer in the sample and producing a lower secondary yield ion than C₆₀⁺ and Ar₈₇₂⁺. For C₆₀⁺ and Ar₈₇₂⁺, their low kinetic energy per atom placed on the surface of a material causes less damage, they have high secondary ion yields and the crater has a similar diameter of bombardment despite the fact that the depth is substantially lower in Ar₈₇₂⁺.¹¹⁴ The energy of the primary ions is transferred to the atoms and molecules in the sample

through a cascade of collisions, commonly known as the "collision cascade." A small part of the energy is transported back to the surface by the collision cascade, resulting in the desorption or sputtering of electrons, neutrals, and secondary ions.

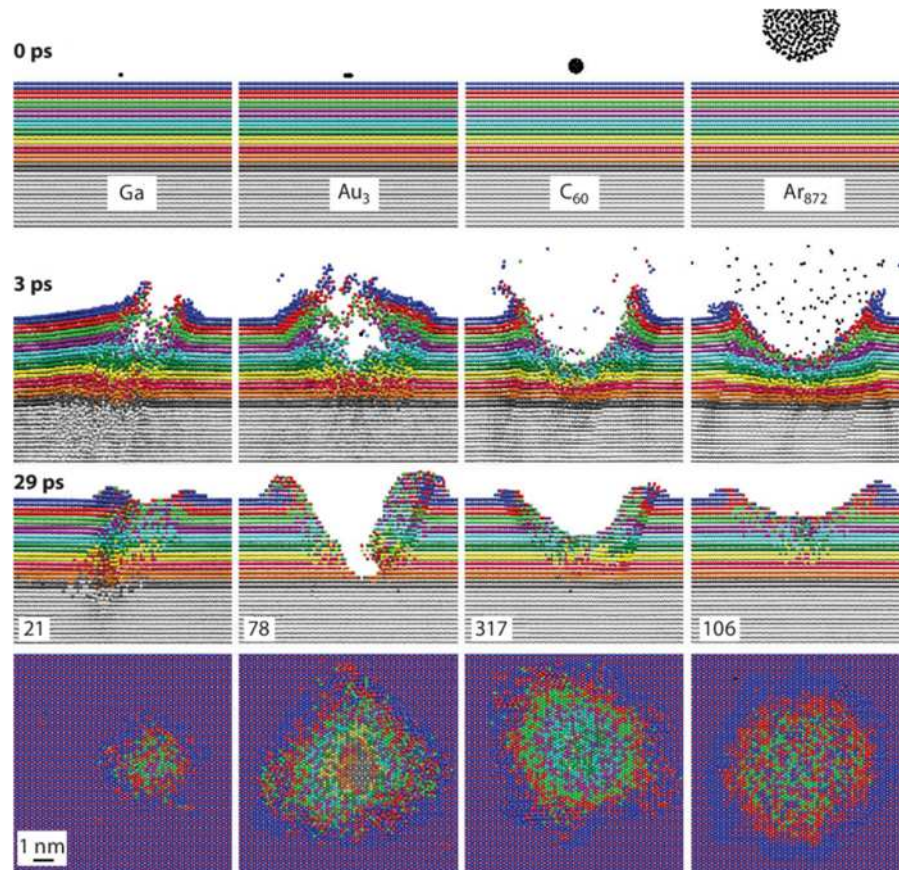


Figure 1.6. Molecular dynamics simulations of 15 keV Ga^+ , Au_3^+ , C_{60}^+ , and Ar_{872}^+ primary ions bombarding an Ag (111) substrate.¹¹³

The coloured layers represent the distance between the Ag layers. The grey layer begins at 4.6 nm depth. The first three rows show a cross section of the substrate, and the last row shows a top view to aid in identifying the damage area. The first row represents the initial state of the crystal, while the second and third rows show the damage's time evolution after 3 ps and 29 ps, respectively. The number in the bottom left corner of the third row displays the number of Ag atoms ejected per primary particle impact.¹¹⁴

1.5.2.3. ToF analyser

In the ToF analyser, the mass of the secondary ions is calculated by measuring their flight time to the detector after they have been transported to the mass spectrometer from point at the surface. In time of flight (ToF) SIMS, the mass of the secondary ions is calculated by measuring their flight time to the detector after they are accelerated from the surface. The secondary ions pass through a mass analyser to be separated according to their mass-to-charge ratio (m/z) following their generation. The following equations, which describe the transformation of potential energy into kinetic energy for all ions in accelerated regions, serve to illustrate this:

$$E_k = \frac{1}{2}mv^2$$

E_k = kinetic energy of particle (J)

m = mass of the particle

v = velocity of the particle

Other types of mass analyser are magnetic sector and quadrupole. Based on the respective mass resolving power, sensitivity, and duty cycle, each mass analyser has its own advantage and limitation.¹¹⁵ SIMS is commonly used in combination with a ToF analyser and provides high spatial resolution and a fast acquisition rate.^{116, 117}

1.5.2.4. Orbitrap analyser

The Orbitrap analyser was developed in the 1990's¹¹⁸ and is utilised in a variety of high-resolution mass spectrometry applications, such as LC/GC-MS, electrospray-MS, MALDI MS, and most recently with the HybridSIMS instrument (specifically the Q-Exactive HF Orbitrap).¹¹⁹ The general concept of an Orbitrap analyser involves capturing secondary ions in a C-trap and then injecting them orthogonally as a packet into the analyser, which consists of an interior spindle and an outer wall.^{118, 119} Voltages are applied from the outer wall and the interior spindle, causing injected ions to oscillate radially in an electric field-held stable trajectory. Each ion with a particular

m/z ratio will oscillate with both a radial vector and an axial vector (z-direction); the latter is detected as fluctuations in the continuous current on the potential plates. This change in current is measured over time and, using Fourier transformation, turned into a frequency domain and then a mass spectrum. The frequency of an ion's axial oscillation is directly proportional to its m/z ratio. Orbitrap analysers can produce a mass resolving power of $> 240,000$ for a peak of m/z 200, that is, $m_1/(m_1-m_2)$ for two partially overlapping peaks¹²⁰, i.e., it can distinguish between two overlapping peaks at this mass by 0.0008 u ($200/240,000$).

Orbitrap analysers are extensively used due to their high mass accuracy (displayed in parts per million (ppm) as the difference between the centre of the observed peak and the expected position). The Orbitrap routinely achieves precisions of 2 ppm and is capable of producing defects in the parts-per-billion range. ToF analysers, on the other hand, routinely attain much lower precision (> 20 ppm) traded off by their faster speeds. MS/MS capabilities are another advantage of the Orbitrap over previous analysers used for analysis. In mass spectrometry, the process of fragmenting a secondary ion into its constituent fragments is used to confirm original assignments, and it is also widely utilised to provide insight into the structural orientation of molecules. This is one of the most common applications of this technique.

The advent of the OrbiTrap analyser with SIMS and its high mass resolving power makes it an increasingly popular tool for biological samples in life science. Biomaterial research has focused on modifying materials chemistry to understand cellular response. Before the advent of the GCIB allowed SIMS data to be collected from organic structures without graphitisation and loss of signal, SIMS analysis of single cells required dynamic regime ($>1 \times 10^{13}$ primary ions/cm²), limiting it to studying elemental ions.¹²¹ Now SIMS can be used to study the spatial distribution of biological molecules within a single cell. Time-of-flight (ToF) detection techniques that allow efficient transmission and simultaneous detection of all ions delivered into the mass spectrometer with the sensitivity required to study the small analytical volumes sputtered under static conditions ($\leq 1 \times 10^{13}$ primary ions/cm²)¹²² have been developed, as have ion sources that can be focused to spot sizes less than 50 nm.

Static SIMS is a surface analytical technique that focuses a pulsed beam of primary ions onto the first top monolayer of the sample surface with a low primary ion beam dose ($<1 \times 10^{13}$ atoms/cm² or less) and each primary ion interacts with an undamaged sample that has not undergone prior primary ion impacts.¹¹⁵ While dynamic SIMS uses a high dose of primary ions, the depth profiles of samples, bulk composition, and detailed distribution of trace elements have high sensitivity and low detection limits.¹²³

1.5.2.5. Quantitative SIMS analysis

The objective of a standard quantitative analysis is to determine the concentration measurement of a specific analyte(s) within a designated system. It is commonly asserted that SIMS is a non-quantitative technique. But, the SIMS technique has the potential to perform a qualitative analysis with a high level of sensitivity, enabling the determination of the spatial distribution and composition of analytes both on the surface and in the depth in systems for which concentration standards are available in order to calibrate chosen ions as means to quantify certain components. However, process of interpreting mass spectrometric signal intensity in a quantitative manner is complex due to the fact that the intensity of secondary ions is not solely dependent on the concentration of the analyte, but is also significantly impacted by factors such as ionisation, sputtering of molecules, and the surrounding environment known as the (*matrix effect*). This has been widely noted for SIMS and other mass spectrometric techniques, not least MALDI where it is actively employed to improve sensitivity.¹²⁴ Numerous mass spectrometry techniques exhibit comparable limitations in quantification, prompting the development of diverse approaches to enhance quantitative information, such as the use of internal standards. Several studies attempted to achieve more reliable quantitative SIMS data, such as mitigating or comprehending the matrix effect and utilising internal standards to compensate for the matrix effect.¹²⁵⁻¹²⁷ The matrix effect is an essential obstacle to the development of the quantitative SIMS.

1.5.3. Metabolomics of macrophage

Metabolomics studies of macrophages are a rapidly increasing area in immunology. Problematic because several of these indicators are expressed by both M1 and M2 macrophage types, and many, particularly surface markers, do not provide significant insight into macrophage functional features.¹²⁸ Immunohistochemistry staining do not target for specific compounds. Metabolite profiling could be a potent technique for greater classification and understanding of macrophage phenotypes. Importantly, the metabolite composition of macrophages has been investigated including proteins, fatty acids, and lipids.¹²⁹ Rattigan et al., successfully identified changes in macrophage metabolism, following stimulation of cells with different proteins.¹³⁰ This seminal study found that IFN treated macrophages had higher levels of protein. Targeted mass spectrometry (LC-MS) was used to identify the lipid profiles of macrophage polarization with IL-4/ IL-13 or LPS. Results showed five classes of glycerophospholipids (GLs) and sphingomyelin (SM). Moreover, the amount of lysophospholipids (lysoGLs) was higher in M2 macrophages than M1 macrophages.¹³¹ In investigations by Masahiro et al., using Capillary Electrophoresis Time-of-Flight Mass Spectrometry (CE-TOFMS) to study macrophages activated with LPS for metabolite profiling showed the highest level of glycine production in amino acids.¹³² Lipid profiling is used to study the levels of arachidonate-containing phospholipids under the inflammatory activation of macrophages.¹³³ These studies, found that PI(20:4/20:4) is an inositol phospholipid molecule that regulates innate immune responses in macrophages. The concentration of PI(20:4/20:4) (10 μ M) the cells enhance the microbicidal capacity of macrophages as determined by reactive oxygen metabolite formation. To obtain a variety of metabolomics from macrophages or organisms, there are several techniques which are enabled to detect the metabolic profiling and each technique has a unique advantage capability. In terms of SIMS over LC-MS, it is direct analysis with the advantage of minimising sample preparation.

1.6. The scope of this thesis

The aim of this project is to characterise the *in vivo* response of polymers with pro- or anti-inflammatory *in vitro* responses that have been identified by a previous polymer micro array screening.^{72, 79} This project deals with the conversion of these polymer hits into model medical devices through coating and *in vivo* assessment in small animal models. Conventional immunohistochemical and staining readouts from the animal models are employed to identify the *in vivo* response at the material-tissue interface. In addition, this project developed the application of the novel 3D OrbiSIMS metabolomics approach to explanted devices for the first time, showing promise in elucidating the mechanism of cell response to the implanted polymers.

There are the main objectives:

1. Developing a method using immunohistochemical methods to isolate single macrophage cells polarised towards the M1 or M2 phenotype from primary monocytes to investigate the impact of morphological differences between the different subsets of macrophages.
2. Investigating and characterizing the metabolic profile of single cells in a naïve state and after cytokine polarisation into M1 and M2 macrophage.
3. Development of sample preparation and analysis protocols to achieve metabolomics of the individual macrophage cell using 3D OrbiSIMS (argon gas cluster ion beams).
4. Preparing model implant devices using novel bio-instructive polymers with immune-modulatory abilities selected from a previous polymer micro array screening and determining the influence of scaled-up polymers on the polarisation of macrophages, focusing on cytokine profiles and phenotype markers.
5. An *in vitro* feasibility study motivated to prepare an effective immune response for *in vivo* study. The polymer coated catheter segments implanted subcutaneously into mice for 28 days. Characteristic metabolites from the *ex vivo* sections adjacent to the implanted foreign body site using 3D OrbiSIMS.

Chapter 2

2. General methods

2.1. Cellular and molecular technique

2.1.1. Monocyte Isolation

Primary cells accurately replicate the *in vivo* tissue environment, and they are extracted directly from human or animal donor tissues for processing and culture under optimum circumstances.¹³⁴ These cells resemble the *in vivo* condition and physiology since they are produced directly from native bodily tissue and not modified. The main advantage of this model is that primary cells preserve functions and behaviours that are similar to those of tissues and organs in living organisms. As a result, they make great model systems for investigating cell physiology and biochemistry, including metabolic studies, signalling studies, drug toxicity.¹³⁵

Buffy coats from donors were provided by the National Blood Services, Sheffield, UK, following ethics committee approval (2009/D055, Research Ethics Committee, Faculty of Medicine and Health Sciences, University of Nottingham). Peripheral blood mononuclear cells (PBMCs) were isolated from heparinised blood by Histopaque-1077 (Sigma-Aldrich) density gradient centrifugation, as previously described.¹³⁶ Monocytes were isolated from PBMCs using the magnetic-activated cell sorting (MACS) isolation technique. This monocyte isolation approach routinely yields over 95% purity for CD14⁺ cells.

2.1.2. The polarization of macrophages

Macrophage polarisation is the process by which macrophages produce distinct functional phenotypes in response to specific microenvironmental stimuli and signals.¹³⁷ The macrophage phenotype has been simplified and divided into two groups: M1 (classically activated macrophages) and M2 (alternatively activated macrophages). This broad classification was generated by *in vitro* studies in which macrophages in culture were treated with cytokines that induced their phenotypic

transition to a particular state.¹³⁸ Following isolation, purified monocytes were suspended in RPMI supplement with 10% foetal bovine serum (FBS), 2mM L-glutamine, 10 ug/ml streptomycin, and 10 U/ml penicillin. Cells were supplemented with a differentiation cocktail consisting of the cytokines to polarise towards M1 or M2 phenotypes. (In this study, the polarization of macrophages, see more detail in chapter 3)

2.1.3. Enzyme linked immunosorbent assay (ELISA)

The ELISA is a commonly used immunological technique used to detect and quantify molecules of antibodies, antigens and peptides and proteins.¹³⁹ There are four different types of ELISA including direct, indirect, sandwich and competitive ELISA¹³⁹ shown in Figure 2.1. In this thesis, a sandwich ELISA was applied to detect cytokine levels. In sandwich ELISAs the cytokine is trapped (“sandwiched”) between a capture antibody and a detection antibody. Initially, the capture antibody (specific for the cytokine of interest) is coated onto the wells of the plate and incubated overnight, plates are washed with wash buffer to remove unbound antibodies. Then the sample or standards are added into the plate and incubated before the wells are washed. A second antibody is added and incubated, followed by wash to leave only those specific for the target of interest and a detection agent (streptavidin-HRP) is added and washed. Finally, the substrate is added to the plate to produce a colour change. The intensity of the colour solution is measured by the absorbance using a plate reader.

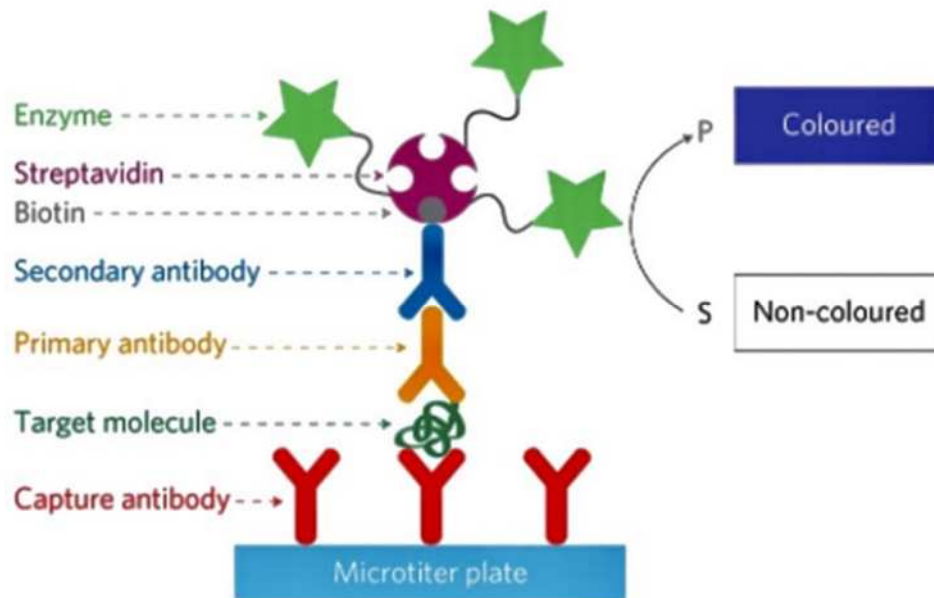


Figure 2.1. Schematic representation of the antigen detection using sandwich ELISA.

Image taken from Rica and Stevens, *Nature Nanotechnology* (2012).¹⁴⁰

2.1.4. Immunofluorescence staining

Immunofluorescence staining is a very important technique in biology research in order to detect specific target antigens of interest on cells or tissue sections^{141, 142}. There are two main methods available to detect antigens exist including, direct or indirect visualization Figure 2.2. Direct immunofluorescence staining requires the use of one antibody. Other indirect immunofluorescence staining requires the use of two antibodies: a primary antibody that binds to the specific target and a fluorophore-tagged secondary antibody, which recognizes and binds to the primary antibody, Indirect immunofluorescence methods have high sensitivity, and amplified fluorophore signals¹⁴¹. In this study indirect immunofluorescence was the approach employed on cell and tissue samples.

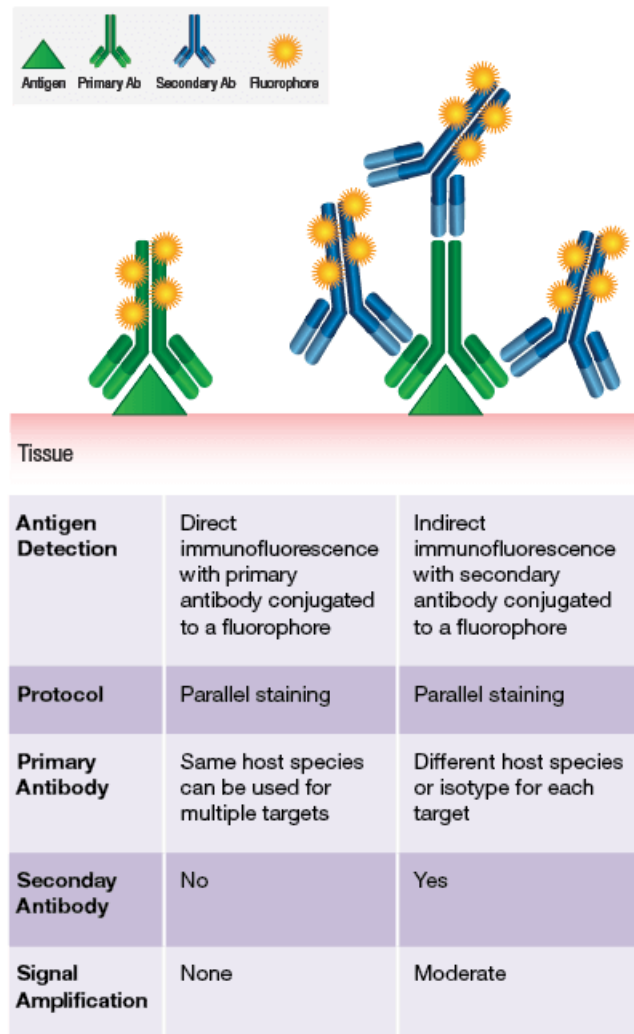


Figure 2.2. Illustration of different immunofluorescence staining between direct and indirect. Image source.¹⁴³

2.2. Polymer synthesis

2.2.1. Thermal polymerisation

Thermal polymerisation is a technique that converts monomers to polymer using a thermally activated initiator.¹⁴⁴ Free radical polymerization (FRP) is a polymerization process in which a polymer is formed by the sequential addition of free-radical building units. The reaction mechanism is divided into three stages¹⁴⁵ initiation, propagation, and termination (Figure 2.3). These states are described as follows: initiation includes the production of active free radical species by the thermal or

photochemical breakdown of initiators. The thermal initiator is homolytically cleaved in response to heat, producing a pair of free radicals. After its generation, the free radical reacts with the monomer functional group to form a chain radical. This is recognized as initiation. Propagation is the next phase of the process. Following the generation of the chain radical, it reacts with monomer units, converting the whole molecule into another radical. This is the beginning of the polymer chain. This radical chain is then extended by reacting with other monomer units. The final step of the polymerization process is termination. Termination starts when all monomers are consumed. Termination can occur as a result of a combination and disproportionation. In the former situation, two expanding polymer chains react with one another to generate a single non-reactive polymer chain. When a hydrogen atom is moved from one radical to the other, two polymers are formed: one with a saturated end and the other with an unsaturated end. In this work, the polymerization of an acrylate was performed using a thermal initiator. The polymer product was characterized by ^1H nuclear magnetic resonance (NMR) spectra. The number-average molecular weight (M_n), weight-average molecular weight (M_w), polydispersity (PDI) were determined by gel permeation chromatography (GPC)

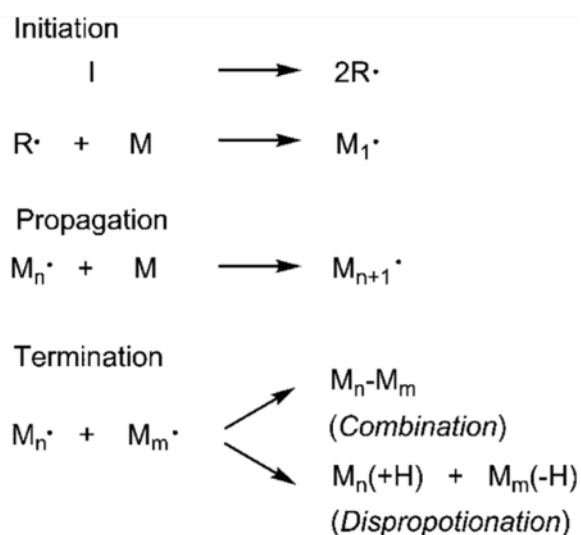


Figure 2.3. Schematic state of free radical polymerization.

The three stages: initiation, propagation, and termination. Image taken from Nakamura and Yamago, *Macromolecules* (2015).¹⁴⁶

2.2.2. Nuclear magnetic resonance spectroscopy (NMR)

NMR is an analytical chemistry technique used to determine the chemical structure of molecules¹⁴⁷. NMR technique can provide detailed information on physical properties as well as molecular conformation, reaction state, conformational exchange, and phase changes. When molecules are placed in a strong magnetic field, the nuclei of certain atoms act as if they were miniature magnets. When a broad spectrum of radio frequency waves is supplied to the sample, the nuclei begin to resonate at their respective frequencies. The nuclear spin is characterised by a quantum number (I) that varies depending on the isotope under consideration. NMR spectroscopy detects only atomic nuclei with $I = 1, 2, 3, \dots$ (NMR-active nuclei, such as ^1H , ^{13}C and ^{15}N). The resonant frequencies of the nuclei are measured and converted into an NMR spectrum, which plots peaks representing all of the correct frequencies on a graph (Figure 2.4). The height of each peak is proportional to the number of nuclei that resonate at that particular frequency. The spectrum consists of a number of peaks with different intensity as a function of a magnitude known as the chemical shift, which is calculated from the Larmor frequency of the different atomic nuclei present in the sample.

^1H NMR is available for characterization the composition, branching, and cross-link of copolymers.¹⁴⁸ During polymerisation, which can be followed in the reaction process by H NMR in order to achieve the desired information, NMR spectra of copolymers were obtained in this study and briefly in chapter 5.

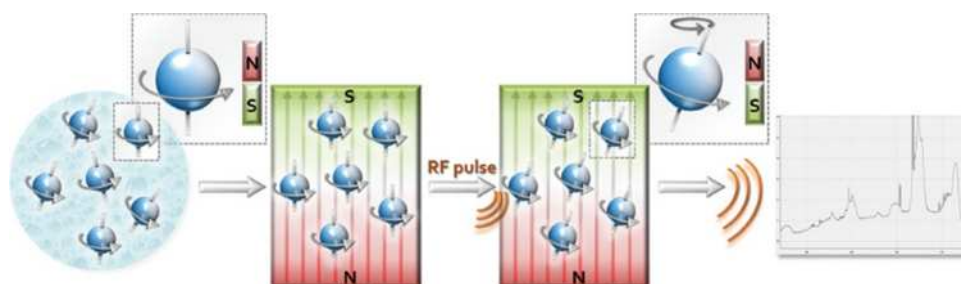


Figure 2.4. Simplified representation of the NMR.

Image taken from Daniela et.al, *LaboratoriumsMedizin* (2015)¹⁴⁹

2.2.3. Gel permeation chromatography (GPC)

Gel permeation chromatography, GPC is widely used for the identification of various analytes has been widely used to analyse polymers. GPC is used to determine the molecular weight, size, and structure of polymers, which has special significance for polymers in determining their molecular weight distribution (MWD).

The number average molecular weight M_n and the weight average molecular weight M_w as well as polydispersity index are calculated using the equation:

$$\bar{M}_n = \frac{\sum n_i M_i}{\sum n_i} = \frac{\sum w_i}{\sum n_i}$$

$$\bar{M}_w = \frac{\sum w_i M_i}{\sum w_i} = \frac{\sum n_i M_i^2}{\sum n_i M_i}$$

$$PD = \frac{\bar{M}_w}{\bar{M}_n}$$

Where,

M_i molecular weight of molecules i

n_i number of molecules with molecular weight i

W_i mass of molecules with molecular weight i

A measure of the polydispersity of a polymer is determined as M_w/M_n . For a polydispersed polymer, $M_w > M_v > M_n$, with the disparities between the average molecular weights increasing as the molecular-weight distribution (MWD) broadens, as demonstrated in Figure 2.5.

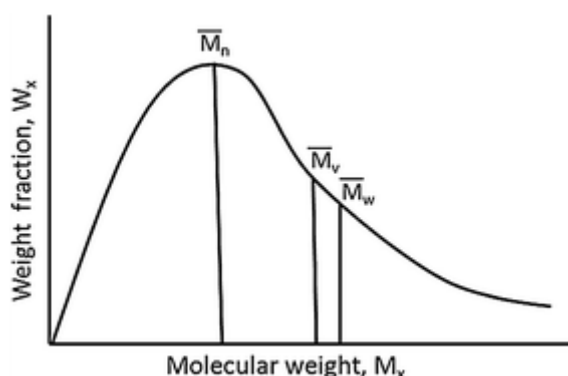


Figure 2.5. Distribution of molecular weights in a typical polymer sample.

Adapted from G. Odian, *Principle of Polymerization, 4th edn.* Wiley Interscience, (2004) ¹⁵⁰

2.3. Surface characterisation techniques

2.3.1. Time of flight – secondary ion mass spectrometry (ToF-SIMS)

ToF-SIMS is a very powerful tool for molecular characterization. ToF-SIMS is widely used for surface chemical analysis of organic and biological materials.¹⁵¹⁻¹⁵³ ToF-SIMS provides molecular information rich mass spectra, with depth and spatial resolution along with chemical sensitivity. Primary ion beam include primary atomic and liquid metal and gas cluster ion beams (Bi_n^+ , Cs^+ , C_{60}^+ , Ar^+ , Ar_n^+ , etc.) that are accelerated by a high potential to impact the surface and generate secondary ion and induce a fragmentation cascade (Figure 2.6a).¹⁵⁴ Neutral species as well as secondary ions (+/-), and electrons are adsorbed from the first few monolayers of the sample. According to the chemical composition of the surface, the dispersed particles are either neutral, positively or negatively charged. Typically, less than 1% of the sputtered materials are charged, and these are detected in either positive or negative ion mode by the mass analyser.

ToF-SIMS has sensitivity down to 20 ppm, mass resolution 7000 at $m/z=29$ with masses ranging from 1 to >10,000 amu. There are three different operation modes of ToF-SIMS analysis including surface spectra, imaging, and depth profiling (Figure 2.6b-d.) ToF-SIMS has also been used to determine the characteristics of polymer structures. Hook et al. carried out ToF-SIMS images which showed distinct fragmentation pathways on each printed as a polymer microarray.¹⁵⁵ They found distinct differences between the intensities for each materials studied. In this work, we achieve surface analysis of copolymer coated samples using ToF-SIMS.

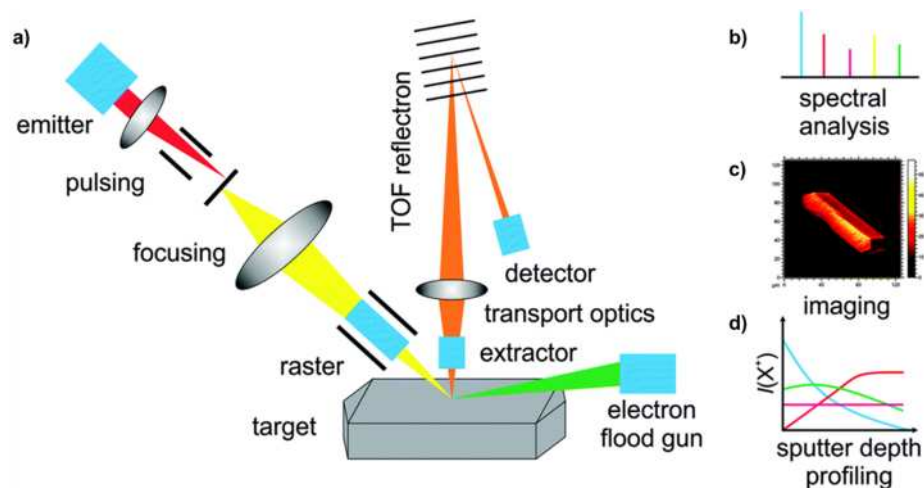


Figure 2.6. Schematic representation of a ToF-SIMS instrument.

a) the functional principle of a ToF-SIMS instrument. b) spectral modes. c) 3D imaging modes and d) depth profile modes. Image was adapted from Hofmann *et al.*, by *Physical Chemistry Chemical Physics*(2014) ¹⁵⁶

ToF-SIMS has been applied to biological samples since its beginning, but only recently with the advent of OrbiSIMS has the ready identification of endogenous molecules using its high mass accuracy and MS-MS capabilities become routine. Lanekoff *et al.*, used ToF-SIMS imaging to identify specific lipids with submicron resolution in a single cell.¹⁵⁷ It has been reported that large biomolecules, such as protein are heavily fragmented by the primary ion beams, resulting in small ($m/z < 200$) amino acid which from protein identity cannot be assigned. Ions detected by ToF-SIMS cannot always be assigned in an unambiguous manner, particularly in the case of complex biological materials to avoid the drawbacks of low mass resolving power and accuracy. The recent development of hybrid instruments such as the 3D OrbiSIMS instruments comprised of both a ToF-SIMS 5 (IONTOF GmbH, Germany) and a Q Exactive HF Orbitrap™ (Thermo Fisher Scientific, Germany), which are commonly used in proteomic and metabolomic research have brought the power to identify endogenous biomolecules to SIMS.

2.3.2. 3D OrbiSIMS

3D OrbiSIMS is a combination of a Time of Flight (ToF) instrument with an Orbitrap analyser. The ToF analyser provides high-speed ToF-imaging but low mass-resolving power. Orbitrap analyser provided high mass-resolving power and mass accuracy but is slow. Mass accuracy is quoted as a reciprocal in parts per million ((ppm) (<2)), high mass-resolving power (>240,000) for a peak of m/z 200 and high sensitivity. The mass-resolving power is calculated using the equation:

$$\text{Mass-resolving power} = m/\Delta m$$

where,

m mass

Δm full width of peak at half maximal height FWHM (Figure 2.7.)

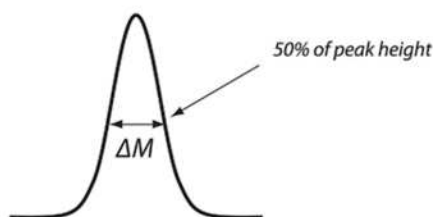


Figure 2.7. Definitions of resolution shows the “full width of the peak at half maximal height (FWHM) or 50% of peak height” definition.

The 3D OrbiSIMS can also perform MS on secondary ion by fragmenting them in a collision gas cell (MS/MS) to provide structural assignments. A diagram of the 3D OrbiSIMS instrument is shown in Figure 2.8a.¹⁵⁸ The principle of 3D OrbiSIMS analysis is based on the use of a focused dual beam and dual analyser (see Figure 2.8b), which shows ten different modes for spectrometry, surface spectra, depth profiling, 2D imaging and 3D imaging. Passarelli et al. demonstrated the advantages of employing a gas cluster ion beam (GCIB), GCIB-Orbitrap over an LMIG-ToF for extremely precise, high-mass resolving power spectral analysis. This is proven by the spectra in Figure 2.8c, which reveal that this mode (blue) has considerably greater resolving power than liquid metal ion gun (LMIG) LMIG-ToF analysis (black). The instrument

is also capable of performing MS/MS on identified species to confirm assignments and brings this technique in-line with other high-resolution mass spectrometry techniques.

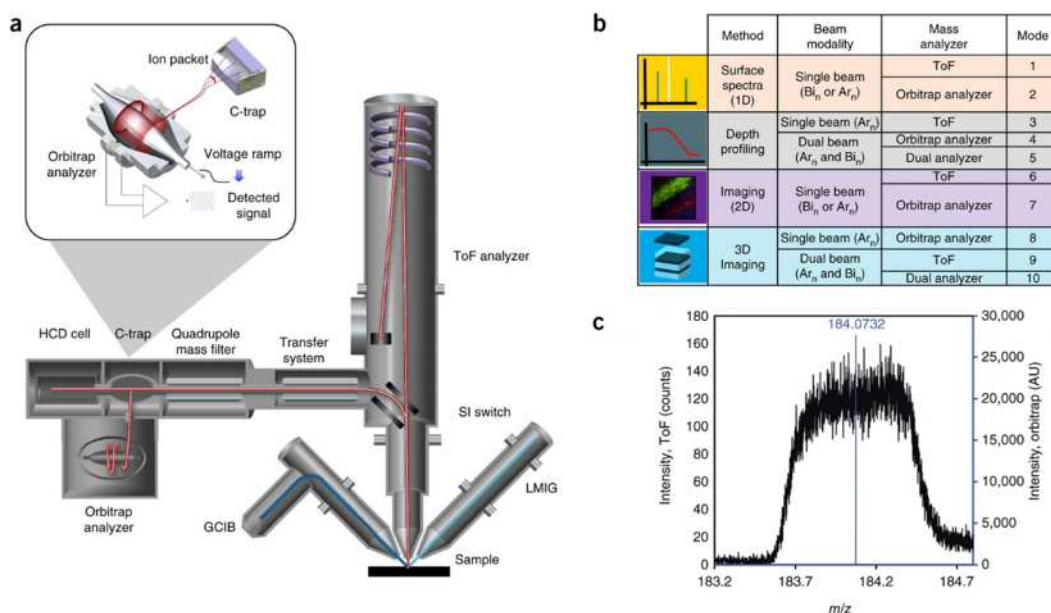


Figure 2.8. The 3D OrbiSIMS spectrometer and mode of operation.

a) A schematic of the 3D OrbiSIMS instrument. b) Chart of methodologies and ten operational modes for spectrometry. c) Demonstrating the superior resolution of the GCIB Orbitrap analysis in comparison to the LMIG ToF setup. Image was adapted from Passarelli et al., *Nature Methods* (2017).¹⁵⁹

3D OrbiSIMS is an exciting new advancement for biomedical imaging, allowing new insights into fundamental biological processes and pharmacological research and development. The 3D OrbiSIMS is provided with high-resolution of argon cluster ion beams for 3D imaging of biomolecular and organics. Recently, argon cluster ion beams have contributed to the advancement of increase ion yields and low-damage primary ion beam technology.¹⁶⁰ A cluster ion is composed of several hundreds to tens of thousands of atoms or molecules held together by interatomic interactions. A number of studies have shown that the larger cluster sizes Ar_{2000} to Ar_{4000} increase the yield of molecular species with low bombardment-induced damage. A cluster size of 3000 is the minimum suggested by *Gilmore et.al.*,¹⁶¹ this increased fragmentation of molecules occurs. Furthermore, as shown in Figure 2.9, this technique has been used to investigate single-cell metabolomic profiling in a rat alveolar macrophage cell with

high spatial resolution and high mass-resolving power using the 3D imaging mode. Passarelli et al. reported that they used 3D OrbiSIMS to identify the chemical formula of each fragment peak assignment in individual macrophage cells, revealing a putatively annotated 127 lipid species by the LIPID MAPS database as well as small biomolecules and metabolite species. The 3D OrbiSIMS is a powerful tool for investigation of metabolites and small molecules.

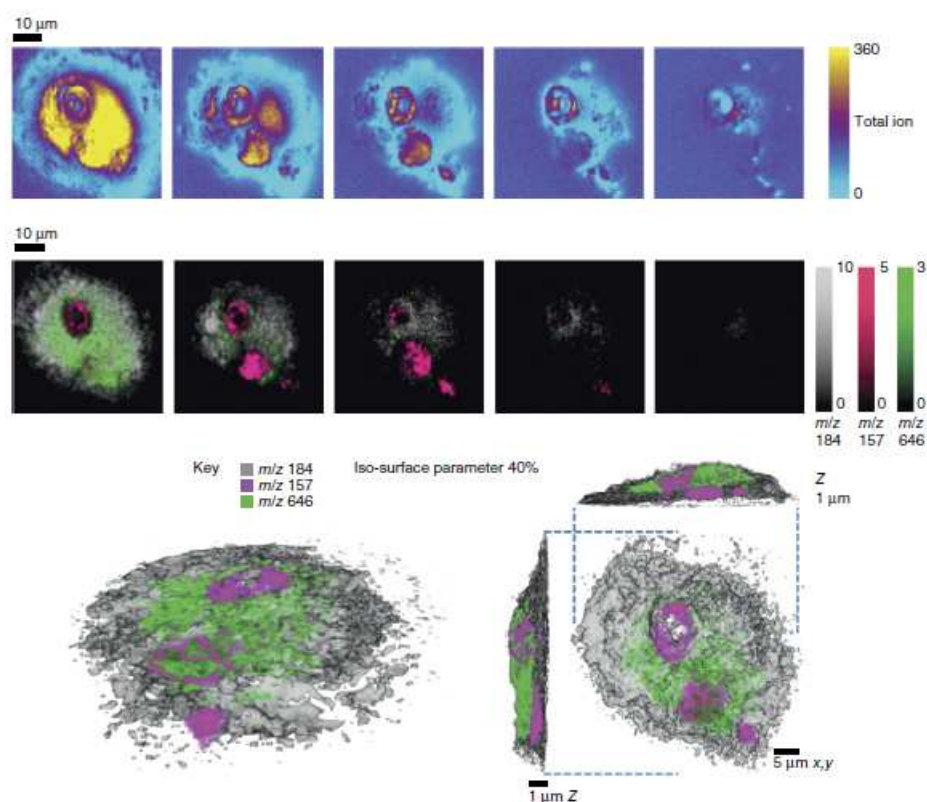


Figure 2.9. MS imaging of individual macrophage cell in rat alveolar, images showing the cell marker of phosphocholine at 184 m/z (gray), nuclear at 157 m/z (pink), and amiodarone $[M+H]^+$ at 646 m/z (green). Image was adapted from Passarelli et al., *Nature Methods* (2017).¹⁵⁸

Since the establishment of 3D OrbiSIMS, there have been several publications in the biomedical field. Meurs et al. compared data analysis from 3D OrbiSIMS to LESA-MS to detect metabolites from pediatric ependymoma tumour tissue and found predominantly nonpolar metabolites detected with 3D OrbiSIMS whereas LESA-MS was unable to identify them. Kotowska et al. demonstrated how the soft ionisation and

high mass resolving power capabilities may produce diagnostic amino acid fragments for protein identification using soft ionisation and high mass resolving power.¹⁶² Starr et al. used the 3D OrbiSIMS to characterize more detail the complex chemistry of the skin *in situ*.¹⁶³ The 3D OrbiSIMS provides a relatively high lateral resolution and chemical specificity for imaging cell components that are too delicate to be isolated from the sample. In the example presented by Aoyagi S. et.al, different biomolecule groups such as phosphocholine, chlorophyll and polysaccharide were observed during an *in situ* analysis of algae membrane.¹⁶⁴ In all study, 3D OrbiSIMS technology was successful in detecting molecular fragments with high mass resolving capability.

The key challenge to characterising this project is to understand the response of the human immune system to implanted biomaterials. Using the potential of 3D OrbiSIMS to achieve unbiased insight into on single cell analysis and *ex vivo* mouse tissue and their response to various biomaterials. This will be predicted to play a role in intercellular communication.

In this project, I applied 3D OrbiSIMS in two ways;

- Using 3D OrbiSIMS analysis to comprehensively examine cellular components with attribute capability demonstrates the potential of direct cell analysis for *in situ* metabolite profiling such as lipids, amino acids and metabolites. A 20 keV Ar₃₀₀₀⁺ analysis beam (mode 4) with a duty cycle of 4.4% and continuous adjacent areas on the cell were analysed for positive and negative polarities, as described in detail in Chapter 4.
- 3D OrbiSIMS technology for *in situ* chemical element analysis of *ex vivo* mouse tissue to bio-instructive polymers. 3D OrbiSIMS analysis was conducted using a Hybrid SIMS with mode 4 (single beam analysis, depth profiling with 20 keV Ar₃₀₀₀⁺, OrbitrapTM analyser), to allows assignments on *ex vivo* mouse tissue and detection of molecular ions of biomolecule groups. Adjacent areas on the tissue samples were analysed, 4 regions surrounding the implant region (catheter-tissue interface) per tissue section slide and 2 regions further away from the implant were consumed with both positive and negative polarity, as described in detail in Chapter 6.

Chapter 3

3. Label-free chemical characterisation of polarised immune cell *in vitro* and host response to implanted bio-instructive polymers *in vivo* using 3D OrbiSIMS

In this chapter, a protocol has been described for the direct analysis of individual cells after *in vitro* differentiation of naïve monocytes into M1 and M2 phenotypes using cytokines and *in vivo* anti- and pro-inflammatory macrophages generated at the site of a foreign body response mouse model following exposure to a catheter section coated. The development of a 3D OrbiSIMS methodology to investigate metabolic changes from *in vitro* and *ex vivo* sample with minimal sample preparation steps.

This manuscript submitted at bio-protocol. (Under review by bio-protocol reviewers)

Authors

Waraporn Suvannapruk^a, Max K Edney^b, Leanne E Fisher^c, Jeni C Luckett^d, Dong-Hyun Kim^a, David J Scurr^a, Amir M Ghaemmaghami^c and Morgan R Alexander^{a,*}

^a Advanced Materials and Healthcare Technologies Division, School of Pharmacy, University of Nottingham, University Park Nottingham, NG7 2RD, United Kingdom.

^b Department of Chemical and Environmental Engineering, Faculty of Engineering, University of Nottingham, University Park Nottingham, NG7 2RD, United Kingdom.

^c Immunology & Immuno-bioengineering Group, School of Life Sciences, Faculty of Medicine and Health Sciences, University of Nottingham, University Park Nottingham, NG7 2RD, United Kingdom.

^d School of Life Sciences, Faculty of Medicine and Health Science, University of Nottingham, University Park Nottingham, NG7 2RD, United Kingdom.

Label-free chemical characterisation of polarised immune cell in vitro and host response to implanted bio-instructive polymers in vivo using 3D OrbiSIMS

Waraporn Suvannapruk¹, Max K Edney², Leanne E Fisher³, Jeni C Lockett⁴, Dong-Hyun Kim¹, David J Scurr¹, Amir M Ghaemmaghami³ and Morgan R Alexander^{1,*}

¹ Advanced Materials and Healthcare Technologies Division, School of Pharmacy, University of Nottingham, University Park Nottingham, NG7 2RD, United Kingdom.

² Department of Chemical and Environmental Engineering, Faculty of Engineering, University of Nottingham, University Park Nottingham, NG7 2RD, United Kingdom.

³ Immunology & Immuno-bioengineering Group, School of Life Sciences, Faculty of Medicine and Health Sciences, University of Nottingham, University Park Nottingham, NG7 2RD, United Kingdom.

⁴ School of Life Sciences, Faculty of Medicine and Health Science, University of Nottingham, University Park Nottingham, NG7 2RD, United Kingdom.

Corresponding Author: *E-mail: morgan.alexander@nottingham.ac.uk

[Abstract]

The 3D OrbiSIMS technique is a powerful tool for metabolic profiling in biological samples. This can be achieved at subcellular spatial resolution, high sensitivity and high mass-resolving power coupled with MS/MS analysis. Characterizing the metabolic signature of macrophage subsets within tissue sections offers great potential to understand the response of the human immune system to implanted biomaterials. Here, we describe a protocol for direct analysis of individual cells after in-vitro differentiation of naïve monocytes into M1 and M2 phenotypes using cytokines. As a first step in vivo, we investigate explanted silicon catheter sections as a medical device in a rodent model of foreign body response. Protocols are presented to allow the host response to different immune instructive materials to be compared. The first demonstration of this capability illustrates the great potential of direct cell and tissue section analysis for in-situ metabolite profiling to probe functional phenotypes using molecular signatures. Details of the in vitro cell approach, materials sample preparation and explant handling are

3.1 Abstract

The 3D OrbiSIMS technique is a powerful tool for metabolic profiling in biological samples. This can be achieved at subcellular spatial resolution, high sensitivity and high mass-resolving power coupled with MS/MS analysis. Characterizing the metabolic signature of macrophage subsets within tissue sections offers great potential to understand the response of the human immune system to implanted biomaterials. Here, we describe a protocol for direct analysis of individual cells after *in vitro* differentiation of naïve monocytes into M1 and M2 phenotypes using cytokines. As a first step *in vivo*, we investigate explanted silicon catheter sections as a medical device in a rodent model of foreign body response. Protocols are presented to allow the host response to different immune instructive materials to be compared. The first demonstration of this capability illustrates the great potential of direct analysis of cell and tissue sectioning for in-situ metabolite profiling to probe functional phenotypes using molecular signatures. Details of the *in vitro* cell approach, materials sample preparation and explant handling are presented in addition to the data acquisition approaches and the involved data analysis pipelines required to achieve useful interpretation of these complex spectra.

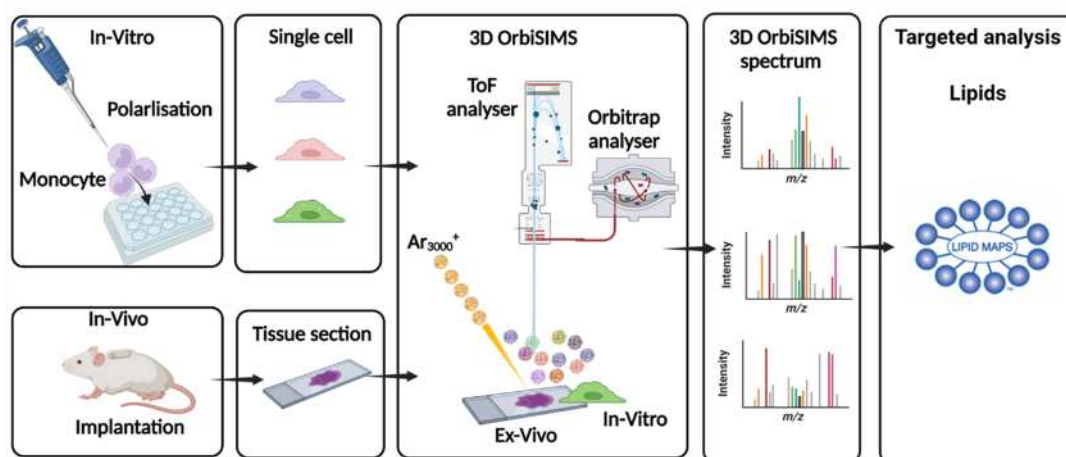


Figure 3.1. Schematic workflow of experiment.

Here, monocyte cells are grown and polarized towards to M1 and M2 macrophages and tissue samples were characterised. A gas cluster argon primary ion beam raster is used to identify and sputter single cells and tissue samples with the resultant complex

spectra compared using multivariate analysis complemented with targeted analysis for lipids.

3.2. Introduction

Mass spectrometry (MS) analysis methods including liquid chromatography-mass spectrometry (LC-MS)¹⁶⁵, liquid extraction surface analysis-mass spectrometry (LESA-MS)¹⁶⁶, matrix-assisted laser desorption/ionization (MALDI), desorption electrospray ionization (DESI) and secondary ion mass spectrometry (SIMS) have been used to detect chemical and biological compounds such as lipids, amino acids, peptides and proteins from cells and tissue samples.^{159, 167-170} Classes of biomolecules, including proteins, lipids and metabolites are vital cellular components that have been characterised and designated to perform specific functions essential to life. LC-MS based metabolite analyses typically start with extraction of the metabolites from the biological samples. Analysis of metabolites using LC-MS has been limited because it requires initial liquid extraction procedures and a significant number of cells (1-6 million) to obtain a sufficient signal, leading to a lack of molecular spatial information.¹⁷¹ LESA-MS technique is a powerful tool for global, high sensitive and multi-analyte analysis ranging from small molecule metabolites to lipids and proteins. This technique has the limitation of involving a solvent-based approach, which allows lipid and small molecule metabolite injection into the analytical instrumentation but loses any spatially resolved information on localisation within the sample. For solvent extraction, sample preparation of cells or tissue for metabolomics have a unique protocol for each molecular class and special importance when applied. Thus, solvent extracted metabolites from cells or tissue samples are specific to the extraction protocol.¹⁷²

Secondary ion mass spectrometry (SIMS) is a direct surface analysis technique that uses a primary ion beam which bombards the surface and generates neutral species and secondary ions¹⁷³, providing high lateral resolutions of <100 nm and high surface sensitivity. An electric field can be used to extract the charge species to obtain mass spectra using the ion flight times, ion images, depth profiles in both 2D and 3D.¹⁷⁴ SIMS surface analysis has also been established for the quantification of small

molecules in biological samples such as cells and tissue samples. Time-of-flight secondary ion MS (ToF-SIMS) is a surface analysis technique^{151, 153} that provides information rich mass, depth and spatial resolution along with chemical sensitivity. However, ToF-SIMS has insufficient mass accuracy and low mass resolving power for metabolite identification.^{175, 176} To overcome the pitfalls of low mass resolving power and accuracy, the 3D OrbiSIMS technique was developed which utilises the SIMS principle with a high mass resolving power (> 240,000 at m/z 200) and accuracy (< 2 ppm) and MS/MS capabilities of the OrbiTrapTM mass analyser.¹⁵⁹

Recently, the capabilities of the 3D OrbiSIMS instrument as a new means to assess the metabolomic profiles of biological samples have been investigated. For example, Kotowska et al., used 3D OrbiSIMS imaging and depth profiling to observe a protein monolayer biochip and the depth distribution of proteins in human skin.¹⁶⁹ The platform has also proved its ability to identify metabolite profiling in macrophages treated with different concentrations of the drug amiodarone.¹⁵⁸ Similarly, Suvannapruk et al. used the novel technique for metabolite identification in individual cells of macrophage subsets.¹⁷⁷ The method of analysis is vital for gaining new insight into metabolomic processes for identifying the metabolites of biological samples.

The development of materials with cell instructive properties could provide an effective biomaterial-based strategy for modulating cell behaviour to minimise adverse immune responses. Rostam et al. reported that changing the surface topography and chemistry of materials can impact macrophage adhesion and polarisation.^{79, 178} In this paper we describe for the first time the development of a 3D OrbiSIMS methodology to investigate metabolic changes derived from single anti- and pro-inflammatory macrophages *in vitro*. We also compare this to metabolic profiles from *in vivo* anti- and pro-inflammatory macrophages generated at the site of a foreign body response mouse model following exposure to a catheter section coated in known macrophage instructive surface chemistries. This method aims to directly analyse the metabolic profiles of macrophage phenotypes from *in vitro* and *in vivo* studies with minimal sample preparation steps.

3.3. Materials and Reagents

3.3.1. Cell culture

1. Buffy coats from healthy volunteers provided by National Blood Services, Sheffield United Kingdom, after obtaining informed consent and following institutional ethics approval (Research Ethics Committee, Faculty of Medicine and Health Sciences, University of Nottingham; FMHS 425-1221).
2. T75 flask (Corning 43064, catalog number: 10492371)
3. 50 mL falcon tube (Sigma-Aldrich T2318)
4. Stripette (Greiner Bio-One, catalog number: 760160)
5. Stripette gun (any vendor)
6. Micropipette (any vendor)
7. Pipette tips of various volumes (Fisher Scientific, catalog number:02-707-401)
8. Forceps (any vendor)
9. Nylon syringe filter 0.22 μm 25 mm (Minisart®, catalog number: 17845)
10. Bijou tubes (Thermo Fisher Scientific, catalog number: 129B)
11. Histopaque (Sigma-Aldrich, catalog number: 11191)
12. Phosphate buffered saline, PBS (Sigma-Aldrich, catalog number: D8537)
13. MidiMACS™ separator (Miltenyi Biotech, catalog number:130-042-302)
14. MACS® multiStand (Miltenyi Biotech, catalog number:130-042-303)
15. CD14 microbeads (Miltenyi Biotech, catalog number: 130-050-201)
16. LS columns (Miltenyi Biotech, catalog number: 130-042-401)
17. Ficoll (Cytiva, catalog number: 1754402)
18. Round glass slides (VWR, catalog number: 631-0149)
19. Glass slides (VWR, catalog number: 631-1553)
20. Tissue-Tek Cryomold Moulds (Agar scientific catalog number: AGG4580)
21. RPMI 1640 medium, (Sigma-Aldrich, catalog number: R0883)
22. Fetal Bovine Serum, FBS (Sigma-Aldrich, catalog number: F9665)
23. L-glutamine (Sigma-Aldrich, catalog number: G7513)
24. Penicillin-streptomycin (Sigma-Aldrich, catalog number: P0781)
25. 24-well plates, uncoated (CytoOne, catalog number: cc77672-7524)
26. Interferon gamma, IFN- γ (Bio Techne, catalog number: 285-IF-100)

27. Granulocyte-macrophage colony-stimulating factor, GM-CSF (Miltenyi Biotech, catalog number: 130-093-868)
28. Interleukin 4, IL-4 (Miltenyi Biotech, catalog number: 130-093-919)
29. Macrophage colony-stimulating factor, M-CSF (Miltenyi Biotech, catalog number: 130-096-493)
30. 70% alcohol (any vendor)
31. Optimal cutting temperature compound (OCT) (Agar scientific, catalog number: AGR1180)
32. Copolymer synthesis
 - CHMA-DMAEMA, pro-inflammatory macrophage (M1-like)
 - CHMA-iDMA, anti-inflammatory macrophage (M2-like)
33. Liquid nitrogen
34. Ammonium formate (Sigma-Aldrich, catalog number: 70221)

3.3.2. Animal study

1. Clinical-grade silicon catheter 13 mm diameter (Teleflex medical, catalog number: RUSCH170003)
2. Polymer synthesis
3. Dichloromethane (any vendor)
4. Female BALB/c mice

3.3.3. Equipment

1. Cell culture hood, class II (any vendor)
2. Scissors (any vendor)
3. Water bath (any vendor)
4. Centrifuge (any vendor)
5. Automated cell counter (any vendor)
6. Cell culture incubator (SANYO, model MC0-18A1C)
7. UV Clave ((any vendor))
8. Refrigerator (4°C) (any vendor)
9. Freezer (-80°C) (SANYO model MDF-C8V1)

10. Cryostat CM3050 (Leica microsystems)
11. Freeze dryer (any vendor)
12. Dip Coating Unit (Holmarc, model HO-TH-01)
13. Vacuum oven (Thermo Fisher Scientific)
14. 3D OrbiSIMS (IONTOF GmbH, Germany and Thermo Fisher Scientific, Germany)

3.3.4. Software

1. SurfaceLab software version 7.1 (ION-TOF, Germany), which utilized the Thermo Fisher provided application programming interface
2. LIPIDMAPS software (<https://www.lipidmaps.org>)

3.4. Consideration before starting

3.4.1. Peripheral blood monocytic cells (PBMCs) isolation

PBMCs are isolated from healthy blood donor buffy coats. Here, we isolated the monocytes that were used to generate macrophages.

3.4.2. Macrophage polarisation

Macrophages play a critical role in modulation of the immune response. Macrophages have a spectrum of functional phenotypes that is determined by the nature of stimuli they encounter. At either ends of this spectrum there are pro-inflammatory (M1 macrophages) and anti-inflammatory (M2 macrophages). *In vitro*, monocytes can be polarised towards M1 and M2 phenotypes using different cytokine cocktails. Here, we investigated and compared the relationship between M1 and M2 macrophage activation methods in human primary monocyte-derived macrophages using cytokines.

3.4.3. Implant sample preparation for *in vivo* studies

In previous work, Rostam et al, have identified polymers with immune-modulatory properties, in particular their ability to induce M1- and M2-like phenotypes in macrophages *in vitro* and *in vivo*.⁷⁹ In this study, we coat silicon catheter segments (dimensions 2.7 mm) with immune-instructive copolymers discovered in the Rostam et al article, to assess their ability to modulate macrophage phenotype in a mouse study of foreign body response.

3.4.4. *Ex vivo* tissue sample preparation for 3D OrbiSIMS

We prepared fresh tissue sections for 3D OrbiSIMS analysis in order to characterise metabolomic profiling of phospholipids in tissue section samples. The catheter and surrounding skin segment after 28 days of implantation were embedded in OCT and sectioned by cryostat.

3.5. Procedure

3.5.1. Preparation of PBMC isolation

1. Arrange equipment (Figure 3.2A).
2. Place a bottle of PBS in a 37°C water bath.
3. Spray the blood bag (50 mL) with 70% ethanol and place into the hood.
4. Cut the blood bag and place it into T75 flask (Figure 3.2B).
5. Top up pre-warmed PBS into T75 flask to a final of 150 mL.
6. Gently shake the flask to mix the blood and PBS.
7. Add 15 mL of Ficoll into each of the 4 falcon tubes (50 mL falcon tube).
8. Transfer 25 mL of blood-PBS mixture into the falcon tubes containing Ficoll using stripette. Angle the falcon tube to ~45-60° and ensure the blood does not mix with the Ficoll. (distinct layers are required).
9. Centrifuge at 1(acceleration/deceleration) | 800 x g | 30 mins | at room temperature (Figure 3.1C).
10. Use a stripette to remove some of the plasma and platelet layer (top layer).

11. Use a pasteur pipette to collect the white PBMC layer from 4 falcon tubes into 2 new falcon tubes.
12. Wash the aspirated PBMCs by adding PBS to a final volume of 50 mL.
13. Centrifuge 3(acceleration/deceleration) | 300 x g | 10 mins | at room temperature
14. After centrifugation, use a stripette to aspirate off the supernatant. Leaving behind two loose pellets.
15. Resuspend one of the pellets in a small amount of PBS and then combine with the second pellet.
16. Gently pipette up and down to reduce clumping.
17. Wash the aspirated PBMCs again with PBS by adding up to a final volume of 50 mL.
18. Centrifuge 3(acceleration/deceleration) | 200 x g | 10 mins | at room temperature.
19. Aspirate off the supernatant.
20. Resuspend the cell pellet in PBS.
21. Centrifuge 3(acceleration/deceleration) | 350 x g | 5 mins | at room temperature then aspirate the supernatant.
22. Prepare the MACS buffer: 50 mL PBS, 200 μ L EDTA and 250 μ L FBS.
23. The cells need to be resuspended and incubated with CD14⁺ beads. The volume of beads required depends on the required number of cells. For example, use 250 μ L of beads if less than 1×10^8 cells are required and up to 500 μ L of beads if more are required.
24. Resuspend the cell pellet in MACS buffer.
25. Add the corresponding volume of CD14⁺ beads (375 μ L when 3 mL MACS Buffer used).
26. Mix well and incubate the cells at 4°C for 20 mins and cover with foil.
27. After the incubation of the cell, add MACS buffer to a final volume of 20 mL into the cell suspension.
28. Centrifuge 3(acceleration/deceleration) | 350 x g | 5 mins | at room temperature.
29. Aspirate off the supernatant and resuspend in 4 mL MACS buffer.
30. Preparing of the MACS columns in hood, including black magnet holder, purple magnets, yellow filters, MS columns, bijou tubes (Figure 3.2D).

31. Wash the columns through with 3 mL MACS buffer each before adding the cell suspension.
32. Slowly pipette the cell suspension through columns.
33. Complete 3 x 3 mL MACS buffer wash steps once the cells have been added.
34. To remove the cells bound to the column, detach the column from the magnet.
35. Add 2 mL of MACS buffer and then use the syringe component to push the cells out into a falcon tube.
36. Count the cells, dilute the cells 1:20 before counting using trypan blue.

Note: Work in a sterile environment and all materials should be sterile. Do not pour off the supernatant, always use a stripette to remove plasma layer (top layer), to not dislodge the PBMCs layer.

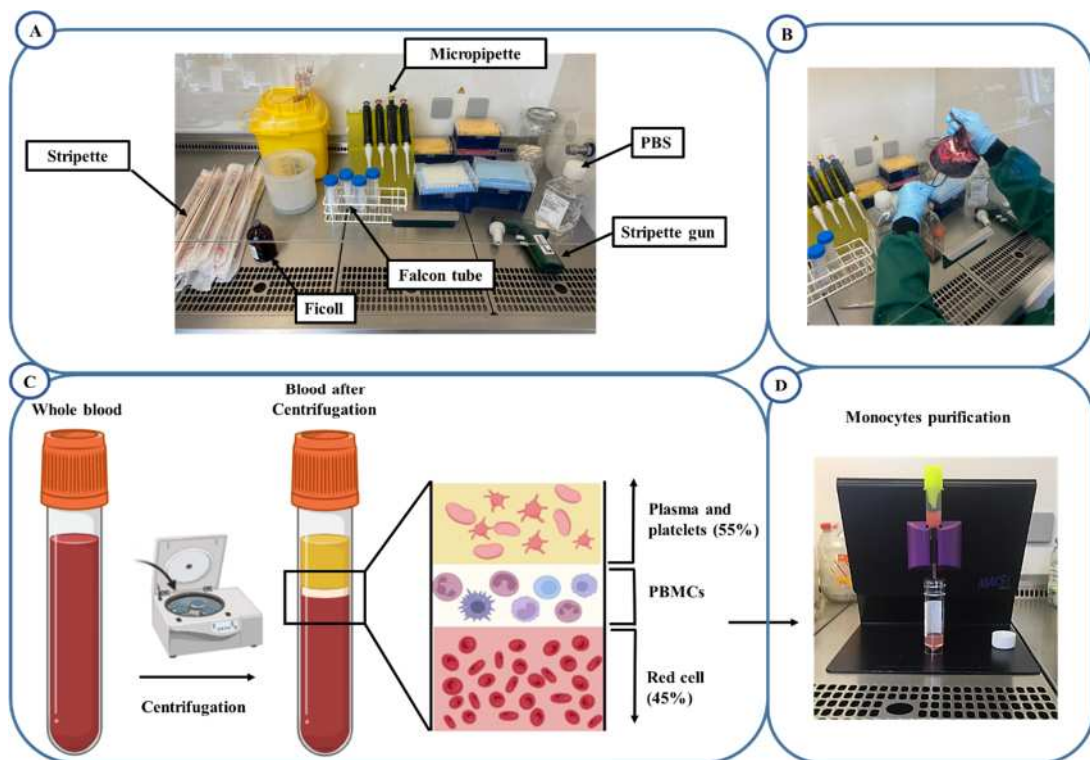


Figure 3.2. Processing of PBMC isolation.

A. Materials and reagents for PBMC isolation. B. Transfer of blood into T75 flask. C. Separation of whole blood components after centrifugation into discrete layers; plasma and platelets (top yellow layer), peripheral blood mononuclear cells (PBMCs) (middle white layer), and erythrocytes (bottom red layer). D. MACS columns for magnetic cell isolation.

3.5.2. Macrophage polarisation

1. Coat round coverslip with 200 μ L of poly-lysine to promote cell attachment.
2. Place the coated coverslips into 24 well plates.
3. Make up RPMI 1640 medium, supplemented with 10% heat inactivated FBS, 2 mM L-glutamine, 100 U/mL penicillin and 100 μ g/mL streptomycin and seed with 1×10^5 isolated monocytes. Place monocytes onto the coated coverslips.
4. Add the different cytokines to the monocytes to generate different macrophage phenotypes:
 - Naïve macrophages; add complete RPMI supplement with 10 ng M-CSF.
 - M1 macrophage; add complete RPMI supplement with 50 ng GM-CSF and 20 ng IFN- γ .
 - M2 macrophage; complete RPMI supplement with 50 ng M-CSF and 20 ng IL-4.
5. Incubate cells at 37°C with a humidified atmosphere of 5% CO₂ for 6 days.
6. On day 3 of incubation, remove 500 μ L of media from each well and replace with fresh medium containing the same concentration and mix of cytokines as on day 0.
7. Remove all supernatants.
8. Wash cells on the coverslips with 1 mL of 150 mM ammonium formate solution for 30 s three times to remove salts which cause unwanted signal suppression in SIMS instrument.
9. Plunge the cell samples into liquid nitrogen.
10. Freeze-dry frozen samples:
 - Switch on power at the rear to cool the chamber (-50°C). This step should take approximately 1 hour.
 - When the chamber is cool, place frozen samples onto shelves and close the lid.
 - Turn on the vacuum pump, the vacuum should be below 26.6 Pascal.
 - Freeze dry samples over a period of 12 hours to remove water.
11. Store in a sealed container at -80°C until analysis.

Note: we use uncoated tissue culture 24 well plates in order to promote cell attachment on the glass coverslip. Personal protective equipment must be worn, including protective gloves specifically designed for cryogenic handling, a closed lab coat, a face shield, and shoes when working with liquid nitrogen.

Cytokines are purchased in powders and reconstituted in stock solution and stored at -80°C.

3.5.3. Implant sample preparation for *in vivo* studies

1. Clinical-grade silicon catheters with a 2.7 mm diameter are cut to a length of 5 mm (Figure 3.3A and B).
2. Attach the catheter wall with microlance needles and clamp it with a dip coater (Figure 3.3C).
3. Dip catheter into Nusil MED1-161 silicone primer, which is made up of tetrapropylsilicate and tetra (2-methoxyethoxy), using dip coater with a dipping and withdrawing rate of 1 mm·min for 30 seconds.
4. Keep the catheter dry at room temperature for 2 min.
5. Make up a copolymer synthesis solution in dichloromethane (5% w/v):
 - CHMA-DMAEMA, pro-inflammatory macrophage (M1-like)
 - CHMA-iDMA, anti-inflammatory macrophage (M2-like)
6. MED1-161 coated catheter dip into the copolymer solution by dip coater with a dipping and withdrawing rate of 1 mm·min for 30 seconds for 2 times. (Figure 3.3C).
7. Dry the catheter overnight at room temperature then dry in a vacuum at 50°C for 7 days to remove solvent. (Figure 3.3D) and implantation (Figure 3.3E).

Note: the step of the catheter drying after coat with the copolymer, leaving them at the room temperature for overnight because if you put directly in vacuum the surface of the catheter, it can get the bubble or not smooth on the catheter surface.

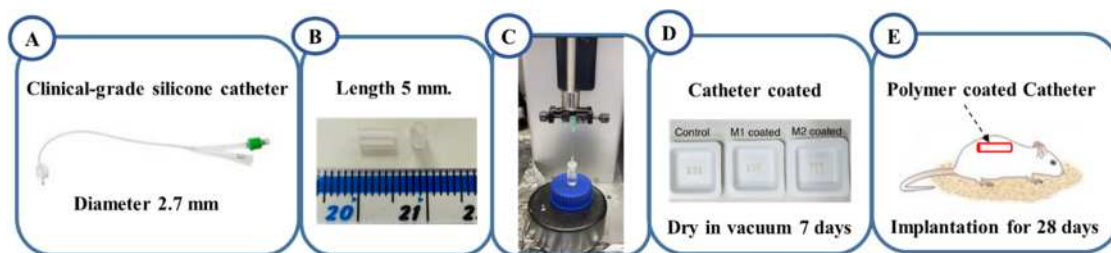


Figure 3.3. Schematic workflow of a catheter coated with copolymer for in vivo study. A. Clinical-grade silicone catheter. B. The catheters were cut to a length of 5 mm. C. Coating of catheter segments in immune instructive chemistries using dip coating. D. Catheter coated sample. E. Coated catheter segments are implanted in mice for 28 days.

3.5.4. *In vivo* study

In vivo studies are approved by the University of Nottingham Animal Welfare and Ethical Review Board and carried out in accordance with Home Office authorisation under project license number PP5768261. Female BALB/c strain, 19-22g mice are used in these studies. Mice are housed in individually ventilated cages (IVCs) under a 12 h light cycle, with access to food and water ad libitum. The weight and clinical condition of the mice are monitored daily. Silicone catheter segments coated with synthesized polymers are sterilized by UV light for a period of 20 min.

1. Catheters are implanted into mice for 28 days, catheters without a coating are used as a control.
2. Carprofen was administered 5 mg/kg for 1 hour prior to surgery.
3. Mice are anesthetised using 2% isoflurane and an area shaved on their flank and cleaned using Hydrex skin cleaner.
4. Catheter is inserted subcutaneously using a trocar needle and displaced 1 cm from insertion site.
5. Gluture skin adhesive used to seal insertion site and the animal is recovered.
6. At the end of the animal studies, on the 28 days, mice are humanely sacrificed by CO₂ euthanasia.

3.5.5. *Ex vivo* tissue sample preparation for 3D OrbiSIMS

The catheter segment and surrounding skin is prepared for 3D OrbiSIMS analysis.

1. Cut the 5.5 cm × 5.5 cm fresh tissue samples into three vertical cross sections and lay them into a mould containing OCT, ensure that cross-sectional layers are facing upwards (Figure 3.4A).
2. Push the sample all the way through the OCT, this is to avoid excessive slicing during cross-sectioning to reach the tissue. While pushing the tissue, be careful to avoid bubbles until none of the tissue remains exposed (Figure 3.4B).
3. Place the mould into liquid nitrogen slowly and carefully to minimize splashing and rapid freezing.
4. After freezing, frozen tissue samples are placed in a cryostat chamber at -20°C.
5. The samples are mounted on a metal “chuck” with OCT and kept frozen at a cutting temperature of -20°C (Figure 3.4C).
6. The sample on the chuck is mounted on the microtome and sectioned using CM1850 cryostat (Leica microsystems) (Figure 3.4D).
7. The tissue sample is cut a thickness of 10 µm and mounted on a slide (Figure 3.4E).
8. Tissue section slides are washed with cold DI water for 30 s three times and cold 70% ethanol for 30 s to remove fat and lipids which can increase the sensitivity of detection for some unwanted molecules.
9. Frozen tissue sections are plunged into liquid nitrogen.
10. Frozen samples are freeze-dried:
 - Switch on power at the rear to cool the chamber (-50°C). This step should take approximately 1 hour.
 - When the chamber is cool, place frozen samples onto shelves and close the lid.
 - Turn on the vacuum pump, the vacuum should be below 26.6 Pascal.
 - Freeze dry samples over a period of 12 hours to remove water.
11. Directly put the slide in a microscope slide box cooled on dry ice.
12. Store the microscope slide box at -80°C until analysis.

Note: Work requires the need to wear proper personal protective equipment (PPE) when handling liquid nitrogen to prevent contact. When sectioning tissue/catheter samples, mount the section quickly using electrostatic effects from the slide.

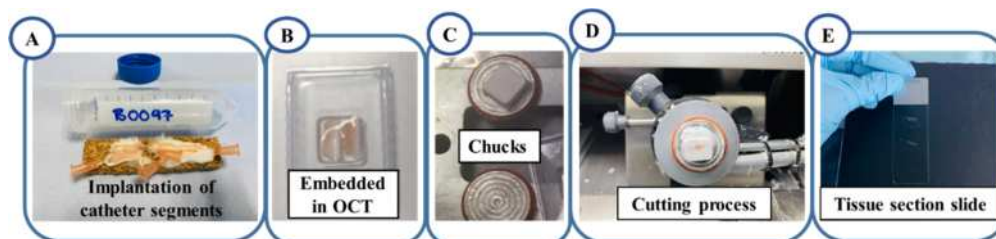


Figure 3.4. Schematic workflow of fresh tissue section preparation for 3D OrbiSIMS.

A. The catheter and surrounding skin segment after 28 days of implantation. B. Tissue embedded in OCT. C. Spread a generous amount of OCT on the metal chuck and quickly lay tissue embedded samples on it. D. Cutting the tissue section using a CM1850 cryostat. E. Mounting tissue section on the glass slide.

3.5.6. 3D OrbiSIMS analysis

1. Take the cell sample slides and tissue section samples on the slides from the -80°C freezer and warm them to room temperature without opening.
2. Mount the sample on the backmount holders or topmount holder and lock with screw, ensure screw are tightened and samples cannot move (Figure 3.5A and B).
3. Take a photo in the photo box of the sample holder before loading it into the instrument to mark the sample location.
4. Get the sample into the instrument, load the sample holder onto the transfer arm via the bayonet socket into the 3D OrbiSIMS instrument airlock for analysis (Figure 3.5C).
5. The Orbitrap analyser should be calibrated using silver cluster ion patterns from a silver foil.
6. 3D Orbitrap secondary ion mass spectrometry (3D OrbiSIMS) analysis conduct using a Hybrid SIMS instrument (IONTOF, GmbH) with Mode 4, depth profile (single beam 20 keV Ar₃₀₀₀⁺, OrbitrapTM analyser).

7. Secondary ions collect using the Q Exactive HF at the 240,000 at m/z 200 mass resolution setting in both positive and negative ion mode.
8. The electron flood gun operates with an energy of 21 eV and an extraction bias of 20 V for charge compensation and the injection time was 500 ms.
9. For all Orbitrap data, mass spectral information collects from a mass range from 75 to 1125 m/z .
10. *In vitro* study, the total ion dose per measurement 3.95×10^{11} ions/cm² a duty cycle of 4.4%, the pressure in the main chamber is maintained at 1.6×10^{-6} mbar using argon gas flooding and continuous GCIB current of 230 pA over an area of $150 \times 150 \mu\text{m}$ with crater size $233.1 \times 233.1 \mu\text{m}$.
Ex vivo study, the total ion dose per measurement 5.21×10^{10} ions/cm² a duty cycle of 4.4%, the pressure in the main chamber is maintained at 8.9×10^{-7} mbar using argon gas flooding and continuous GCIB current of 230 pA over an area of $100 \times 100 \mu\text{m}$ with crater size $180.0 \times 180.0 \mu\text{m}$.
11. Move the stage to a sample area of interest (Figure 3.5D and E).
12. For cell sample analysis, 3 cells per samples with positive and negative polarity.
For tissue sample analysis, 4 areas surrounding the foreign body site per one tissue section slide with both positive and negative polarity.

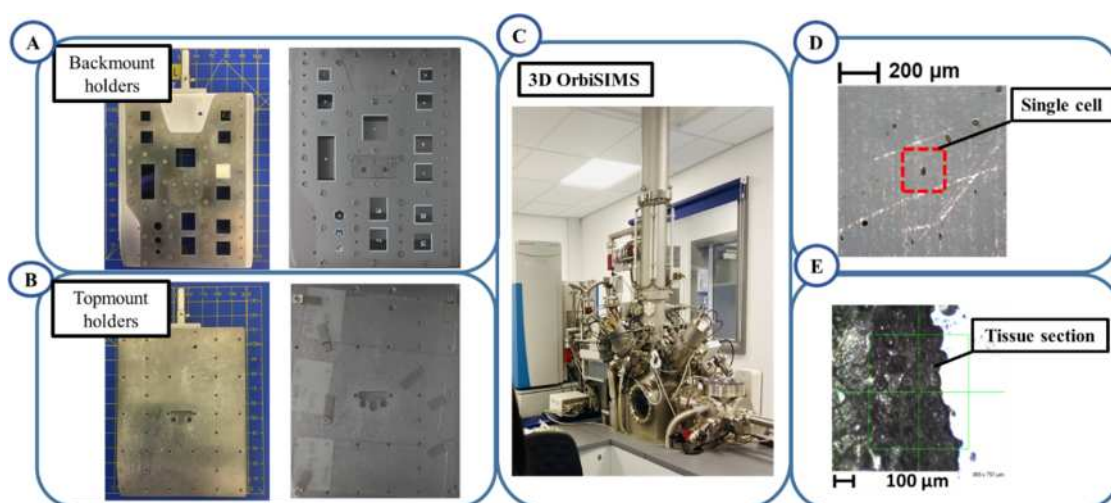


Figure 3.5. Transfer sample to the stage.

A. Backmount holder to fix the sample (left), cell on coverslip samples mount on the backmount holder (right). B. Topmount holder to fix the sample (left), tissue section slides mount on the topmount (right) C. 3D OrbiSIMS instrument at the University of Nottingham. D and E. The optical images of single cells and tissue section acquire within the instrument before analysis by the gas cluster ion beam.

3.5.7. Data analysis

Analyse data by using SurfaceLab software version 7.1 (ION-TOF, Germany).

1. Open data of each sample on SurfaceLab software, select the data an itax file and click open.
2. The peak lists are created by SurfaceLab.
3. Search peaks: the minimum peak area as 1000 which distinguished a real from a noise peak determine using a peak search with surface lab software.
4. Discount all peaks below this number as being noise peak and not include in further data analysis.
5. Export peak list as secondary mass ion and secondary intensity from the software.
6. Import the peak lists from the OrbiTrap analysis of the single macrophage cells and tissue section sample into LIPIDMAPS database to identify the lipids species (Figure 3.6A-C).

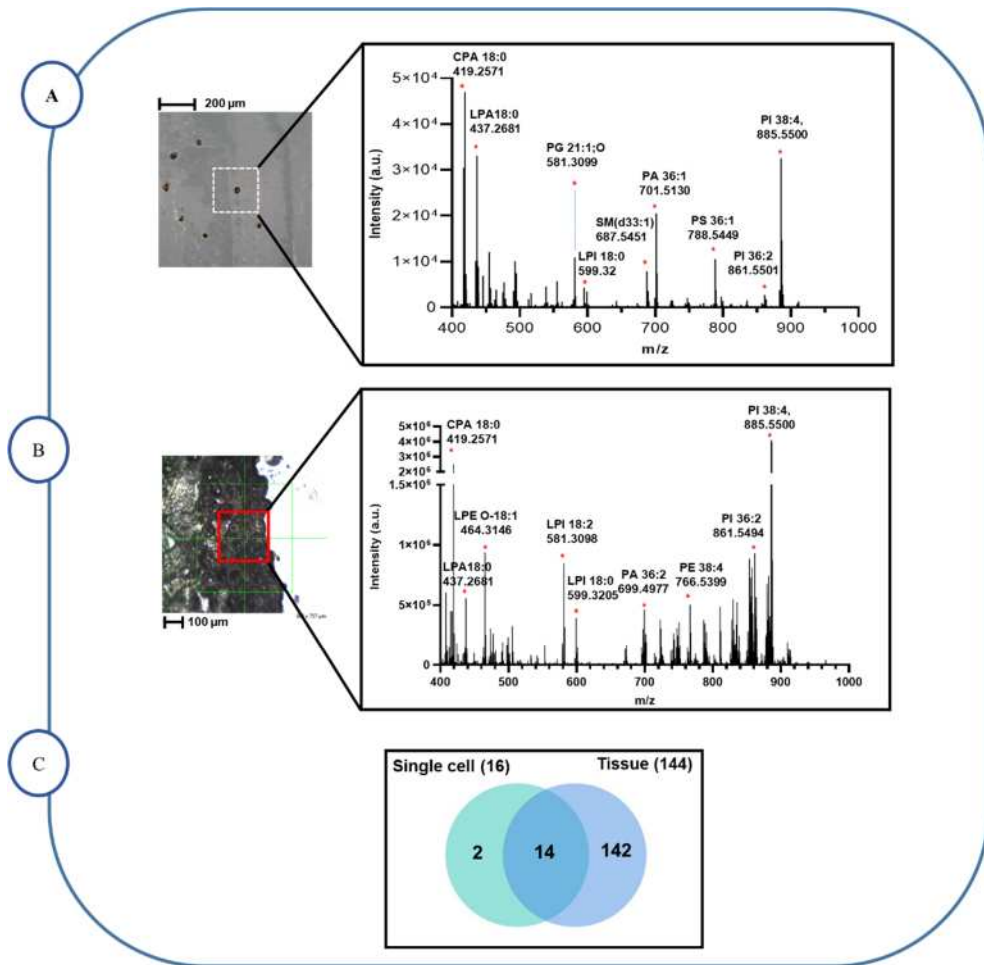


Figure 3.6. Identification of phospholipid in single macrophages and tissue section samples.

A. Negative ion mass spectrum 3D OrbiSIMS of the lipid fragments from a single cell macrophage, 16 lipids identified. B. Negative ion mass spectrum 3D OrbiSIMS of the lipid fragments from a tissue section sample, 144 lipids identified C. Venn diagram comparing the number of lipid compounds in single macrophages cells and ex vivo tissue sections by 3D OrbiSIMS measurement, 14 lipid compounds were common to both samples, 2 lipids and 142 lipids unique were in single macrophage cells and tissue section sample respectively.

Recipes

RPMI 1640 medium supplemented with 10% heat inactivated FBS, 2 mM L-glutamine, 100 U/mL penicillin-streptomycin.

150 mM Ammonium formate

Dissolve 18.9 mg of ammonium formate to a final volume of 20 mL in deionized water.

3.6. Conclusion

In this chapter we detail the methods we have developed to achieve direct analysis of the metabolic profiles of human monocyte derived M0, M1 and M2 macrophage phenotypes at single cell level and explanted silicon catheter sections for chemical characterisation of polarised immune cells *in vitro* and the host response to implanted bio-instructive polymers *in vivo* using 3D OrbiSIMS. 3D OrbiSIMS technique provides a powerful instrument to discover molecules in single cell macrophages and supporting tissue samples. In the initial stage of sample preparation in *in vitro*, monocytes were differentiated into naïve, M1 and M2 phenotypes using cytokines and freeze dry cell sample before analysis. Use of *ex vivo* analysis with OCT, cryostat for sectioning and freeze drying. Our sample preparation approach of single cells and tissue allows identification of metabolites by the new technique as 3D OrbiSIMS. This is a significant methodological advance as 3D OrbiSIMS requires millions fewer cells than the traditional mass spectrometry approaches. Another advantage is that the cells so not require removal from the substrate, a capability that we utilise in our analysis of tissue sections in order to probe functional phenotypes using molecular signatures. We hope that this protocol for sample preparation will be suitable and prove to be compatible for common metabolite profiling of biological samples and this approach has further application for characterisation of immune cells *in vitro*, on implanted medical devices and sensors, along with in the field of therapeutics and immune dysregulation.

Chapter 4

4. Single-Cell Metabolic Profiling of Macrophages Using 3D OrbiSIMS: Correlations with Phenotype

The aim of this chapter/article is to develop sample preparation and analysis protocols to achieve metabolomic profiles of human monocyte derived to M0, M1 and M2 macrophages at the single cell level using an Ar₃₀₀₀⁺ cluster primary ion beam using 3D OrbiSIMS.

This article published in Analytical Chemistry 2022; June 17, 2022

(DOI: 10.1021/acs.analchem.2c01375)

Authors

Waraporn Suvannapruk^a, Max K Edney^b, Dong-Hyun Kim^a, David J Scurr^a, Amir M Ghaemmaghami^c and Morgan R Alexander^a

^a Advanced Materials and Healthcare Technologies Division, School of Pharmacy, University of Nottingham, University Park Nottingham, NG7 2RD, United Kingdom.

^b Department of Chemical and Environmental Engineering, Faculty of Engineering, University of Nottingham, University Park Nottingham, NG7 2RD, United Kingdom.

^c Immunology & Immuno-bioengineering Group, School of Life Sciences, Faculty of Medicine and Health Sciences, University of Nottingham, University Park Nottingham, NG7 2RD, United Kingdom.

Single-Cell Metabolic Profiling of Macrophages Using 3D OrbiSIMS: Correlations with Phenotype

Waraporn Suvannapruk, Max K. Edney, Dong-Hyun Kim, David J. Scurr, Amir M. Ghaemmaghami, and Morgan R. Alexander*

Cite This: *Anal. Chem.* 2022, 94, 9389–9398

Read Online

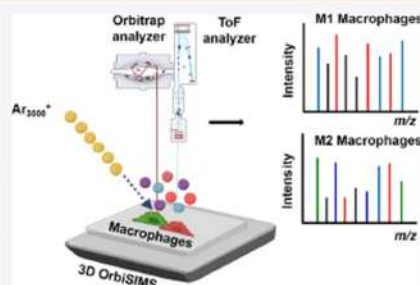
ACCESS |

Metrics & More

Article Recommendations

Supporting Information

ABSTRACT: Macrophages are important immune cells that respond to environmental cues acquiring a range of activation statuses represented by pro-inflammatory (M1) and anti-inflammatory (M2) phenotypes at each end of their spectrum. Characterizing the metabolic signature (metabolic profiling) of different macrophage subsets is a powerful tool to understand the response of the human immune system to different stimuli. Here, the recently developed 3D OrbiSIMS instrument is applied to yield useful insight into the metabolome from individual cells after *in vitro* differentiation of macrophages into naïve, M1, and M2 phenotypes using different cytokines. This analysis strategy not only requires more than 6 orders of magnitude less sample than traditional mass spectrometry approaches but also allows the study of cell-to-cell variance. Characteristic metabolites in macrophage subsets are identified using a targeted lipid and data-driven multivariate approach highlighting amino acids and other small molecules. The diamino acids alanyl-asparagine and lipid sphingomyelin SM(d18/16:0) are uniquely found in M1 macrophages, while pyridine and pyrimidine are observed at increased intensity in M2 macrophages, findings which link to known biological pathways. The first demonstration of this capability illustrates the great potential of direct cell analysis for *in situ* metabolite profiling with the 3D OrbiSIMS to probe functional phenotype at the single-cell level using molecular signatures and to understand the response of the human body to implanted devices and immune diseases.



INTRODUCTION

Macrophages are the sentinels and regulators of the human immune system; they display remarkable stimulus-induced functional plasticity, which is key in their ability in responding to a diverse range of pathogens, foreign objects, and dead cells resulting from tissue injury. Following infection or tissue damage, macrophages acquire a spectrum of functional phenotypes that are exemplified by pro-inflammatory (M1) and anti-inflammatory (M2) phenotypes at each end of the spectrum, with these subsets expressing unique biomarkers.¹ *In vitro*, classically activated M1 macrophages are generated by polarizing monocyte-derived naïve macrophages (M0) with a mix of cytokines including interferon γ and granulocyte macrophage colony-stimulating factor (GM-CSF).^{2,3} M1-like macrophages play an important role in pathogen clearance, and their sustained activation is linked to postinjury tissue damage. As indicated by their name, they secrete high levels of pro-inflammatory cytokines such as TNF- α , IL-12, and IL-1 β , and metabolically they are known to turn on glycolysis, the pentose phosphate pathway, and fatty acid synthesis.^{4–7} M2 macrophages on the other hand can be polarized using interleukin-4 (IL-4) and macrophage colony-stimulating factor (M-CSF)^{8,9} and have been implicated in tissue repair and remodeling; however, their sustained activation has been linked to the

promotion of fibrosis. M2-like macrophages typically produce high levels of regulatory cytokines such as IL-10 and TGF- β and, unlike M1 macrophages, rely on the TCA cycle to support oxidative phosphorylation and fatty acid oxidation which generate ATP.^{10–12}

The traditional approach for phenotyping macrophages relies on quantifying their transcription factors, cytokine profile, or expression of surface markers for different subsets. M1 macrophages had the highest expression of calprotectin and produced high levels of TNF- α , whereas M2 macrophages have a higher expression of mannose receptor (CD206) and produce high levels of IL-10.^{13–16} However, this is problematic since some of these markers are expressed by both M1 and M2 macrophage types, and importantly many, especially surface markers do not provide meaningful insight into macrophage functional properties.^{17,18}

Received: March 29, 2022

Accepted: June 3, 2022

Published: June 17, 2022



4.1. Abstract

Macrophages are important immune cells that respond to environmental cues acquiring a range of activation statuses represented by pro-inflammatory (M1) and anti-inflammatory (M2) phenotypes at each end of their spectrum. Characterizing the metabolic signature (metabolic profiling) of different macrophage subsets is a powerful tool to understand the response of the human immune system to different stimuli. Here, the recently developed 3D OrbiSIMS instrument is applied to yield useful insight into the metabolome from individual cells after *in vitro* differentiation of macrophages into naïve, M1, and M2 phenotypes using different cytokines. This analysis strategy not only requires more than 6 orders of magnitude less sample than traditional mass spectrometry approaches but also allows the study of cell-to-cell variance. Characteristic metabolites in macrophage subsets are identified using a targeted lipid and data-driven multivariate approach highlighting amino acids and other small molecules. The diamino acids alanyl-asparagine and lipid sphingomyelin SM(d18/ 16:0) are uniquely found in M1 macrophages, while pyridine and pyrimidine are observed at increased intensity in M2 macrophages, findings which link to known biological pathways. The first demonstration of this capability illustrates the great potential of direct cell analysis for *in situ* metabolite profiling with the 3D OrbiSIMS to probe functional phenotype at the single-cell level using molecular signatures and to understand the response of the human body to implanted devices and immune diseases.

4.2. Introduction

Macrophages are the sentinels and regulators of the human immune system; they display remarkable stimulus-induced functional plasticity, which is key in their ability in responding to a diverse range of pathogens, foreign objects, and dead cells resulting from tissue injury. Following infection or tissue damage, macrophages acquire a spectrum of functional phenotypes that are exemplified by pro-inflammatory (M1) and anti-inflammatory (M2) phenotypes at each end of the spectrum, with these subsets expressing unique biomarkers.¹⁷⁹ *in vitro*, classically activated M1 macrophages are generated by polarizing monocyte-derived naïve macrophages (M0) with a mix of

cytokines including interferon γ and granulocyte macrophage colony-stimulating factor (GM-CSF).^{43, 180} M1-like macrophages play an important role in pathogen clearance, and their sustained activation is linked to postinjury tissue damage. As indicated by their name, they secrete high levels of pro inflammatory cytokines such as TNF- α , IL-12, and IL-1 β , and metabolically they are known to turn on glycolysis, the pentose phosphate pathway, and fatty acid synthesis.¹⁸¹⁻¹⁸⁴ M2 macrophages on the other hand can be polarized using interleukin-4 (IL-4) and macrophage colony-stimulating factor (M-CSF)^{185, 186} and have been implicated in tissue repair and remodeling; however, their sustained activation has been linked to the promotion of fibrosis. M2-like macrophages typically produce high levels of regulatory cytokines such as IL-10 and TGF- β and, unlike M1 macrophages, rely on the tricarboxylic acid cycle (TCA cycle) to support oxidative phosphorylation and fatty acid oxidation which generate ATP.^{49, 187, 188}

The traditional approach for phenotyping macrophages relies on quantifying their transcription factors, cytokine profile, or expression of surface markers for different subsets. M1 macrophages had the highest expression of calprotectin and produced high levels of TNF- α , whereas M2 macrophages have a higher expression of mannose receptor (CD206) and produce high levels of IL-10.^{54, 136, 189, 190} However, this is problematic since some of these markers are expressed by both M1 and M2 macrophage types, and importantly many, especially surface markers do not provide meaningful insight into macrophage functional properties.^{46, 128}

Metabolomics is a powerful analytical tool¹⁹¹ that shows promise for distinguishing between macrophage subsets by identifying subtle yet key differences between their metabolic profiles. Metabolomics was developed to investigate the metabolic state of cells that closely correlates with their instantaneous functional state, including their response to stimuli from their environment.⁹¹ There are a wide range of techniques for metabolic analysis including mass spectrometry. Liquid chromatography–mass spectrometry (LC-MS) is a powerful tool for quantifying a range of small biomolecules and identifying known and unknown metabolites present in biological samples. This has been employed widely for identifying biomarkers of inflammatory diseases, drug discovery, and in the study of cellular metabolic profiles.¹⁹²⁻¹⁹⁵ Despite recent

advances in determining the metabolic phenotype of various pathologies using conventional LC-MS based techniques,¹⁹⁶⁻¹⁹⁸ characterizing the metabolome of different cells that are thought to play an important role in the development of such pathologies (e.g., macrophage subsets) is still in its formative stages partly due to the need for a large number of cells (>1 million cells) to obtain adequate signal.^{94, 199} Furthermore, LC-MS based techniques require complex and extensive sample preparation procedures including metabolic quenching and extraction of intracellular metabolites from cells using organic solvents. These procedures that target one metabolite type can lead to incomplete sampling and biased quantification of small molecules in biological samples due to rapid turnover and loss of metabolites.^{94, 179, 200} Moreover, cell samples are homogenized (metabolite extraction) during the sample preparation, thus losing the architecturally intact and physiologically relevant structure of the tissue and cells and eliminating the potential to correlate the spatial distribution of metabolites to morphology. Time-of-flight secondary ion MS (ToF-SIMS) is a direct surface analysis technique with minimal sample preparation, which can perform chemical imaging and depth profiling of cells.^{201, 202} Previous attempts at metabolic profiling using this technique targeted key molecules such as lipids and cholesterol on the mast cell.²⁰³ Touboul et al. applied ToF-SIMS imaging to study metabolites and mechanisms of disease on the tissue sample.²⁰⁴ The development of TOF-SIMS with polyatomic primary beams has provided the benefits of high molecular yields and low subsurface damage.²⁰⁵ But ToF-SIMS has been limited to resolving and detecting metabolites.²⁰⁶ However, ToF-SIMS has not been used widely for metabolite profiling of cells because its poor mass resolving power hinders confident identification of endogenous metabolites.²⁰⁷

The 3D OrbiSIMS is a recently developed technique bringing together the state-of-the-art Orbitrap analyser with ToF SIMS.¹⁵⁸ 3D OrbiSIMS combines the strengths of a TOF analyser with its fast imaging acquisition time and high spatial resolution (240,000) of the OrbitrapTM (parts-per-million (ppm) (<2)) and mass accuracy, high sensitivity, and tandem MS (MS/MS) capability. The technique uses an argon gas cluster primary ion beam (GCIB), affording a low energy per atom (E/n), and has been shown to liberate and unambiguously identify large diagnostic chemical species such as lipids and peptides.^{158, 162} Passarelli et al. have used this novel technique for

metabolite profiling of macrophages treated with different concentrations of an exogenous compound, the drug amiodarone, imaging it with endogenous compounds in single cells. In a tissue section of mouse brain, they identified lipid and amino acid fragments and were able to image a single cell in a tissue section.¹⁵⁸ Hodgkinson et al. have recently used 3D OrbiSIMS images to observe metabolites in multiple mesenchymal stem cells (MSCs) using ToF and Orbitrap.²⁰⁸

Single-cell SIMS analysis represents an exciting method for single-cell metabolomic profiling to probe intercell variations. Here, we use 3D OrbiSIMS to investigate the metabolic profiles of human monocyte-derived M0, M1, and M2 macrophages at single-cell level, leading to identifying characteristic ions that are related to known biological processes for each subset.

4.3. Methods

4.3.1. Sample preparation

Buffy coats from healthy donors were collected from the National Blood Service (National Blood Service, Sheffield, U.K.), following ethics committee approval (2009/D055, Research Ethics Committee, Faculty of Medicine and Health Sciences, University of Nottingham). Peripheral blood mononuclear cells (PBMCs) were isolated from heparinized blood by Histopaque-1077 (Sigma-Aldrich) density gradient centrifugation, as previously described.¹³⁶ A total of 2×10^5 monocytes were seeded on indium tin oxide (ITO) glass slides and cultured in RPMI supplement with 10% fetal bovine serum (FBS), 10 $\mu\text{g}/\text{mL}$ streptomycin, 2 mM glutamine, and 10 U/mL penicillin. Monocytes M0 were differentiated into M1 and M2 macrophages by the addition of 20 ng/mL M-CSF, 50 ng/mL GM-CSF, and 20 ng/mL IFN- α (R&D Systems), 50 ng/mL M-CSF, and 20 ng/mL IL-4, respectively, as described previously.⁷⁹ All cytokines were from Miltenyi Biotec unless otherwise stated (Figure A4.1.). The cells were incubated in a 37 °C incubator in a humidified atmosphere of 5% CO_2 for 6 days. On day 3 of incubation, we replaced 500 μL of medium with fresh media supplemented with the same concentration and mix of cytokines that were used for cell stimulation on day 0. Cell supernatant was harvested on day 6 for cytokine analysis and cell were collected for analysis.

4.3.2. Analysis of macrophages surface phenotype

This was carried out as previously described with some modifications.¹³⁶ Briefly, on day 6, the cells were fixed in 4% paraformaldehyde in PBS for 10 min at room temperature (RT). This was followed by washing cells with 3% bovine serum albumin (BSA) and 1% glycine (Fischer Scientific) in PBS. The cells were then incubated with appropriately diluted primary antibodies; 2 µg/mL mouse anti-human calprotectin (27E10) (Thermo Scientific) and 1 µg/mL rabbit antihuman MR (CD206) (Abcam) in 5% goat serum (GS) for 1 h followed by three times washing with PBS and addition of appropriately diluted secondary antibodies; and 8 µg/mL Rhodamine Red-x goat anti-mouse IgG(H + L) (Life Technologies) and 8 µg/mL Alexa Fluor 488 goat anti-rabbit (H+L) in 5% goat serum (GS) and further 1 h incubation at RT in the dark followed by three times washing with PBS. The nuclei of the cells were stained with 4',6-diamidino-2- phenylindole (DAPI, 20,000 ng/mL) for 5 min at RT in the dark. The cells were washed, dried, and finally mounted onto a slide with mounting media (Prolong antifade kit). The stained cells were imaged using ZOE fluorescence cell imager. Images were analysed using CellProfiler Cell Image Analysis Software, and fluorescence images of the expression of MR and calprotectin marker were analysed to determine the intensity of MR and calprotectin.

4.3.3. Cytokine Quantification

On day 6, supernatants were collected for cytokine assay. The levels of IL-10 and TNF- α in the culture media were measured by DuoSet ELISA kit (R&D Systems) following manufacturer's instructions.

4.3.4. 3D OrbiSIMS analysis

To remove salts that cause unwanted signal suppression in SIMS, the cells on ITO slides from the cell culture experiments were put in a container and then 1 mL of 150 mM ammonium formate solution was added for 30 s three times. The sample was plunge-frozen in liquid nitrogen and freeze-dried over a period of 12 h to remove water. The sample was subsequently stored in a sealed container and stored at -80 °C

until analysis. Prior to OrbiSIMS analysis, the sample was warmed to room temperature without opening and then loaded into the 3D OrbiSIMS instrument airlock for analysis.

3D OrbiSIMS analysis was performed using a HybridSIMS instrument (IONTOF, GmbH) with Mode 4 (single beam 20 keV Ar_{3000}^+ , OrbitrapTM analyser) of the instrument using an Ar_{3000}^+ primary ion beam of energy of 20 keV a duty cycle of 4.4% and continuous GCIB current of 230 pA, over an area of $150 \times 150 \mu\text{m}^2$ with crater size $233.1 \times 233.1 \mu\text{m}^2$ in the mass range of m/z 75-1125. The electron flood gun was operated with an energy of 21 eV and an extraction bias of 20 V. for charge compensation. The pressure in the main chamber was maintained at 1.6×10^{-6} mbar using argon gas flooding. The OrbitrapTM cycle time was set to 200 μs . OrbitrapTM analyser was operated in positive and negative ion mode at the 240,000 at m/z 200 mass resolution setting. The injection time was 500 ms, the total ion dose per measurement was 3.95×10^{11} ions/ cm^2 . Adjacent areas on the cell were analysed for positive and negative polarities. In each case an entire cell was consumed during each polarity analysis. Eighteen cells were consumed in total (3 cells per type and 1 cell per polarity).

4.3.5. Principal component analysis (PCA)

3D OrbiSIMS spectra contained hundreds of ions, and the mass spectra of samples superficially appear similar to each other. Depth profile accumulation spectra of all single cells analysed for M0, M1, and M2 macrophages (three cells of each type, nine in total) were each normalized to their respective total ion count in SurfaceLab 7 software. A peak list containing the intense ions (minimum ion count threshold was determined in each case as being greater than assigned noise signals) was then constructed with normalized intensities. A common peak list containing each ion for all samples was then constructed in SurfaceLab 7 software, which contained 724 positive ions. We performed PCA on this dataset to summarize differences in sample chemistry using PCA Bundle software.

4.3.6. Data processing and metabolites identification.

Peak assignments were created by IonTOF SurfaceLab 7. Amino acid fragments were assigned using an Xcalibur software to create the peak lists of each cell type. 3D OrbiSIMS spectra were exported as .txt files. Metabolites results were searched against the Human Metabolome Database²⁰⁹ with 5 ppm mass tolerance for putative annotation. The full method is depicted as a schematic in Figure 4.1.

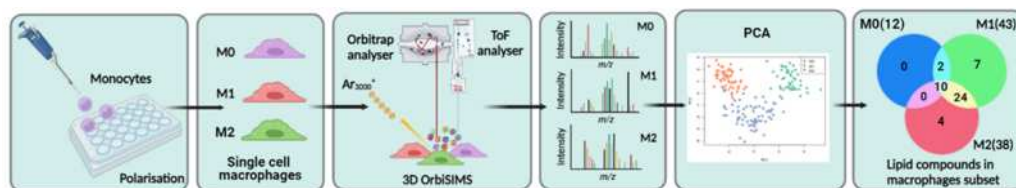


Figure 4.1. Schematic workflow of single cell metabolomic profiling using 3D OrbiSIMS.

Here, monocytes cells M0, are grown on an ITO substrate and polarized towards to M1 and M2 macrophages. A gas cluster argon primary ion beam raster is used to identify and sputter single cells with the resultant complex spectra compared using multivariate analysis complemented with targeted analysis.

4.4. Results and Discussion

4.4.1. Characterization of macrophage marker expression and cytokines analysis.

Before analysis with 3D OrbiSIMS, we first polarized monocyte cells (M0) into different macrophage phenotypes (M1 and M2) shown in Figure 4.2a. The surface phenotype and cytokine profile of each subset were characterized using optical microscopy and ELISA respectively. Data presented in Figure A4.1 in Appendix 4, show that M1 macrophages had the highest expression of calprotectin and produced high levels of TNF- α , whereas M2 macrophages have a higher expression of mannose receptor (CD206) and produce high levels of IL-10. These are in line with the expected phenotype of these cells that we and others have previously shown.^{72, 78, 210, 211}

4.4.2. Targeted lipid analysis

We performed 3D OrbiSIMS analysis on single cells of each type, where the cells were sequentially consumed by sputtering using the Ar_{3000}^+ gas cluster ion beam. The optical images of single cells acquired within the instrument before and after analysis by the gas cluster ion beam are shown in Figure 4.2b. Peak lists from the OrbiTrap analysis of the cells were first analysed using a targeted approach by matching peaks with ions of lipid species from the LIPID MAPS database based on their mass.²¹² A representative negative mass spectrum of lipids from a single-macrophage cell is presented in Figure 4.2c. The number of lipid species found in each macrophage subset and common to each are summarized in Figure 4.2d. A greater number of lipid compounds were detected in M1 macrophages than in M0 and M2. The identity of these presented in Table A4.1 and Table A4.5 in Appendix 4, including phosphatidylinositol lipid species such as PI 34:1, PI 36:1, and PI 38:3, which were highest in M1, while PI 34:1, PI 36:1, and PI 38:3 were not detected in M0 (Figure 4.2f and Table A4.1 in Appendix 4). Free fatty acid species, FA 16:0, FA 18:0, and FA 18:1 were lowest in M0 and highest in M2 samples (Figure 4.2g and Table A4.1 in Appendix 4). M1 polarization is associated with the activation of fatty acid synthesis. While M2 macrophages are known to have increased fatty acid oxidation and enhanced metabolism and upregulated activities that are associated with tissue remodeling or wound healing.²¹³ Passarelli¹⁵⁸ studied lipid compounds in tissue section by 3D OrbiSIMS and using the LIPID MAPS database putatively annotate 127 lipid species including glycerophospholipids, fatty acids, sterols and sphingolipids. Despite reducing the analyte amount to that of single cells, we identified 15 lipid ions in common shown in Figure A4.3a and Table A4.1 in Appendix 4.

Metabolomic profiling is typically undertaken on many cells using LC-MS, for example. To assess the performance of 3D OrbiSIMS compared to LC-MS data from analysis of many cells, we compared putatively assigned lipids in the LIPID MAPS database from our work using primary macrophages to those detected in the LC-MS study of Abuawad et al. undertaken on a macrophage cell line, which used 6 million cells.⁹⁴ Venn diagram (Figure 4.2e, Table A4.1 and Figure A4.3b in Appendix 4) shows how many lipids were obtained in common and how many unique lipid species were detected from LC-MS and 3D OrbiSIMS. For 3D OrbiSIMS data in a negative

polarity mode, 47 lipids were identified putatively and 17 of the same lipid compounds were identified in both the 3D OrbiSIMS and LCMS analysis. In the case of LC-MS studies, 212 putatively annotated lipids were identified in positive and negative polarities including glycerophospholipids, fatty acyls, and fatty acids.⁹⁴ Notably, 30 lipid compounds were putatively identified uniquely using 3D OrbiSIMS, which were not detected in the LC-MS measurement, including fatty acids species FA16:1, FA18:0, FA20:4, and FA22:4 (Table A4.1 in Appendix 4).

The identification of some representative putative lipid assignment was confirmed using sequential mass spectrometry analysis in the OrbiTrap (MS/MS). In negative-ion mode spectra, several phosphatidylinositol lipid species were observed in macrophage cells. The product ion spectrum of phosphatidylinositol secondary ions is shown in Figure 4.2h-i. In the MS/MS spectrum is the precursor ion $[M-H]^-$ at m/z 861.5494, $[C_{45}H_{82}O_{13}P]^-$ assigned as PI (36:2). The main product ions of the precursor PI (36:2) ion are the signature fragments of the PI head group, $[C_6H_{10}PO_8]^-$ at m/z 241.0118 and two C18:1 fatty acid moieties are represented by the $[C_{18}H_{33}O_2]^-$ peak at m/z 281.3486 (Figure 4.2h). The structure of PI (38:4) at m/z 885.5498 was confirmed based on the detection of the PI head group ions, $[C_6H_{10}PO_8]^-$ at m/z 241.0, and two fatty acid moieties from these lipids are C18:0, $[C_{18}H_{35}O_2]^-$ at m/z 283.2642 and C20:4, $[C_{20}H_{31}O_2]^-$ at m/z 303.2327 (Figure 4.2i). MS/MS spectra of PA and PC lipids are reported in Figure A4.3 c-d and Table A4.2. in Appendix 4.

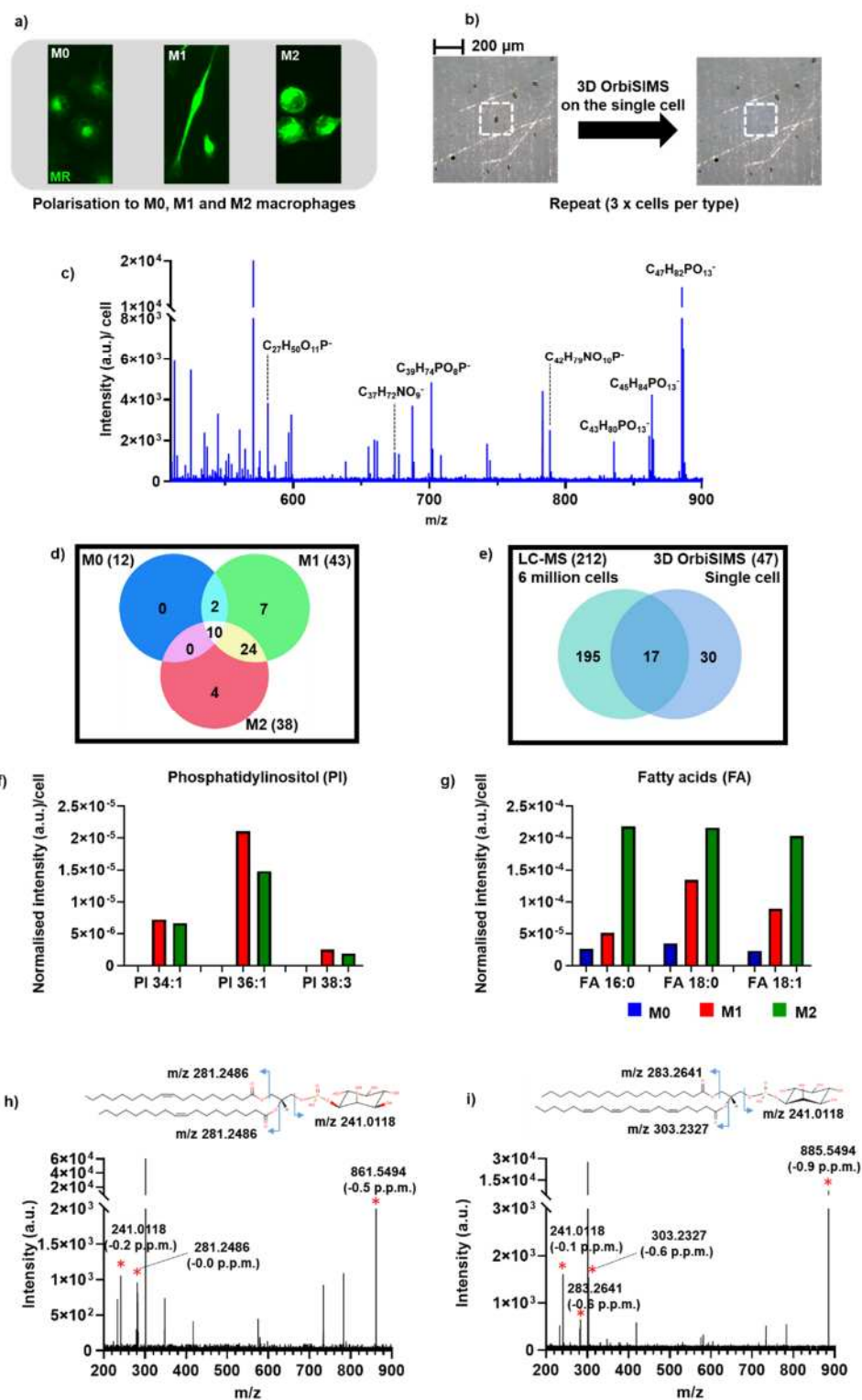


Figure 4.2. Lipid on single cell by 3D OrbiSIMS analysis.

a) Fluorescent images of single cell macrophages stained for mannose receptor, b) White image of the M0 cell type before (left) and after (right) 3D OrbiSIMS depth profiling, showing consumption of the cell by the gas cluster ion beam. Targeted metabolomics approach of assigning lipid species in 3D OrbiSIMS data and comparison to LC-MS data from reference.⁹⁴ c) Negative ion mass spectrum 3D

OrbiSIMS of the lipid fragments from a single cell macrophage. d) Venn diagram comparison of the number lipid compounds which detected in macrophages subsets using 3D OrbiSIMS. e) Venn diagram comparing the number of lipid compounds in macrophages by LC-MS and 3D OrbiSIMS measurement, 212 lipids were identified in THP-1 macrophages extracts using LC-MS, 47 lipids were identified by 3D OrbiSIMS and 17 lipid compounds were common to both techniques. Normalized intensity of lipid classes with characteristic ion data shown f) phosphatidylinositol species (PI) and g), fatty acids. Species of phosphatidylinositol (PI) confirmation by MS/MS. h) MS/MS product spectrum of PI (36:2) corresponding to [M-H]⁻ ion at m/z 861.5494. i) MS/MS product spectrum of PI (38:4) corresponding to [M-H]⁻ ion at m/z 885.5498.

Lipids, such as phospholipids and glycolipids are major components of the cell membrane²¹³ and key species in understanding metabolic pathways. Phospholipids are the main component of the cell lipid bilayer comprising two long fatty acid chains, a triglyceride linking a phospholipid head with various alkyl groups, namely, ethanolamine, inositol, serine, glycerol, and choline such as phosphatidylethanolamine, phosphatidylinositol, phosphatidylserine, phosphatidylglycerol, and phosphatidylcholine (Figure 4.3a). Glycerphospholipids have five classes, which are subdivided based on polar head groups (common alkyl groups) including PC, PI, PA, PS, and PE.^{213, 214} We found lipids with the head group: PC, PI, PS, and PE, included in Table A4.3. in Appendix 4. All phenotypes expressed the lipid head group with a short alkylated chain with ions such as C₅H₁₄NO⁺, C₂H₆PO₄⁺ and C₅H₁₅NPO₄⁺²¹⁵ (Figure 4.3b, c, d and Table A4.3. in Appendix 4). Intense negative ions assigned to this class included phosphatidylethanolamine (C₂H₅NPO₃⁻), phosphatidylcholine (C₄H₁₁NPO₄⁻), phosphatidylglycerol (C₃H₆PO₅⁻), phosphatidylinositol (C₆H₁₀PO₈⁻), sulfatide (HSO₄⁻) and sphingolipids (C₂H₄PO₄⁻) (Table A4.3. in Appendix 4). Lipid compounds that we found in our samples have previously been observed in the analysis of the individual lipids using ToF-SIMS.²¹⁴

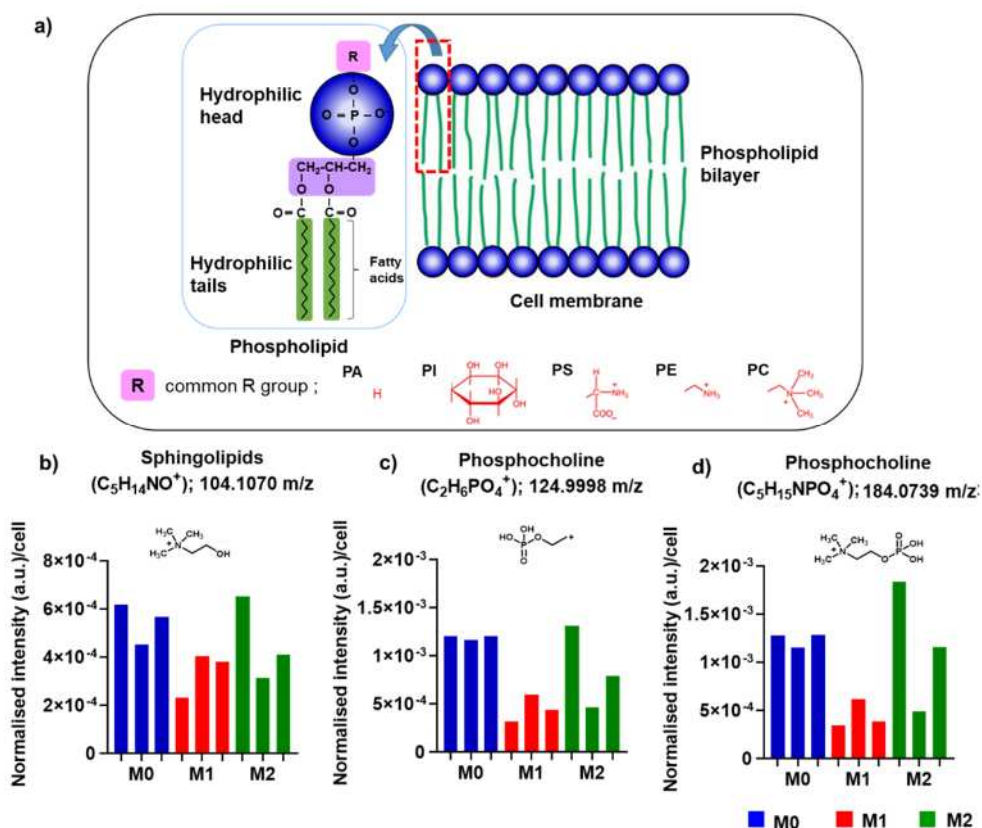


Figure 4.3. a) Schematic of the membrane lipid components. b) Normalized intensity of lipids in three separate cells for each macrophage polarization with comparison of each phenotype in positive polarity $C_5H_{14}NO^+$ (sphingolipids, SP, m/z 104.1070), c) $C_2H_6PO_4^+$ (phosphocholines, PC, m/z 124.9998) and d) $C_5H_{15}NPO_4^+$ (phosphocholines, PC, m/z 184.0739).

4.4.3. Untargeted analysis approaches

To discern subtle differences in the macrophage metabolome and expand beyond the targeted lipid analysis, we undertook an untargeted analysis of the secondary ion data using principal component analysis (PCA) of the three macrophage subsets and their analytical repeats. The resultant scores plot of the first three principal components (PCs) for the positively charged ions in the 3D OrbiSIMS data discriminated all three macrophage subsets and replicate measurements clustered together. Scores (PC1, 2, and 3) and loading plots for three cell types are shown in Figure 4.4a and PC4 is shown in Figure A4.6. in Appendix 4. Scores revealed molecular similarity between replicates and each macrophage subset shows statistically unique secondary ions, leading to clear chemical separation of each phenotypic macrophage subset. Loadings of the first four

components highlighted ions responsible for chemical differences between macrophage types. PC1 showed that amino acids were more intense in the spectra from M2 macrophages (Figure 4a and b). The second component was associated with chemistry from M0 macrophages and included positively ionizing lipid fragments containing CHNOP-containing ions such as $C_5H_{15}NO_4P^+$ (m/z, 184.07) and $C_2H_6PO_4^+$ (m/z, 124.99) (Figure 4.4c). The third component differentiated between certain lipids and amino acids (Figure 4.4d), and scores plots show this chemistry was most prominent in M1 macrophages (Figure A4.7-8. in Appendix 4).

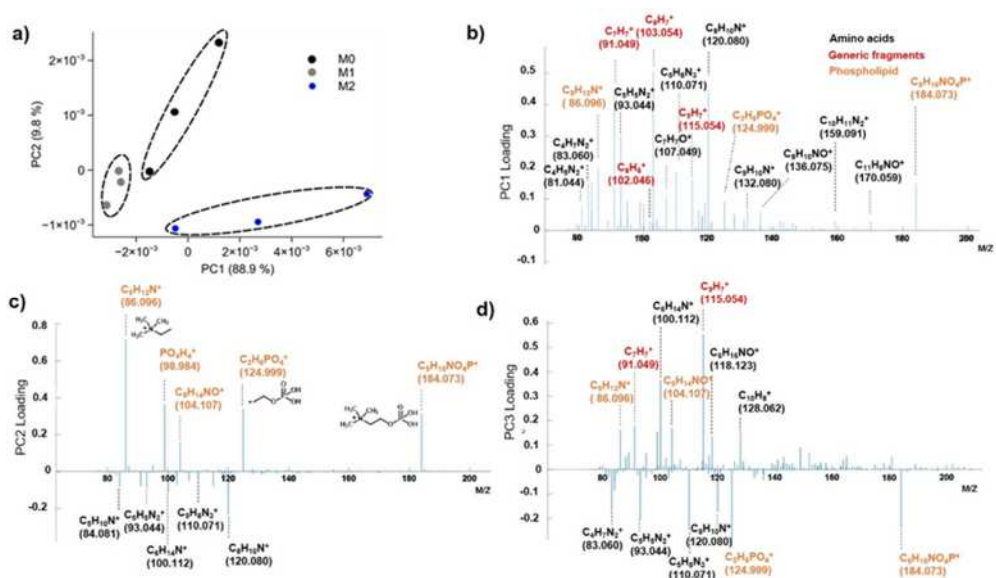


Figure 4.4. Principal component analysis (scores and loadings) for different macrophage subsets results.

a) Principal component scores plots of PC1 and PC2 for the 3D OrbiSIMS spectra of M0, M1 and M2 macrophage on positive polarity. Loading plot on positive polarity data for the first three principal components, peaks were assigned based on amino acid maker (black), phospholipid maker (orange) and generic which non-specific ion fragments (red). b) PC1, c) PC2 and d) PC3.

4.4.4. Amino acid assignments

Loadings from PCA were interrogated and identified ions that may be assigned to specific amino acid fragments (Figure 4.5a-g). Assignments from both polarities were made by comparing fragments identified by ToF-SIMS in previous SIMS studies of amino acids assigned from analysis of proteins and free amino acids.²¹⁶⁻²¹⁸ In total, 39 amino acid fragment ions were assigned from the single cells and were present in all samples (Table A4.4. in Appendix 4), which we attribute to 13 amino acids from proteins. These include histidine, phenylalanine, which has an important function in immune tolerance controlled by tetrahydrobiopterin synthesis to produce the NO by iNOS in activated macrophages.²¹⁹ Tyrosine is produced by phenylalanine degradation, which is a precursor of melanin synthesis.²²⁰ Melanin can be reduced the pro-inflammatory mediator such as TNF α , IL-1b, IL-6 and IL-10 from monocytes and macrophages, and induce the production of the anti-inflammatory cytokines from leucocytes.²²¹ Tryptophan is produced by indoleamine-2,3-dioxygenase (IDO), which converts tryptophan to kynurenine. Tryptophan metabolism could prevent therapeutic targets in treating age-related diseases associated with inflammation and extend health and life span.²²² Arginine²²³ had the lowest intensity in the M1 macrophage (Figure 4.5e). M1 macrophages are known to exhibit high expression of the enzyme nitric oxide synthase, which metabolises arginine to nitric oxide (NO) and citrulline.²²⁴ It is known that M2 macrophages promote the hydrolysis of arginine towards urea and ornithine, which promotes cell proliferation and repair. Therefore, amino acid is used differently in M1 and M2 macrophages; it seems to be a key resource to support polarization and function of both M1 and M2 macrophages. This shows that our single cell metabolomic profiling using 3D OrbiSIMS successfully detected different levels of amino acids and lipids in M0, M1, and M2 and linked the chemical compounds to known macrophage functions. Comparison of ions observed by 3D OrbiSIMS and free amino acids reference spectra acquired by ToF-SIMS did not show matches²¹⁶ – suggesting they are derived from larger protein structures (Table A4.4. in Appendix 4). In nearly all cases M2 macrophages showed higher intensity of amino acid fragments than in M0 and M1 (Figure A4.5. and Table A4.4. in Appendix 4).

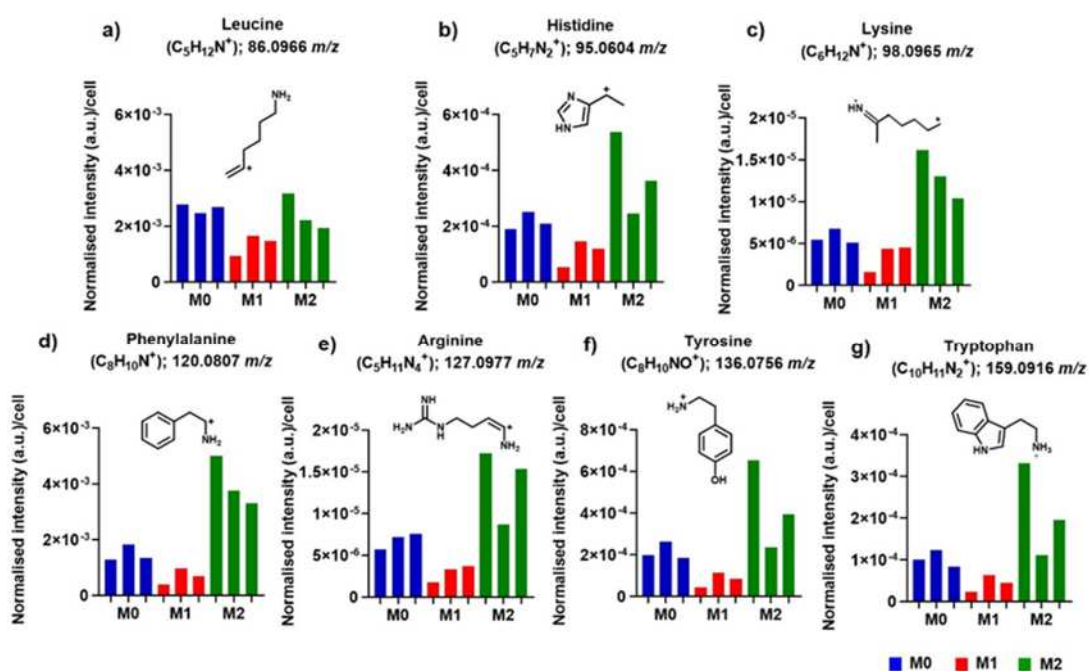


Figure 4.5. Characteristic amino acid fragments were detected in macrophage polarization in positive ion mode.

The normalized intensity per cell spectral for a) $C_5H_{12}N^+$ (leucine, m/z 86.0966), b) $C_5H_7N_2^+$ (histidine, m/z 95.0604), c) $C_6H_{12}N^+$ (lysine, m/z 98.0965), d) $C_8H_{10}N^+$ (phenylalanine, m/z 120.0807), e) $C_5H_{11}N_4^+$ (arginine, m/z 127.0977), f) $C_8H_{10}NO^+$ (tyrosine, m/z 136.0756) and g) $C_{10}H_{11}N_2^+$ (tryptophan, m/z 159.0916).

4.4.5. Metabolite identification

We correlated ions from 3D OrbiSIMS parent spectra of the single cells to the Human Metabolome Database and found unique metabolites belonging to each subset (Figure 4.6 and Table A4.6. in Appendix 4). For example, 5-bromopyridine $[M + Na]^+$ (m/z 180.9374) had high ion intensity in M2 macrophages but was not observed in the M1 macrophages (Figure 4.6 a-c). The pyridine moiety is an integral part of anti-inflammatory agents; it is known to induce macrophage growth and has been shown to inhibit the formation of tumor necrosis factor stimulants such as lipopolysaccharide.²²⁵ This is in agreement with our data, which shows the high intensity of pyridine moieties in the anti-inflammatory M2 macrophage compared to no detection in the pro-inflammatory M1 phenotype. This clearly shows how 3D OrbiSIMS data from a single cell could be used to predict macrophage phenotype. The dipeptide alanylarginine and the lipid sphingomyelin (SM) (d18:1/16:0) were

detected uniquely in M1 macrophages. They are both implicated in pro-inflammatory cellular responses^{226, 227}, and were not found in M2 cells (Figure 4.6 d-e). SM lipids are considered very important for the preservation of immune cell activation and function.²²⁷ Sphingomyelin is known to convert to ceramide, which plays a key role in inducing pro-inflammatory gene expression with the synergistic effect of LPS.²²⁸ Moreover, potent M1 polarizing cytokines such as TNF- α and IFN- γ have been shown to induce ceramide production, which might further augment M1 macrophage polarization.²²⁹

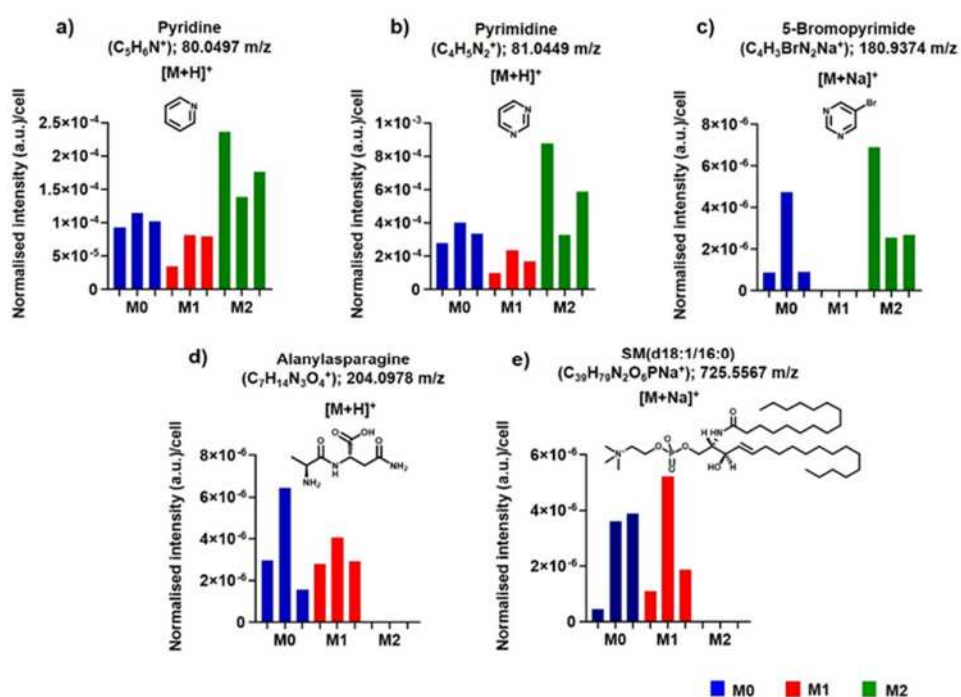


Figure 4.6. Metabolites significantly affected by macrophage polarization toward the M1 and M2.

a) Pyridine [$M+H$]⁺ at m/z 80.0497, b) Pyrimidine [$M+H$]⁺ at m/z 81.0449 and c) 5-bromopyrimidine [$M+Na$]⁺ at m/z 180.9374. Pyrimidine metabolisms were observed at increased intensity in M2 macrophages comparing to M1 macrophage d). Alanylasparagine [$M+H$]⁺ at m/z 204.0978, e) SM(d18:1/16:0) [$M+Na$]⁺ at m/z 725.5567 are represented uniquely in M1 macrophages.

4.5. Conclusions

In this work, we have shown that metabolites can be detected by direct analysis of single-macrophage cells using a gas cluster primary beam using 3D OrbiSIMS. We found that we could detect differences in the metabolite profiles of naïve (M0), proinflammatory (M1), and anti-inflammatory (M2) macrophages. These intensity differences can be linked to the pro and anti-inflammatory nature of different macrophage types. Coupled with principal component analysis of single-macrophage cells, this analytical technique allowed us to accurately assign several key species including amino acid fragments, lipids, and other small molecules known to play a role in cell metabolism. This approach will allow in situ characterization of single cells to help understand the response of the human body to different environmental insults/stimulations, including exposure to biomaterials, therapeutics, and immune dysregulation from *in vitro* cell samples and tissue biopsies.

Chapter 5

5. Polymer synthesis for cell instructive coatings

5.1. Introduction

Polymers have previously been highlighted in many experimental studies to be able to instruct different cell types, influencing attachment density and phenotype.^{230, 231} Copolymer can be used to combining properties from two or more polymers. Rostam *et al.* reported the use of a combine of (meth)acrylate and (meth)acrylamide monomer library screened for their potential to stimulate human monocyte differentiation into various macrophage phenotypes.⁷⁹ Burroughs et al. developed molded ChemoTopoChip polymer samples to discover acceptable materials for bone regeneration, combinations of chemistry and microtopography also produce immunomodulatory stimuli, polarising macrophages toward a pro-healing phenotype.²³² Furthermore, they can act synergistically to provide performance superior to the individual component.^{233, 234}

Free radical polymerization (FRP) is a method of polymer synthesis that is readily applicable to a large number of monomers and requires moderate synthesis conditions compared to other polymerization techniques.^{235, 236} Depending on the type of initiator, FRP can either be achieved with a photochemical or a thermal initiator, FRP reaction mechanism consists of three stages: initiation, propagation, and termination as described in Chapter 2, section 2.2.1. Thermal FRP uses an initiator that produces a pair of free radicals in response to heat. These free radicals interact with the functional groups in the monomer, which results in the monomer being polymerized. As a result of the reaction, a batch of polymer is produced, which may subsequently be solubilized and coated onto a variety of surfaces and substrates, making the FRP process extremely flexible. In contrast to photochemical initiator FRP, which requires specific surfaces to be coated and treated with UV light, thermal initiator FRP does not have this requirement. For this reason, thermal initiator FRP was selected as the polymerization process for the material.

The synthesis and characteristics of the copolymers can provide desirable properties for medical applications such as biofilm prevention, adhesion of stem cells and

improvement of wound healing properties.^{22, 237} Acrylates and methacrylates monomers are widely used for forming polymeric biomaterials. They have an optical clarity, good mechanical properties and bacterial biofilm resistance.^{238, 239} Specifically, using copolymer ethylene glycoldicyclopentenyl ether acrylate and (di(ethylene glycol) methylether methacrylate coated into silicone urinary catheters, indicating that copolymer coated decreased the attachment of bacteria *in vivo*.²⁴⁰ Hydrocarbon pendant moieties, especially with ring structures found to resist bacterial biofilm formation.²⁴¹ Recently, using high throughput microarrays was developed methacrylate polymers with reduce fungal attachment, bacteria attachment and immune instructive.²⁴¹⁻²⁴³

In most cases, implants are perceived as foreign bodies by immune cells and can result in chronic and persistent inflammation. Implants can therefore have a profound effect on the host immune response. The implantation of such devices frequently results in a host immune reaction known as the foreign body response (FBR). The FBR initiates acute and chronic inflammation, which are significant considerations in the design and development of implantable medical devices and FBR as described in section 1.1.3 and Figure 1.2. To a lesser extent, all patients exhibit undesirable responses to implants if monitored for long enough, such as aseptic loosening of dental screws and hip and knee joints. To reduce chronic and persistent inflammation, new materials that instruct immune responses to promote healing are needed. Screening of libraries have identified cell-instructive polymers, these can be used for as coating. A biomedical implant, consisting of samples coated with copolymer libraries to identify biomaterial surface morphology and surface chemistry that influence macrophage polarization *in vitro* has been proposed.

Rostam *et al.* used high throughput microarray screening methods to identify immune-instructive polymers from a screen of 141 (meth)acrylate monomers by monocytes polarisation to pro-inflammatory (M1) or anti-inflammatory (M2) phenotypes *in vitro*; these are the ability to induce M1 and M2 phenotypes in macrophages and *in vivo*, to access the copolymer coating for modulation of immune response responses (Figure 5.1).^{79, 243} Here, I have investigated coating coverslips with the macrophage biased copolymers to create new immune informative biomedical implants. Therefore, it is

beneficial to have an in-depth understanding of the host inflammatory and immune system to biomaterials, as this would help the development of biomaterials that will exert appropriate biological functions.

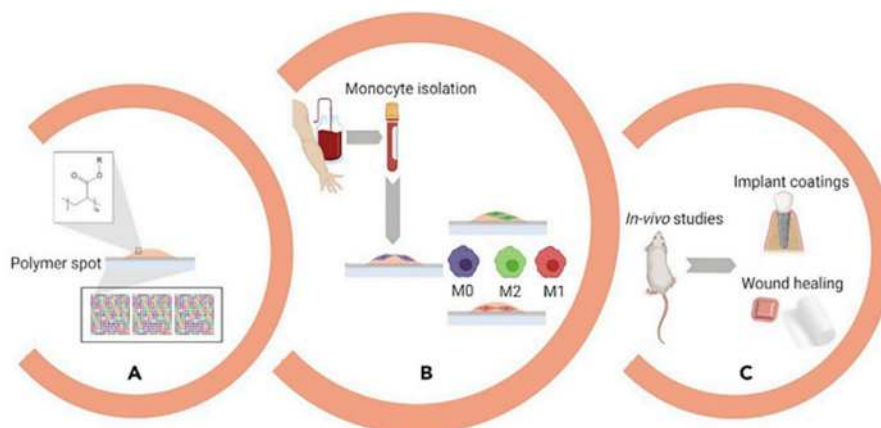


Figure 5.1. Schematic of the high-throughput screening approach used to identify pro- or anti-inflammatory hit polymers in vitro and in vivo.

Image was adapted from Rostam et al., Matter (2020)⁷⁹

It was hypothesized that the utilization of immune-instructive polymers from acrylate monomer could lead to the discovery of novel materials capable of altering macrophage responses. In this chapter, the use of methacrylate monomers to synthesize copolymers via a thermal polymerization method and subsequently coat coverslips has been investigated. ¹H NMR was used to characterize the composition of copolymers. GPC was used to determine the number average molecular weight (Mn), weight-average molecular weight (Mw) and molecular weight distribution (MWD) of copolymers. Samples were analyzed using ToF-SIMS to characterize the surface chemistry of synthesized polymers. Furthermore, new focus on identifying synthetic polymer biomaterials, to investigate the immune-modulatory effects of copolymers on monocyte differentiation into macrophage phenotypes.

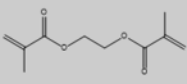
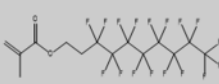
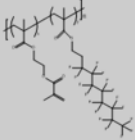
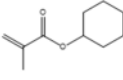
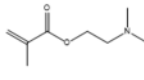
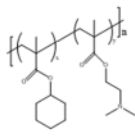
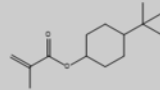
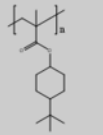
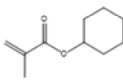
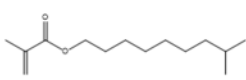
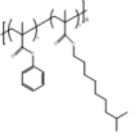
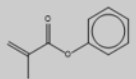
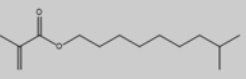
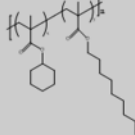
5.2. Materials and methods

Monomers were purchased from Sigma-Aldrich, UK and used as received. Toluene and dichloromethane (analytical grade) were ordered from Fisher Scientific, UK. 2,2 azobis(4-methoxy-2,4-dimethylvaleronitrile (AIBN) was purchased from Sigma-Aldrich, UK. MED1-161 which is a silicone primer was purchased from Nusil Technology LLC, USA. Round glass coverslips were obtained from VWR®, UK.

5.2.1. Synthesis of copolymers

Synthesis worked was carried out using two defined monomers at a 2:1 ratio (w/v). The monomer solution was prepared in toluene at a 1:3 ratio (w/v) and using 2,2 azobis(4-methox-2,4-dimethylvaleronitrile (AIBN, 0.5% w/v) and bis[(disfluorobory)diphenylglyoximato]cobalt(II) (CoPhBF, 1000ppm). The chemical structure of the monomers is shown in Table 1. The solution was degassed under argon for 30 min. The copolymerization was mixed and stirred at 85°C in oil bath for 24 hours. After that, the copolymer was precipitated in methanol washed well to remove any un-reacted monomer and then filtered. Finally, the precipitated copolymer was dried in vacuum oven at room temperature for 7 days.

Table 5.1. Monomers name and chemical structures and reaction parameters.

Code	Monomer 1 name/structure (66%)	Monomer 2 name/structure (33%)	Time (h)	T (°C)	Polymer
M0	 Ethylene glycol dimethacrylate (EGDMA)	 Heptafluorodecyl methacrylate (HDFDMA)	24	85	
M1-1	 Cyclohexyl methacrylate (CHMA)	 Dimethylamino- ethylmethacrylate (DMAEMA)	24	85	
M1-2	 Tertbutylcyclohexyl methacrylate (tBCHMA)		24	85	
M2-1	 Cyclohexyl methacrylate (CHMA)	 Isodecyl methacrylate (iDMA)	24	85	
M2-2	 Phenyl methacrylate (PhMA)	 Isodecyl methacrylate (iDMA)	24	85	

5.2.2. Characterization of the copolymers

Characterization of the copolymer was performed to identify their properties using NMR and GPC. The surface chemistry of the coating was determined by ToF-SIMS. *In vitro*, monocyte cells were seeded and culture for 6 days and characterised. The full method is depicted as a schematic in Figure 5.2.

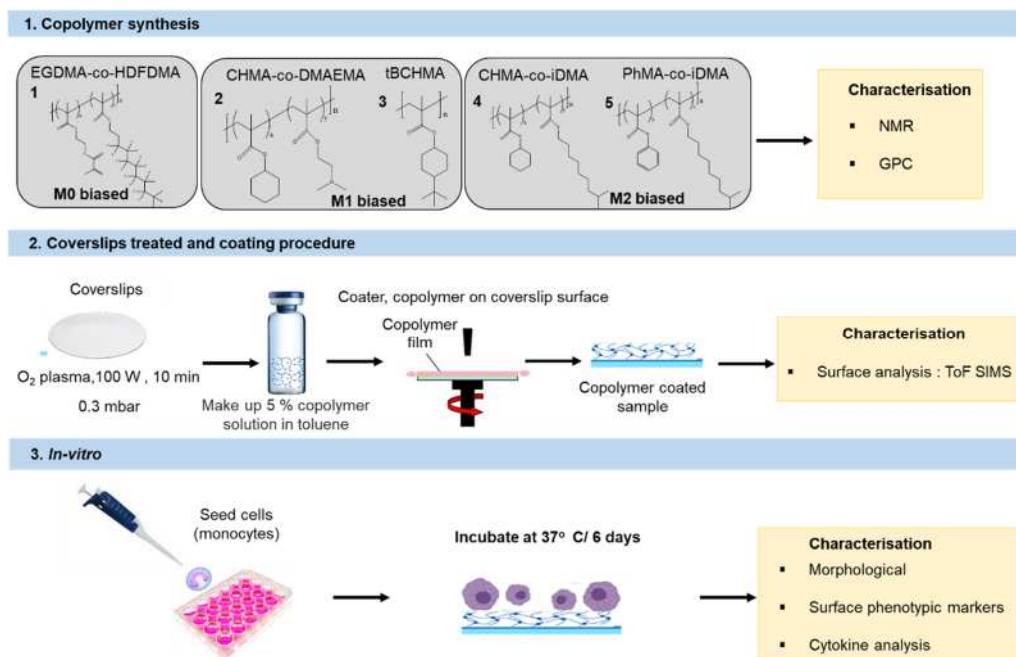


Figure 5.2. Schematic of the characterization of the copolymers.

1st step, five copolymer synthesis were characterized by NMR and GPC. Follow the coating step, surface analysis was performed by ToF-SIMS. The last step of the in vitro study was observed by morphological, surface phenotypic markers and cytokine analysis.

5.2.2.1. Nuclear magnetic resonance spectroscopy (NMR)

The structure of copolymers was analyzed by NMR spectroscopy ¹H NMR spectra of copolymers were obtained with Bruker DPX-300 spectrometer, NMR 400 MHz. Copolymers were dissolved in CDCl₃ solution (EGDMA-co-HDFDMA, CHMA-co-DMAEMA, tBCHMA, CHMA-co-iDMA, and PhMA-co-iDMA). Chemical shifts were recorded in δH (in ppm). For spectral analysis, MestReNova 14.2.1[©] 2021 (Mestrelab Research S. L.) was utilised.

5.2.2.2. Gel permeation chromatography (GPC)

The number-average molecular weight (M_n), weight-average molecular weight (M_w) and polydispersity (PDI) of the copolymer were determined through the use of gel permeation chromatography (GPC), Waters Corporation, USA. Samples were

dissolved in tetrahydrofuran (THF) (2mg/ml) and then filtered using nylon 66 membrane (pore size 0.45 μm) before injection. Column set: PLgel 10 μm mixed B 2 columns, (MW resolving range = 500-10,000,000). The samples were flowed 1ml/min, temperature at 35 °C.

5.2.3. Sample preparation and characterisation of chemical copolymer surface

5.2.3.1. Preparation of copolymer coated on glass substrates

Glass coverslips were coated with synthesized polymers for later biological assay and characterization. The glass coverslips were treated by O₂ plasma for 5 minutes before coating. The copolymers solution in toluene (5% w/v) were coated onto coverslips surface by spin coating at 2000 rpm for 15 seconds. Samples were dried overnight at room temperature then dried in vacuum at 50 °C for 7 days to remove solvent.

5.2.3.2. Time-of-flight secondary ion mass spectrometry

The surface chemistry of samples was determined using ToF-SIMS. ToF-SIMS measurements were performed using ToF-SIMS IV instrument (IONToF, GmbH, Munster, Germany) with a bismuth cluster primary ion source (25 keV Bi₃⁺) analysis, the primary ion dose was preserved < 10¹² ion/cm² to ensure static condition, the cycle time was set to 100 us using a raster random mode by 256 x 256 pixels over the area 500 x 500 μm of each copolymer area on the copolymer coated coverslips.

The results were analysed in SurfaceLab 7. Calibration of positive mode spectra was made using C⁺, H⁺, O⁺ and N⁺ ions. Negative mode spectra were calibrated to C⁻, H⁻, and CN⁻.

5.2.4. *In vitro* study

5.2.4.1. Cell culture

Monocytes were isolated from buffy coat as described in section 3.5.1. Isolated monocytes were seeded on polymer coverslip coated at density of cell 5×10⁵ in RPMI

1640 medium, supplemented with 10% heat inactivated FBS, 2 mM L-glutamine, 100 µg/ml streptomycin and 100 µg/ml penicillin. Cells were incubated at 37°C incubator with humidified atmosphere of 5% CO₂ for 6 days. On day 3 of incubation, 500 µL of medium was replaced with fresh media. Cell supernatant was harvested on day 6 for cytokine analysis and cell were collected for analysis.

5.2.4.2. Cytotoxicity assay

ToxiLight® was utilised to determine the level of viability. Cell viability on different polymers was determined. On day 6 of macrophage culture, 100 µl of Tris acetate was added into each polymer culture plate. For the dead cell control well added 100 µl Lysis Buffer (here, need the cell in the well to be killed). The plate was incubated for 10 minutes at room temperature. 25 µl of each polymer cell suspension was transferred to a white 96-well plate, 100 µl of the adenylate kinase (AK) detection reagent was added. The assay plate was incubated for 5 minutes at room temperature and was read on a GloMax Discover (Promega) at a luminometer. Set the luminometer to take a 1 second integrated reading of the appropriate wells.

5.2.4.3. Immunostaining for M1 and M2 surface markers

After activation of the macrophages for 6 days the supernatant and samples were collected, then they were washed with PBS for 3 times. Cells were fixed in 4% paraformaldehyde in PBS for 10 min. Fixation was carried out at room temperature, then the samples were washed with PBS three times, and then added 3% Bovine Serum Albumin (BSA) and 1% Glycine (Fischer Scientific) in PBS and incubated at room temperature for 30 minutes. The samples were washed twice with 0.2% Tween 20 in PBS then were added 5% goat serum in PBS and incubated at room temperature for 30 min, then the cells were added appropriately diluted primary antibodies; 2µg/ml of mouse anti-human calprotectin (27E10) (Thermo scientific) and 1µg/ml of rabbit anti-human MR (CD206) (Abcam) in 5% goat serum (GS) then incubated at room temperature for 1 hour. Next, the samples were washed with 0.2% Tween 20 in PBS for 3 times, then added appropriately diluted secondary antibodies; 8µg/ml of Rhodamine Red-x goat anti-mouse IgG(H+L) (life Technologies) and 8µg/ml of Alexa

Fluor 488 goat anti-rabbit (H+L) in 5% goat serum (GS) then incubated at room temperature for 1 hour in the dark. The samples were washed with 0.2% Tween 20 in PBS for 3 times. Added appropriately diluted 2000 ng/ml of 4', 6-Diamidino-2-Phenylindole (DAPI), incubated for 5 min. The samples were washed three times with 0.2% Tween 20 in PBS, dried, and mounted onto slides with mounting media (a Prolong antifade kit), with the edges of the coverslips sealed with nail polish.

5.2.4.4. Image analysis

The stained cells were imaged with a microscope ZOE™ fluorescent cell imager (Bio-Rad Laboratories), and any background fluorescence was subtracted using ImageJ, fluorescence images of macrophage expression of M1 and M2 marker were analysed to identify the intensity of calprotectin and mannose receptor. Mean fluorescence intensity (MFI) for calprotectin and mannose receptor expressed was used to determined.

5.2.4.5. Cytokines production

Supernatants from each polymer were collected for cytokine assays. The levels of IL-10, CCL18, TNF- α and IL-1 β in the culture media were measured by ELISA, this was done according to manufacturer instruction (DuoSet Ancillary Reagent Kit2). Capture antibody coated 384 well microplate with 25 μ l per well of dilution capture antibody. The microplate was sealed and incubated overnight at room temperature then washed three times with wash buffer (0.05% Tween® in PBS). Blocked microplate by adding 75 μ l of Reagent Dilution to each well, then they were incubated at room temperature for 1 hour, three times with wash buffer. The microplates are ready for sample addition. 25 μ l supernatant of sample were add into microplate with capture antibody coated and incubated for 1.5 hours at room temperature, then washed with wash buffer for 3 times, added detection antibody and incubated for 1 hour at room temperature and then washed with wash buffer for 3 times. Dilution of Streptavidin-HRP were added into microplate, and incubated, then the microplate was washed for 3 times. Substrate solution: 1:1 mixture of color reagent A (H₂O₂) and colour reagent B

(Tetramethylbenzidine) was added, then incubated for 20 min at room temperature and then 12.5 μ l of stop solution: 2N H₂SO₄ to each well. The plates were read using a GloMax® Discover microplate reader (brand Promega) at 460 nm and 560 nm.

5.3. Results

5.3.1. Characterisation of copolymer

5.3.1.1. NMR

A total of five of copolymers were synthesized by thermal free radical polymerization. The ¹H NMR spectrum of synthesized copolymers are presented in Figure 5.3(a-e) Methyl protons of EGDMA and HDFDMA monomer/copolymer at δ 4.4 and 2.6 respectively as in Figure 5.3a. The vinyl structure at the chemical shifts of 5.6 and 6.2 ppm of EGDMA monomer chemical shifts and the peak at 5.6 ppm confirm that it is methacrylate monomer.²⁴⁴ In Figure 5.3b the 1H and 2H peaks correspond to protons on the CDCl₃ solvent, the cyclohexyl ring of CHMA, the methyl substituent of DMAEMA respectively. The cyclohexyl ring protons of CHMA can be seen as a small singlet at δ 4.5 ppm in Figure 5.3c. Signals of the 1H proton in the ring of CHMA and iDMA copolymers at 4.6 ppm (1H) and 3.9 ppm (2H) of CHMA-co-iDMA have been shown in Figure 5.3d. The characteristic peaks at chemical shifts of 3.9 can be attributed to iDMA as shown in Figure 5.3e. The peak of 1H protons in phenyl ring of PhMA are shown between 7-7.5 roughly as shown in Figure A5.2 of Appendix 5. In summary, the copolymers from Figure 5.3 b-e do not have a peak at 5.5 ppm, indicating there isn't any unreacted methacrylate monomer in the sample. This indicates that the polymerization process showed high conversion. The ¹H NMR spectra for monomers are presented in Figure A5.1-4 of Appendix 5.

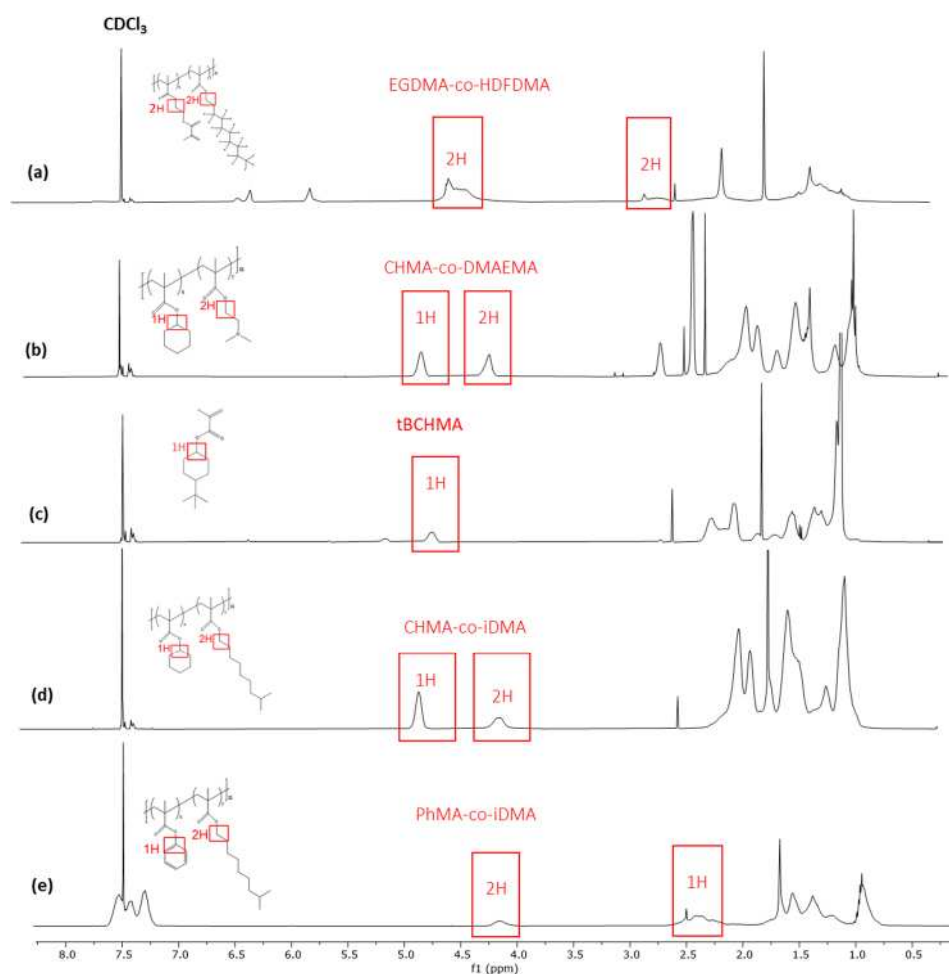


Figure 5.3. ^1H NMR spectrum of synthesis copolymers.

(a) EGDMA-co-HDFDMA, (b) CHMA-DMAEMA, (c) tBCHMA, (d) CHMA-co-iDMA, (e) PhMA-co-iDMA.

5.3.1.2. GPC

The number average molecular weights (M_n), weight-average molecular weight (M_w), and polydispersity (PDI) of copolymer samples are shown in Table 5.2 and Figure A5.2-5. The molecular weights of copolymer (M_w); analysis by GPC indicated M_w of 14,877 g/mol EGDMA-co-HDFDMA, 20,480 g/mol for CHMA-co-DMAEMA, 3,833 g/mol for tBCHMA, 55,864 g/mol for CHMA-co-iDMA and 8,007 g/mol for PhMA-co-iDMA. CHMA-co-DMAEMA, tBCHMA and PhMA-co-iDMA shown low molecular weight. While CHMA-co-DMAEMA and CHMA-co-iDMA shown high molecular weight. CHMA monomer in the reaction mixture lead to induce molecular

weight, CHMA has cyclohexyl pendant group into the copolymer also affect hence entanglement in copolymer. In fact, the copolymer with lower molecular weight polymer have molecular movement than higher molecular weight.²⁴⁵ This is the reason for narrowing polydispersity of the tBCHMA, CHMA-co-DMAEMA and PhMA-co-iDMA copolymers were 1.35 to 1.71. While polydispersity of EGDMA-co-HDFDMA and CHMA-co-iDMA were 2.42 and 2.49. Comparing between CHMA-co-iDMA and PhMA-co-iDMA, it was found that the molecular weights of PhMA-co-iDMA were dramatically lower than those of CHMA-co-iDMA because the PhMA radical or phenyl group is of high resonance stability, resulting in the slow growing radicals of PhMA monomer to polymerize. The GPC result of each copolymer are presented in Figure A5.5-9 of Appendix 5

Table 5.2. Molecular weights and molecular weight distribution

Copolymer	Mn (g/mol)	Mw (g/mol)	Polydispersity (PDI)
EGDMA-co- HDFDMA	6,128	14,877	2.42
CHMA-co-DMAEMA	13,243	20,480	1.54
tBCHMA	2,821	3,833	1.35
CHMA-co-iDMA	22,387	55,864	2.49
PhMA-co-iDMA	4,662	8,007	1.71

5.3.1.3. ToF-SIMS characterisation of chemical copolymer surface

ToF-SIMS analysis of the copolymer was employed to characterise the copolymer coated coverslips. To determine the unique ion associated with the structure and the homogeneity of polymer films coated on coverslips, ToF-SIMS surface analysis was utilised. Both positive and negative ion spectra were collected for each polymer film. The coating was evaluated by locating specific ion identifiers that were specific to each polymer film. Figure 5.4-5.8 shows the positive ToF-SIMS spectra and ion image of copolymers; CHMA-co-HDFDMA, CHMA-co-DMAEMA, tBCHMA, CHMA-co-iDMA and PhMA-co-iDMA. Figure 5.4a shows the positive ToF-SIMS spectrum of CHMA-co-HDFDMA. The distribution of chemistries on the polymer CHMA-co-HDFDMA coated coverslips are shown in Figure 5.4b, polymer of monomer HDFDMA, which contained a fluorinated ion, a number of fluorinated ions (CF^+) were observed, at m/z 41 (C_3H_5^+) and at m/z 69 ($\text{C}_4\text{H}_5\text{O}^+$) ion was observed for methacrylate.²⁴⁶ The whole ToF-SIMS positive ion spectrum of M1-1 biased copolymer (CHMA-co-DMAEMA) coated coverslips, a number of characteristic ions from the methacrylate monomers backbone which synthesized in CHMA-co-DMAEMA copolymer was observed for $\text{C}_4\text{H}_5\text{O}^+$, the intensity of $\text{C}_6\text{H}_{11}^+$ ion which cyclohexyl ring in CHMA and $\text{C}_4\text{H}_8\text{N}^+$ and $\text{C}_4\text{H}_{10}\text{N}^+$ ions were characterised of 2-(dimethylamino)ethyl as shown in Figure 5.5. ToF-SIMS ion spectra and images of copolymer tBCHMA with peak at m/z 57 (C_4H_9^+), 69 ($\text{C}_4\text{H}_5\text{O}^+$) and 83 ($\text{C}_6\text{H}_{11}^+$) corresponding to monomers backbone of tBCHMA (Figure 5.6). Results in Figure 5.7. are from spectra and images in copolymer CHMA-co-iDMA were detected as $\text{C}_4\text{H}_5\text{O}^+$, $\text{C}_6\text{H}_{11}^+$, C_2H_5^+ , C_3H_5^+ , C_4H_9^+ ion and show the location of chemical structures of polymers. The peak corresponding to copolymer PhMA-co-iDMA produced in ToF-SIMS spectra was clearly detected at m/z 29 (C_2H_5^+), 41 (C_3H_5^+), 57 (C_4H_9^+), 59 ($\text{C}_4\text{H}_5\text{O}^+$), and 77 (C_6H_5^+) ions, C_6H_5^+ ion which phenyl in PhMA as shown in Figure 5.8. ToF-SIMS analysis allows for the chemical identification of polymer coating surfaces. It was noted that the ion distribution demonstrated that the polymer was uniformly coated on the coverslips.

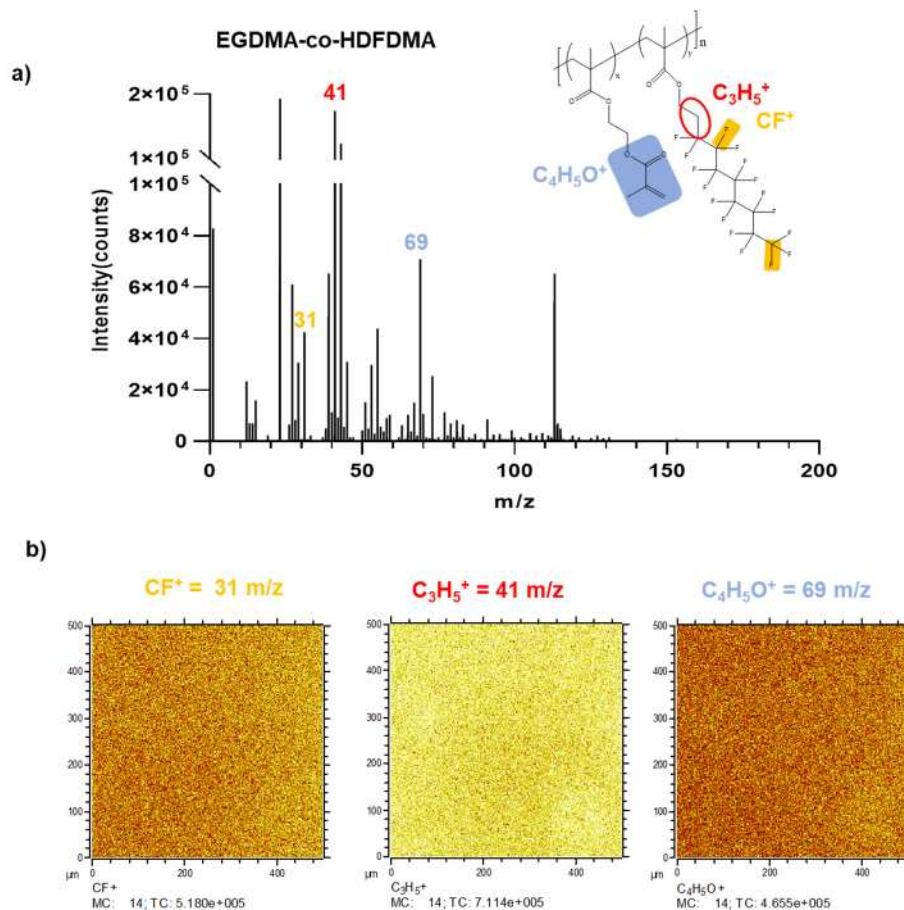


Figure 5.4. ToF-SIMS spectra and ion image of copolymers; CHMA-co-HDFDMA.

a) ToF-SIMS positive ion spectrum of copolymer (EGDMA-co-HDFDMA) coated coverslips, where the inset spectrum shows the peak of CF^+ at $m/z = 31$ (orange), $C_3H_5^+$ at $m/z = 41$ (red) and $C_4H_5O^+$ at $m/z = 69$ (light-blue). b) ToF-SIMS 2D chemical ion maps of copolymer (EGDMA-co-HDFDMA) coated coverslips. ($n=3$)

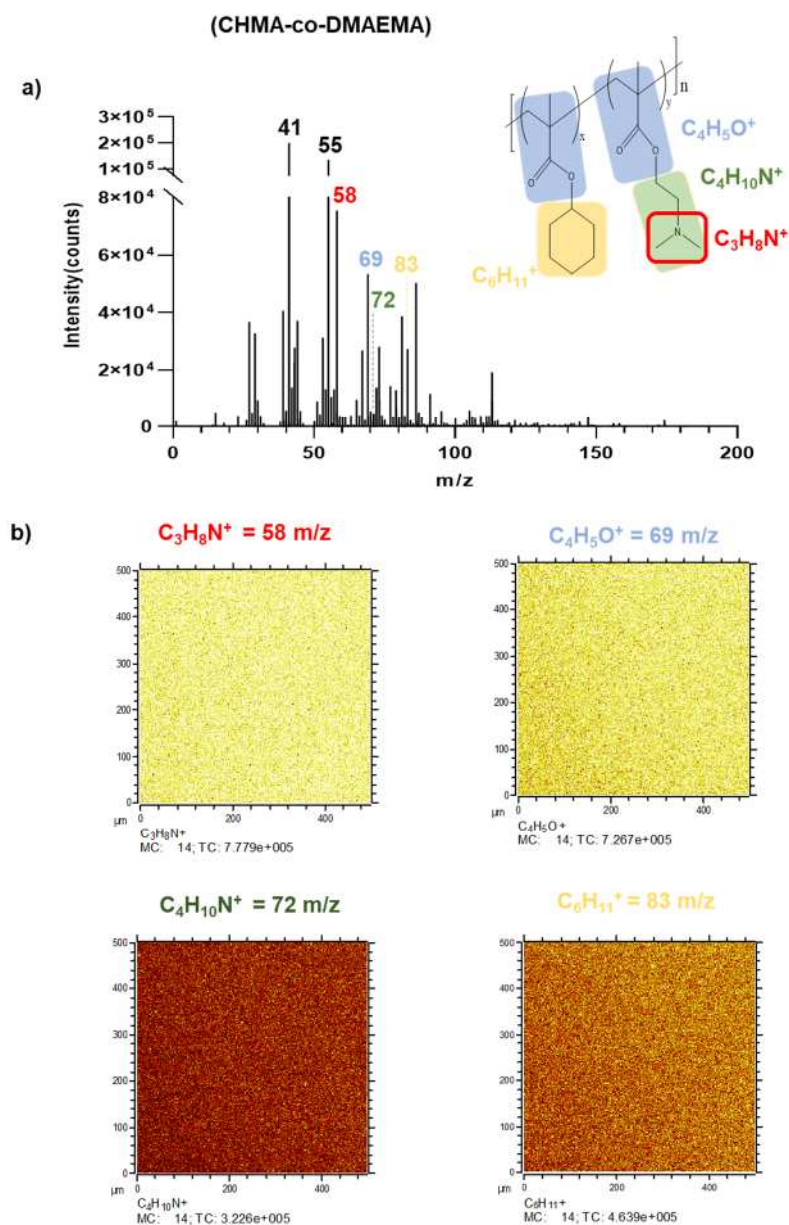


Figure 5.5. ToF-SIMS spectra and ion image of copolymers; CHMA-co-DMAEMA.

a) ToF-SIMS positive ion spectrum of copolymer (CHMA-co-DMAEMA) coated coverslips, where the inset spectrum show the peak of the $[M+H]^+$ of $C_4H_5O^+$ at $m/z = 69$ (blue), $C_4H_{10}N^+$ at $m/z = 72$ (green) and $C_6H_{11}^+$ at $m/z = 83$ (yellow). b) ToF-SIMS 2D chemical ion maps of copolymer (CHMA-co-DMAEMA) coated coverslips. ($n=3$)

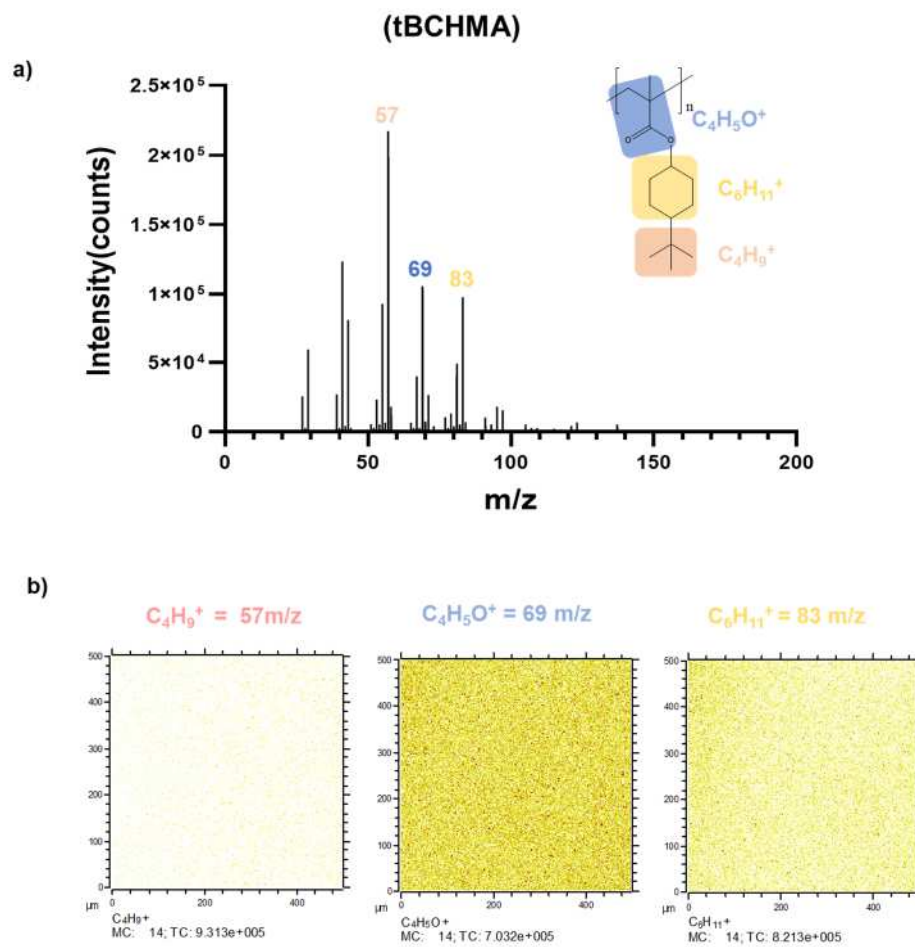


Figure 5.6. ToF-SIMS spectra and ion image of copolymers; tBCHMA.

a) ToF-SIMS positive ion spectrum from copolymer (tBCHMA) coated coverslips, where the inset spectrum shows the peak of the $C_4H_9^+$ at $m/z = 57$ (pink), $C_4H_5O^+$ at $m/z = 69$ (light blue), and $C_6H_{11}^+$ at $m/z = 83$ (yellow). b) ToF-SIMS 2D chemical ion maps of copolymer (tBCHMA) coated coverslips. ($n=3$)

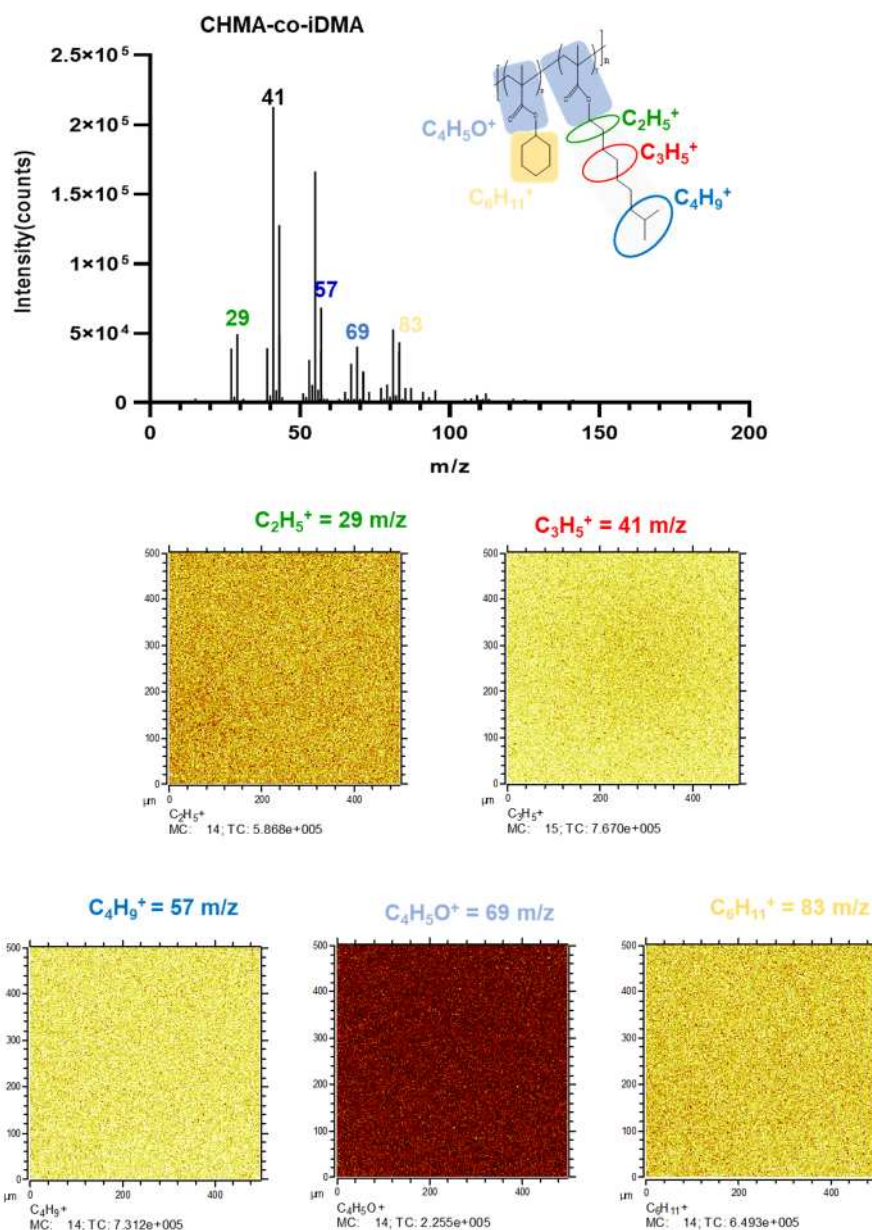


Figure 5.7. ToF-SIMS spectra and ion image of copolymers; CHMA-co-iDMA

a) ToF-SIMS positive ion spectrum from copolymer (CHMA-co-iDMA) coated coverslips, where the inset spectrum shows the peak of the C₂H₅⁺ at m/z = 29 (green), C₃H₅⁺ at m/z = 43 (red), C₄H₉⁺ at m/z = 57 (dark-blue), C₄H₅O⁺ at m/z = 69 (light-blue), and C₆H₁₁⁺ at m/z = 83 (yellow). b) ToF-SIMS 2D chemical ion maps of copolymer (CHMA-co-iDMA) coated coverslips. (n=3)

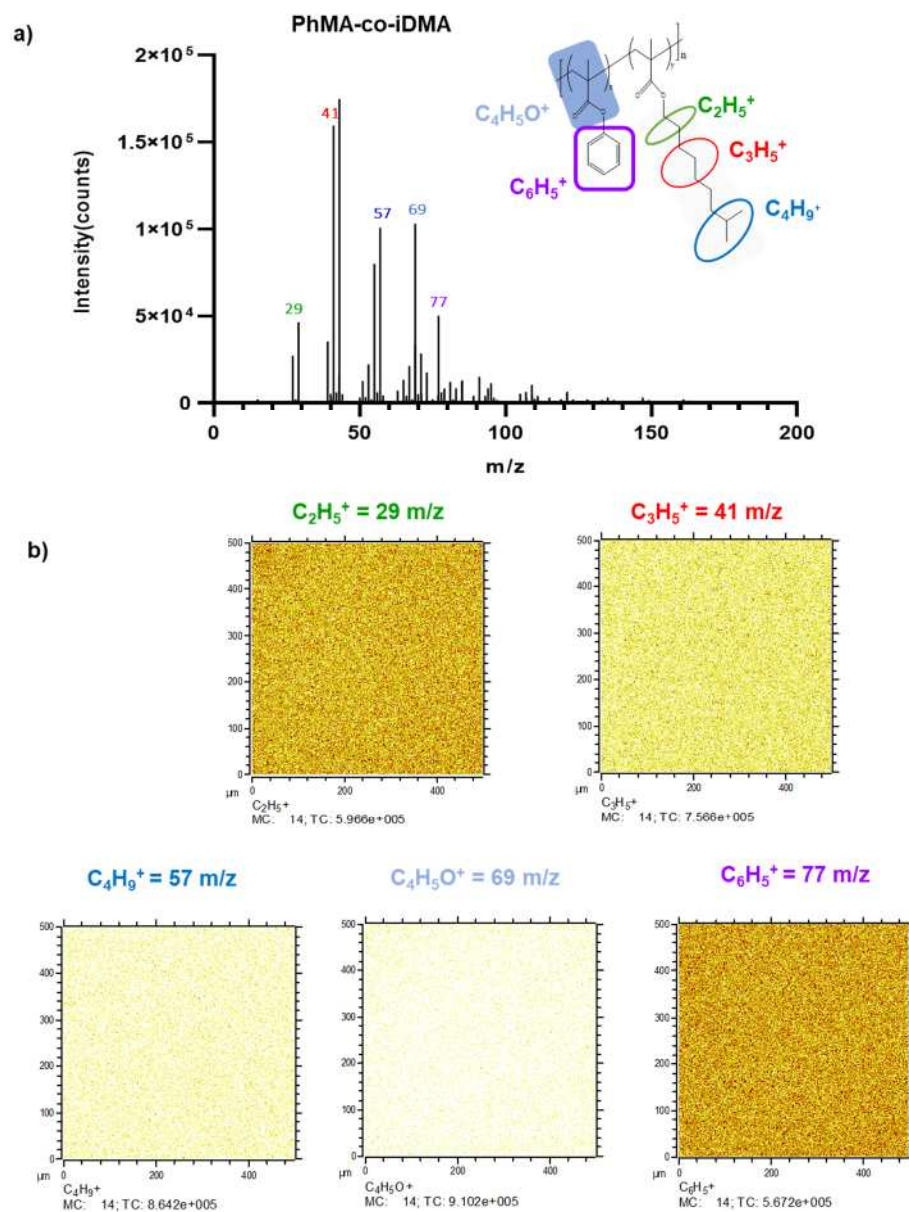


Figure 5.8. ToF-SIMS spectra and ion image of copolymers; PhMA-co-iDMA

a) ToF-SIMS positive ion spectrum from copolymer (PhMA-co-iDMA) coated coverslips, where the inset spectrum shows the peak of the $C_2H_5^+$ at $m/z = 29$ (green), $C_3H_5^+$ at $m/z = 41$ (red), $C_4H_9^+$ at $m/z = 57$ (dark-blue), $C_4H_5O^+$ at $m/z = 69$ (light-blue), and $C_6H_5^+$ at $m/z = 77$ (yellow). b) ToF-SIMS 2D chemical ion maps of copolymer (CHMA-co-iDMA) coated coverslips. ($n=3$)

5.3.1.4. Evaluation of macrophages viability on polymer surface

After polymers were coated on the coverslip, their capacity to support cell viability was checked. According to the viability assessments, monocytes were cultured on coverslip as a control (M0, M1 and M2) and polymer surfaces for 6 days and were subjected to a viability assay. At the first stage of the experiment, polymers coated coverslips were placed in the vacuum oven (<50 mTorr) for 7 days to remove solvent and they were further washed with PBS overnight, before being used for monocyte culture. After measuring the fluorescence, the values from the polymer conditions were compared to the values from a dead cell as a control. Toxicity after 6 days culture of each polymer condition was not significantly different and they were shown to have high cell viability on all five polymers surface in Figure 5.9. Hence, a polymer was considered cytocompatibility if it consistently supported up to 90% cell viability compared to a dead cell. Therefore, they were considered for further experiments.

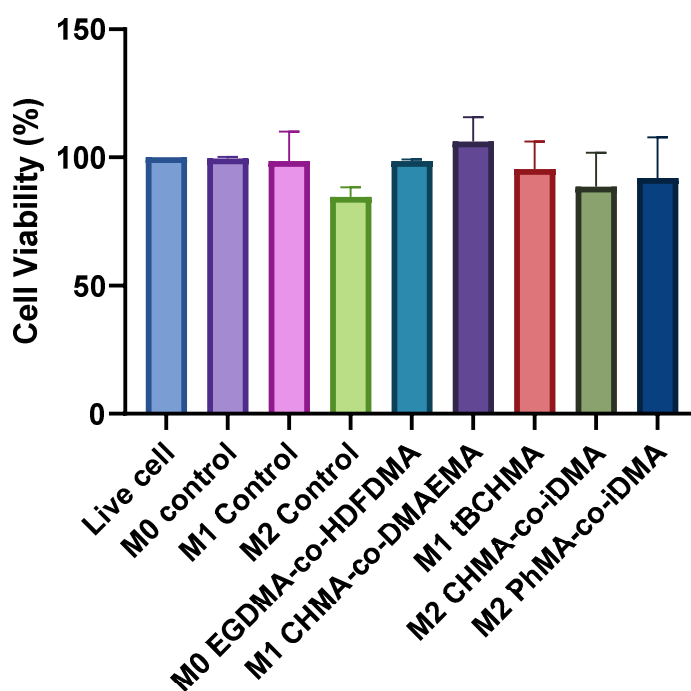


Figure 5.9. Assessment of toxicity on polymer surfaces by ToxiLight assay. Fluorescence measured each polymer condition normalised to live cell maximum baseline, suggesting high cell viability on the five polymers surface.

5.3.1.5. Expression of surface markers on polymer coated

To investigate the impact of surface chemistry on polymer (EGDMA-co-HDFDMA, CHMA-co-DMAEMA, tBCHMA, CHMA-co-iDMA, and PhMA-co-iDMA). Expression of M1 and M2 surface phenotypic marker, calprotectin and mannose receptor (MR) was characterised using fluorescence microscopy (Figure 5.10.a) According to the results of observations and measurements of the fluorescence intensities in Figure 5.10 b-c, both polymers M1-biased had the highest expression of calprotectin, compared to polymers M2 biased. Whereas polymers M2 biased (CHMA-co-iDMA, and PhMA-co-iDMA) were found to express the highest level of MR and very low levels of calprotectin.

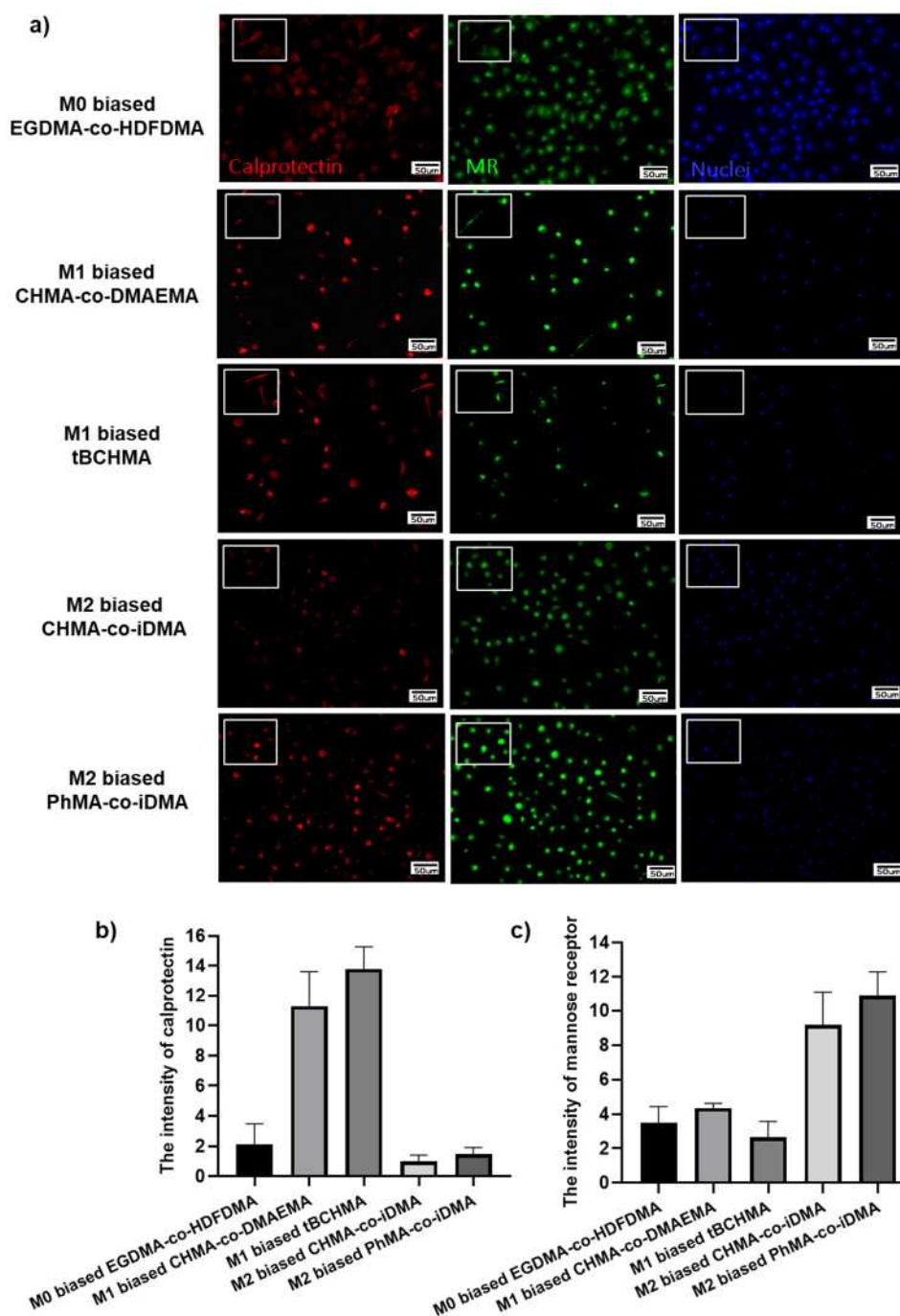


Figure 5.10. Expression of surface phenotypic markers in M1 and M2.

a). Fluorescent images of macrophages stained for calprotectin (27E10 antigen, red), mannose receptor (MR, green) and nuclei (blue) were stained with DAPI., images were taken under 20 x magnification and the scale bar = 50 μ m. b and c) The intensity of calprotectin and mannose receptor is shown on polymer surface images. Data is presented as mean \pm S.D of N=3.

5.3.1.6. Cytokines analysis

To find out the effect of macrophage polarization on polymer surfaces. Supernatants from the different polymer surfaces were obtained for cytokine analysis. Polymer M1-biased CHMA-co-DMAEMA induced the highest level of the pro-inflammatory cytokines TNF- α and IL-1beta as can be seen on Figure 5.11a and b. On the other hand, polymer M2 biased produced significantly lower amounts of the pro-inflammatory cytokines TNF- α and IL-1beta compared to other polymers. For IL-10 and CCL-18 cytokines analysis, polymer M2 biased CHMA-co-iDMA, produced the highest level of IL-10 and CCL-18 as shown in Figure 5.11c and d, while polymer M1biased tBCHMA produced the least levels of IL-10.

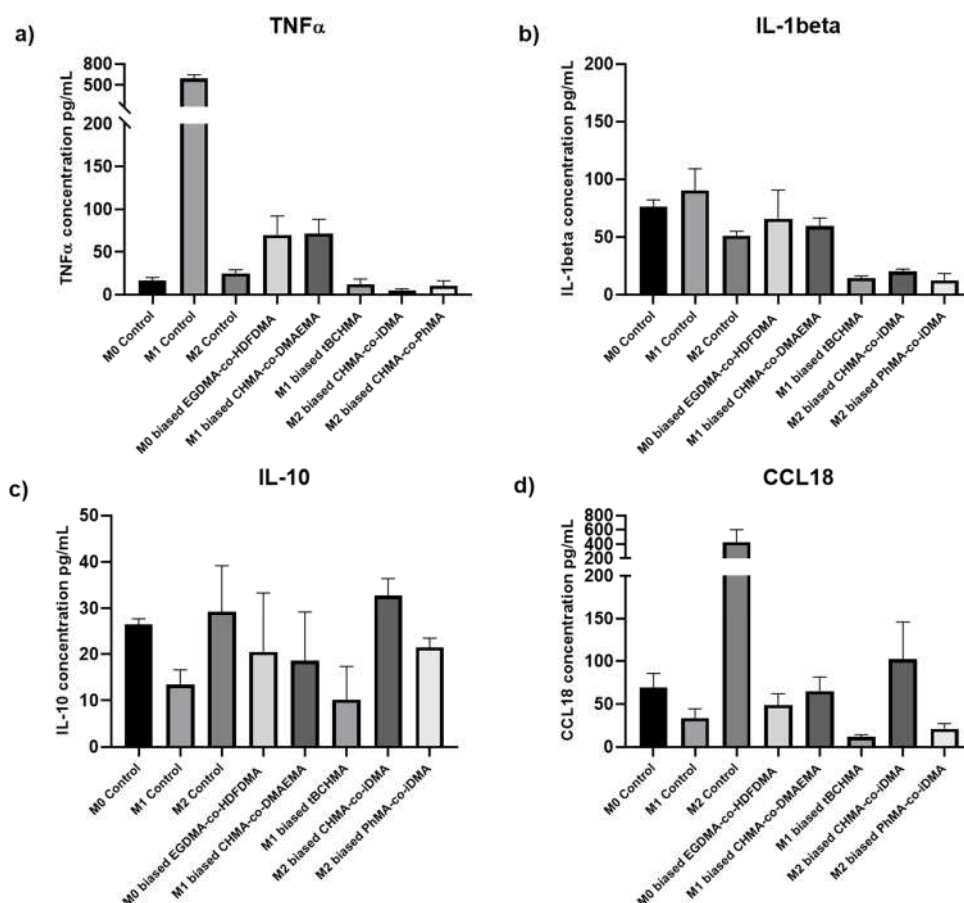


Figure 5.11. Comparison of cytokines production by different polymer surface.

Supernatants of each polymer cultured for 6 days were measured by the enzyme-linked immunosorbent assay. a) TNF- α , b) IL-1beta, c) IL-10 and d) CCL-18.

5.4. Discussion

Synthetic polymers are being used in the medical industry for a number of applications such as cardiovascular stents, catheters, orthopaedic coatings, and dental diseases. These polymers are well-suited for their intended uses because of their unique physiochemical characteristics. It has been shown that most polymeric materials induce general and specifically macrophage inflammation.²⁴⁷ This has been linked to a variety of issues, hence the requirement for more biocompatible materials. It is generally acknowledged that macrophages are extremely flexible, assuming a variety of morphologies in response to microenvironmental cues. Due to their plasticity, it is acceptable to assert that macrophages can acquire a mixed phenotype, exhibiting both M1 and M2 characteristics.²⁴⁸ As a result, a panel of M1 and M2 related markers, macrophage functions, and their impacts on other cell types are indicated for the proper evaluation of macrophage phenotype. In accordance with this, certain polymers found to have impacted macrophage polarisation in an earlier polymer screening were subjected⁷⁹ to additional research.

Selected polymers from previous work by Rostam *et al.*⁷⁹ were scaled-up using thermal initiator FRP. FRP syntheses have been used as a route to the ability to control polymer properties such as molecular weight and polydispersity. these has distinct advantages. Additionally, thermal FRP may subsequently be solubilized and coat onto a variety of surfaces and substrates without UV light treat as photochemical initiator FRP. All five hit polymers were successfully synthesised from their monomers using thermal initiator FRP. Initial studies focused on polymer bulk properties on scaled-up polymers, such as NMR, Mw, PDI, and surface analysis. The NMR formation of polymer is clearly evident from the disappearance of the monomer. This result was assessed as successful by the investigation initiator FRP. Mw and PDI results show the copolymer has a lower Mw and exhibits a higher PDI. PDI of polymers provides information regarding the distribution of polymer chains in the polymer. In polymers with a monodisperse chain, the polydispersity value is 1.0. On the other hand, polymer with high PDI is more heterogenous.

The synthesised polymers were coated onto glass coverslips by spin coating and the coated substrate were analysed with ToF-SIMS. All copolymer coated coverslips were

successfully prepared and chemically distinct from each other. ToF-SIMS results showed that the initial attempts to coat onto coverslip with copolymers have presented the surface details of chemical structures from each copolymer. Moreover, the synthetic polymers were coated on glass coverslips, and ToF-SIMS analysis demonstrated that they formed uniformly coated films. This ToF-SIMS data has confirmed the presence of the polymer on the surface of samples and can be used to correlate future biological results to relevant surface chemistry functionalities.

Following polymer properties, the second study focused on cell viability on coated coverslips. Cytotoxicity on polymer coated coverslips was influenced by thermal polymerisation. Toxicity on all polymers following thermal polymerisation was not significantly different of % toxicity and they were non-toxic. Polymers were used to investigate their effect on macrophage polarisation. In that study, polymer CHMA-co-DMAEMA and tBCHMA were identified to induce pro-inflammatory macrophages (hence M1-biased polymers), whereas polymer CHMA-co-iDMA and PhMA-co-iDMA induced anti-inflammatory macrophages (hence, M2-biased polymers). One stimulatory polymer CHMA-co-DMAEMA was observed to activate macrophage response as shown by the higher production of pro-inflammatory cytokines (TNF γ and IL-1 β) as well as expression of M1 surface phenotypic marker. Other polymers CHMA-co-iDMA gave indication for anti-inflammatory cytokines production. In addition, polymer CHMA-co-iDMA and PhMA-co-iDMA showed high expression of M2 surface phenotypic marker.

In vivo, macrophages engage in interactions with other immune and tissue repair cells, hence influencing their activity.²⁴⁹ This suggests that the kinds of functions carried out by these other cells are dependent on the types and levels of inflammatory mediators produced by macrophages. These soluble mediators are created by the immune system. It is commonly established that an abnormally high level of inflammatory mediator generation in reaction to biomaterials leads to dysfunction in the activities of tissue repair cells. Controlling the production of cytokines by macrophages in the surroundings of implant sites can therefore be an effective method for managing fibrosis as a reaction to implants. Regardless of the variances that were detected throughout biological investigations, an analysis of the cytokines that were released

by macrophages on various polymers demonstrated either an over expression or a down regulation of essential M1 and M2 cytokines.

In summary, the five polymers identified from the Rostam et al study, were successfully synthesised by thermal FRP and analytically characterised.⁷⁹ In addition, the synthesised polymers were coated onto glass coverslips and ToF-SIMS analysis revealed that uniformly coated films were formed. Further, the polymers were observed to augment the secretion profile of cytokines, expression of surface phenotypes towards distinct pro- or anti macrophage phenotypes. Based on these results, five polymers that represented each of the classified phenotypic groups. Therefore, all polymers were chosen to act as a proof-of-concept model, with plans to use two polymers based on cytokine assay and their ability to produce M1 and M2 phenotypes in macrophages as polymer CHMA-co-DMAEMA and CHMA-co-iDMA for *in vivo*.

Chapter 6

6. Modulation of local host metabolite response to subcutaneous implantation by novel immune-instructive polymers in a mouse model using the 3D OrbiSIMS

Manuscripts in preparation

This chapter aims to study the immune response to the polymers, silicon catheter sections were explanted and analysed using both conventional immunohistochemistry techniques and 3D OrbiSIMS in situ metabolite profiling to determine the immune response of tissue surrounding the implanted foreign body. This study utilised the 3D OrbiSIMS depth profile analysis mode on *ex vivo* mouse samples whose positive and negative polarity surrounded the foreign body site. We detected targeted and untargeted signatures of pro- or anti-inflammatory polymers implanted to identify metabolites, including lipids, amino acids and other small molecules.

Authors

Waraporn Suvannapruk,^a Leanne E Fisher,^b Jeni C Lockett,^c Max K Edney,^d Dong-Hyun Kim,^a David J Scurr,^a Amir M Ghaemmaghami,^b and Morgan R Alexander ^{a*}

^a Advanced Materials and Healthcare Technologies Division, School of Pharmacy, University of Nottingham, University Park Nottingham, NG7 2RD, United Kingdom.

^b Immunology & Immuno-bioengineering Group, School of Life Sciences, Faculty of Medicine and Health Sciences, University of Nottingham, University Park Nottingham, NG7 2RD, United Kingdom.

^c School of Life Sciences, Faculty of Medicine and Health Science, University of Nottingham, University Park Nottingham, NG7 2RD, United Kingdom.

^d Department of Chemical and Environmental Engineering, Faculty of Engineering, University of Nottingham, University Park Nottingham, NG7 2RD, United Kingdom.

Corresponding Author: *E-mail: morgan.alexander@nottingham.ac.uk

6.1. Abstract

A key goal for implanted medical devices is that they do not elicit a detrimental immune response. Macrophages play critical roles in modulation of the host immune response and are the major cells responsible for eliciting persistent inflammatory responses against implanted biomaterials. We investigate two novel non-eluting immune-instructive polymers that stimulate pro- or anti-inflammatory responses in macrophages *in vitro*, for their ability to modulate foreign body responses against subcutaneously implanted silicone in mice. The tissue surrounding the implant is sectioned to assess the response of the polymers compared to silicone rubber. Immunofluorescent staining reveals responses consistent with pro or anti-inflammatory responses previously described for these polymers. For the first time we apply 3D OrbiSIMS analysis to provide spatial analysis of the metabolite signature in the tissue surrounding the implant, providing insight into the metabolite response in the host tissue. For the pro-inflammatory (M1-polymer), glycerolipids such as monoacylglycerols (MG) and diacylglycerols (DG) are observed at increased intensity. While for the anti-inflammatory (M2-polymer) the number of phospholipid species detected decrease and the compounds pyridine and pyrimidine increase. These findings link to observations of small molecule signature of single cell M2 macrophages *in vitro*. This link illustrates the power of metabolite characterisation by the 3D OrbiSIMS to gain insight into the mechanism of bio-instructive materials as medical devices and to inform on the foreign body response to biomaterials.

6.2. Introduction

Medical devices are ubiquitous in modern medicine, from coronary stents, catheters, hip/knee replacements, and the everyday contact lens. Patients can suffer adverse immune reactions to implanted devices, leading to chronic inflammation, pain, and on occasion, implant failure.²⁵⁰ The foreign body response and chronic inflammation in the implant microenvironment can be detrimental for the long-term survival and function of implanted materials/tissues.²⁵¹ Macrophages play a critical role in orchestrating the so-called foreign body response against implanted materials.^{46, 252}

Macrophages could perpetuate chronic inflammation or enhance tissue healing depending on the phenotype they adopt in response to biomaterials.^{184, 253} Therefore, control of inflammatory responses by modulating macrophage phenotype may improve better implant integration. This has led to significant interest in designing novel bio-instructive materials with positive interactions with the immune system to induce a favourable macrophage response to a medical device.^{50, 254-257}

The traditional approach to characterise macrophage phenotype during the foreign body response relies on immunohistochemistry for markers that are typically associated with the pro-inflammatory and anti-inflammatory macrophages, such as nitric oxide synthase (iNOS) and the anti-inflammatory arginase-1 (Arg-1) respectively.^{79, 258, 259} One limitation of this approach is the co-expression of both iNOS and Arg-1 markers on many macrophages that makes it difficult to determine their functional phenotype accurately, and therefore a range of cell surface markers have also been identified by immunohistochemistry to profile macrophages.¹²⁸ As an alternative to immunohistochemistry, here we investigate an approach using the metabolomic signature of cells and tissues to both identify changes within the small molecule population at the host/material interface and provide insight into the related molecular changes within the tissue.

Metabolomics is defined as the comprehensive analysis of metabolites in a biological sample, is an emerging technique that has the potential to improve diagnosis and treatment.¹⁹¹ Metabolomic information provides an in-depth understanding of complex molecular interactions in biological systems and is the information that is closest to cell phenotype.²⁶⁰ Metabolomics technology is established as a means to accelerate the discovery and validation of metabolic disease markers, here we explore its power for assessing the influence of bio-instructive implants.

Studies of the metabolites in tissues have used a variety of instrumental and data processing techniques based on targeted and/or non-targeted techniques²⁶¹ such as liquid chromatography mass spectrometry (LC-MS), liquid extraction surface analysis-mass spectrometry (LESA-MS), light microscopy and MALDI-imaging MS²⁶¹ and secondary ion mass spectrometry (SIMS). LC-MS is the most commonly used analytical method for metabolomics. Typically, LC-MS-based metabolite analyses proceed with the extraction of metabolites from tissue samples. LC-MS

requires a significant amount of tissue, for example as presented by Woodward et al., using metabolomics to classify brain tumour tissue required at least 10 mg to obtain a sufficient signal.²⁶² LESA-MS uses solvent extraction on a tissue surface sample to extract and ionise analytes of interest.²⁶³ LESA-MS was used by Meurs et al., to identify metabolites in paediatric ependymoma tumour tissue but LESA was unable to detect non-polar metabolites.²⁶⁴ Time-of-flight secondary ion mass spectrometry (ToF-SIMS) has been used to identify small molecules in biological samples, with a high sensitivity for lipids.^{265, 266} For application in animal studies, Palmquist et al. characterised the bone-implant interface imaging analysis by ToF-SIMS and analysed the chemical and structural.²⁶⁷ However, ToF-SIMS has been limited by its low mass resolving power, and it has not been applied widely to metabolite identification due to associated limitations in assignment certainty.¹⁷⁶ In pursuit of greater assignment specificity of ions, a hybrid of ToF instrument with greater mass resolving power has been developed, utilising SIMS with the Orbitrap mass spectrometer.¹⁵⁹

3D OrbiSIMS is a direct surface analysis technique. This technique enables biological molecule identification using intact diagnostic molecular fragments, generated by a low energy argon gas cluster primary ion beam with high spatial resolution, high mass resolving power (>240,000) for a peak of m/z 200, and mass accuracy (<2 ppm).¹⁵⁹ This capability has been demonstrated on a variety of tissue and cell samples, assigning lipids, proteins, amino acids, peptide fragments of proteins and a selection of other small molecules.^{162, 163, 177, 268} Furthermore, studies of metabolomics that use 3D OrbiSIMS do not need to use chemically fixed cells or liquid extraction procedures and antibody-based cell markers or stains are not a requirement. Freezing of the sample is required to capture the metabolic state, e.g. Linke et al.²⁶⁹ Recently used 3D OrbiSIMS imaging to observe the metabolite characteristics in brain tumour tissue samples to identify clinically relevant molecular metabolism driven subgroup specific phenotypes which was a similar sample preparation approach to previous studies.¹⁵⁹

264

Here, we applied 3D OrbiSIMS analysis to investigate whether there was a molecular signature for different pro- or anti-inflammatory macrophages at the interface of tissue implanted materials. We retrieved implants 28 days after implantation in a subcutaneous murine model using freeze dehydration before analysis. Characteristic

metabolites from the histological sections adjacent to the implanted foreign body site were identified using a combination of a targeted database approach to identifying lipids and a data driven multivariate approach which highlighted amino acids and other small molecules that we interpreted by comparison with the literature on macrophage metabolomics.

6.3. Experimental

6.3.1. Implant sample preparation

Clinical-grade silicone rubber catheters with a 13 mm external diameter were cut to a length of 5 mm (cylinder shape). To secure in an automated dip coating rig, microlance needles were inserted into the catheter wall and clamped. The catheters were prepared by dipping them into Nusil MED1-161 silicone primer, which is made up of tetrapropylsilicate and tetra (2-methoxyethoxy) in 50% v/v acetone and withdrawing rate of 1 mm/min for 30 seconds. They were then dried at room temperature for 2 min. MED1-161 coated catheters were dip-coated into a copolymer solution of each of the polymers (5 % w/v) in dichloromethane with a dipping and withdrawing rate of 1 mm/min for 30 seconds twice. Copolymers were synthesised via a thermal free radical polymerisation method, purified by precipitation into an excess of methanol and then were characterised by NMR and GPC. The polymers used had previously been identified as polarising macrophages *in vitro* and modulating foreign body response *in vivo*: Poly(cyclohexyl methacrylate-co-dimethylamino-ethyl methacrylate), pCHMA-DMAEMA (referred to as M1-polymer) which induce pro-inflammatory macrophage or poly(cyclohexyl methacrylate-co-isodecyl methacrylate), pCHMA-iDMA polymer (referred to as M2-polymer) which induce anti-inflammatory macrophage phenotype.⁷⁹ Coated catheters were dried overnight at room temperature then dried in a vacuum at 50 °C (<0.3 mbar) for 7 days to remove solvent. The chemical structure of the monomers and copolymers pCHMA-co-DMAEMA and pCHMA-co-iDMA are presented in Table A6.1. in Appendix 6

6.3.2. *In vivo* models

In vivo studies were approved by the University of Nottingham Animal Welfare and Ethical Review Board and carried out in accordance with Home Office authorization under project license number PP5768261. Female BALB/c mice, 19-22 g were used in these studies and were housed in individually ventilated cages (IVCs) under a 12 h light cycle, with access to food and water ad libitum. The weight and clinical condition of the mice were monitored daily. UV light was used for 20 minutes to sterilise the catheter segments prior to implantation. All segments were implanted subcutaneously into mice for 28 days, 3 mice/ each polymer. At the end of the animal studies, on day 28, mice are humanely sacrificed by CO₂ euthanasia. The polymer identity was blinded to the researchers until the end of the data quantification. Figure 6.1. shows the schematic diagram of the experimental studies.

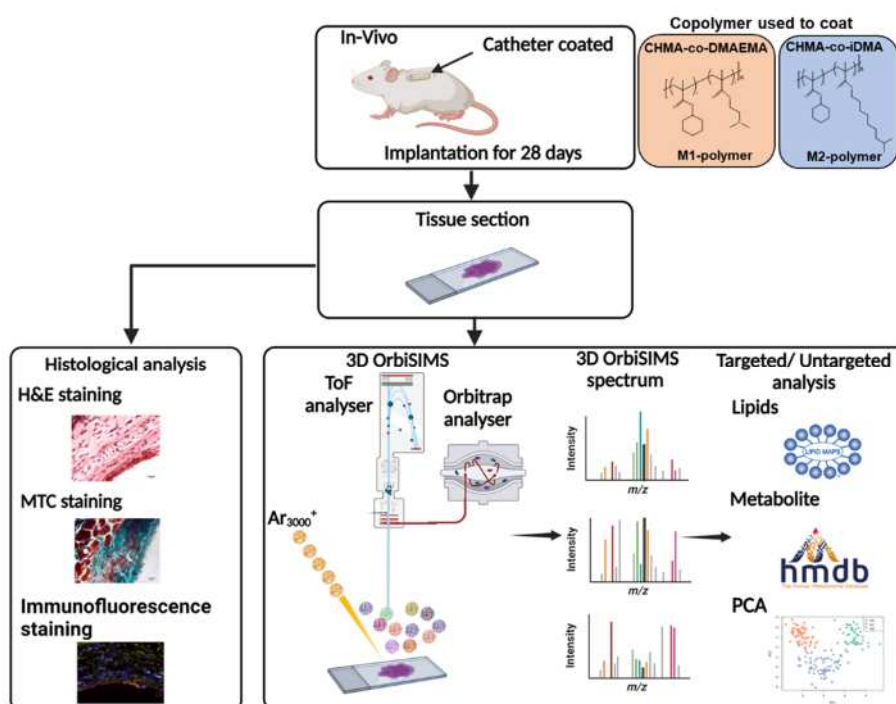


Figure 6.1. Schematic of the *in vivo* studies experimental.

Catheters coated with the copolymers were implanted subcutaneously into a mouse model of foreign body response for 28 days. Following implantation, fresh tissue samples were cut and mounted onto glass slides. For histological analysis, tissue

sections were stained with H&E to assess tissue structure, MTC to analyse collagen thickness as an indication of fibrosis and IHC stains to characterise the macrophage phenotype at the catheter-tissue interface. The GCIB was rastered across the tissue section with the Orbitrap analyser measuring the mass spectrum to analyse each sample with the resultant complex spectra compared using multivariate analysis complemented with targeted analysis., including lipids and metabolites.

6.3.3. Histological Analysis

The catheter segments and surrounding skin after 28 days of implantation were cut to approximately 5.5 cm × 5.5 cm and were embedded in optimal cutting temperature compound (OCT). Following embedding, the tissue was placed in a cryostat chamber at -20°C and sliced into 15 µm thick sections (CM1850, Leica microsystems). The foreign body response to the polymer coatings was assessed by staining with haematoxylin and eosin (H&E) and Masson's trichrome (MTC) using optimised protocols contained in Tables A6.2 and Table A6.3, in Appendix 6 respectively. Following H&E staining, images were recorded using an Axioplan microscope (Zeiss) with a 40X objective to count the number of macrophages and neutrophils (field of view 100 µm x 100 µm) N=2 and n=3. With MTC staining, each sample was captured at 10X magnification, and the thickness of the collagen was measured by taking four measurements from the top to the bottom of the distinct layer: one at the top, one down and the other two further away cross of the images of each sample, N=3 and n=1.

6.3.4. Macrophage phenotype analysis

The method used was taken from Rostam *et al.*⁷⁹ Tissue sections were stained to identify the macrophage phenotype at the catheter-tissue interface. This was carried out using the pro-inflammatory marker inducible nitric oxide synthase (iNOS) and the anti-inflammatory marker arginase-1 (Arg-1). The processing of the macrophage phenotype is shown in Table A6.4.⁷⁹ The stained cells were imaged with a Zeiss LSM880C confocal microscope, and any background fluorescence was subtracted using ImageJ. The mean raw fluorescence intensity density of the region of interest around the foreign body site was used to measure the sum of all pixels in the given

area and at least five different fields of view were randomly examined in each tissue section. We used a signal-to-noise ratio (SNR) of 2 as the detection threshold for fluorescence intensity measurements by ImageJ software. The fluorescence intensity ratio of M2-like macrophages to M1-like macrophages was calculated for each region.

6.3.5. 3D OrbiSIMS analysis

After tissue sectioning, the slices of tissue supported on slides were gently washed 3 times with cold distilled water for 30 s, 1 time with cold 70% ethanol for 30 s and then 3 times with 1 mL of 150 mM ammonium formate solution for 30 s to remove salts which can decrease the sensitivity of molecules in SIMS by signal suppression.²⁷⁰ Tissue slides were plunge frozen in liquid nitrogen and then freeze dried for 12 hours to remove water whilst retaining some degree of 3D structure. The samples were subsequently stored in a microscope slide box container at -80 °C until analysis. Prior to OrbiSIMS analysis, the sample was warmed to room temperature without opening and then mounted onto the instrument sample holder and loaded into the 3D OrbiSIMS for analysis. 3D OrbiSIMS analysis was conducted with a Hybrid SIMS instrument (IONTOF, Germany) using Mode 4 which comprised single Ar_{3000}^+ primary ion beam of energy of 20 keV a duty cycle of 4.4% and continuous GCIB current of 2.3 A, over an area of $100 \times 100 \mu\text{m}$ with crater-size $180.0 \times 180.0 \mu\text{m}$ collecting data using the OrbiTrap analyser in the mass range of m/z 75-1125. The electron flood gun was operated with an energy of 21 eV and an extraction bias of 20 V. for charge compensation. The pressure in the main chamber was maintained at 8.9×10^{-7} mbar using argon gas flooding. The OrbitrapTM cycle time was set to 200 μs . The Orbitrap analyser was operated in positive and negative ion mode at the mass resolving power setting of 240,000 (at m/z 200). The secondary ion injection time was 500 ms, the total ion dose per measurement was 5.21×10^{10} ions/ cm^2 . Adjacent areas on the tissue samples were analysed, 4 regions surrounding the implant region (catheter-tissue interface) per one tissue section slide and 3 regions further away the implant (next to implant, mid-point and next to the dermis) were consumed with both positive and negative polarity.

One 3D OrbiSIMS image using the 20 keV Ar_{3000}^+ analysis beam with a 2 μm diameter probe was acquired. The 20 μm analysis beam was configured as described in the spectra acquisition section. The 5 μm imaging beam duty cycle set to 37.7% and GCIB current was 2.3A. The images were run on the area of $450 \times 450 \mu\text{m}$ using random raster mode. The cycle time was set to 400 μs . Argon gas flooding was in operation; to aid charge compensation, pressure in the main chamber was maintained at 9.0×10^{-7} mbar using argon gas flooding. The images were collected in negative polarity, in mass range 75–1125 m/z . The injection time was set to 500 ms, the total ion dose per measurement was 1.61×10^{13} . Mass-resolving power was set to 240,000 at 200 m/z . All data analysis was carried out using Surface Lab 7.1 software (IONTOF GmbH).

6.3.6. Principal component analysis (PCA)

The 3D OrbiSIMS spectra contained many secondary ions. Principal component analysis was applied to the data set to provide unbiased identification of the differences between each tissue sample. Spectra of all tissue samples were acquired by accumulating data from a single area, 4 areas of each sample were acquired, with each normalized to their respective total ion count in SurfaceLab 7 software.

A peak list was constructed, containing the ions above the minimum ion count intensity, which was determined in each case as being greater than assigned noise signals (1428 peaks in the positive polarity spectra). Multivariate analysis of 3D OrbiSIMS results was done in simsMVA (<https://mvatools.com/>), using Matlab.²⁷¹ The peak list was normalized to total ion count and applied to 4 regions of interest on all samples. The data was pre-processed by Poisson scaling and mean centring. PCA was run in algorithm mode, retaining all principal components.

6.4. Results and discussions

6.4.1. Pro- and anti-inflammatory macrophage polymers influence immune cell infiltration and collagen deposition

Polymers inducing *in vitro* polarisation of monocytes to M1-like or M2-like macrophages were synthesised by the thermal free radical polymerisation and coated onto clinical-grade silicone catheter segments using a dip coater. The *in vivo* response to these novel polymers was compared to each other and widely employed silicone rubber biomedical polymer by subcutaneous implantation into a mouse model of foreign body response for 28 days. Upon recovery of the implants and surrounding skin, tissues were processed, sectioned using either freeze drying for OrbiSIMS analysis, or staining with H&E or MTC or immunohistochemical labelling with iNOS and arginase 1 marker to characterise the inflammatory response, collagen deposition and phenotype marker respectively. The staining and labelling result are presented in Figure A6.1, revealing that a higher number of macrophages were recruited to the tissue surrounding the PDMS catheter segment compared to the coatings which did not significantly differ from each other (Figure A6.1a). A low number of neutrophils was recruited to the M2-polymer, (Figure A6.1b) likely to be due to phagocytosis-induced cell death at the earlier stage of the inflammatory response. Figure A6.1c shows the thickness of collagen deposition M2-polymer had significantly greater collagen deposition compared to PDMS and M1-polymer coated catheters. M1-polymer demonstrated more inflammatory macrophages than the M2-polymer (Figure 6.1d). These results are consistent with previous *in vivo* studies of these polymers, although provide a more detailed analysis of the host response before.⁷⁹

6.4.2. Characterisation of local metabolite changes to implants

3D OrbiSIMS analysis of mouse tissue samples was used to characterise the areas surrounding the foreign body site in both positive and negative secondary ion modes. Principal component analysis (PCA) was initially applied as the most suitable technique for distinguishing chemical differences from the complex OrbiSIMS spectra

from the local host-implant interface spectra (Figure 6.2). The scores of the first and second principal components are presented in Figure 6.2a, highlighting the chemical differences between the M2 and M1 samples most significantly. The loadings graph (Figure 6.2b.) presents the spectra components responsible for the chemical separation of the samples, in this case dominated by the glycerolipids fragments associated preferentially with the pro-inflammatory polymer implant. The series of intense peaks are assigned to glycerol lipids including monoacylglycerols (MG) and diacylglycerols (DG) at m/z 551.5035 (MG 32:2), m/z 575.5035 (MG 34:4), m/z 577.5191 (MG 34:3), m/z 601.5193 (DG O-36:5). The negative score on PC1 was associated amino acids from polymer M2-like such as peak at m/z 91.0545 and m/z 130.0652 (tryptophan), and m/z 103.0543 and m/z 120.0808 (phenylalanine).

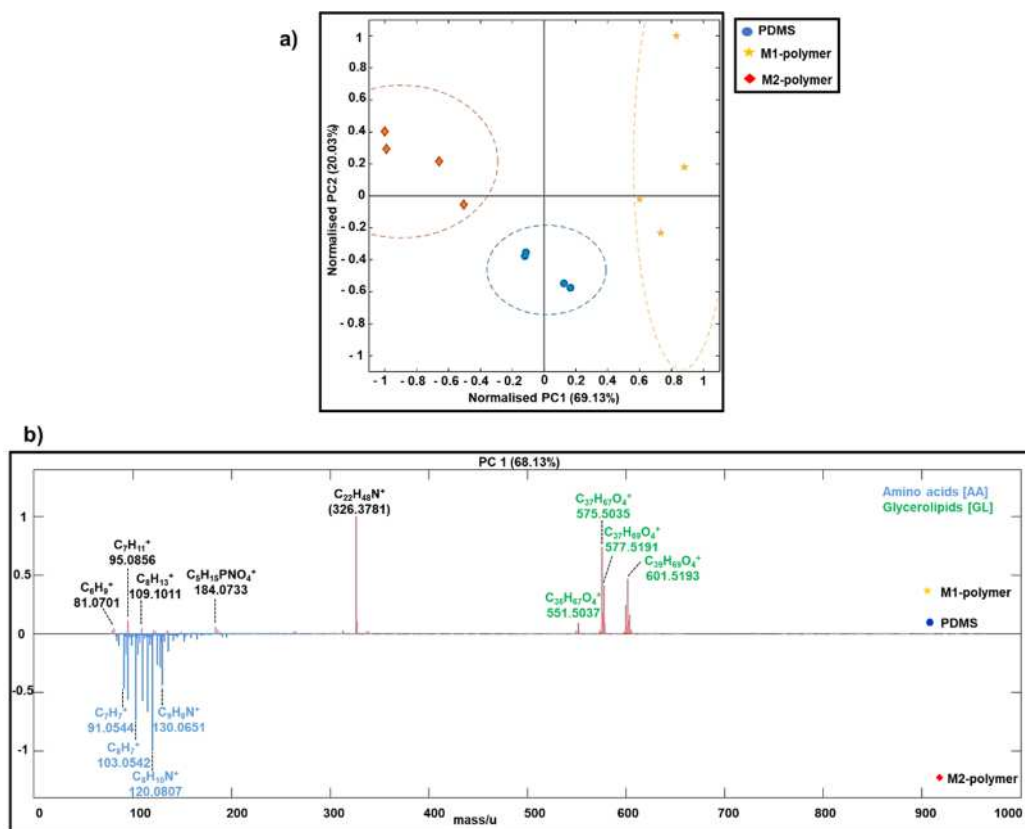


Figure 6.2. Principal component analysis (scores and loadings) for different tissue samples.

a) Principal component scores plot of PC1 and PC2 for the 3D OrbiSIMS spectra of PDMS, M1-polymer and M2-polymer tissue section samples on positive polarity. b)

Principal component analysis of 3 different tissue samples, loadings plots of the first (PC1) and (PC2) principal components and peak were assigned based on glycerolipids marker (green) and amino acids marker (blue). The peak at m/z 326.3781 (didecyldimethyl ammonium), is a commercial surface disinfectant unintentionally introduced to the tissue samples somewhere in the sample handling process.

6.4.3. M1 polymer significantly increased lipids in close proximity to the implant

Quantifying the peak intensities, it is apparent that the glycerol lipid balance changes most strongly with M1-polymer coating identity in Figure 6.3a. Knowing the importance of phospholipids, despite their not appearing in the PCA, we incorporated them in the peak intensity comparison and found that M1-polymer had higher intensity phospholipids than M2-polymer they followed similar trends glycerol lipids. It has been demonstrated that glycerolipid production influences immune cell activity and enhances inflammation.³³ To probe the distribution of glycerol lipids as a function of the distance in the subcutaneous adipose tissue from the implant, mass spectra were acquired from three different areas (next to the implant, mid-point and next to the dermis) as shown in Figure 6.3b. and compared to that of glycerolipid for each implant (Figure 6.3c-e and Table A6.5). as shown in Figure 6.3b. and compared to that of glycerolipid for each implant (Figure 6.3c-e and Table A6.5). The M1-polymer implant was associated with a higher intensity of glycerolipid compared to PDMS and M2-polymer coated catheters (Figure 6.3d). No such clear correlations were seen for the PDMS or the M2-polymer implant.

As expected, this indicated that glycerolipid are increased in pro-inflammatory tissues. A glycerolipid combines glycerol and at least one fatty acid. Glycerolipid are the main long-term energy-storing molecules in mammalian cells and second messenger signalling lipid.²⁷² Thus, much of the stored fat in the adipose tissues of animals consists primarily of glycerolipids.²⁷³ Monoacylglycerols (MG), diacylglycerols (DG) and triacylglycerols (TG) are types of glycerolipids.²⁷⁴ As its name suggests, MG consists of a glycerol molecule connected to a single fatty acid. The two components are connected through an ester bond. DG is a glycerolipid composed of a glycerol

molecule and two fatty acid chains linked by ester bonds. It has been demonstrated that glycerolipid production influences immune cells activity and enhances inflammation.^{275, 276} For example, DG functions as a second messenger that modulates the activation of protein kinase C (PKC), an enzyme that contributes in T cell activation and proliferation, hence preserving the integrity of the cell membrane.^{277, 278} The accumulation of DG can lead to a state of lipotoxicity, which causes cell dysfunction and apoptosis, and can also induce diabetes and cancer.²⁷⁹ This work demonstrates that our tissue metabolomic profiling with 3D OrbiSIMS successfully detected differential glycerolipid levels in tissue.

Phospholipid compounds were detected at lower levels than the glycerol lipids, but the number common and unique species to the three tissues are compared in Figure 6.3f. A higher number of phospholipid compounds were detected in M1-polymer than PDMS and M2-polymer. A total of 128 lipid compounds were identified in M1-polymer and 63 lipid ions in common and 4 in M2-polymer tissue uniquely using the LIPID MAPS database (Table A6.6). The list of unique phospholipid signatures in each sample as shown in Figure 6.3g.

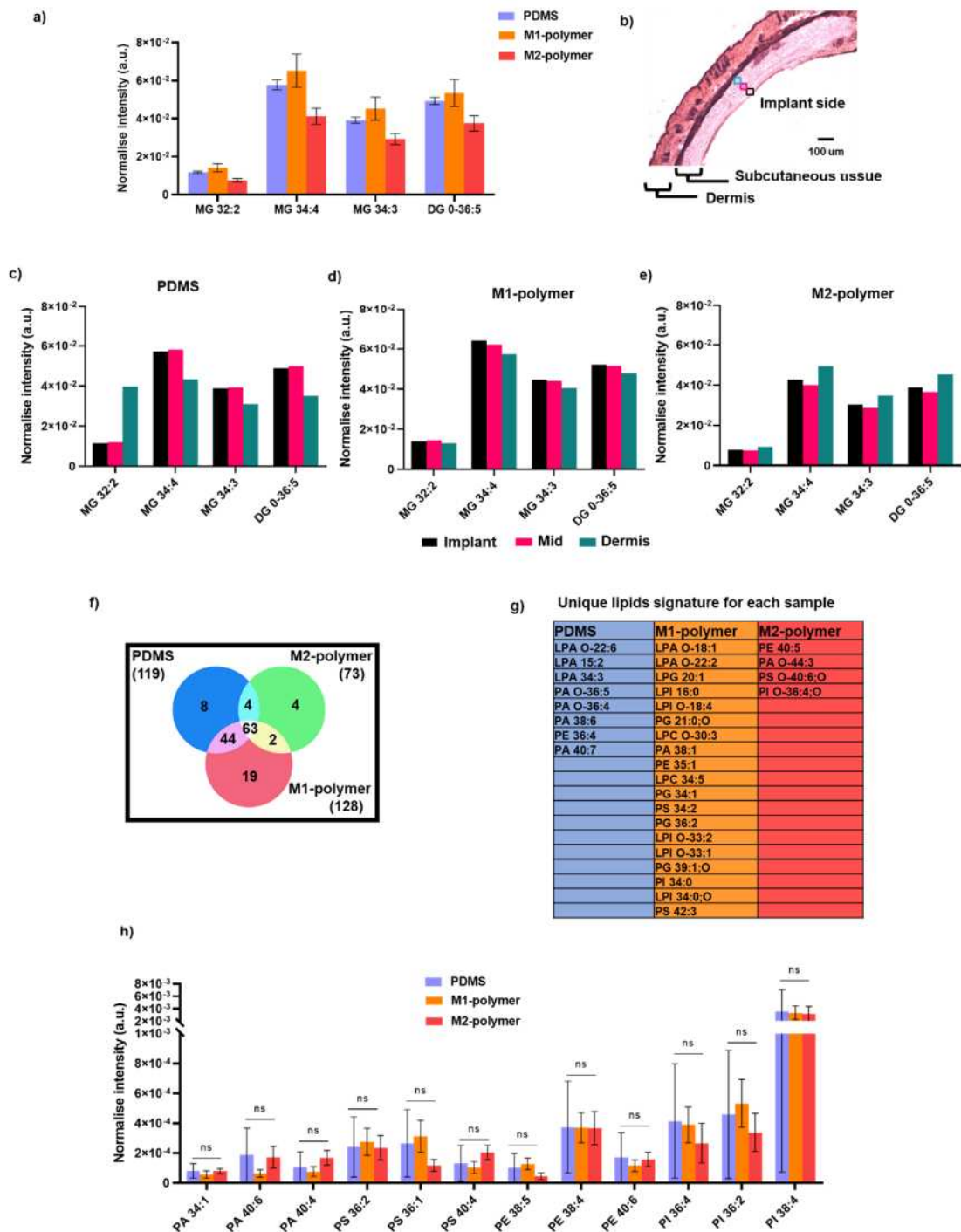


Figure 6.3. Quantification of characteristic lipid fragments intensity were detected by OrbiSIMS in positive and negative ion mode.

a) The normalized intensity of four different glycerolipid species in each tissue samples. b) H&E stain image shows the three regions further away the implant was analysed, implant (black), mid-point (pink) and dermis (sky blue). The normalized intensity of glycerolipid as a function of distance from the implant in each sample c) PDMS, d) M1-polymer and e) M2- polymer. f) Venn diagram comparison of the number of lipid compounds detected in 3 different tissue samples using 3D OrbiSIMS

and unique lipids signature for each sample. g) The list of unique lipids signature in each sample. h) Normalized intensity of lipids in three separate sample.

Almost all phospholipid species, PS, PE and PI in M1-polymer showed a higher intensity than M2-polymer (Figure 6.3h and Table A6.7). However, a low signal from the PA species was also observed in M1-polymer. Lipids are essential structural components of cell membranes, influencing membrane fluidity, ion exchange, and apoptotic signals and also major energy storage component.²⁸⁰ Several authors have demonstrated that targeting lipid metabolism in macrophages can enhance the results of mouse models of chronic inflammation. As a result, the tissue from next to the M1-polymer which is pro-inflammatory tissue sections with a high number of lipids, indicated that lipid uptake causes an increase in reactive oxygen species (ROS) in macrophages, leading to mitochondrial dysfunction and impaired OXPHOS.^{281, 282} It is believed that this prevents polarization into the anti-inflammatory phenotype and contributes to the progression of chronic inflammation.²⁸³ Recent research has focused on the various biological impacts of PA produced by activated macrophages and numerous other cells.^{284, 285} Particularly intriguing is the fact that PA functions as an intermediary messenger for several selective pro-inflammatory targets. PA has been reported to protect LPS-induced septic mice by pharmacologic inhibition.²⁸⁶

The confirmation of the identification of some example putative lipid assignments was achieved using sequential mass spectrometry in the OrbiTrap (MS/MS) of tissue section sample. We performed MS/MS on key ions, the resulting spectra (Figure A6.3a-d), contained the negative ions assigned as the PA and PI. Moreover, MS/MS experimented with the identity of the lipid fragments in the tissue sample which were clearly visible in the whole survey spectrum and MS/MS can provide information on the lipid species, fatty acid moiety, and lipid class.

6.4.4. Imaging of lipids in the tissue

Using the GCIB in imaging mode, the distribution of phospholipids in the 450×450 μm images from an area of the subcutaneous adipose tissue interface adjacent to the implant appears intense and uniformly distributed, shown in (Figure 6.4). An optical ion image of the tissue is presented in Figure 6.4a. and the total secondary ion image is presented in Figure 6.4b with representative molecular ions of the phospholipids classes PA, PS, PE and PI shown in Figure 6.4c. The PI ions were the most intense compared to other lipid species the distribution of each ion seemed similar. In Figure 6.4d, we mapped the species of PI 38:4, $[\text{C}_{47}\text{H}_{82}\text{O}_{13}\text{P}]^-$ and $[\text{C}_6\text{H}_{10}\text{PO}_8]^-$ ion corresponding to the PI head group, and two fatty acids are represented by FA 18:0 $[\text{C}_{18}\text{H}_{35}\text{O}_2]^-$ peak at m/z 283.2642 and FA 20:0 $[\text{C}_{20}\text{H}_{31}\text{O}_2]^-$ peak at m/z 303.2327. We also mapped the nuclear marker and overlaid with the PI 34:4 marker is shown in Figure 6.4e. The ion contribution of nuclear marker $[\text{HP}_2\text{O}_6]^-$ at m/z 158.9056 is mapped in blue, and PI 34:4 at m/z 885.5500 is mapped in red. The nuclear marker intensity distribution is more closely correlated to the phospholipids than the glycerides, indicating that a proportion of these lower intensity former species are generated from cells.

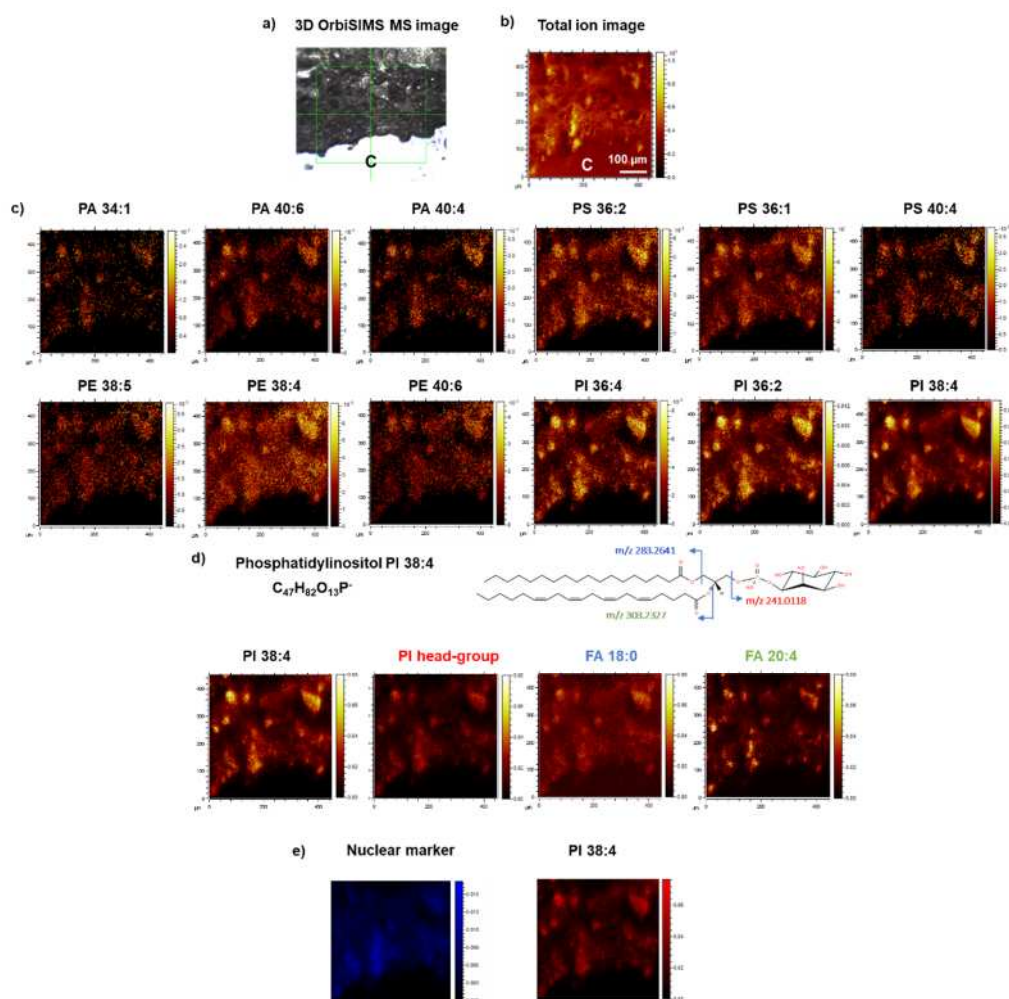


Figure 6.4. Chemical imaging of tissue sample.

a) View of the area where OrbiSIMS optical ion images were acquired (area of $450\ \mu\text{m} \times 450\ \mu\text{m}$). (b–d) 3D OrbiSIMS ion images were recorded in the negative ion mode, (b) total ion image, (c) ion image of the sum of phospholipid specie ions including PA, PS, PE and PI which are divided by total intensity. d) The main ion of PI (38:4), showing the contribution of PI (38:4) ion are the signature fragments of PI head group, two fatty acids fragments (FA 18:0 and FA 20:4) and e) RGB ion images showing PA 34:4 (red) and nuclear marker (blue).

6.4.5. Amino acid ion intensities are higher for M2 polymer implants

The loading plot in Figure 6.2b indicated that the intensity of amino acid ions were strongly associated with the M2 polymer implant shown in Figure 6.5a. A total of 52 amino acid fragments were assigned from the tissue sample presented in Table A6.8. Those differentiating between the samples are plotted in Figure 6.5a, with the M2-polymer implant exhibiting the highest intensities. Comparing the ions versus distance from the implant in Figure 6.5b-d it was apparent that for the M1 polymer implant, the highest amino acid ion intensities were at the subcutaneous adipose tissue abutting the interface with the implant or the dermis.

The amino acid intensities were more similar with distance for the PDMS and M2-polymer implants (Figure 6.5b and d). The characteristic amino acid ions seen are consistent being fragments from proteins. Kotowska et al.¹⁶² gathered lysozyme fragments in spectrum from a protein monolayer sample, with the Arginine -Glycine (RG) amino acid pairs of lysozyme detected at m/z 214.1295 $[\text{C}_8\text{H}_{16}\text{N}_5\text{O}_2]^+$. Then we assigned this protein fragment with tissue sample, the peak intensity comparison and found that M1-polymer had lower intensity than PDMS and M2-polymer as shown in Figure 6.5e-g and Table A6.9. Thus, the trends seen appear to relate to the production of protein-it may relate to the observation that the M1 polymer induced the thinnest collagen FBR layer.

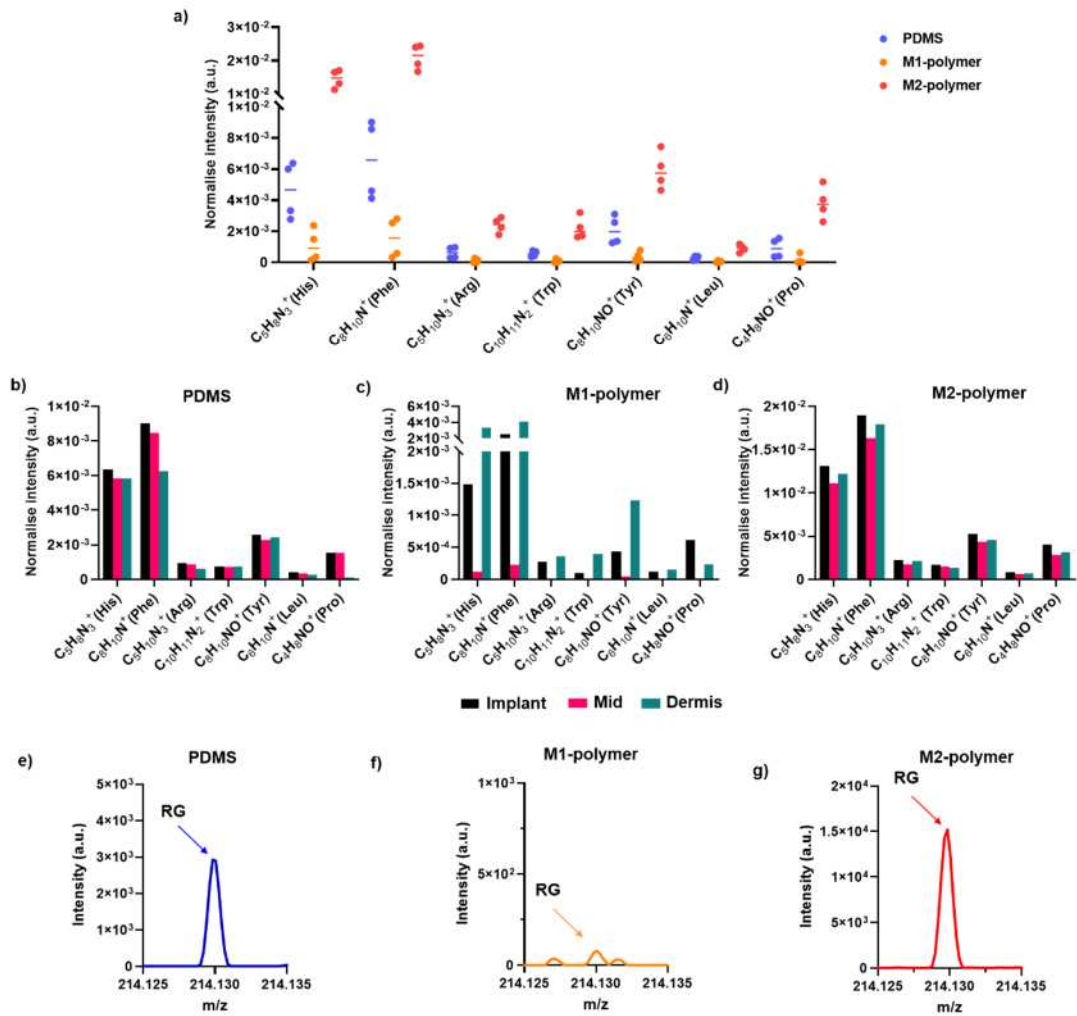


Figure 6.5. Characteristic amino acid fragments were detected in tissue section in positive ion mode.

a) The normalized intensity of amino acid fragments in each sample, PDMS (blue), M1-polymer (orange) and M2-polymer (red). The normalized intensity of amino acids with further away the implant in each sample b) PDMS, c) M1-polymer and d) M2-polymer, implant (black), mid-point (pink) and dermis (sky blue). e-g) The spectrum of amino acids with RG sequences from each tissue sample.

6.4.6. Other small molecules

We compared the tissue sample result with unique metabolites of single cell macrophage subsets, which our previous work that used the Human Metabolome Database to assign non lipid and amino acid molecules found to be significantly altered by cytokine stimulation.¹⁷⁷ We found that for single cells, pyridine ($C_5H_6N^+$) and pyrimidine ($C_4H_5N_2^+$) had high ion intensity after M2 polarisation. This is consistent with our findings that pyridine moieties are intense in tissue adjacent to M2-polymer while being much lower in intensity for tissue adjacent to M1-polymer implants (Figure 6.6a and b). The *in vitro* intensity versus the *ex vivo* intensity of pyridine and pyrimidine were compared and were shown to be highly correlative (simple linear regression curves: $R^2 = 0.9125$ for pyridine; $R^2 = 0.8237$ for pyrimidine), indicating that *in vitro* studies are able to predict *ex vivo* pyridine and pyrimidine intensities.

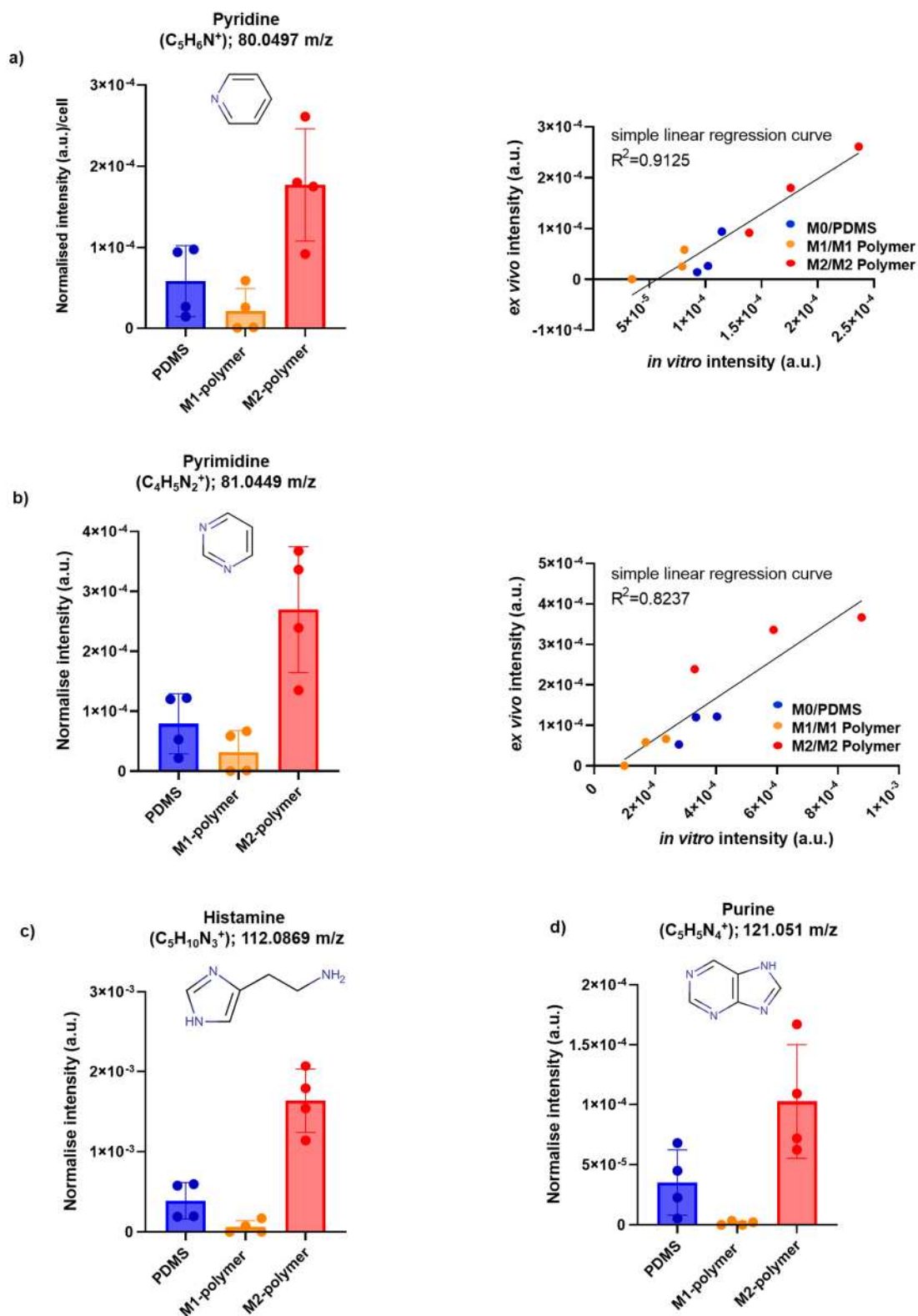


Figure 6.6. Metabolites detected in tissue significantly affected by M2-polymer.

a) and b) Comparing the compounds pyridine and pyrimidine in tissue sample and single cell macrophages were similarly trend. c) Histamine and d) Purine are represented uniquely in tissue adjacent to M2-polymer.

The compounds histamine ($C_5H_{10}N_3^+$) and purine ($C_5H_5N_4^+$) were detected uniquely in tissue from M2-polymer implantation (Figure 6.6c and d). They are both connected to cellular reactions that are anti-inflammatory. Histamine can promote wound healing in skin lesions, inhibit tumour growth, and modulate inflammation in models of colitis and experimental autoimmune encephalomyelitis (EAE).²⁸⁷ Purine, a common substrate in living organisms, is essential for cellular proliferation and a key regulator of the immune system. Multiple enzymes carefully regulate the purine *de novo* and salvage pathways, and malfunction in these enzymes results in excessive cell proliferation and immunological imbalance, which leads to tumour growth.²⁸⁸ Furthermore, purine has antioxidant and anti-inflammatory properties, as well as a role in cell energy homeostasis.²⁸⁹ These correlations between single cell analysis and *ex vivo* tissues stimulated by implanted polymers support the use of molecular characterisation to link and predict *in vivo* performance from *in vitro* observation; highlighting the important role of molecular characterisation in probing molecular mechanistic understanding.

6.5. Conclusions

We report a new label-free direct analysis strategy to provide molecular insight into the host-implant interface using 3D OrbiSIMS. This study provides a detailed molecular characterization of tissue sections, allowing information on the distribution of metabolites, lipids and amino acids. A silicone catheter section coated with different immune-instructive polymers was used as an example medical device in a rodent model of foreign body response. Novel M1-polymer and M2-polymer implants correlated with distinct tissue metabolite profiles revealed by 3D OrbiSIMS. These were found to correlate with single cell analysis of polarised macrophages highlighting the power of this approach in elucidating cell responses in complex biological context. This approach will be beneficial in the design of novel bio-instructive materials that present positive interactions with the immune system to induce a pro-healing macrophage response following implantation.

Chapter 7

7.1. Summary

This thesis developed the first in situ method for single-cell macrophage metabolomic profiling and identified characteristic metabolites on *ex vivo* tissue sections using an Ar₃₀₀₀⁺ cluster primary ion beam and related the species to implant induced inflammation using 3D OrbiSIMS. This is relevant for studies of the functional phenotypes of macrophage cells in culture¹³⁶ and examining the response of tissue surrounding novel implants and the foreign body reaction.⁷⁹ If we understand the functional phenotype at the single-cell level using molecular signatures the enables the cell-cell variation to external stimuli such as materials, drugs, vaccines and their delivery vehicles to be studied as well as biomarkers of disease. The ability to obtain molecular information from the response of the human body to implanted devices will support the development of immune-instructive biomaterials for application in the medical device and regenerative medicine fields.

The methods that were developed during this PhD to achieve direct analysis of the metabolic profiles of human monocyte derived M0, M1 and M2 macrophage phenotypes at the single cell level and host response to implanted bio-instructive polymers *in vivo* using 3D OrbiSIMS are presented in detail in Chapter 4 and Chapter 6. Characteristic metabolites can be detected by direct analysis of single macrophages using 3D OrbiSIMS. This technique allows the identification of lipids, amino acids and small molecules without liquid extraction and destructive sample preparation compared with LC-MS techniques. Conceptually, this allows the distribution of the metabolites to be imaged, although this was not explored due to the low signal intensity of most of the metabolites. This is a significant methodological advance/advantage as 3D OrbiSIMS requires millions fewer cells than the traditional mass spectrometry approaches. Another advantage is that the cells do not require removal from the substrate. Furthermore, 3D OrbiSIMS is a direct surface analysis technique that allows for the analysis of a non-chemically fixed cell without the use of antibody-based cell markers.

The mass resolving power of OrbiSIMS and the resulting molecular specificity of ions assigned by this approach allowed the assignment of metabolic signatures and by comparison, the identification of common peaks in the spectra of different macrophage subsets. The results were compared between cytokine induced macrophage phenotypes. The assignments of prominent lipids were confirmed by the MS/MS capability of the 3D OrbiSIMS. We have also successfully investigated the sample preparation and technique using 3D OrbiSIMS for identification, resulting in identification of the metabolite profiling of macrophage phenotypes approach an optimum (Chapter 3).

To investigate the effect on tissue of implants, first investigated polymers identified to induce pro- or anti-inflammatory phenotypes in human macrophages *in vitro* (Chapter 5).⁷⁹ Commercially available methacrylate monomers were first synthesized into copolymers via a thermal polymerization method and subsequently coated onto coverslips. A total of 5 polymers were assessed for their ability to polarise towards the M1 or M2 phenotype. Analysis of *in vitro* macrophage phenotype using immunohistochemical analysis after 6 days of culture on the polymers, confirmed the ability of each polymer to polarise macrophages. PolyCHMA-co-DMAEMA consistently induced macrophage polarisation towards an M1-like phenotype. On the other hand, polyCHMA-co-iDMA promoted a higher amount of M2-like macrophage phenotype. Then we tested these immune-instructive polymers using an *in vivo* experiment using a foreign body mouse model (Chapter 6). pCHMA-co-DMAEMA (referred to as M1-polymer) and pCHMA-co-iDMA (referred to as M2-polymer) were coated on clinical-grade silicon catheters using a dip coater. The different tissue reactions to polymer coated silicone tubing is consistent with the pro- and anti-inflammatory responses of macrophages *in vitro*.⁷⁹

Catheters coated with the copolymers were implanted subcutaneously into a mouse model of foreign body response for 28 days. To investigate the response to the polymers, silicon catheter sections were explanted and analysed using both standard immunohistochemical methods and 3D OrbiSIMS *in situ* metabolite profiling to assess the immune response of tissue surrounding the implanted foreign body site. We utilised the 3D OrbiSIMS depth profile analysis mode on *ex vivo* mouse samples which

regions surround the foreign body site in both positive and negative polarity. Targeted phospholipid analysis and untargeted signatures (glycerolipid and amino acids) for each sample were detected in the spectra of the tissue section. PCA was used to identify differences between the different sample locations. The score plot showed that the molecular signals from the tissue adjacent to each polymer set did cluster and were separated from each other, with exploration of the loadings identifying that these were due to significant differences in their glycerol lipid and amino acid identity. To understand the meaning of this chemical signature identity, the literature studying macrophage metabolome responses was surveyed, with the most notable finding being lipids were associated in M1-like (polymer-M1) and amino acids in M2-like (polymer-M2).

It has been illustrated that the 3D OrbiSIMS technique can provide a detailed molecular characterization of *ex vivo* mouse tissue, with this seen to induce chemically specific reaction to different implanted immune-instructive polymers. This approach will allow the *in situ* characterization of *ex vivo* tissue sections to help understand the immune response to medical implants to inform the design of immune-instructive biomaterials for clinically as therapeutics and immune dysregulation.

Findings from this thesis demonstrate the capability of metabolomic analysis by 3D OrbiSIMS to achieve unbiased insight into cellular phenotype at the resolution of a single cell in culture. This is also possible with explanted devices to improve understanding of their response to various implanted biomaterials.

7.2. Further work

Further development of the methodology of single cell preparation should include investigation of the limits of detection in both spectral and imaging modes. Cryogenic conditions could be used to improve signal intensity, which would increase metabolite detection at the single cell level. Zhang et al.,¹²² showed this by identifying the characteristic biomolecules in the frozen-hydrated state yields a 10000-fold enhance in signal intensity for polar molecules. Extension of the reference point of metabolites

studied in this work, such as lipids and amino acids, together with computational data analysis of the 3D OrbiSIMS datasets by molecular formula prediction (MFP)²⁹⁰ for chemical software to improve automated annotation of the peaks detected and quantify the confidence in the formula predicted.

3D OrbiSIMS is a significantly advanced of qualitative analysis direct surface technique with high sensitivity, but the main drawback of this technique is that it is not a quantitative analysis; i.e. it is not possible to readily achieve quantification of concentration measurement on cell and tissue sections, and relative intensities may be misleading due to vastly different ionisation of different species, plus the local matrix may significantly effect intensity of identical species. Comparison with LC-MS to build standards for quantitative analysis of molecules distribution on tissue sections would be beneficial in improving the understanding of the limits in quantification.

References

1. Pavlovic, M., What Are Biomaterials? In *Bioengineering: A Conceptual Approach*, Pavlovic, M., Ed. Springer International Publishing: Cham, 2015; pp 229-244.
2. Lam, M. T.; Wu, J. C., Biomaterial applications in cardiovascular tissue repair and regeneration. *Expert review of cardiovascular therapy* **2012**, *10* (8), 1039-49.
3. Huzum, B.; Puha, B.; Necoara, R. M.; Gheorghevici, S.; Puha, G.; Filip, A.; Sirbu, P. D.; Alexa, O., Biocompatibility assessment of biomaterials used in orthopedic devices: An overview (Review). *Experimental and therapeutic medicine* **2021**, *22* (5), 1315.
4. Saini, M.; Singh, Y.; Arora, P.; Arora, V.; Jain, K., Implant biomaterials: A comprehensive review. *World journal of clinical cases* **2015**, *3* (1), 52-7.
5. Tuna, E. B.; Oshida, Y.; Ozen, B.; Gjorgievska, E.; Tuzuner, T., Biomaterials for Dental Applications. *BioMed research international* **2017**, *2017*, 2520536.
6. Zhou, G.; Groth, T., Host Responses to Biomaterials and Anti-Inflammatory Design-a Brief Review. *Macromolecular bioscience* **2018**, *18* (8), e1800112.
7. Kiradzhyska, D. D.; Mantcheva, R. D., Overview of Biocompatible Materials and Their Use in Medicine. *Folia medica* **2019**, *61* (1), 34-40.
8. Yang, K.; Zhou, C.; Fan, H.; Fan, Y.; Jiang, Q.; Song, P.; Fan, H.; Chen, Y.; Zhang, X., Bio-Functional Design, Application and Trends in Metallic Biomaterials. *International journal of molecular sciences* **2017**, *19* (1).
9. Serrano-Aroca, Á.; Deb, S., Acrylic-Based Materials for Biomedical and Bioengineering Applications. 2020; pp 1-21.
10. Ajekwene, K., Properties and Applications of Acrylates. 2020; pp 35-46.
11. Khan, F.; Tanaka, M.; Ahmad, S. R., Fabrication of polymeric biomaterials: a strategy for tissue engineering and medical devices. *Journal of Materials Chemistry B* **2015**, *3* (42), 8224-8249.
12. Chalifoux, P., Acrylic and other resins: Provisional restorations. 2015; pp 197-230.
13. Hook, A. L.; Chang, C.-Y.; Yang, J.; Lockett, J.; Cockayne, A.; Atkinson, S.; Mei, Y.; Bayston, R.; Irvine, D. J.; Langer, R.; Anderson, D. G.; Williams, P.; Davies, M. C.; Alexander, M. R., Combinatorial discovery of polymers resistant to bacterial attachment. *Nature Biotechnology* **2012**, *30* (9), 868-875.
14. Hazar Yoruç, A.; Sener, B., A Roadmap of Biomedical Engineers and Milestones Cont. 2012; pp 67-114.
15. Fu, J.; Su, Y.; Qin, Y.-X.; Zheng, Y.; Wang, Y.; Zhu, D., Evolution of metallic cardiovascular stent materials: A comparative study among stainless steel, magnesium and zinc. *Biomaterials* **2020**, *230*, 119641.
16. Zaffe, D.; Bertoldi, C.; Consolo, U., Element release from titanium devices used in oral and maxillofacial surgery. *Biomaterials* **2003**, *24* (6), 1093-1099.
17. Quinn, J.; McFadden, R.; Chan, C.-W.; Carson, L., Titanium for Orthopedic Applications: An Overview of Surface Modification to Improve Biocompatibility and Prevent Bacterial Biofilm Formation. *iScience* **2020**, *23* (11), 101745.
18. Saikia, K. C.; Bhattacharya, T. D.; Bhuyan, S. K.; Talukdar, D. J.; Saikia, S. P.; Jitesh, P., Calcium phosphate ceramics as bone graft substitutes in filling bone tumor defects. *Indian journal of orthopaedics* **2008**, *42* (2), 169-72.

19. Gao, J.; Su, Y.; Qin, Y.-X., Calcium phosphate coatings enhance biocompatibility and degradation resistance of magnesium alloy: Correlating in vitro and in vivo studies. *Bioactive Materials* **2021**, *6* (5), 1223-1229.
20. Afzal, A., Implantable zirconia bioceramics for bone repair and replacement: A chronological review. *Materials Express* **2014**, *4*.
21. Paxton, N. C.; Allenby, M. C.; Lewis, P. M.; Woodruff, M. A., Biomedical applications of polyethylene. *European Polymer Journal* **2019**, *118*, 412-428.
22. Maitz, M. F., Applications of synthetic polymers in clinical medicine. *Biosurface and Biotribology* **2015**, *1* (3), 161-176.
23. Kenny, S. M.; Buggy, M., Bone cements and fillers: A review. *Journal of Materials Science: Materials in Medicine* **2003**, *14* (11), 923-938.
24. Lewis, G., Nucleus pulposus replacement and regeneration/repair technologies: present status and future prospects. *Journal of biomedical materials research. Part B, Applied biomaterials* **2012**, *100* (6), 1702-20.
25. Kirchhof, S.; Goepferich, A. M.; Brandl, F. P., Hydrogels in ophthalmic applications. *European Journal of Pharmaceutics and Biopharmaceutics* **2015**, *95*, 227-238.
26. Armugam, A.; Teong, S. P.; Lim, D. S. W.; Chan, S. P.; Yi, G.; Yew, D. S.; Beh, C. W.; Zhang, Y., Broad spectrum antimicrobial PDMS-based biomaterial for catheter fabrication. *Biomaterials Research* **2021**, *25* (1), 33.
27. Lin, C.-C.; Anseth, K. S., PEG Hydrogels for the Controlled Release of Biomolecules in Regenerative Medicine. *Pharmaceutical Research* **2009**, *26* (3), 631-643.
28. Li, J.; Fartash, B.; Hermansson, L., Hydroxyapatite-alumina composites and bone-bonding. *Biomaterials* **1995**, *16* (5), 417-22.
29. Oprea, M.; Voicu, S. I., Cellulose Composites with Graphene for Tissue Engineering Applications. *Materials* **2020**, *13* (23), 5347.
30. Kiran, A. S. K. A. R., Seeram, *An Introduction to Biomaterials Science and Engineering*.
31. Jones, J. A.; Chang, D. T.; Meyerson, H.; Colton, E.; Kwon, I. K.; Matsuda, T.; Anderson, J. M., Proteomic analysis and quantification of cytokines and chemokines from biomaterial surface-adherent macrophages and foreign body giant cells. *Journal of biomedical materials research. Part A* **2007**, *83* (3), 585-96.
32. Klopffleisch, R.; Jung, F., The pathology of the foreign body reaction against biomaterials. *Journal of biomedical materials research. Part A* **2017**, *105* (3), 927-940.
33. Carnicer-Lombarte, A.; Chen, S. T.; Malliaras, G. G.; Barone, D. G., Foreign Body Reaction to Implanted Biomaterials and Its Impact in Nerve Neuroprosthetics. *Frontiers in bioengineering and biotechnology* **2021**, *9*, 622524.
34. van Furth, R.; Cohn, Z. A.; Hirsch, J. G.; Humphrey, J. H.; Spector, W. G.; Langevoort, H. L., The mononuclear phagocyte system: a new classification of macrophages, monocytes, and their precursor cells. *Bulletin of the World Health Organization* **1972**, *46* (6), 845-52.
35. Shi, C.; Pamer, E. G., Monocyte recruitment during infection and inflammation. *Nature reviews. Immunology* **2011**, *11* (11), 762-74.
36. Volkman, A.; Chang, N. C.; Strausbauch, P. H.; Morahan, P. S., Differential effects of chronic monocyte depletion on macrophage populations. *Laboratory investigation; a journal of technical methods and pathology* **1983**, *49* (3), 291-8.
37. Shi, C.; Pamer, E. G., Monocyte recruitment during infection and inflammation. *Nature Reviews Immunology* **2011**, *11* (11), 762-774.

38. Murray, P. J.; Wynn, T. A., Protective and pathogenic functions of macrophage subsets. *Nature Reviews Immunology* **2011**, *11* (11), 723-737.
39. Porcheray, F.; Viaud, S.; Rimaniol, A. C.; Leone, C.; Samah, B.; Dereuddre-Bosquet, N.; Dormont, D.; Gras, G., Macrophage activation switching: an asset for the resolution of inflammation. *Clinical and experimental immunology* **2005**, *142* (3), 481-9.
40. Mantovani, A.; Sica, A.; Sozzani, S.; Allavena, P.; Vecchi, A.; Locati, M., The chemokine system in diverse forms of macrophage activation and polarization. *Trends in immunology* **2004**, *25* (12), 677-86.
41. Brown, B. N.; Valentin, J. E.; Stewart-Akers, A. M.; McCabe, G. P.; Badylak, S. F., Macrophage phenotype and remodeling outcomes in response to biologic scaffolds with and without a cellular component. *Biomaterials* **2009**, *30* (8), 1482-91.
42. García, S.; Krausz, S.; Ambarus, C. A.; Fernández, B. M.; Hartkamp, L. M.; van Es, I. E.; Hamann, J.; Baeten, D. L.; Tak, P. P.; Reedquist, K. A., Tie2 signaling cooperates with TNF to promote the pro-inflammatory activation of human macrophages independently of macrophage functional phenotype. *PloS one* **2014**, *9* (1), e82088.
43. Hoeksema, M. A.; Glass, C. K., Nature and nurture of tissue-specific macrophage phenotypes. *Atherosclerosis* **2019**, *281*, 159-167.
44. Meng, F.; Lowell, C. A., Lipopolysaccharide (LPS)-induced macrophage activation and signal transduction in the absence of Src-family kinases Hck, Fgr, and Lyn. *The Journal of experimental medicine* **1997**, *185* (9), 1661-70.
45. Lukic, A.; Larssen, P.; Fauland, A.; Samuelsson, B.; Wheelock, C. E.; Gabrielsson, S.; Radmark, O., GM-CSF- and M-CSF-primed macrophages present similar resolving but distinct inflammatory lipid mediator signatures. *FASEB journal : official publication of the Federation of American Societies for Experimental Biology* **2017**, *31* (10), 4370-4381.
46. Martinez, F. O.; Gordon, S., The M1 and M2 paradigm of macrophage activation: time for reassessment. *F1000prime reports* **2014**, *6*, 13.
47. Saqib, U.; Sarkar, S.; Suk, K.; Mohammad, O.; Baig, M. S.; Savai, R., Phytochemicals as modulators of M1-M2 macrophages in inflammation. *Oncotarget* **2018**, *9* (25), 17937-17950.
48. Fleming, B. D.; Mosser, D. M., Regulatory macrophages: setting the threshold for therapy. *European journal of immunology* **2011**, *41* (9), 2498-502.
49. Vogel, D. Y.; Glim, J. E.; Stavenuiter, A. W.; Breur, M.; Heijnen, P.; Amor, S.; Dijkstra, C. D.; Beelen, R. H., Human macrophage polarization in vitro: maturation and activation methods compared. *Immunobiology* **2014**, *219* (9), 695-703.
50. Sridharan, R.; Cameron, A. R.; Kelly, D. J.; Kearney, C. J.; O'Brien, F. J., Biomaterial based modulation of macrophage polarization: a review and suggested design principles. *Materials Today* **2015**, *18* (6), 313-325.
51. Bose, S.; Bandyopadhyay, A., Chapter 1 - Introduction to Biomaterials. In *Characterization of Biomaterials*, Bandyopadhyay, A.; Bose, S., Eds. Academic Press: Oxford, 2013; pp 1-9.
52. Kim, S. Y.; Nair, M. G., Macrophages in wound healing: activation and plasticity. *Immunology & Cell Biology* **2019**, *97* (3), 258-267.
53. Durafourt, B. A.; Moore, C. S.; Zammit, D. A.; Johnson, T. A.; Zaguia, F.; Guiot, M. C.; Bar-Or, A.; Antel, J. P., Comparison of polarization properties of human adult microglia and blood-derived macrophages. *Glia* **2012**, *60* (5), 717-27.

54. Schraufstatter, I. U.; Zhao, M.; Khaldoyanidi, S. K.; Discipio, R. G., The chemokine CCL18 causes maturation of cultured monocytes to macrophages in the M2 spectrum. *Immunology* **2012**, *135* (4), 287-98.
55. Mantovani, A.; Sozzani, S.; Locati, M.; Allavena, P.; Sica, A., Macrophage polarization: tumor-associated macrophages as a paradigm for polarized M2 mononuclear phagocytes. *Trends in immunology* **2002**, *23* (11), 549-55.
56. Ahmed, I.; Ismail, N., M1 and M2 Macrophages Polarization via mTORC1 Influences Innate Immunity and Outcome of Ehrlichia Infection. *Journal of cellular immunology* **2020**, *2* (3), 108-115.
57. Onuki, Y.; Bhardwaj, U.; Papadimitrakopoulos, F.; Burgess, D. J., A review of the biocompatibility of implantable devices: current challenges to overcome foreign body response. *Journal of diabetes science and technology* **2008**, *2* (6), 1003-15.
58. Thevenot, P.; Hu, W.; Tang, L., Surface chemistry influences implant biocompatibility. *Current topics in medicinal chemistry* **2008**, *8* (4), 270-80.
59. Franz, S.; Rammelt, S.; Scharnweber, D.; Simon, J. C., Immune responses to implants - a review of the implications for the design of immunomodulatory biomaterials. *Biomaterials* **2011**, *32* (28), 6692-709.
60. Anderson, J. M.; Rodriguez, A.; Chang, D. T., Foreign body reaction to biomaterials. *Seminars in immunology* **2008**, *20* (2), 86-100.
61. Boersema, G. S.; Grotenhuis, N.; Bayon, Y.; Lange, J. F.; Bastiaansen-Jenniskens, Y. M., The Effect of Biomaterials Used for Tissue Regeneration Purposes on Polarization of Macrophages. *BioResearch open access* **2016**, *5* (1), 6-14.
62. Hams, E.; Bermingham, R.; Fallon, P. G., Macrophage and Innate Lymphoid Cell Interplay in the Genesis of Fibrosis. *Frontiers in immunology* **2015**, *6*, 597.
63. Medzhitov, R., Origin and physiological roles of inflammation. *Nature* **2008**, *454* (7203), 428-435.
64. Morais, J. M.; Papadimitrakopoulos, F.; Burgess, D. J., Biomaterials/tissue interactions: possible solutions to overcome foreign body response. *The AAPS journal* **2010**, *12* (2), 188-96.
65. Grotenhuis, N.; Bayon, Y.; Lange, J. F.; Van Osch, G. J.; Bastiaansen-Jenniskens, Y. M., A culture model to analyze the acute biomaterial-dependent reaction of human primary macrophages. *Biochemical and biophysical research communications* **2013**, *433* (1), 115-20.
66. Slee, J. B.; Christian, A. J.; Levy, R. J.; Stachelek, S. J., Addressing the Inflammatory Response to Clinically Relevant Polymers by Manipulating the Host Response Using ITIM Domain-Containing Receptors. *Polymers* **2014**, *6* (10), 2526-2551.
67. Londono, R.; Badylak, S. F., Chapter 1 - Factors Which Affect the Host Response to Biomaterials. In *Host Response to Biomaterials*, Badylak, S. F., Ed. Academic Press: Oxford, 2015; pp 1-12.
68. Yu, T.; Tutwiler, V. J.; Spiller, K., The Role of Macrophages in the Foreign Body Response to Implanted Biomaterials. In *Biomaterials in Regenerative Medicine and the Immune System*, Santambrogio, L., Ed. Springer International Publishing: Cham, 2015; pp 17-34.
69. Diegelmann, R. F.; Evans, M. C., Wound healing: an overview of acute, fibrotic and delayed healing. *Frontiers in bioscience : a journal and virtual library* **2004**, *9*, 283-9.
70. Mitragotri, S.; Lahann, J., Physical approaches to biomaterial design. *Nature materials* **2009**, *8* (1), 15-23.

71. Lerman, M. J.; Lembong, J.; Muramoto, S.; Gillen, G.; Fisher, J. P., The Evolution of Polystyrene as a Cell Culture Material. *Tissue engineering. Part B, Reviews* **2018**, *24* (5), 359-372.
72. Rostam, H. M.; Singh, S.; Salazar, F.; Magennis, P.; Hook, A.; Singh, T.; Vrana, N. E.; Alexander, M. R.; Ghaemmaghami, A. M., The impact of surface chemistry modification on macrophage polarisation. *Immunobiology* **2016**, *221* (11), 1237-1246.
73. Celiz, A. D.; Smith, J. G.; Patel, A. K.; Hook, A. L.; Rajamohan, D.; George, V. T.; Flatt, L.; Patel, M. J.; Epa, V. C.; Singh, T.; Langer, R.; Anderson, D. G.; Allen, N. D.; Hay, D. C.; Winkler, D. A.; Barrett, D. A.; Davies, M. C.; Young, L. E.; Denning, C.; Alexander, M. R., Discovery of a Novel Polymer for Human Pluripotent Stem Cell Expansion and Multilineage Differentiation. *Advanced materials (Deerfield Beach, Fla.)* **2015**, *27* (27), 4006-12.
74. Champion, J. A.; Mitragotri, S., Role of target geometry in phagocytosis. *Proceedings of the National Academy of Sciences of the United States of America* **2006**, *103* (13), 4930-4.
75. Webster, T. J.; Ergun, C.; Doremus, R. H.; Siegel, R. W.; Bizios, R., Specific proteins mediate enhanced osteoblast adhesion on nanophase ceramics. *Journal of biomedical materials research* **2000**, *51* (3), 475-83.
76. Yixing Tian, H. L., Brian W. Sheldon, Thomas J. Webster, Sichen Yang, Huilin Yang, Lei Yang, Surface energy-mediated fibronectin adsorption and osteoblast responses on nanostructured diamond. *J. Mater. Sci. Technol.* **2019**, *35* (5), 817-823.
77. Faia-Torres, A. B.; Guimond-Lischer, S.; Rottmar, M.; Charnley, M.; Goren, T.; Maniura-Weber, K.; Spencer, N. D.; Reis, R. L.; Textor, M.; Neves, N. M., Differential regulation of osteogenic differentiation of stem cells on surface roughness gradients. *Biomaterials* **2014**, *35* (33), 9023-32.
78. Vassey, M. J.; Figueredo, G. P.; Scurr, D. J.; Vasilevich, A. S.; Vermeulen, S.; Carlier, A.; Luckett, J.; Beijer, N. R. M.; Williams, P.; Winkler, D. A.; de Boer, J.; Ghaemmaghami, A. M.; Alexander, M. R., Immune Modulation by Design: Using Topography to Control Human Monocyte Attachment and Macrophage Differentiation. *Advanced science (Weinheim, Baden-Wurtemberg, Germany)* **2020**, *7* (11), 1903392.
79. Rostam, H. M.; Fisher, L. E.; Hook, A. L.; Burroughs, L.; Luckett, J. C.; Figueredo, G. P.; Mbadugha, C.; Teo, A. C. K.; Latif, A.; Kämmerling, L.; Day, M.; Lawler, K.; Barrett, D.; Elsheikh, S.; Ilyas, M.; Winkler, D. A.; Alexander, M. R.; Ghaemmaghami, A. M., Immune-Instructive Polymers Control

Macrophage Phenotype and Modulate the

Foreign Body Response In Vivo. *Matter* **2020**, *2* (6), 1564-1581.

80. Pinu, F. R.; Beale, D. J.; Paten, A. M.; Kouremenos, K.; Swarup, S.; Schirra, H. J.; Wishart, D., Systems Biology and Multi-Omics Integration: Viewpoints from the Metabolomics Research Community. *Metabolites* **2019**, *9* (4).
81. German, J. B.; Hammock, B. D.; Watkins, S. M., Metabolomics: building on a century of biochemistry to guide human health. *Metabolomics : Official journal of the Metabolomic Society* **2005**, *1* (1), 3-9.
82. Fiehn, O., Combining genomics, metabolome analysis, and biochemical modelling to understand metabolic networks. *Comparative and functional genomics* **2001**, *2* (3), 155-68.

83. Forsberg, E. M.; Huan, T.; Rinehart, D.; Benton, H. P.; Warth, B.; Hilmers, B.; Siuzdak, G., Data processing, multi-omic pathway mapping, and metabolite activity analysis using XCMS Online. *Nature Protocols* **2018**, *13* (4), 633-651.
84. Liu, X.; Locasale, J. W., Metabolomics: A Primer. *Trends in biochemical sciences* **2017**, *42* (4), 274-284.
85. Wijnands, K. A.; Castermans, T. M.; Hommen, M. P.; Meesters, D. M.; Poeze, M., Arginine and citrulline and the immune response in sepsis. *Nutrients* **2015**, *7* (3), 1426-63.
86. Nikolaus, S.; Schulte, B.; Al-Massad, N.; Thieme, F.; Schulte, D. M.; Bethge, J.; Rehman, A.; Tran, F.; Aden, K.; Häsler, R.; Moll, N.; Schütze, G.; Schwarz, M. J.; Waetzig, G. H.; Rosenstiel, P.; Krawczak, M.; Szymczak, S.; Schreiber, S., Increased Tryptophan Metabolism Is Associated With Activity of Inflammatory Bowel Diseases. *Gastroenterology* **2017**, *153* (6), 1504-1516.e2.
87. Long, N. P.; Nghi, T. D.; Kang, Y. P.; Anh, N. H.; Kim, H. M.; Park, S. K.; Kwon, S. W., Toward a Standardized Strategy of Clinical Metabolomics for the Advancement of Precision Medicine. *Metabolites* **2020**, *10* (2), 51.
88. Fiehn, O., Metabolomics – the link between genotypes and phenotypes. *Plant Molecular Biology* **2002**, *48* (1), 155-171.
89. Duffield, P. H.; Netting, A. G., Methods for the quantitation of abscisic acid and its precursors from plant tissues. *Analytical biochemistry* **2001**, *289* (2), 251-9.
90. Ribnicky, D. M.; Cooke, T. J.; Cohen, J. D., A microtechnique for the analysis of free and conjugated indole-3-acetic acid in milligram amounts of plant tissue using a benchtop gas chromatograph-mass spectrometer. *Planta* **1998**, *204* (1), 1-7.
91. Patti, G. J.; Yanes, O.; Siuzdak, G., Innovation: Metabolomics: the apogee of the omics trilogy. *Nature reviews. Molecular cell biology* **2012**, *13* (4), 263-9.
92. Surrati, A.; Linforth, R.; Fisk, I. D.; Sottile, V.; Kim, D. H., Non-destructive characterisation of mesenchymal stem cell differentiation using LC-MS-based metabolite footprinting. *The Analyst* **2016**, *141* (12), 3776-87.
93. Jansson, J.; Willing, B.; Lucio, M.; Fekete, A.; Dicksved, J.; Halfvarson, J.; Tysk, C.; Schmitt-Kopplin, P., Metabolomics Reveals Metabolic Biomarkers of Crohn's Disease. *PloS one* **2009**, *4* (7), e6386.
94. Abuawad, A.; Mbadugha, C.; Ghaemmaghmi, A. M.; Kim, D.-H., Metabolic characterisation of THP-1 macrophage polarisation using LC-MS-based metabolite profiling. *Metabolomics : Official journal of the Metabolomic Society* **2020**, *16* (3), 33.
95. Feucherolles, M.; Poppert, S.; Utzinger, J.; Becker, S. L., MALDI-TOF mass spectrometry as a diagnostic tool in human and veterinary helminthology: a systematic review. *Parasites & Vectors* **2019**, *12* (1), 245.
96. Hrabák, J.; Chudácková, E.; Walková, R., Matrix-assisted laser desorption ionization-time of flight (maldi-tof) mass spectrometry for detection of antibiotic resistance mechanisms: from research to routine diagnosis. *Clinical microbiology reviews* **2013**, *26* (1), 103-14.
97. Fuchs, B.; Schiller, J., MALDI-TOF MS Analysis of Lipids from Cells, Tissues and Body Fluids. In *Lipids in Health and Disease*, Quinn, P. J.; Wang, X., Eds. Springer Netherlands: Dordrecht, 2008; pp 541-565.
98. Takáts, Z.; Wiseman, J. M.; Gologan, B.; Cooks, R. G., Mass Spectrometry Sampling Under Ambient Conditions with Desorption Electrospray Ionization. *Science (New York, N.Y.)* **2004**, *306* (5695), 471-473.

99. Parrot, D.; Papazian, S.; Foil, D.; Tasdemir, D., Imaging the Unimaginable: Desorption Electrospray Ionization - Imaging Mass Spectrometry (DESI-IMS) in Natural Product Research. *Planta medica* **2018**, *84* (9-10), 584-593.
100. Altelaar, A. F. M.; Taban, I. M.; McDonnell, L. A.; Verhaert, P. D. E. M.; de Lange, R. P. J.; Adan, R. A. H.; Mooi, W. J.; Heeren, R. M. A.; Piersma, S. R., High-resolution MALDI imaging mass spectrometry allows localization of peptide distributions at cellular length scales in pituitary tissue sections. *International Journal of Mass Spectrometry* **2007**, *260* (2), 203-211.
101. Vickerman, J. C., Molecular imaging and depth profiling by mass spectrometry—SIMS, MALDI or DESI? *Analyst* **2011**, *136* (11), 2199-2217.
102. Benninghoven, A., Surface analysis by Secondary Ion Mass Spectrometry (SIMS). *Surface Science* **1994**, *299-300*, 246-260.
103. Mahoney, C. M., Cluster secondary ion mass spectrometry of polymers and related materials. *Mass Spectrometry Reviews* **2010**, *29* (2), 247-293.
104. Ryan, K. E.; Wojciechowski, I. A.; Garrison, B. J., Reaction Dynamics Following keV Cluster Bombardment. *The Journal of Physical Chemistry C* **2007**, *111* (34), 12822-12826.
105. Weibel, D.; Wong, S.; Lockyer, N.; Blenkinsopp, P.; Hill, R.; Vickerman, J. C., A C60 primary ion beam system for time of flight secondary ion mass spectrometry: its development and secondary ion yield characteristics. *Anal Chem* **2003**, *75* (7), 1754-64.
106. Weibel, D. E.; Lockyer, N.; Vickerman, J. C., C60 cluster ion bombardment of organic surfaces. *Applied Surface Science* **2004**, *231-232*, 146-152.
107. Seah, M. P., Universal Equation for Argon Gas Cluster Sputtering Yields. *The Journal of Physical Chemistry C* **2013**, *117* (24), 12622-12632.
108. Winograd, N., Gas Cluster Ion Beams for Secondary Ion Mass Spectrometry. *Annual review of analytical chemistry (Palo Alto, Calif.)* **2018**, *11* (1), 29-48.
109. Shen, K.; Wucher, A.; Winograd, N., Molecular Depth Profiling with Argon Gas Cluster Ion Beams. *The Journal of Physical Chemistry C* **2015**, *119*, 15316-15324.
110. Yamada, I.; Matsuo, J.; Toyoda, N.; Kirkpatrick, A., Materials processing by gas cluster ion beams. *Materials Science & Engineering R-reports - MAT SCI ENG R* **2001**, *34*, 231-295.
111. Icarscom.net, ToF-SIMS Analysis for Surface Characterization. **2013**.
112. ULVAC-PHI, I., Surface analysis techniques. **2014**.
113. Postawa, Z., Molecular Dynamics Simulations, the Theoretical Partner to dynamic cluster SIMS Experiments. 2013; p 151.
114. Vickerman, J. C., Briggs, D., ToF-SIMS: surface analysis by mass spectrometry. **2013**.
115. Guilhaus, M., MASS SPECTROMETRY | Time-of-Flight. In *Encyclopedia of Analytical Science (Second Edition)*, Worsfold, P.; Townshend, A.; Poole, C., Eds. Elsevier: Oxford, 2005; pp 412-423.
116. Dubey, M.; Brison, J.; Grainger, D. W.; Castner, D. G., Comparison of Bi(1), Bi(3) and C(60) primary ion sources for ToF-SIMS imaging of patterned protein samples. *Surface and interface analysis : SIA* **2011**, *43* (1-2), 261-264.
117. Sanyova, J.; Cersoy, S.; Richardin, P.; Lapr evote, O.; Walter, P.; Brunelle, A., Unexpected Materials in a Rembrandt Painting Characterized by High Spatial Resolution Cluster-TOF-SIMS Imaging. *Analytical Chemistry* **2011**, *83* (3), 753-760.

118. Hu, Q.; Noll, R. J.; Li, H.; Makarov, A.; Hardman, M.; Graham Cooks, R., The Orbitrap: a new mass spectrometer. *Journal of Mass Spectrometry* **2005**, *40* (4), 430-443.
119. Zubarev, R. A.; Makarov, A., Orbitrap Mass Spectrometry. *Analytical Chemistry* **2013**, *85* (11), 5288-5296.
120. A, G. M.; G, T. B.; Chen, T.; N, K. K.; A, M. M.; R, P. R.; B, M. R.; Xian, F., Mass resolution and mass accuracy: how much is enough? *Mass spectrometry (Tokyo, Japan)* **2013**, *2* (Spec Iss), S0009.
121. Vidot, K.; Gaillard, C.; Rivard, C.; Siret, R.; Lahaye, M. Cryo-laser scanning confocal microscopy of diffusible plant compounds *Plant Methods* [Online], 2018, p. 89. PubMed. <http://europepmc.org/abstract/MED/30344615>
- <https://doi.org/10.1186/s13007-018-0356-x>
- <https://europepmc.org/articles/PMC6186079>
- <https://europepmc.org/articles/PMC6186079?pdf=render> (accessed 2018).
122. Zhang, J.; Brown, J.; Scurr, D. J.; Bullen, A.; MacLellan-Gibson, K.; Williams, P.; Alexander, M. R.; Hardie, K. R.; Gilmore, I. S.; Rakowska, P. D., Cryo-OrbiSIMS for 3D Molecular Imaging of a Bacterial Biofilm in Its Native State. *Anal Chem* **2020**, *92* (13), 9008-9015.
123. Peres, P.; Choi, S.-Y.; Desse, F.; Bienvenu, P.; Roure, I.; Pipon, Y.; Gaillard, C.; Moncoffre, N.; Sarrasin, L.; Mangin, D., Dynamic SIMS for materials analysis in nuclear science. *Journal of Vacuum Science & Technology B* **2018**, *36* (3), 03F117.
124. Ellis, S. R.; Bruinen, A. L.; Heeren, R. M., A critical evaluation of the current state-of-the-art in quantitative imaging mass spectrometry. *Analytical and bioanalytical chemistry* **2014**, *406* (5), 1275-89.
125. Panuwet, P.; Hunter, R. E., Jr.; D'Souza, P. E.; Chen, X.; Radford, S. A.; Cohen, J. R.; Marder, M. E.; Kartavenka, K.; Ryan, P. B.; Barr, D. B., Biological Matrix Effects in Quantitative Tandem Mass Spectrometry-Based Analytical Methods: Advancing Biomonitoring. *Critical reviews in analytical chemistry* **2016**, *46* (2), 93-105.
126. Shard, A. G.; Spencer, S. J.; Smith, S. A.; Havelund, R.; Gilmore, I. S., The matrix effect in organic secondary ion mass spectrometry. *International Journal of Mass Spectrometry* **2015**, *377*, 599-609.
127. Grasserbauer, M., Quantitative Secondary Ion Mass Spectrometry. *Journal of Research of the National Bureau of Standards* **1988**, *93* (3), 510.
128. Ambarus, C. A.; Krausz, S.; van Eijk, M.; Hamann, J.; Radstake, T. R.; Reedquist, K. A.; Tak, P. P.; Baeten, D. L., Systematic validation of specific phenotypic markers for in vitro polarized human macrophages. *Journal of immunological methods* **2012**, *375* (1-2), 196-206.
129. Galván-Peña, S.; O'Neill, L. A., Metabolic reprogramming in macrophage polarization. *Frontiers in immunology* **2014**, *5*, 420.
130. Rattigan, K. M.; Pountain, A. W.; Regnault, C.; Achcar, F.; Vincent, I. M.; Goodyear, C. S.; Barrett, M. P., Metabolomic profiling of macrophages determines the discrete metabolomic signature and metabolomic interactome triggered by polarising immune stimuli. *PloS one* **2018**, *13* (3), e0194126.
131. Zhang, C.; Wang, Y.; Wang, F.; Wang, Z.; Lu, Y.; Xu, Y.; Wang, K.; Shen, H.; Yang, P.; Li, S.; Qin, X.; Yu, H., Quantitative profiling of glycerophospholipids

during mouse and human macrophage differentiation using targeted mass spectrometry. *Scientific reports* **2017**, 7 (1), 412.

132. Sugimoto, M.; Sakagami, H.; Yokote, Y.; Onuma, H.; Kaneko, M.; Mori, M.; Sakaguchi, Y.; Soga, T.; Tomita, M., Non-targeted metabolite profiling in activated macrophage secretion. *Metabolomics : Official journal of the Metabolomic Society* **2012**, 8 (4), 624-633.

133. Gil-de-Gómez, L.; Astudillo, A. M.; Meana, C.; Rubio, J. M.; Guijas, C.; Balboa, M. A.; Balsinde, J., A phosphatidylinositol species acutely generated by activated macrophages regulates innate immune responses. *Journal of immunology (Baltimore, Md. : 1950)* **2013**, 190 (10), 5169-77.

134. Bochenek, M. A.; Delcassian, D.; Anderson, D. G., Chapter 22 - Challenges in the development of immunoisolation devices. In *Principles of Tissue Engineering (Fifth Edition)*, Lanza, R.; Langer, R.; Vacanti, J. P.; Atala, A., Eds. Academic Press: 2020; pp 403-418.

135. Li, Z., 5.40 - In Vitro Micro Tissue and Organ Models for Toxicity Testing☆. In *Comprehensive Biotechnology (Third Edition)*, Moo-Young, M., Ed. Pergamon: Oxford, 2019; pp 535-549.

136. Rostam, H. M.; Reynolds, P. M.; Alexander, M. R.; Gadegaard, N.; Ghaemmaghami, A. M., Image based Machine Learning for identification of macrophage subsets. *Scientific Reports* **2017**, 7 (1), 3521.

137. Wynn, T. A.; Chawla, A.; Pollard, J. W., Macrophage biology in development, homeostasis and disease. *Nature* **2013**, 496 (7446), 445-55.

138. Mills, C. D.; Kincaid, K.; Alt, J. M.; Heilman, M. J.; Hill, A. M., M-1/M-2 macrophages and the Th1/Th2 paradigm. *Journal of immunology (Baltimore, Md. : 1950)* **2000**, 164 (12), 6166-73.

139. Alhaji, M.; Farhana, A., Enzyme Linked Immunosorbent Assay. In *StatPearls*, StatPearls Publishing

Copyright © 2022, StatPearls Publishing LLC.: Treasure Island (FL), 2022.

140. de la Rica, R.; Stevens, M. M., Plasmonic ELISA for the ultrasensitive detection of disease biomarkers with the naked eye. *Nature Nanotechnology* **2012**, 7 (12), 821-824.

141. Im, K.; Mareninov, S.; Diaz, M. F. P.; Yong, W. H., An Introduction to Performing Immunofluorescence Staining. *Methods Mol Biol* **2019**, 1897, 299-311.

142. Odell, I. D.; Cook, D., Immunofluorescence techniques. *The Journal of investigative dermatology* **2013**, 133 (1), e4.

143. Cell signaling technology, I., What Is Immunohistochemistry (IHC) Staining? **2022**.

144. Moad, G.; Rizzardo, E.; Solomon, D. H., 10 - Other Initiating Systems. In *Comprehensive Polymer Science and Supplements*, Allen, G.; Bevington, J. C., Eds. Pergamon: Amsterdam, 1989; pp 141-146.

145. Bagheri, A.; Boniface, S.; Fellows, C. M., Reversible-Deactivation Radical Polymerisation: chain polymerisation made simple. *Chemistry Teacher International* **2021**, 3 (2), 19-32.

146. Nakamura, Y.; Yamago, S., Termination Mechanism in the Radical Polymerization of Methyl Methacrylate and Styrene Determined by the Reaction of Structurally Well-Defined Polymer End Radicals. *Macromolecules* **2015**, 48 (18), 6450-6456.

147. Reif, B.; Ashbrook, S. E.; Emsley, L.; Hong, M., Solid-state NMR spectroscopy. *Nature Reviews Methods Primers* **2021**, 1 (1), 2.

148. Chakrapani, S. B.; Minkler, M. J.; Beckingham, B. S., Low-field (1)H-NMR spectroscopy for compositional analysis of multicomponent polymer systems. *The Analyst* **2019**, *144* (5), 1679-1686.
149. Baumstark, D.; Pagel, P.; Eiglsperger, J.; Pfahlert, V.; Huber, F., NMR spectroscopy – a modern analytical tool for serum analytics of lipoproteins and metabolites. *LaboratoriumsMedizin* **2015**, *38* (s1).
150. Introduction. In *Principles of Polymerization*, 2004; pp 1-38.
151. Yoon, S.; Lee, T. G., Biological tissue sample preparation for time-of-flight secondary ion mass spectrometry (ToF-SIMS) imaging. *Nano Convergence* **2018**, *5* (1), 24.
152. Scoutaris, N.; Hook, A. L.; Gellert, P. R.; Roberts, C. J.; Alexander, M. R.; Scurr, D. J., ToF-SIMS analysis of chemical heterogeneities in inkjet micro-array printed drug/polymer formulations. *Journal of materials science. Materials in medicine* **2012**, *23* (2), 385-91.
153. Denbigh, J. L.; Lockyer, N. P., ToF-SIMS as a tool for profiling lipids in cancer and other diseases. *Materials Science and Technology* **2015**, *31* (2), 137-147.
154. Bonnin, E. A.; Rizzoli, S. O., Novel Secondary Ion Mass Spectrometry Methods for the Examination of Metabolic Effects at the Cellular and Subcellular Levels. *Frontiers in Behavioral Neuroscience* **2020**, *14*.
155. Hook, A. L.; Scurr, D. J., ToF-SIMS analysis of a polymer microarray composed of poly(meth)acrylates with C6 derivative pendant groups. *Surface and Interface Analysis* **2016**, *48* (4), 226-236.
156. Hofmann, J. P.; Rohnke, M.; Weckhuysen, B. M., Recent advances in secondary ion mass spectrometry of solid acid catalysts: large zeolite crystals under bombardment. *Physical Chemistry Chemical Physics* **2014**, *16* (12), 5465-5474.
157. Lanekoff, I.; Kurczy, M. E.; Adams, K. L.; Malm, J.; Karlsson, R.; Sjövall, P.; Ewing, A. G., An in situ fracture device to image lipids in single cells using ToF-SIMS. *Surface and Interface Analysis* **2011**, *43* (1-2), 257-260.
158. Passarelli, M. K.; Pirkl, A.; Moellers, R.; Grinfeld, D.; Kollmer, F.; Havelund, R.; Newman, C. F.; Marshall, P. S.; Arlinghaus, H.; Alexander, M. R.; West, A.; Horning, S.; Niehuis, E.; Makarov, A.; Dollery, C. T.; Gilmore, I. S., The 3D OrbiSIMS-label-free metabolic imaging with subcellular lateral resolution and high mass-resolving power. *Nature methods* **2017**, *14* (12), 1175-1183.
159. Passarelli, M. K.; Pirkl, A.; Moellers, R.; Grinfeld, D.; Kollmer, F.; Havelund, R.; Newman, C. F.; Marshall, P. S.; Arlinghaus, H.; Alexander, M. R.; West, A.; Horning, S.; Niehuis, E.; Makarov, A.; Dollery, C. T.; Gilmore, I. S., The 3D OrbiSIMS—label-free metabolic imaging with subcellular lateral resolution and high mass-resolving power. *Nature Methods* **2017**, *14* (12), 1175-1183.
160. Sheraz née Rabbani, S.; Berrueta Razo, I.; Kohn, T.; Lockyer, N. P.; Vickerman, J. C., Enhancing Ion Yields in Time-of-Flight-Secondary Ion Mass Spectrometry: A Comparative Study of Argon and Water Cluster Primary Beams. *Analytical Chemistry* **2015**, *87* (4), 2367-2374.
161. Gilmore, I.; Havelund, R.; Pirkl, A.; Passarelli, M.; Newman, C.; Moellers, R.; Arlinghaus, H.; Panina, Y., Label-free Imaging of Biomolecules in Murine Brain Sections Using the 3D OrbiSIMS. *Protoc Exch* **2017**.
162. Kotowska, A. M.; Trindade, G. F.; Mendes, P. M.; Williams, P. M.; Aylott, J. W.; Shard, A. G.; Alexander, M. R.; Scurr, D. J., Protein identification by 3D OrbiSIMS to facilitate in situ imaging and depth profiling. *Nature communications* **2020**, *11* (1), 5832.

163. Starr, N. J.; Khan, M. H.; Edney, M. K.; Trindade, G. F.; Kern, S.; Pirkl, A.; Kleine-Boymann, M.; Elms, C.; O'Mahony, M. M.; Bell, M.; Alexander, M. R.; Scurr, D. J., Elucidating the molecular landscape of the stratum corneum. *Proceedings of the National Academy of Sciences* **2022**, *119* (12), e2114380119.
164. Aoyagi, S.; Kodama, Y.; Passarelli, M. K.; Vorng, J.-L.; Kawashima, T.; Yoshikiyo, K.; Yamamoto, T.; Gilmore, I. S., OrbiSIMS Imaging Identifies Molecular Constituents of the Perialgal Vacuole Membrane of *Paramecium bursaria* with Symbiotic *Chlorella variabilis*. *Analytical Chemistry* **2019**, *91* (22), 14545-14551.
165. Abuawad, A.; Mbadugha, C.; Ghaemmaghami, A. M.; Kim, D. H., Metabolic characterisation of THP-1 macrophage polarisation using LC-MS-based metabolite profiling. *Metabolomics : Official journal of the Metabolomic Society* **2020**, *16* (3), 33.
166. Eikel, D.; Vavrek, M.; Smith, S.; Bason, C.; Yeh, S.; Korfmacher, W. A.; Henion, J. D., Liquid extraction surface analysis mass spectrometry (LESA-MS) as a novel profiling tool for drug distribution and metabolism analysis: the terfenadine example. *Rapid communications in mass spectrometry : RCM* **2011**, *25* (23), 3587-96.
167. Cajka, T.; Fiehn, O., Comprehensive analysis of lipids in biological systems by liquid chromatography-mass spectrometry. *Trends Analyt Chem* **2014**, *61*, 192-206.
168. Rauh, M., LC-MS/MS for protein and peptide quantification in clinical chemistry. *Journal of Chromatography B* **2012**, *883-884*, 59-67.
169. Kotowska, A. M.; Trindade, G. F.; Mendes, P. M.; Williams, P. M.; Aylott, J. W.; Shard, A. G.; Alexander, M. R.; Scurr, D. J., Protein identification by 3D OrbiSIMS to facilitate in situ imaging and depth profiling. *Nature Communications* **2020**, *11* (1), 5832.
170. Meurs, J.; Scurr, D. J.; Lourdasamy, A.; Storer, L. C. D.; Grundy, R. G.; Alexander, M. R.; Rahman, R.; Kim, D.-H., Sequential Orbitrap Secondary Ion Mass Spectrometry and Liquid Extraction Surface Analysis-Tandem Mass Spectrometry-Based Metabolomics for Prediction of Brain Tumor Relapse from Sample-Limited Primary Tissue Archives. *Analytical Chemistry* **2021**, *93* (18), 6947-6954.
171. Tuli, L.; Resson, H. W., LC-MS Based Detection of Differential Protein Expression. *J Proteomics Bioinform* **2009**, *2*, 416-438.
172. Basu, S. S.; Randall, E. C.; Regan, M. S.; Lopez, B. G. C.; Clark, A. R.; Schmitt, N. D.; Agar, J. N.; Dillon, D. A.; Agar, N. Y. R., In Vitro Liquid Extraction Surface Analysis Mass Spectrometry (ivLESA-MS) for Direct Metabolic Analysis of Adherent Cells in Culture. *Analytical Chemistry* **2018**, *90* (8), 4987-4991.
173. Sigmund, P., *Phys. Rev.* **1969**, *184*, 383.
174. Walker, A. V., Secondary Ion Mass Spectrometry. In *Encyclopedia of Spectroscopy and Spectrometry (Third Edition)*, Lindon, J. C.; Tranter, G. E.; Koppenaal, D. W., Eds. Academic Press: Oxford, 2017; pp 44-49.
175. Shon, H. K.; Yoon, S.; Moon, J. H.; Lee, T. G., Improved mass resolution and mass accuracy in TOF-SIMS spectra and images using argon gas cluster ion beams. *Biointerphases* **2016**, *11* (2), 02A321.
176. Green, F. M.; Gilmore, I. S.; Seah, M. P., Mass Spectrometry and Informatics: Distribution of Molecules in the PubChem Database and General Requirements for Mass Accuracy in Surface Analysis. *Analytical Chemistry* **2011**, *83* (9), 3239-3243.
177. Suvannapruk, W.; Edney, M. K.; Kim, D.-H.; Scurr, D. J.; Ghaemmaghami, A. M.; Alexander, M. R., Single-Cell Metabolic Profiling of Macrophages Using 3D OrbiSIMS: Correlations with Phenotype. *Analytical Chemistry* **2022**, *94* (26), 9389-9398.

178. Rostam, H. M.; Singh, S.; Vrana, N. E.; Alexander, M. R.; Ghaemmaghami, A. M., Impact of surface chemistry and topography on the function of antigen presenting cells. *Biomaterials Science* **2015**, *3* (3), 424-441.
179. Montenegro-Burke, J. R.; Sutton, J. A.; Rogers, L. M.; Milne, G. L.; McLean, J. A.; Aronoff, D. M., Lipid profiling of polarized human monocyte-derived macrophages. *Prostaglandins & other lipid mediators* **2016**, *127*, 1-8.
180. Jaguin, M.; Houlbert, N.; Fardel, O.; Lecureur, V., Polarization profiles of human M-CSF-generated macrophages and comparison of M1-markers in classically activated macrophages from GM-CSF and M-CSF origin. *Cellular immunology* **2013**, *281* (1), 51-61.
181. Tannahill, G. M.; Curtis, A. M.; Adamik, J.; Palsson-McDermott, E. M.; McGettrick, A. F.; Goel, G.; Frezza, C.; Bernard, N. J.; Kelly, B.; Foley, N. H.; Zheng, L.; Gardet, A.; Tong, Z.; Jany, S. S.; Corr, S. C.; Haneklaus, M.; Caffrey, B. E.; Pierce, K.; Walmsley, S.; Beasley, F. C.; Cummins, E.; Nizet, V.; Whyte, M.; Taylor, C. T.; Lin, H.; Masters, S. L.; Gottlieb, E.; Kelly, V. P.; Clish, C.; Auron, P. E.; Xavier, R. J.; O'Neill, L. A., Succinate is an inflammatory signal that induces IL-1 β through HIF-1 α . *Nature* **2013**, *496* (7444), 238-42.
182. Newsholme, P.; Curi, R.; Gordon, S.; Newsholme, E. A., Metabolism of glucose, glutamine, long-chain fatty acids and ketone bodies by murine macrophages. *The Biochemical journal* **1986**, *239* (1), 121-5.
183. Atri, C.; Guerfali, F. Z.; Laouini, D., Role of Human Macrophage Polarization in Inflammation during Infectious Diseases. *International journal of molecular sciences* **2018**, *19* (6).
184. Mosser, D. M.; Edwards, J. P., Exploring the full spectrum of macrophage activation. *Nature reviews. Immunology* **2008**, *8* (12), 958-69.
185. Stein, M.; Keshav, S.; Harris, N.; Gordon, S., Interleukin 4 potently enhances murine macrophage mannose receptor activity: a marker of alternative immunologic macrophage activation. *The Journal of experimental medicine* **1992**, *176* (1), 287-92.
186. Fleetwood, A. J.; Dinh, H.; Cook, A. D.; Hertzog, P. J.; Hamilton, J. A., GM-CSF- and M-CSF-dependent macrophage phenotypes display differential dependence on type I interferon signaling. *Journal of leukocyte biology* **2009**, *86* (2), 411-21.
187. Huang, S. C.; Everts, B.; Ivanova, Y.; O'Sullivan, D.; Nascimento, M.; Smith, A. M.; Beatty, W.; Love-Gregory, L.; Lam, W. Y.; O'Neill, C. M.; Yan, C.; Du, H.; Abumrad, N. A.; Urban, J. F., Jr.; Artyomov, M. N.; Pearce, E. L.; Pearce, E. J., Cell-intrinsic lysosomal lipolysis is essential for alternative activation of macrophages. *Nature immunology* **2014**, *15* (9), 846-55.
188. Durafourt, B. A.; Moore, C. S.; Zammit, D. A.; Johnson, T. A.; Zaguia, F.; Guiot, M.-C.; Bar-Or, A.; Antel, J. P., Comparison of polarization properties of human adult microglia and blood-derived macrophages. *Glia* **2012**, *60* (5), 717-727.
189. Bertani, F. R.; Mozetic, P.; Fioramonti, M.; Iuliani, M.; Ribelli, G.; Pantano, F.; Santini, D.; Tonini, G.; Trombetta, M.; Businaro, L.; Selci, S.; Rainer, A., Classification of M1/M2-polarized human macrophages by label-free hyperspectral reflectance confocal microscopy and multivariate analysis. *Scientific reports* **2017**, *7* (1), 8965.
190. Gordon, S., Alternative activation of macrophages. *Nature reviews. Immunology* **2003**, *3* (1), 23-35.
191. Clish, C. B., Metabolomics: an emerging but powerful tool for precision medicine. *Cold Spring Harbor molecular case studies* **2015**, *1* (1), a000588.
192. MacMullan, M. A.; Dunn, Z. S.; Graham, N.; Yang, L.; Wang, P., Quantitative Proteomics and Metabolomics Reveal Biomarkers of Disease as Potential

- Immunotherapy Targets and Indicators of Therapeutic Efficacy. *Theranostics* **2019**, *9* (25), 7872-7888.
193. Naviaux, R. K.; Naviaux, J. C.; Li, K.; Bright, A. T.; Alaynick, W. A.; Wang, L.; Baxter, A.; Nathan, N.; Anderson, W.; Gordon, E., Metabolic features of chronic fatigue syndrome. *Proceedings of the National Academy of Sciences of the United States of America* **2016**, *113* (37), E5472-80.
194. Cui, L.; Lee, Y. H.; Kumar, Y.; Xu, F.; Lu, K.; Ooi, E. E.; Tannenbaum, S. R.; Ong, C. N., Serum Metabolome and Lipidome Changes in Adult Patients with Primary Dengue Infection. *PLOS Neglected Tropical Diseases* **2013**, *7* (8), e2373.
195. Rossi, D. T., Integrating automation and LC/MS for drug discovery bioanalysis. *Journal of automated methods & management in chemistry* **2002**, *24* (1), 1-7.
196. Grebe, S. K.; Singh, R. J., LC-MS/MS in the Clinical Laboratory - Where to From Here? *The Clinical biochemist. Reviews* **2011**, *32* (1), 5-31.
197. Dumas, M. E.; Kinross, J.; Nicholson, J. K., Metabolic phenotyping and systems biology approaches to understanding metabolic syndrome and fatty liver disease. *Gastroenterology* **2014**, *146* (1), 46-62.
198. Amin, A. M., The metabolic signatures of cardiometabolic diseases: Does the shared metabolite offer new therapeutic targets? *Lifestyle Medicine* **2021**, *2* (1), e25.
199. Wang, H.; Hu, J.-h.; Liu, C.-c.; Liu, M.; Liu, Z.; Sun, L.-x., LC-MS based cell metabolic profiling of tumor cells: a new predictive method for research on the mechanism of action of anticancer candidates. *RSC Advances* **2018**, *8* (30), 16645-16656.
200. Zhang, C.; Wang, Y.; Wang, F.; Wang, Z.; Lu, Y.; Xu, Y.; Wang, K.; Shen, H.; Yang, P.; Li, S.; Qin, X.; Yu, H., Quantitative profiling of glycerophospholipids during mouse and human macrophage differentiation using targeted mass spectrometry. *Scientific reports* **2017**, *7* (1), 412.
201. Passarelli, M. K.; Newman, C. F.; Marshall, P. S.; West, A.; Gilmore, I. S.; Bunch, J.; Alexander, M. R.; Dollery, C. T., Single-Cell Analysis: Visualizing Pharmaceutical and Metabolite Uptake in Cells with Label-Free 3D Mass Spectrometry Imaging. *Anal Chem* **2015**, *87* (13), 6696-702.
202. Newman, C. F.; Havelund, R.; Passarelli, M. K.; Marshall, P. S.; Francis, I.; West, A.; Alexander, M. R.; Gilmore, I. S.; Dollery, C. T., Intracellular Drug Uptake-A Comparison of Single Cell Measurements Using ToF-SIMS Imaging and Quantification from Cell Populations with LC/MS/MS. *Anal Chem* **2017**, *89* (22), 11944-11953.
203. Piehowski, P. D.; Davey, A. M.; Kurczyk, M. E.; Sheets, E. D.; Winograd, N.; Ewing, A. G.; Heien, M. L., Time-of-flight secondary ion mass spectrometry imaging of subcellular lipid heterogeneity: Poisson counting and spatial resolution. *Anal Chem* **2009**, *81* (14), 5593-602.
204. Touboul, D.; Roy, S.; Germain, D. P.; Chaminade, P.; Brunelle, A.; Laprevote, O., MALDI-TOF and cluster-TOF-SIMS imaging of Fabry disease biomarkers. *International Journal of Mass Spectrometry* **2007**, *260*, 158-165.
205. Armitage, E. G.; Kotze, H. L.; Lockyer, N. P., Imaging of metabolites using secondary ion mass spectrometry. *Metabolomics : Official journal of the Metabolomic Society* **2013**, *9* (1), 102-109.
206. Agüi-Gonzalez, P.; Jähne, S.; Phan, N. T. N., SIMS imaging in neurobiology and cell biology. *Journal of Analytical Atomic Spectrometry* **2019**, *34* (7), 1355-1368.

207. Gilmore, I. S.; Heiles, S.; Pieterse, C. L., Metabolic Imaging at the Single-Cell Scale: Recent Advances in Mass Spectrometry Imaging. *Annual review of analytical chemistry (Palo Alto, Calif.)* **2019**, *12* (1), 201-224.
208. Hodgkinson, T.; Tsimbouri, P. M.; Llopis-Hernandez, V.; Campsie, P.; Scurr, D.; Childs, P. G.; Phillips, D.; Donnelly, S.; Wells, J. A.; O'Brien, F. J.; Salmeron-Sanchez, M.; Burgess, K.; Alexander, M.; Vassalli, M.; Oreffo, R. O. C.; Reid, S.; France, D. J.; Dalby, M. J., The use of nanovibration to discover specific and potent bioactive metabolites that stimulate osteogenic differentiation in mesenchymal stem cells. *Sci Adv* **2021**, *7* (9), eabb7921.
209. Wishart, D. S.; Feunang, Y. D.; Marcu, A.; Guo, A. C.; Liang, K.; Vázquez-Fresno, R.; Sajed, T.; Johnson, D.; Li, C.; Karu, N.; Sayeeda, Z.; Lo, E.; Assempour, N.; Berjanskii, M.; Singhal, S.; Arndt, D.; Liang, Y.; Badran, H.; Grant, J.; Serra-Cayuela, A.; Liu, Y.; Mandal, R.; Neveu, V.; Pon, A.; Knox, C.; Wilson, M.; Manach, C.; Scalbert, A., HMDB 4.0: the human metabolome database for 2018. *Nucleic acids research* **2018**, *46* (D1), D608-d617.
210. Singh, S.; Awuah, D.; Rostam, H. M.; Emes, R. D.; Kandola, N. K.; Onion, D.; Htwe, S. S.; Rajchagool, B.; Cha, B.-H.; Kim, D.; Tighe, P. J.; Vrana, N. E.; Khademhosseini, A.; Ghaemmaghami, A., Unbiased Analysis of the Impact of Micropatterned Biomaterials on Macrophage Behavior Provides Insights beyond Predefined Polarization States. *ACS Biomaterials Science & Engineering* **2017**, *3* (6), 969-978.
211. Pan, Y.; Yu, Y.; Wang, X.; Zhang, T., Tumor-Associated Macrophages in Tumor Immunity. *Frontiers in immunology* **2020**, *11*.
212. Fahy, E.; Sud, M.; Cotter, D.; Subramaniam, S., LIPID MAPS online tools for lipid research. *Nucleic acids research* **2007**, *35* (suppl_2), W606-W612.
213. Chaffey, N., *Alberts, B., Johnson, A., Lewis, J., Raff, M., Roberts, K. and Walter, P. Molecular biology of the cell. 4th edn.* Ann Bot. 2003 Feb;91(3):401. doi: 10.1093/aob/mcg023.
214. Ostrowski, S. G.; Szakal, C.; Kozole, J.; Roddy, T. P.; Xu, J.; Ewing, A. G.; Winograd, N., Secondary ion MS imaging of lipids in picoliter vials with a buckminsterfullerene ion source. *Anal Chem* **2005**, *77* (19), 6190-6.
215. Adams, K. J.; DeBord, J. D.; Fernandez-Lima, F., Lipid specific molecular ion emission as a function of the primary ion characteristics in TOF-SIMS. *J Vac Sci Technol B Nanotechnol Microelectron.* **2016**, *34* (5), 051804.
216. Wagner, M. S.; Castner, D. G., Characterization of Adsorbed Protein Films by Time-of-Flight Secondary Ion Mass Spectrometry with Principal Component Analysis. *Langmuir* **2001**, *17* (15), 4649-4660.
217. Kawecki, M.; Bernard, L., Database of proteinogenic amino acid reference spectra for Bismuth-cluster ToF-SIMS. II. Positive polarity. *Surf. Sci. Spectra* **2018**, *25* (1), 015002.
218. Kawecki, M.; Bernard, L., Database of proteinogenic amino acid reference spectra for Bismuth-cluster ToF-SIMS. I. Negative polarity. *Surf. Sci. Spectra* **2018**, *25* (1), 015001.
219. Shi, W.; Meininger, C. J.; Haynes, T. E.; Hatakeyama, K.; Wu, G., Regulation of tetrahydrobiopterin synthesis and bioavailability in endothelial cells. *Cell Biochem. Biophys.* **2004**, *41* (3), 415-34.
220. Kim, S. W.; Mateo, R. D.; Yin, Y.-L.; Wu, G., Functional Amino Acids and Fatty Acids for Enhancing Production Performance of Sows and Piglets. *Asian-Australas. J. Anim. Sci.* **2007**, *20* (2), 295-306.

221. Basu, S.; Dasgupta, P. S., Dopamine, a neurotransmitter, influences the immune system. *J. Neuroimmunol.* **2000**, *102* (2), 113-24.
222. Sorgdrager, F. J. H.; Naudé, P. J. W.; Kema, I. P.; Nollen, E. A.; Deyn, P. P. D., Tryptophan Metabolism in Inflammaging: From Biomarker to Therapeutic Target. *Front. Immunol.* **2019**, *10*, 2565-2565.
223. Hibbs, J. B., Jr.; Taintor, R. R.; Vavrin, Z., Macrophage cytotoxicity: role for L-arginine deiminase and imino nitrogen oxidation to nitrite. *Science (New York, N.Y.)* **1987**, *235* (4787), 473-6.
224. Rath, M.; Müller, I.; Kropf, P.; Closs, E. I.; Munder, M., Metabolism via Arginase or Nitric Oxide Synthase: Two Competing Arginine Pathways in Macrophages. *Frontiers in Immunology* **2014**, *5*.
225. Hamdy, N. A.; Gamal-Eldeen, A. M., New pyridone, thioxopyridine, pyrazolopyridine and pyridine derivatives that modulate inflammatory mediators in stimulated RAW 264.7 murine macrophage. *Eur. J. Med. Chem.* **2009**, *44* (11), 4547-56.
226. Suzuki, F.; Okayasu, H.; Tashiro, M.; Hashimoto, K.; Yokote, Y.; Akahane, K.; Hongo, S.; Sakagami, H., Effect of lignins and their precursors on nitric oxide, citrulline and asparagine production by mouse macrophage-like Raw 264.7 cells. *Anticancer Res.* **2002**, *22* (5), 2719-24.
227. Olivera, A.; Rivera, J., Sphingolipids and the Balancing of Immune Cell Function: Lessons from the Mast Cell. *J. Immunol.* **2005**, *174* (3), 1153-1158.
228. de Araujo Junior, R. F.; Eich, C.; Jorquera, C.; Schomann, T.; Baldazzi, F.; Chan, A. B.; Cruz, L. J., Ceramide and palmitic acid inhibit macrophage-mediated epithelial-mesenchymal transition in colorectal cancer. *Mol. Cell. Biochem.* **2020**, *468* (1-2), 153-168.
229. Spiegel, S.; Foster, D.; Kolesnick, R., Signal transduction through lipid second messengers. *Curr. Opin. Cell Biol.* **1996**, *8* (2), 159-167.
230. Kühn, S.; Sievers, J.; Stoppa, A.; Träber, N.; Zimmermann, R.; Welzel, P. B.; Werner, C., Cell-Instructive Multiphasic Gel-in-Gel Materials. *Advanced Functional Materials* **2020**, *30* (26), 1908857.
231. Matsumoto, T.; Mooney, D. J., Cell instructive polymers. *Advances in biochemical engineering/biotechnology* **2006**, *102*, 113-37.
232. Burroughs, L.; Amer, M. H.; Vasey, M.; Koch, B.; Figueredo, G. P.; Mukonoweshuro, B.; Mikulskis, P.; Vasilevich, A.; Vermeulen, S.; Dryden, I. L.; Winkler, D. A.; Ghaemmaghami, A. M.; Rose, F. R. A. J.; de Boer, J.; Alexander, M. R., Discovery of synergistic material-topography combinations to achieve immunomodulatory osteoinductive biomaterials using a novel in vitro screening method: The ChemoTopoChip. *Biomaterials* **2021**, *271*, 120740.
233. Astete, C. E.; Sabliov, C. M., Synthesis and characterization of PLGA nanoparticles. *Journal of biomaterials science. Polymer edition* **2006**, *17* (3), 247-89.
234. Burroughs, L.; Amer, M. H.; Vasey, M.; Koch, B.; Figueredo, G. P.; Mukonoweshuro, B.; Mikulskis, P.; Vasilevich, A.; Vermeulen, S.; Dryden, I. L.; Winkler, D. A.; Ghaemmaghami, A. M.; Rose, F.; de Boer, J.; Alexander, M. R., Discovery of synergistic material-topography combinations to achieve immunomodulatory osteoinductive biomaterials using a novel in vitro screening method: The ChemoTopoChip. *Biomaterials* **2021**, *271*, 120740.
235. Krishna Rao, K. S. V.; Kummara, M. R., A Review on Radical Polymerization Used for Design and Development of Biomaterials” by NOVA Publications. 2012; pp 175-198.

236. Antony, G. J. M.; Jarali, C. S.; Aruna, S. T.; Raja, S., Tailored poly(ethylene) glycol dimethacrylate based shape memory polymer for orthopedic applications. *Journal of the Mechanical Behavior of Biomedical Materials* **2017**, *65*, 857-865.
237. Esquivel-Guzmán, J. A.; Zaragoza-Galán, G.; Ortíz-Palacios, J.; Rivera, E., Synthesis and characterization of novel polymers bearing fluorescein units: thermal and optical properties. *Designed Monomers and Polymers* **2012**, *15* (6), 561-574.
238. Barim, G.; Gokhun Yayla, M.; Degirmenci, M., Copolymerization of cyclohexene-3-yl methyl methacrylate with styrene: synthesis, characterization, monomer reactivity ratios, and thermal properties. *Designed Monomers and Polymers* **2014**, *17* (7), 610-616.
239. Singh, T.; Hook, A. L.; Lockett, J.; Maitz, M. F.; Sperling, C.; Werner, C.; Davies, M. C.; Irvine, D. J.; Williams, P.; Alexander, M. R., Discovery of hemocompatible bacterial biofilm-resistant copolymers. *Biomaterials* **2020**, 120312.
240. Hook, A. L.; Chang, C. Y.; Yang, J.; Lockett, J.; Cockayne, A.; Atkinson, S.; Mei, Y.; Bayston, R.; Irvine, D. J.; Langer, R.; Anderson, D. G.; Williams, P.; Davies, M. C.; Alexander, M. R., Combinatorial discovery of polymers resistant to bacterial attachment. *Nature biotechnology* **2012**, *30* (9), 868-875.
241. Dundas, A. A.; Sanni, O.; Dubern, J.-F.; Dimitrakakis, G.; Hook, A. L.; Irvine, D. J.; Williams, P.; Alexander, M. R., Validating a Predictive Structure–Property Relationship by Discovery of Novel Polymers which Reduce Bacterial Biofilm Formation. *Advanced Materials* **2019**, *31* (49), 1903513.
242. Vallieres, C.; Hook, A. L.; He, Y.; Crucitti, V. C.; Figueredo, G.; Davies, C. R.; Burroughs, L.; Winkler, D. A.; Wildman, R. D.; Irvine, D. J.; Alexander, M. R.; Avery, S. V., Discovery of (meth)acrylate polymers that resist colonization by fungi associated with pathogenesis and biodeterioration. *Science advances* **2020**, *6* (23), eaba6574.
243. Rostam, H.; Fisher, L.; Lockett, J.; Burroughs, L.; Mbadugha, C.; Winkler, D.; Figueredo, G.; Alexander, M.; Ghaemmaghani, A., *Discovery of 'immune-instructive' materials for medical applications*. 2019.
244. Sugumaran, D.; Abd Karim, K. J., *Removal of copper (II) ion using chitosan-graft-poly(methyl methacrylate) as adsorbent*. 2017.
245. Rahaman, M.; Parvez, M. A.; Soares, J. B. P.; Hussein, I. A., Effect of Polymerization Conditions on Thermal and Mechanical Properties of Ethylene/1-Butene Copolymer Made with Ziegler-Natta Catalysts. *International Journal of Polymer Science* **2014**, *2014*, 654260.
246. Huang, H. L.; Goh, S. H.; Lai, D. M. Y.; Huan, C. H. A., ToF-SIMS studies of poly(methyl methacrylate-co-methacrylic acid), poly(2,2,3,3,3-pentafluoropropyl methacrylate-co-4-vinylpyridine) and their blends. *Applied Surface Science* **2004**, *227* (1), 373-382.
247. Wang, Y.; Papadimitrakopoulos, F.; Burgess, D. J., Polymeric "smart" coatings to prevent foreign body response to implantable biosensors. *J Control Release* **2013**, *169* (3), 341-347.
248. Brown, B. N.; Badylak, S. F., Expanded applications, shifting paradigms and an improved understanding of host-biomaterial interactions. *Acta biomaterialia* **2013**, *9* (2), 4948-55.
249. Oishi, Y.; Manabe, I., Macrophages in inflammation, repair and regeneration. *International immunology* **2018**, *30* (11), 511-528.
250. Kzhyshkowska, J.; Gudima, A.; Riabov, V.; Dollinger, C.; Lavallo, P.; Vrana, N. E., Macrophage responses to implants: prospects for personalized medicine. *Journal of Leukocyte Biology* **2015**, *98* (6), 953-962.

251. Franz, S.; Rammelt, S.; Scharnweber, D.; Simon, J. C., Immune responses to implants – A review of the implications for the design of immunomodulatory biomaterials. *Biomaterials* **2011**, *32* (28), 6692-6709.
252. McWhorter, F. Y.; Wang, T.; Nguyen, P.; Chung, T.; Liu, W. F., Modulation of macrophage phenotype by cell shape. *Proceedings of the National Academy of Sciences* **2013**, *110* (43), 17253-17258.
253. Boehler, R. M.; Graham, J. G.; Shea, L. D., Tissue engineering tools for modulation of the immune response. *BioTechniques* **2011**, *51* (4), 239-254.
254. Benoit, M.; Desnues, B.; Mege, J.-L., Macrophage Polarization in Bacterial Infections. *The Journal of Immunology* **2008**, *181* (6), 3733-3739.
255. Anderson, J. M.; Miller, K. M., Biomaterial biocompatibility and the macrophage. *Biomaterials* **1984**, *5* (1), 5-10.
256. Fisher, L. E.; Kämmerling, L.; Alexander, M. R.; Ghaemmaghami, A. M., Immune-instructive materials as new tools for immunotherapy. *Current opinion in biotechnology* **2022**, *74*, 194-203.
257. Veiseh, O.; Vegas, A. J., Domesticating the foreign body response: Recent advances and applications. *Advanced drug delivery reviews* **2019**, *144*, 148-161.
258. Mattila, J. T.; Ojo, O. O.; Kepka-Lenhart, D.; Marino, S.; Kim, J. H.; Eum, S. Y.; Via, L. E.; Barry, C. E., 3rd; Klein, E.; Kirschner, D. E.; Morris, S. M., Jr.; Lin, P. L.; Flynn, J. L., Microenvironments in tuberculous granulomas are delineated by distinct populations of macrophage subsets and expression of nitric oxide synthase and arginase isoforms. *Journal of immunology (Baltimore, Md. : 1950)* **2013**, *191* (2), 773-84.
259. Scanga, C. A.; Mohan, V. P.; Tanaka, K.; Alland, D.; Flynn, J. L.; Chan, J., The inducible nitric oxide synthase locus confers protection against aerogenic challenge of both clinical and laboratory strains of Mycobacterium tuberculosis in mice. *Infection and immunity* **2001**, *69* (12), 7711-7.
260. Seydel, C., Single-cell metabolomics hits its stride. *Nature Methods* **2021**, *18* (12), 1452-1456.
261. Rappez, L.; Stadler, M.; Triana, S.; Gathungu, R. M.; Ovchinnikova, K.; Phapale, P.; Heikenwalder, M.; Alexandrov, T., SpaceM reveals metabolic states of single cells. *Nature Methods* **2021**, *18* (7), 799-805.
262. Woodward, A.; Pandele, A.; Abdelrazig, S.; Ortori, C. A.; Khan, I.; Uribe, M. C.; May, S.; Barrett, D. A.; Grundy, R. G.; Kim, D. H.; Rahman, R., Integrated Metabolomics and Transcriptomics Using an Optimised Dual Extraction Process to Study Human Brain Cancer Cells and Tissues. *Metabolites* **2021**, *11* (4).
263. Harkin, C.; Smith, K. W.; Cruickshank, F. L.; Logan Mackay, C.; Flinders, B.; Heeren, R. M. A.; Moore, T.; Brockbank, S.; Cobice, D. F., On-tissue chemical derivatization in mass spectrometry imaging. *Mass spectrometry reviews* **2022**, *41* (5), 662-694.
264. Meurs, J.; Scurr, D. J.; Lourdasamy, A.; Storer, L. C. D.; Grundy, R. G.; Alexander, M. R.; Rahman, R.; Kim, D.-H., Sequential 3D OrbiSIMS and LESA-MS/MS-based metabolomics for prediction of brain tumor relapse from sample-limited primary tissue archives. *bioRxiv* **2021**, 2020.07.15.182071.
265. Debois, D.; Bralet, M.-P.; Le Naour, F.; Brunelle, A.; Laprévotte, O., In Situ Lipidomic Analysis of Nonalcoholic Fatty Liver by Cluster TOF-SIMS Imaging. *Analytical Chemistry* **2009**, *81* (8), 2823-2831.
266. Brulet, M.; Seyer, A.; Edelman, A.; Brunelle, A.; Fritsch, J.; Ollero, M.; Laprévotte, O., Lipid mapping of colonic mucosa by cluster TOF-SIMS imaging and

multivariate analysis in *cftr* knockout mice [S]. *Journal of Lipid Research* **2010**, *51* (10), 3034-3045.

267. Palmquist, A.; Emanuelsson, L.; Sjövall, P., Chemical and structural analysis of the bone-implant interface by TOF-SIMS, SEM, FIB and TEM: Experimental study in animal. *Applied Surface Science* **2012**, *258* (17), 6485-6494.

268. Zhang, J.; Brown, J.; Scurr, D. J.; Bullen, A.; MacLellan-Gibson, K.; Williams, P.; Alexander, M. R.; Hardie, K. R.; Gilmore, I. S.; Rakowska, P. D., Cryo-OrbiSIMS for 3D Molecular Imaging of a Bacterial Biofilm in Its Native State. *Analytical Chemistry* **2020**, *92* (13), 9008-9015.

269. Linke, F.; Johnson, J. E. C.; Kern, S.; Bennett, C. D.; Lourdasamy, A.; Lea, D.; Clifford, S. C.; Merry, C. L. R.; Stolnik, S.; Alexander, M. R.; Peet, A. C.; Scurr, D. J.; Griffiths, R. L.; Grabowska, A. M.; Kerr, I. D.; Coyle, B., Identifying new biomarkers of aggressive Group 3 and SHH medulloblastoma using 3D hydrogel models, single cell RNA sequencing and 3D OrbiSIMS imaging. *Acta Neuropathologica Communications* **2023**, *11* (1), 6.

270. Piwowar, A. M.; Lockyer, N. P.; Vickerman, J. C., Salt Effects on Ion Formation in Desorption Mass Spectrometry: An Investigation into the Role of Alkali Chlorides on Peak Suppression in Time-of-Flight-Secondary Ion Mass Spectrometry. *Analytical Chemistry* **2009**, *81* (3), 1040-1048.

271. Trindade, G. F.; Abel, M.-L.; Watts, J. F., *simsMVA*: A tool for multivariate analysis of ToF-SIMS datasets. *Chemometrics and Intelligent Laboratory Systems* **2018**, *182*, 180-187.

272. Cohen, P.; Miyazaki, M.; Socci, N. D.; Hagge-Greenberg, A.; Liedtke, W.; Soukas, A. A.; Sharma, R.; Hudgins, L. C.; Ntambi, J. M.; Friedman, J. M., Role for stearoyl-CoA desaturase-1 in leptin-mediated weight loss. *Science (New York, N.Y.)* **2002**, *297* (5579), 240-3.

273. Höring, M.; Krautbauer, S.; Hiltl, L.; Babl, V.; Sigrüener, A.; Burkhardt, R.; Liebisch, G., Accurate Lipid Quantification of Tissue Homogenates Requires Suitable Sample Concentration, Solvent Composition, and Homogenization Procedure-A Case Study in Murine Liver. *Metabolites* **2021**, *11* (6).

274. Boudière, L.; Michaud, M.; Petroustos, D.; Rébeillé, F.; Falconet, D.; Bastien, O.; Roy, S.; Finazzi, G.; Rolland, N.; Jouhet, J.; Block, M. A.; Maréchal, E., Glycerolipids in photosynthesis: composition, synthesis and trafficking. *Biochimica et biophysica acta* **2014**, *1837* (4), 470-80.

275. Huang, Y. L.; Morales-Rosado, J.; Ray, J.; Myers, T. G.; Kho, T.; Lu, M.; Munford, R. S., Toll-like receptor agonists promote prolonged triglyceride storage in macrophages. *The Journal of biological chemistry* **2014**, *289* (5), 3001-12.

276. Vozenilek, A. E.; Navratil, A. R.; Green, J. M.; Coleman, D. T.; Blackburn, C. M. R.; Finney, A. C.; Pearson, B. H.; Chrast, R.; Finck, B. N.; Klein, R. L.; Orr, A. W.; Woolard, M. D., Macrophage-Associated Lipin-1 Enzymatic Activity Contributes to Modified Low-Density Lipoprotein-Induced Proinflammatory Signaling and Atherosclerosis. *Arteriosclerosis, Thrombosis, and Vascular Biology* **2018**, *38* (2), 324-334.

277. Carrasco, S.; Merida, I., Diacylglycerol-dependent binding recruits PKC θ and RasGRP1 C1 domains to specific subcellular localizations in living T lymphocytes. *Molecular biology of the cell* **2004**, *15* (6), 2932-42.





278. Quann, E. J.; Merino, E.; Furuta, T.; Huse, M., Localized diacylglycerol drives the polarization of the microtubule-organizing center in T cells. *Nature immunology* **2009**, *10* (6), 627-35.


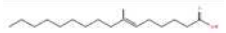




279. Rockenfeller, P.; Smolnig, M.; Diessl, J.; Bashir, M.; Schmiedhofer, V.; Knittelfelder, O.; Ring, J.; Franz, J.; Foessler, I.; Khan, M. J.; Rost, R.; Graier, W. F.; Kroemer, G.; Zimmermann, A.; Carmona-Gutierrez, D.; Eisenberg, T.; Büttner, S.; Sigrist, S. J.; Kühnlein, R. P.; Kohlwein, S. D.; Gourlay, C. W.; Madeo, F., Diacylglycerol triggers Rim101 pathway-dependent necrosis in yeast: a model for lipotoxicity. *Cell Death & Differentiation* **2018**, *25* (4), 767-783.
280. van Meer, G.; Voelker, D. R.; Feigenson, G. W., Membrane lipids: where they are and how they behave. *Nature reviews. Molecular cell biology* **2008**, *9* (2), 112-24.
281. Zorov, D. B.; Juhaszova, M.; Sollott, S. J., Mitochondrial reactive oxygen species (ROS) and ROS-induced ROS release. *Physiological reviews* **2014**, *94* (3), 909-50.
282. Batista-Gonzalez, A.; Vidal, R.; Criollo, A.; Carreño, L. J., New Insights on the Role of Lipid Metabolism in the Metabolic Reprogramming of Macrophages. *Frontiers in Immunology* **2020**, *10*.
283. Yang, X.; Li, Y.; Li, Y.; Ren, X.; Zhang, X.; Hu, D.; Gao, Y.; Xing, Y.; Shang, H., Oxidative Stress-Mediated Atherosclerosis: Mechanisms and Therapies. *Frontiers in Physiology* **2017**, *8*.
284. Kusner, D. J.; Hall, C. F.; Jackson, S., Fcγ Receptor-Mediated Activation of Phospholipase D Regulates Macrophage Phagocytosis of IgG-Opsonized Particles. *The Journal of Immunology* **1999**, *162* (4), 2266-2274.
285. Bandyopadhyay, R.; Basu, M., Involvement of PL-D in the alternate signal transduction pathway of macrophages induced by an external stimulus. *Molecular and Cellular Biochemistry* **2000**, *203* (1), 127-133.
286. Rice, G. C.; Brown, P. A.; Nelson, R. J.; Bianco, J. A.; Singer, J. W.; Bursten, S., Protection from endotoxic shock in mice by pharmacologic inhibition of phosphatidic acid. *Proceedings of the National Academy of Sciences of the United States of America* **1994**, *91* (9), 3857-61.
287. Branco, A. C. C. C.; Yoshikawa, F. S. Y.; Pietrobon, A. J.; Sato, M. N., Role of Histamine in Modulating the Immune Response and Inflammation. *Mediators of Inflammation* **2018**, *2018*, 9524075.
288. Liu, J.; Hong, S.; Yang, J.; Zhang, X.; Wang, Y.; Wang, H.; Peng, J.; Hong, L., Targeting purine metabolism in ovarian cancer. *Journal of Ovarian Research* **2022**, *15* (1), 93.
289. Díaz-Muñoz, M.; Hernández-Muñoz, R.; Butanda-Ochoa, A., Structure-activity features of purines and their receptors: implications in cell physiopathology. *Molecular Biomedicine* **2022**, *3* (1), 5.
290. Edney, M. K.; Kotowska, A. M.; Spanu, M.; Trindade, G. F.; Wilmot, E.; Reid, J.; Barker, J.; Aylott, J. W.; Shard, A. G.; Alexander, M. R.; Snape, C. E.; Scurr, D. J., Molecular Formula Prediction for Chemical Filtering of 3D OrbiSIMS Datasets. *Analytical Chemistry* **2022**, *94* (11), 4703-4711.





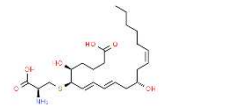
Appendix

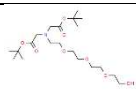
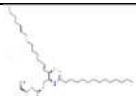


Appendix 4:

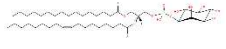

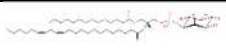

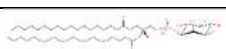
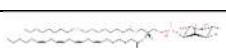
Table A4.1. Putative annotation of lipid compounds in negative ion spectrum of M0, M1 and M2 macrophages, (* detect in THP- macrophages polarisation by LC-MS methods, ++ detect in tissue section by 3D OrbiSIMS methods, 15 lipid ion in common)







Name	Exact mass (m/z)	Formula [M-H] ⁻	Structure	Information	M0 macrophage		M1 macrophage		M2 macrophage	
					Mass error p.p.m	Area (AU)	Mass error p.p.m	Area (AU)	Mass error p.p.m	Area (AU)
Fatty acids (FA)										
FA 14:0++	227.2029	C ₁₄ H ₂₇ O ₂		https://www.lipidmaps.org/databases/lmsd/LMFA01010014?LMID=LMFA01010014					-0.3	11520.55
FA 15:0*	241.2180	C ₁₅ H ₂₉ O ₂		https://www.lipidmaps.org/databases/lmsd/LMFA01010015?LMID=LMFA01010015			0.2	1009	-0.1	10743.61
FA 16:0*++	255.2331	C ₁₆ H ₃₁ O ₂		https://www.lipidmaps.org/databases/lmsd/LMFA01010001?LMID=LMFA01010001	0.6	27104.51	0.6	35229.2	0.4	279005.29
FA 16:1++	253.2175	C ₁₆ H ₂₉ O ₂		https://www.lipidmaps.org/databases/lmsd/LMFA01010001?LMID=LMFA01010001			0.7	3711.72	0.3	31572.26

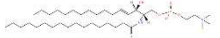

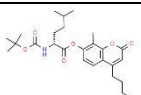
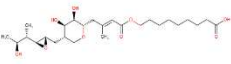

				msd/LMFA01020133?LMID=LMFA01020133						
FA 17:0*	269.2500	C ₁₇ H ₃₃ O ₂		https://www.lipidmaps.org/databases/msd/LMFA01010017?LMID=LMFA01010017			1.6	1471.17	0.8	14539.28
FA 17:1	267.2324	C ₁₇ H ₃₁ O ₂		https://www.lipidmaps.org/databases/msd/LMFA01020203?LMID=LMFA01020203					0.8	3760.23
FA 18:0++	283.2645	C ₁₈ H ₃₅ O ₂		https://www.lipidmaps.org/databases/msd/LMFA01010018?LMID=LMFA01010018	0.1	36410	0.1	92587.99	0.1	276538.49
FA18:1*·++	281.2486	C ₁₈ H ₃₃ O ₂		https://www.lipidmaps.org/databases/msd/LMFA01030002?LMID=LMFA01030002	-0.1	24011.28	0.0	61453.28	0.1	258961.75
FA18:2*·++	279.2330	C ₁₈ H ₃₁ O ₂		https://www.lipidmaps.org/databases/msd/LMFA01030110?LMID=LMFA01030110			-0.2	4568.31	-0.2	22519.37
FA 20:3++	305.2487	C ₂₀ H ₃₃ O ₂		https://www.lipidmaps.org/databases/			0.2	1964.59	0.1	18144.56

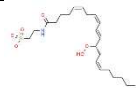
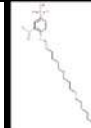
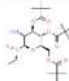
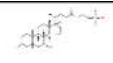
				msd/LMFA01030157?LMID=LMFA01030157						
FA 20:4++	303.2330	C ₂₀ H ₃₁ O ₂		https://www.lipidmaps.org/databases/msd/LMFA01030173?LMID=LMFA01030173	0.1	13466.62	0.2	17907.53	-0.2	97974.75
FA 20:5	301.2155	C ₂₀ H ₂₉ O ₂		https://www.lipidmaps.org/databases/msd/LMFA01030180?LMID=LMFA01030180			-1.2	1101.58	-0.7	4707.33
FA 22:4++	331.2659	C ₂₂ H ₃₅ O ₂		https://www.lipidmaps.org/databases/msd/LMFA01030177?LMID=LMFA01030177			-0.4	1367.55		
FA 22:5++	329.2483	C ₂₂ H ₃₃ O ₂		https://www.lipidmaps.org/databases/msd/LMFA01030182?LMID=LMFA01030182			-0.1	2114.64	-0.4	13811.97
10,11-Dihydro-12R-hydroxy-leukotriene E4	457.2513	C ₂₃ H ₃₉ NO ₆ S		https://www.chemspider.com/Chemical-Structure.30776621.html?rid=38c09e7f-61b7-4979-ab22-	2.0	4412.21	1.8	86282.52	2.0	163681.7

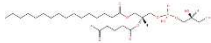
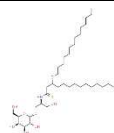
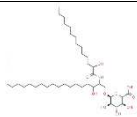
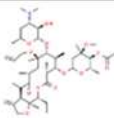
				a819af4f8fc9&page_num=0						
Acyl carnitines (CAR)										
CAR 13:0;O4	420.2605	C ₂₀ H ₃₈ NO ₈		https://www.chemspider.com/Chemical-Structure.29332391.html?rid=d3f9c4dc-e823-49a3-89b1-6764b5d8a075&page_num=0			-0.9	2857.85	-0.3	4585.07
CAR 30:1;O4	656.5096	C ₃₇ H ₇₀ NO ₈		https://www.chemspider.com/Chemical-Structure.9356447.html?rid=b7c87349-3c4d-4500-a83d-65fe8798c905	-1.6	3556.00	-1.0	1675.98		
Phosphatidylinositol (PI)										
PI(18:0/0:0)	599.3216	C ₂₇ H ₅₂ O ₁₂ P		https://www.lipidmaps.org/databases/lmsd/LMGP06050004?LMID=LMGP06050004			0.1	4145.31	0.7	1782.87
PI 18:0-20:3*	887.5661	C ₄₇ H ₈₄ O ₁₃ P		https://www.lipidmaps.org/databases/lmsd/LMGP06010192?LMID=LMGP06010192			0.9	1467.16	0.4	3557.49

PI 34:1* [·] ++	835.5353	C ₄₃ H ₈₀ O ₁₃ P		https://www.lipidmaps.org/databases/lmsd/LMGP06010001?LMID=LMGP06010001			0.1	5002.39	-0.4	8495.28
PI 36:1*	863.5556	C ₄₅ H ₈₄ O ₁₃ P		https://www.lipidmaps.org/databases/lmsd/LMGP06010074?LMID=LMGP06010074			-0.4	14522.95	-0.4	18920.7
PI 36:2*	861.5484	C ₄₅ H ₈₂ O ₁₃ P		https://www.lipidmaps.org/databases/lmsd/LMGP06010075?LMID=LMGP06010075			-0.5	4305.54	-0.2	10060.63
PI 38:3* [·] ++	883.5316	C ₄₇ H ₈₀ O ₁₃ P		https://www.lipidmaps.org/databases/lmsd/LMGP06010193?LMID=LMGP06010193			1.1	1727.55	-0.4	2419.38
PI 38:4* [·] ++	885.5498	C ₄₇ H ₈₂ O ₁₃ P		https://www.lipidmaps.org/databases/lmsd/LMGP06010010?LMID=LMGP06010010	0.0	5922.51	-0.3	18814.16	-0.2	61319.66
PI 40:5*	911.5749	C ₄₉ H ₈₄ O ₁₃ P		https://www.lipidmaps.org/databases/lmsd/LMGP06010307?LMID=LMGP06010307					0.1	1651.6

Phosphatidylserine (PS)										
PS 36:1*.*.*	788.5419	C ₄₂ H ₇₉ NO ₁₀ P		https://www.lipidmaps.org/databases/lmsd/LMGP03010025?LMID=LMGP03010025					-0.4	11220.87
Phosphatidylphosphates (PA)										
PA 18:0	437.2686	C ₂₁ H ₄₂ O ₇ P		https://www.lipidmaps.org/databases/lmsd/LMGP10050005?LMID=LMGP10050005			-0.9	3121.27	-0.7	9217.13
PA 36:2++	701.5123	C ₃₉ H ₇₄ O ₈ P		https://www.lipidmaps.org/databases/lmsd/LMGP10010037?LMID=LMGP10010037	-0.6	3262.63	0.0	4862.41	0.0	21753.07
CPA(16:0)*	391.2230	C ₁₉ H ₃₆ O ₆ P		https://www.lipidmaps.org/databases/lmsd/LMGP00000057?LMID=LMGP00000057			0.3	1864.02		
CPA(18:1)	417.2409	C ₂₁ H ₃₈ O ₆ P		https://www.lipidmaps.org/databases/lmsd/LMGP00000056?LMID=LMGP00000056			-2.0	1259.00	0.1	2988.96
CPA(18:0)	419.2567	C ₂₁ H ₄₀ O ₆ P		https://www.lipidmaps.org/databases/lmsd/LMGP00000056?LMID=LMGP00000056	-0.3	4362.96	0.0	17874.25	0.1	47590.02

				msd/LMGP000000 55?LMID=LMGP0 0000055						
Phosphosphingolipids										
SM(d16:1/ 17:0)*	687.5443	C ₃₈ H ₇₆ N ₂ O ₆ P		https://www.lipidmaps.org/databases/lmsd/LMSP03010037?LMID=LMSP03010037	-0.5	3554.85	0.1	2446.42		
Sterol lipids										
ST 25:3;O5;G	474.2855	C ₂₇ H ₄₀ NO ₆		https://hmdb.ca/metabolites/HMDB0014907	-1.4	8322.27	-1.0	200400.34	-0.9	399983.97
ST 24:4;O5;G*	458.2537	C ₂₆ H ₃₆ NO ₆		https://www.chemspider.com/Chemical-Structure.60759728.html?rid=05e4d48b-63f7-477a-8156-da70419dd935			-0.5	18364.54	-0.5	33536.62
ST 20:0;O4;Hex	499.2868	C ₂₆ H ₄₃ O ₉		https://hmdb.ca/metabolites/HMDB0014554			1.3	1014.16	1.8	10687.51
ST 22:0;O3;S	443.2328	C ₂₂ H ₃₇ NO ₆ S		https://www.chemspider.com/Chemical-Structure.3350310.html?rid=130191b8-3c36-46d9-b3d4-			1.4	1886.76		

				296830171ba3&page_num=0						
ST 22:1;O3;S	441.2198	C ₂₂ H ₃₅ NO ₆ S		https://www.chemspider.com/Chemical-Structure.58170237.html?rid=037a593e-79b6-4af1-a59c-6390522403f6&page_num=0			1.0	2408.43		
ST 24:0;O3;S	471.2636	C ₂₄ H ₄₁ NO ₆ S		https://www.chemspider.com/Chemical-Structure.4409329.html?rid=bfff8ff0-bfb2-4dce-a96c-3e3ae452f9b4&page_num=0			0.5	1474.87		
ST 21:0;O6;T	490.2467	C ₂₃ H ₄₀ NO ₈ S		https://www.chemspider.com/Chemical-Structure.9180690.html?rid=094670ed-8195-4a32-b287-aa54719e317d			0.9	2238.07		
ST 24:1;O4;T*	498.2899	C ₂₆ H ₄₄ NO ₆ S		https://www.lipidmaps.org/databases/lmsd/LMST05040005?LMID=LMST05040005			0.8	1886.64	0.1	17797.04

Oxidized glycerophosphoglycerols										
POV-PG	581.3093	C ₂₇ H ₅₀ O ₁₁ P		https://www.lipidmaps.org/databases/lmsd/LMGP20060015?LMID=LMGP20060015			-0.3	10462.39	-0.4	17074.60
Neutral glycosphingolipids										
HexCer 31:0;O3	674.5200	C ₃₇ H ₇₂ NO ₉		https://www.chemspider.com/Chemical-Structure.8592531.html?rid=741950d8-7717-4e0c-8da7-d5ad707948b4&page_num=0	-1.8	5835.93	-1.2	3370.13	-1.7	6039.87
HexCer 32:1;O4	702.5152	C ₃₈ H ₇₂ NO ₁₀		https://www.chemspider.com/Chemical-Structure.8093797.html?rid=1d47af1c-9779-475d-b311-e2257580b65b&page_num=0			0.3	1225.62		
Hex2Cer 33:6;O2	836.5296	C ₄₅ H ₇₅ NO ₁₃		http://www.chemspider.com/Chemical-Structure.8661076.html?rid=efc8a648-46ce-45c7-81ef-93db23a492c3&page_num=0			-0.4	1629.11	-1.1	2151.49

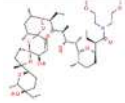
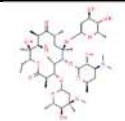
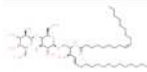
HexCer 42:6;O6	864.5605	C ₄₄ H ₈₂ NO ₁₂		http://www.chemspider.com/Chemical-Structure.58989989.html?rid=76203e10-d373-481f-a6c1-ea3ac92770e5			-0.3	8612.37	-0.4	8940.41
Hex2Cer 31:3;O5	862.5459	C ₄₃ H ₇₆ NO ₁₆		http://www.chemspider.com/Chemical-Structure.34524087.html?rid=5e63d254-76da-42fd-bad5-2925cb83a702			-0.5	2467.17	-0.7	2598.76
Hex2Cer 36:2;O2	886.5529	C ₄₈ H ₈₈ NO ₁₃		http://www.chemspider.com/Chemical-Structure.24765751.html?rid=de2bc5ec-b095-4640-b2c8-ea5bc80867cd&page_num=0			0.1	10416.22	-0.3	28614.61

Table A4.2. Summary of phospholipids identified in macrophage phenotype by 3D OrbiSIMS MS/MS in a negative ion mode.

Phosphatidylinositol PI 38:4 (P-18:0/20:4)		
<i>m/z</i>	Formula	ID
241.0118	$C_6H_{10}O_8P^-$	Head group
283.2642	$C_{18}H_{35}O_2^-$	FA[18:0-H] ⁻
303.2327	$C_{20}H_{31}O_2^-$	FA[20;4-H] ⁻
885.5498	$C_{47}H_{82}O_{13}P^-$	M-H ⁻

Phosphatidylinositol PI 36:2 (18:0/18:2)		
<i>m/z</i>	Formula	ID
241.0118	$C_6H_{10}O_8P^-$	Head group
281.2486	$C_{18}H_{33}O_2^-$	FA[18:1-H] ⁻
861.5494	$C_{45}H_{82}O_{13}P^-$	M-H ⁻

Phosphatidylphosphate CPA 18:0		
<i>m/z</i>	Formula	ID
152.9950	$C_3H_6O_5P^-$	Head group
283.2642	$C_{18}H_{35}O_2^-$	FA[18:0-H] ⁻
419.2567	$C_{21}H_{40}O_6P^-$	M-H ⁻

Sphingomyelin SM(d16:1/17:0)		
<i>m/z</i>	Formula	ID
168.0430	$C_4H_{11}NO_4P^-$	Head group
269.2486	$C_{17}H_{33}O_2^-$	FA[17:0-H] ⁻
687.544	$C_{38}H_{76}NO_4P^-$	M-H ⁻

Table A4.3. Characteristic fragments of lipids class in spectra both of positive and negative ions.

Exact mass (m/z)	Assignment	Amino acids	M0 macrophage		M1 macrophage		M2 macrophage	
			Mass error p.p.m	Intensity (AU)	Mass error p.p.m	Intensity (AU)	Mass error p.p.m	Intensity (AU)
PA								
122.0007	C ₂ H ₅ NPO ₃ ⁻	Phosphoethanolamine	0.0	13284.48	-0.3	10267.38	0.4	16141.54
PC								
124.9998	C ₂ H ₆ PO ₄ ⁺	Phosphocholines	-0.4	1967962.06	-0.1	383873.28	-0.5	824104.54
184.0739	C ₅ H ₁₃ NPO ₄ ⁺	Phosphocholines	-0.5	1857923.96	-0.4	383873.23	-0.8	588869.19
168.0429	C ₄ H ₁₁ NPO ₄ ⁻	Phosphocholines	-1.1	3488.00	1.2	3643.00	-0.8	17622.00
PG								
152.9957	C ₃ H ₆ PO ₅ ⁻	Phosphatidylglycerols	-0.9	6709.45	-0.7	18474.48	-0.8	46522.86
PI								
241.0119	C ₆ H ₁₀ PO ₈ ⁻	Phosphatidylinositol	0.3	6709.00	0.2	18518.00	0.3	46586.00
Sulfatide								
96.9660	HSO ₄ ⁻	Sulfatide	-0.9	950273.38	-1.1	249561.18	-1.1	291906.45
Sphingolipids								
104.1070	C ₅ H ₁₄ NO ⁺	Sphingolipids	-0.1	955132.00	-0.7	53874.00	-0.6	29350.00
122.9830	C ₂ H ₄ PO ₄ ⁻	Sphingolipids	2.3	227.00	-0.3	18497.00	-0.4	49393.00

Table A4.4. Characteristic molecular ion and fragments of amino acid in 3D OrbiSIMS spectra.

Exact mass (m/z)	Assignment	Amino acids	M0 macrophage		M1 macrophage		M2 macrophage	
			Mass error p.p.m	Intensity (AU)	Mass error p.p.m	Intensity (AU)	Mass error p.p.m	Intensity (AU)
Positive								
86.0966	C ₅ H ₁₂ N ⁺	Leucine	2.0	4268839.21	2.0	1029255.17	1.6	2445367.60
81.0449	C ₄ H ₅ N ₂ ⁺	Histidine	2.4	428865.21	2.4	146241.30	2.0	392938.68
82.0527	C ₄ H ₆ N ₂ ⁺	Histidine	1.9	81132.91	2.0	23550.63	1.8	48841.26
83.0606	C ₄ H ₇ N ₂ ⁺	Histidine	2.2	905324.65	2.3	275942.28	1.9	784924.33
93.0448	C ₅ H ₅ N ₂ ⁺	Histidine	1.2	1677517.08	1.3	563937.95	0.9	1561973
94.0526	C ₅ H ₆ N ₂ ⁺	Histidine	0.7	9340.83	0.5	1942.23	1.0	6855.31
95.0604	C ₅ H ₇ N ₂ ⁺	Histidine	0.7	293808.21	0.8	91140.71	0.5	240892.58
84.0446	C ₄ H ₆ NO ⁺	Glutamic acids	2.0	360845.09	2.2	80797.67	1.8	303815.74
84.0810	C ₅ H ₁₀ N ⁺	Lysine	2.1	683779.2	2.1	187785.78	1.8	754508.03
96.0808	C ₆ H ₁₀ N ⁺	Lysine	0.5	35752.77	0.6	12291.68	0.4	31007.58

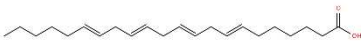
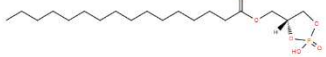
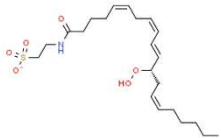
98.0965	C ₆ H ₁₂ N ⁺	Lysine	1.1	8394.46	0.1	2693.80	-0.3	7228.64
86.0601	C ₄ H ₈ NO ⁺	Hydroxyproline	1.6	5974.06	2.6	954.91	1.0	4416.48
118.0650	C ₈ H ₇ O ⁺	Phenylalanine	-0.2	504576.41	-0.3	151938.27	-0.7	458877.85
120.0807	C ₈ H ₁₀ N ⁺	Phenylalanine	-0.5	1989542.7	-0.5	599777.58	-0.9	2235680.19
121.0647	C ₈ H ₉ O ⁺	Phenylalanine	-0.7	8243.94	-0.4	2368.80	-0.9	7618.23
98.0237	C ₄ H ₄ NO ₂ ⁺	Asparagine	1.5	6988.88	0.0	1600.15	0.1	5574.41
100.0869	C ₄ H ₁₀ N ₃ ⁺	Arginine	0.3	8686.98	0.6	2413.67	0.1	9960.78
110.0712	C ₅ H ₈ N ₃ ⁺	Arginine	-0.5	1014232.03	-0.5	264559.98	-0.9	943230.8
112.0868	C ₅ H ₁₀ N ₃ ⁺	Arginine	-0.9	28856.67	-0.9	8970.61	-1.3	17015.06
127.0978	C ₅ H ₁₁ N ₄ ⁺	Arginine	-0.9	8731.00	-0.4	2034.00	-0.9	7716.00
107.0491	C ₇ H ₇ O ⁺	Threonine	-0.4	530421.32	-0.4	187460.56	-0.9	564306.94
117.0572	C ₈ H ₇ N ⁺	Tryptophan	-0.8	475079.27	-0.8	174457.23	-1.2	370176.13
120.0444	C ₇ H ₆ NO ⁺	Tryptophan	-0.3	31388.02	-0.4	13576.44	-0.7	31572.26
130.0651	C ₉ H ₈ N ⁺	Tryptophan	-0.3	2692601.54	-0.4	2692601.54	-0.7	2794719.52
132.0806	C ₉ H ₁₀ N ⁺	Tryptophan	-0.6	396541.56	-0.6	396541.56	-1.1	337720.8
157.0759	C ₁₀ H ₉ N ₂ ⁺	Tryptophan	-0.7	31002.22	-0.6	11047.56	-1.0	20794.57

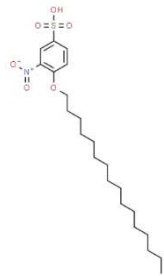
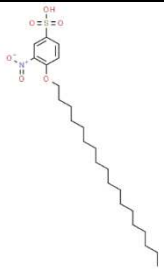
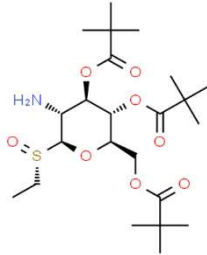
158.0836	C ₁₀ H ₁₀ N ₂ ⁺	Tryptophan	-1.0	15252.33	-0.3	4563.37	-1.1	12266.31
159.0916	C ₁₀ H ₁₁ N ₂ ⁺	Tryptophan	-0.7	156283.59	-0.7	39548.78	-1.1	148183.53
170.0599	C ₁₁ H ₈ NO ⁺	Tryptophan	-0.7	147148.99	-0.8	37508.96	-1.2	142721.79
131.0491	C ₉ H ₇ O ⁺	Tyrosine	-0.8	14207.59	-0.6	6063.81	-1.1	10037.3
136.0757	C ₈ H ₁₀ NO ⁺	Tyrosine	-0.3	307949.99	-0.3	71204.87	-0.7	292039.96
143.0729	C ₁₀ H ₉ N ⁺	Tyrosine	-0.5	156282.11	-0.5	65032.31	-0.9	143203.51
80.0497	C ₅ H ₆ N ⁺	Leucine	2.4	143515.88	2.4	50761.58	1.8	105975.73
89.0387	C ₇ H ₅ ⁺	Generic fragment	1.6	285219.17	1.6	128542.2	1.2	203516.01
91.0499	C ₇ H ₇ ⁺	Generic fragment	1.4	2867598.83	1.5	1089582.69	1.1	2445367.60
102.0464	C ₈ H ₆ ⁺	Generic fragment	0.2	257110.43	0.2	109913.98	-0.3	176507.47
103.0542	C ₈ H ₇ ⁺	Generic fragment	0.0	3401198.8	0.0	1289107.03	-0.4	2824757.5
105.0698	C ₈ H ₉ ⁺	Generic fragment	-0.3	143062.27	-0.4	54402.24	-0.7	92956.82
117.0572	C ₈ H ₈ N ⁺	Generic fragment	-0.9	291934.15	-0.9	107415.65	-1.3	252342.79
Negative								
81.0455	C ₄ H ₅ N ₂ ⁻	Generic	-3.7	13447.05	-4.3	6158.27	-4.5	5764.27
82.0295	C ₄ H ₄ NO ⁻	Multiple amino acids	-3.9	42953.75	-4.1	24967.88	-4	26289.81

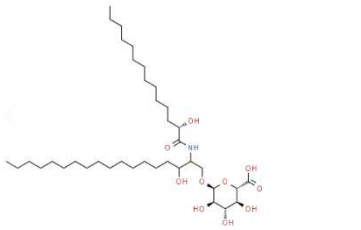
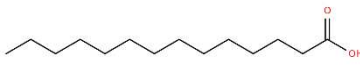
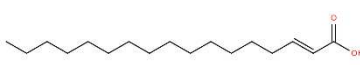
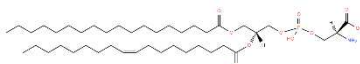
87.0086	C ₃ H ₃ O ₃ ⁻	Generic	-2.5	19349.63	-3	13630.85	-2.9	12496.62
93.0344	C ₆ H ₅ O ⁻	Multiple amino acids	-1.6	221874.12	-1.6	143277.52	-1.6	172089.69
93.0457	C ₅ H ₅ N ₂ ⁻	Multiple amino acids	-1.5	152901.43	-1.5	64905.94	-1.8	86316.64
97.0083	C ₈ H ⁻	Generic	-0.9	139922.84	-1	102640.84	-1.1	128993
98.0247	C ₄ H ₄ NO ₂ ⁻	Multiple amino acids	-0.8	156072.36	-0.6	30090.86	-1	39461.92
99.0087	C ₄ H ₃ O ₃ ⁻	Generic	-0.7	9056.85	-1.2	3475.35	-0.6	2379.78
99.0563	C ₄ H ₇ N ₂ O ⁻	Multiple amino acids	-0.4	15224.83	-0.6	6868.53	-0.4	9753.44
100.0404	C ₄ H ₆ NO ₂ ⁻	Multiple amino acids	-0.4	10370.05	-0.5	4504.56	-0.6	4189.82
108.0455	C ₆ H ₆ NO ⁻	Multiple amino acids	0.2	27212.24	0	19465.43	-0.1	20992.92
108.0567	C ₅ H ₆ N ₃ ⁻	Histidine	0.1	31897.4	0.1	11492.48	0	9320.24
110.0248	C ₅ H ₄ NO ₂ ⁻	Multiple amino acids	0	80874.52	-0.3	39262.47	-0.2	48553.79
112.0404	C ₅ H ₆ NO ₂ ⁻	Multiple amino acids	0	50993.13	0	20200.69	-0.1	17039.8
113.0357	C ₄ H ₅ N ₂ O ₂ ⁻	Generic	0.2	69892.94	0	29246.45	0.1	40773.6
116.0506	C ₈ H ₆ N ⁻	Multiple amino acids	-0.2	450076.59	-0.3	298477.35	-0.3	365321.71
118.0662	C ₈ H ₈ N ⁻	Multiple amino acids	0	59255.9	-0.3	41356.12	-0.3	49696.81
119.0502	C ₈ H ₇ O ⁻	Generic	-0.6	1244476.29	-0.6	549492.19	-0.7	621331

128.0353	C ₅ H ₆ NO ₃ ⁻	Multiple amino acids	-0.4	56823.82	-0.4	5812.54	-0.9	21709.08
134.0611	C ₈ H ₈ NO ⁻	Generic	-0.6	85468.4	-0.6	95478.63	-0.7	96558.98

Table A4.5. Show unique lipids signature for each phenotype; 7 unique for M1 and 4 unique for M2.

Mass m/z	Name	Formula	Structure	Information	Mass error p.p.m	Area (AU)
M1						
331.2659	Fatty acids FA (22:4)	C ₂₂ H ₃₅ O ₂		https://www.lipidmaps.org/databases/lmsd/LMFA04000050?LMID=L MFA04000050	-0.4	1367.55
391.2230	CPA(16:0) 1-hexadecanoyl-sn-glycero-2,3-cyclic-phosphate	C ₁₉ H ₃₆ O ₆ P		https://www.lipidmaps.org/databases/lmsd/LMGP00000057?LMID=L MGP00000057	0.3	1864.02
441.2198	ST 22:1;O3;S icosatetraenoyl]amino }ethanesulfonate	C ₂₂ H ₃₅ NO ₆ S		https://www.chemical-structure.58170237.html?rid=037a593e-79b6-4af1-	1.0	2408.43

				a59c-6390522403f6&page_num=0		
443.2328	ST 22:0;O3;S 4-(Hexadecyloxy)-3-nitrobenzenesulfonic acid	C ₂₂ H ₃₇ NO ₆ S		https://www.chemspider.com/Chemical-Structure.3350310.html?rid=130191b8-3c36-46d9-b3d4-296830171ba3&page_num=0	1.4	1886.76
471.2636	ST 24:0;O3;S 3-Nitro-4-(octadecyloxy)benzenesulfonic acid	C ₂₄ H ₄₁ NO ₆ S		https://www.chemspider.com/Chemical-Structure.4409329.html?rid=bfff8ff0-bfb2-4dce-a96c-3e3ae452f9b4&page_num=0	0.5	1474.87
490.2467	ST 21:0;O6;T (1S)-2-Amino-1,5-anhydro-2-deoxy-3,4,6-tris-O-(2,2-dimethylpropanoyl)-1-[(S)-ethylsulfinyl]-D-glucitol	C ₂₃ H ₄₀ NO ₈ S		https://www.chemspider.com/Chemical-Structure.9180690.html?rid=094670ed-8195-4a32-b287-aa54719e317d	0.9	2238.07

702.5152	HexCer 32:1;O4 Tetradecanamide	$C_{38}H_{72}NO_{10}$		https://www.chemspider.com/Chemical-Structure.8093797.html?rid=1d47af1c-9779-475d-b311-e2257580b65b&page_num=0	0.3	1225.62
M2						
227.2029	Fatty acid FA (14:0) Tetradecanoic acid	$C_{14}H_{27}O_2$		https://www.lipidmaps.org/database/lmsd/LMFA01010014?LMID=LMFA01010014	-0.3	11520.55
267.2324	Fatty acid FA (17:1) 2-heptadecylenic acid	$C_{42}H_{79}NO_{13}P$		https://www.lipidmaps.org/database/lmsd/LMFA01030059?LMID=LMFA01030059	0.8	3760.23
788.5419	PS (36:1) 1-octadecanoyl-2-(9Z-octadecenoyl)-sn-glycero-3-phosphoserine	$C_{42}H_{79}NO_{13}P$		https://www.lipidmaps.org/database/lmsd/LMGP03010025?LMID=LMGP03010025	-0.4	11220.87

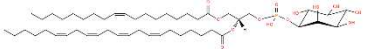
911.5749	PI (40:5) 1-(9Z-octadecenoyl)-2-(7Z,10Z,13Z,16Z-docosatetraenoyl)-glycero-3-phospho-(1'-myo-inositol)	$C_{49}H_{84}O_{13}P$		https://www.lipidmaps.org/databases/lmsd/LMGP06010307?LMID=L MGP06010307	0.1	1651.6
----------	---	-----------------------	---	---	-----	--------

Table A4.6. Metabolite M0, M1 and M2 macrophages search by human metabolome data base

Name	Mass m/z	Adduct	Structure	Human metabolome data base (ID)	M0 macrophage		M1 macrophage		M2 macrophage	
					Mass error p.p.m	Area (AU)	Mass error p.p.m	Area (AU)	Mass error p.p.m	Area (AU)
Pyridine	80.0496	[M+H]	C ₅ H ₆ N	HMDB 0000926	2.4	144905.32	2.4	51158.97	1.8	106529.3 7
Pyrimidine	81.0449	[M+H]	C ₄ H ₅ N ₂	HMDB0003361	2.4	431385.01	2.4	147450.11	2.0	396498.0 9
N-Nitroso- pyrrolidine	83.0605	[M+H-H ₂ O]	C ₄ H ₇ N ₂	HMDB0031642	2.2	907701.19	2.3	276877.39	1.9	787296.8 8
1Aminocyclopr opancarboxylic acid	84.0445	[M+H-H ₂ O]	C ₄ H ₆ NO	HMDB0036458	2.0	363612.61	2.2	81270.59	1.8	306227.1 5
Piperidine	86.0965	[M+H]	C ₅ H ₁₂ N	HMDB0034301	2.0	4294975.4 7	2.0	1035148.9 9	1.6	1425026. 04

Methcathinone	91.0543	[M+H+NH ₄]	C ₁₀ H ₁₃ NO	HMDB0041927	1.4	2888641.0 7	1.5	1099076.4 6	1.1	2469613
5-Bromopyrimidine	180.9374	[M+Na]	C ₄ H ₃ N ₂ Na Br	HMDB0062280	1.3	1340.51	3.6	0	0.9	3084.15
Alanylasparagine	204.0977	[M+H]	C ₇ H ₁₄ N ₃ O 4	HMDB0028682	-0.7	6796.17	-0.3	2872.9	6.0	0
SM(d18:1/16:0)	725.5558	[M+Na]	C ₃₉ H ₇₉ N ₂ O ₆ PNa	HMDB0010169	-1.3	3805.42	-1.0	1118.04	5.7	0

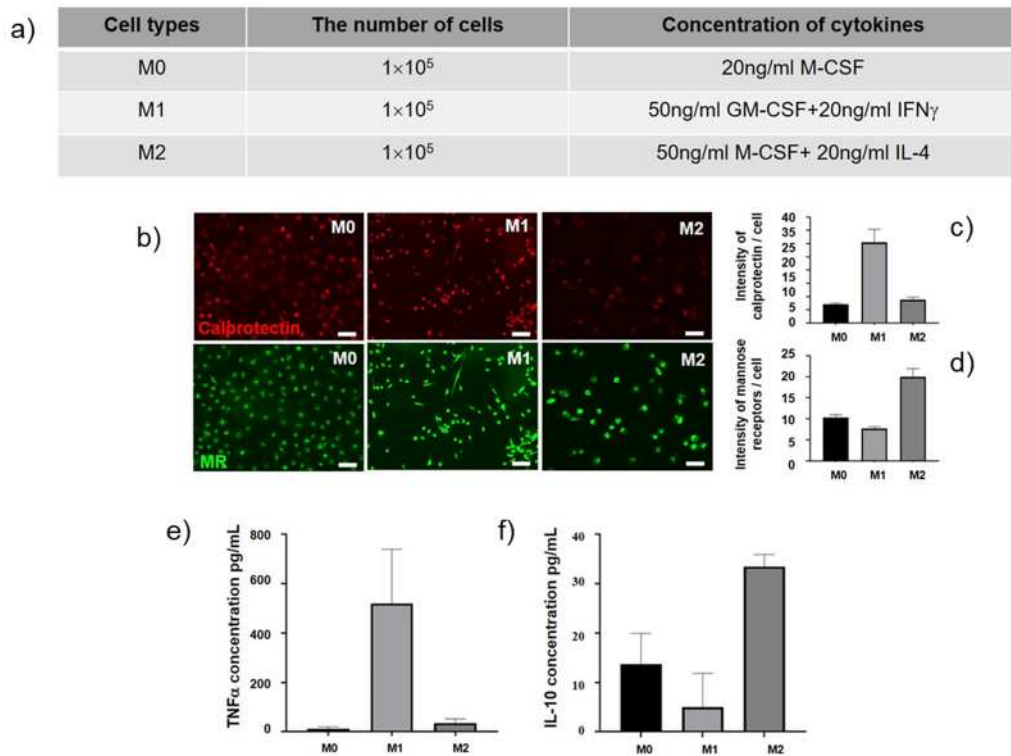


Figure A4.1. a) The concentration of the cytokines for M0, M1 and M2 macrophages activation. Fluorescent images of macrophages stained for calprotectin and mannose receptor. b) Calprotectin (red), and mannose receptor (green), images were taken under 20 x magnification and scale bar = 50 μ m. c) The intensity of calprotectin per cell in macrophage images. d) The intensity of mannose receptor per cell in macrophage images. Comparison of cytokines production by different macrophage subsets, supernatants of each macrophage subsets cultured for 6 days were measured by the enzyme-linked immunosorbent assay. e) TNF- α and f) IL-10; N=3. The intensity of cell on each slide was quantified using CellProfiler.

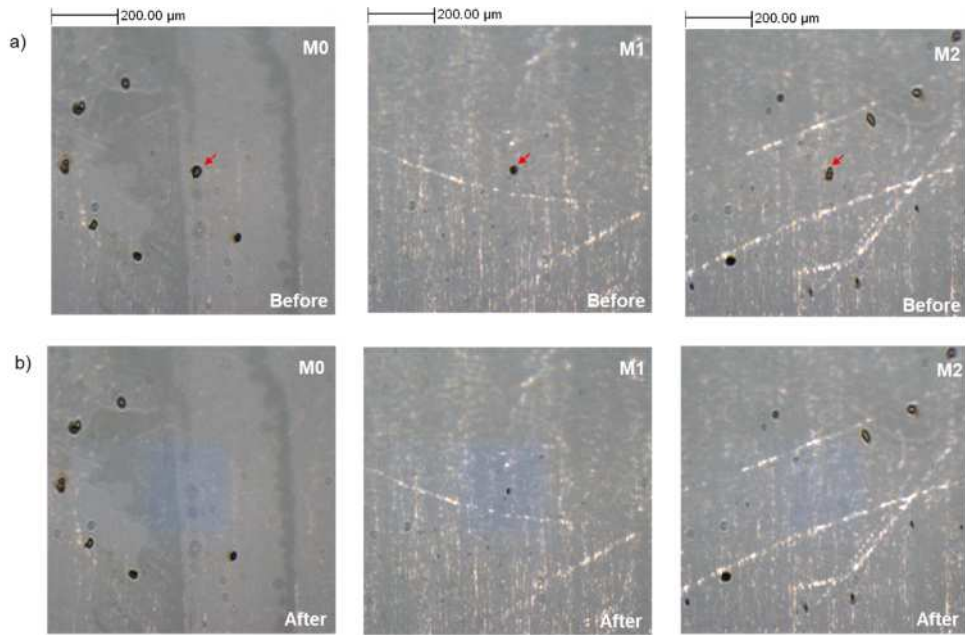


Figure A4.2. 3D OrbiSIMS MS image of the macrophage single cell a) before and b) after analysis. Images were taken over the area 500 x 500 μm and scale bar = 200 μm .

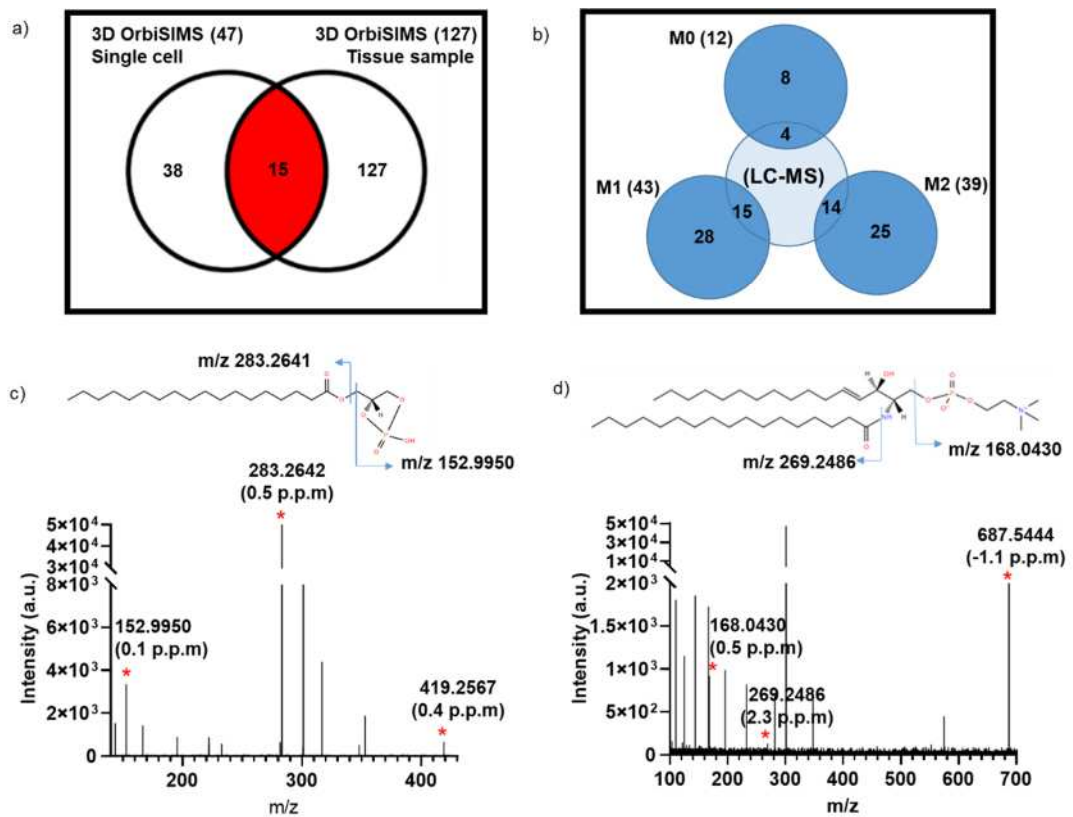


Figure A4.3. a) Venn diagram comparison of the number lipid compounds which detected in single cell macrophages subsets and tissue sample using 3D OrbiSIMS. b)

Comparison the number of lipids compounds in M0, M1 and M2 macrophages using 3D OrbiSIMS and macrophages using LC-MS. Abuawad et al identified, 212 lipids in THP-1 macrophages cell line extracts using LC-MS. The number of lipids were identified in macrophages polarisation using 3D OrbiSIMS, the lipids was mainly number of M0 macrophage (12), M1 macrophage (43) and M2 macrophage (39). Seventeen of lipids compound was the same species in 3D OrbiSIMS and LC-MS protocol. Negative ion mode 3D OrbiSIMS MS/MS spectrum of the precursor ion $[M-H]^-$ at m/z 419.2567, $[C_{21}H_{40}O_6P]^-$ recognized as CPA (18:0) c) and SM at m/z 687.5444, $[C_{38}H_{76}NO_4P]^-$ d)

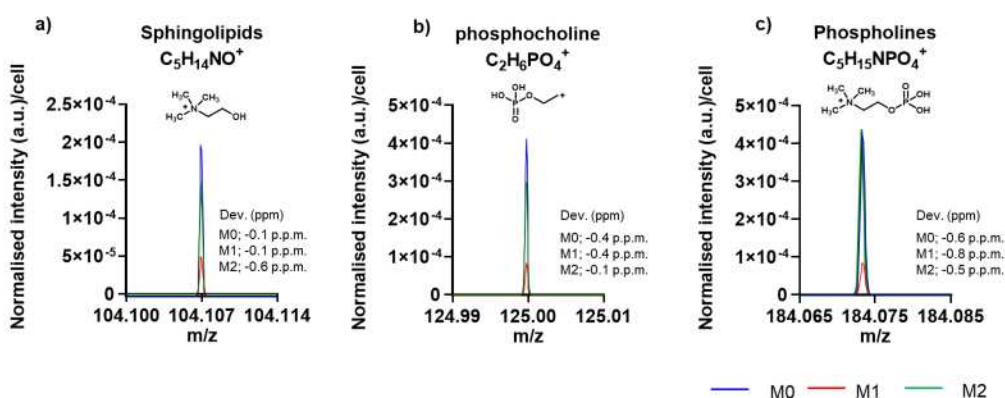


Figure A4.4. 3D OrbiSIMS of lipid class from a single cell macrophage. Normalised spectra of lipids in macrophage polarisation with comparison of each phenotypes in positive polarity. a) $C_5H_{14}NO^+$ (sphingolipids, SP, m/z 104.1070), b) $C_2H_6PO_4^+$ (phosphocholines, PC, m/z 124.9998) and c) $C_5H_{15}NPO_4^+$ (phosphocholines, PC, m/z 184.0739).

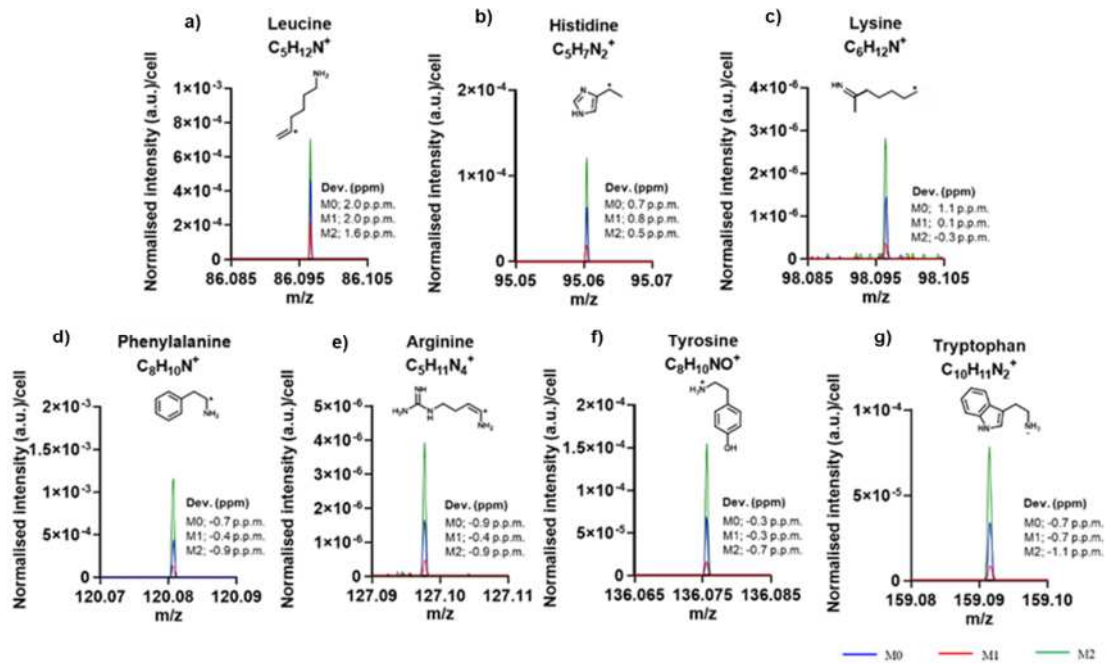


Figure A4.5. 3D OrbiSIMS spectrum of amino acids from a single cell macrophage. Normalised spectral of amino acids in macrophage polarisation with comparison of each phenotype in positive polarity a) leucine ($C_5H_{12}N^+$), b) histidine ($C_5H_7N_2^+$), c) lysine ($C_6H_{12}N^+$), d) phenylalanine ($C_8H_{10}N^+$), e) arginine ($C_5H_{11}N_4^+$), f) tyrosine ($C_8H_{10}NO^+$), g) tryptophan ($C_{10}H_{11}N_2^+$).

Positive polarity

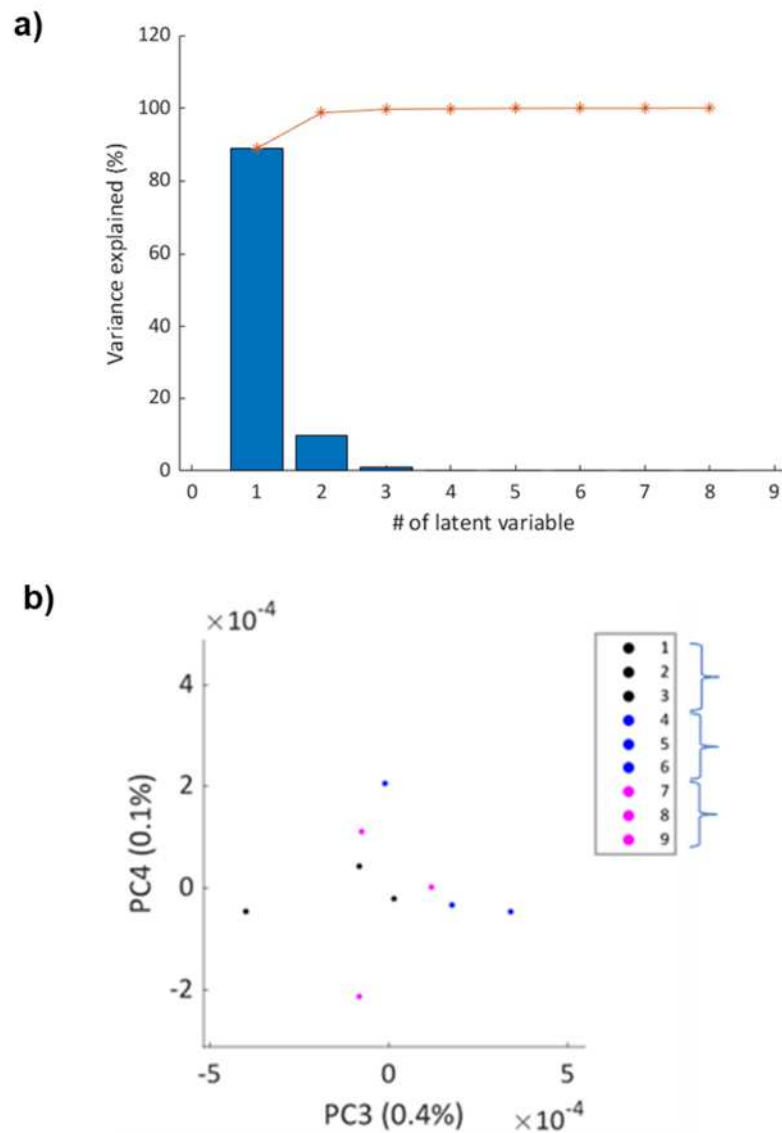


Figure A4.6. a) A bar chart showing the proportion of total data variance that is explained by the principal components of positive polarity 3D OrbiSIMS datasets. b) PC3 and PC4 scores.

Negative polarity

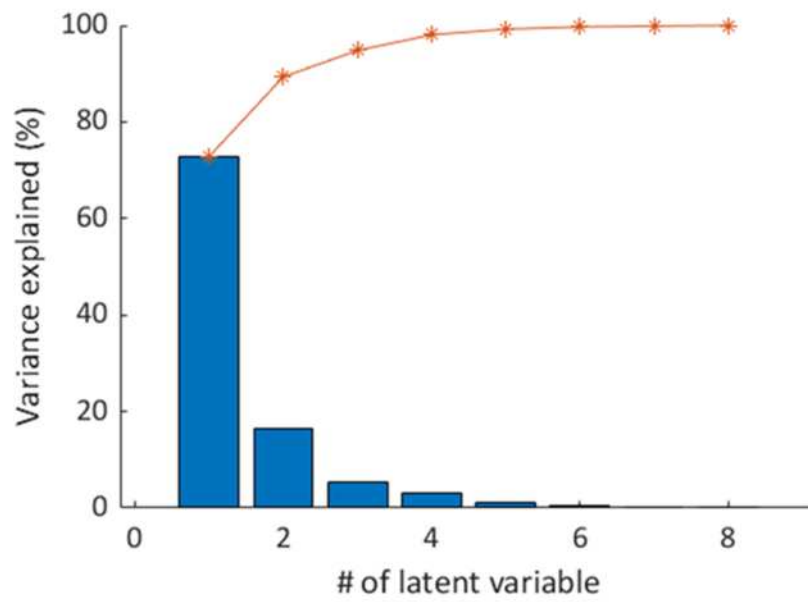


Figure A4.7. A bar chart showing the proportion of total data variance that is explained by the principal components of negative polarity 3D OrbiSIMS datasets.

Scores of PC1 and PC2

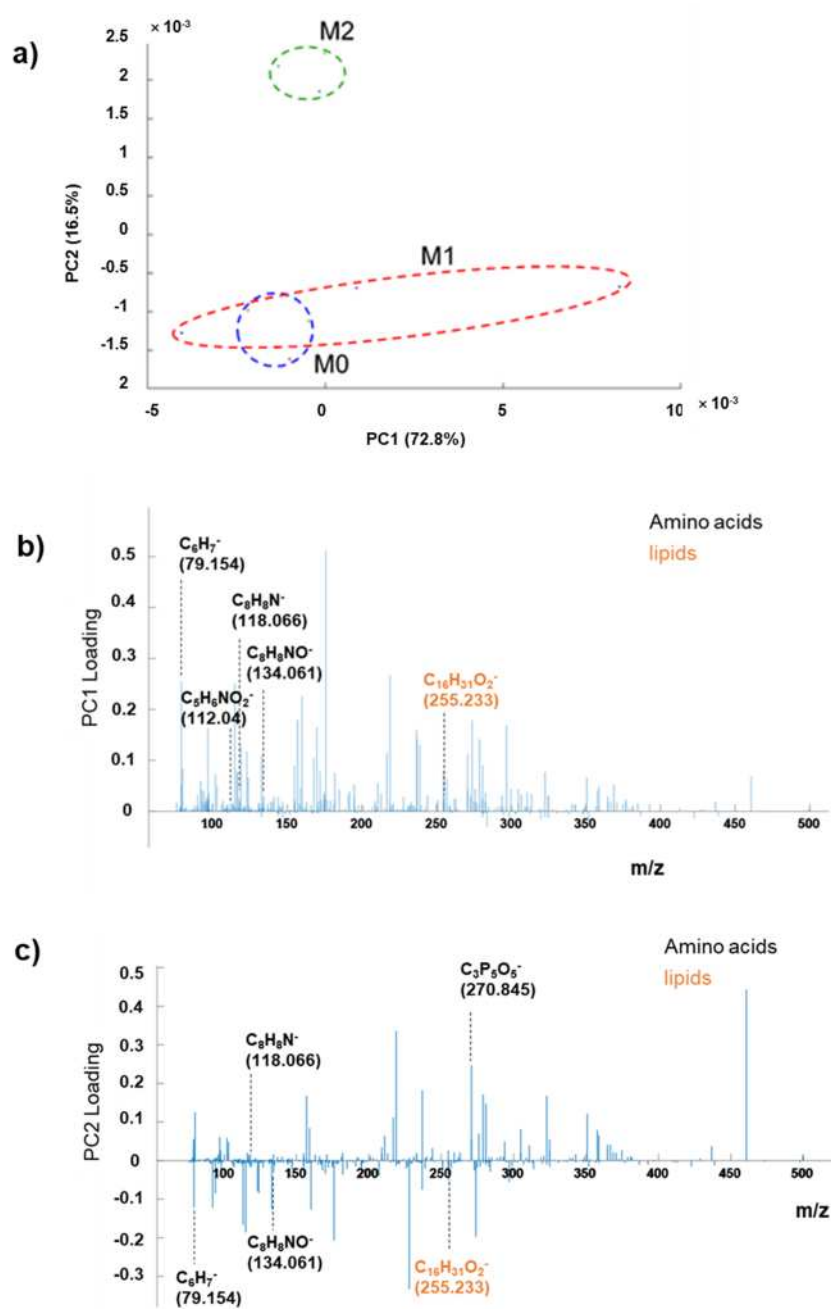


Figure A4.8. Principal component analysis on 3D OrbiSIMS negative polarity datasets. a) Scores of the first two principal components (PC). b) Loadings of PC1 and c) Loading of PC2. We attributed the $C_{16}H_{31}O_2^-$ as a larger lipid fragment due to its structural similarity to the larger lipid fragments, however we note it may also arise from fatty acids too.

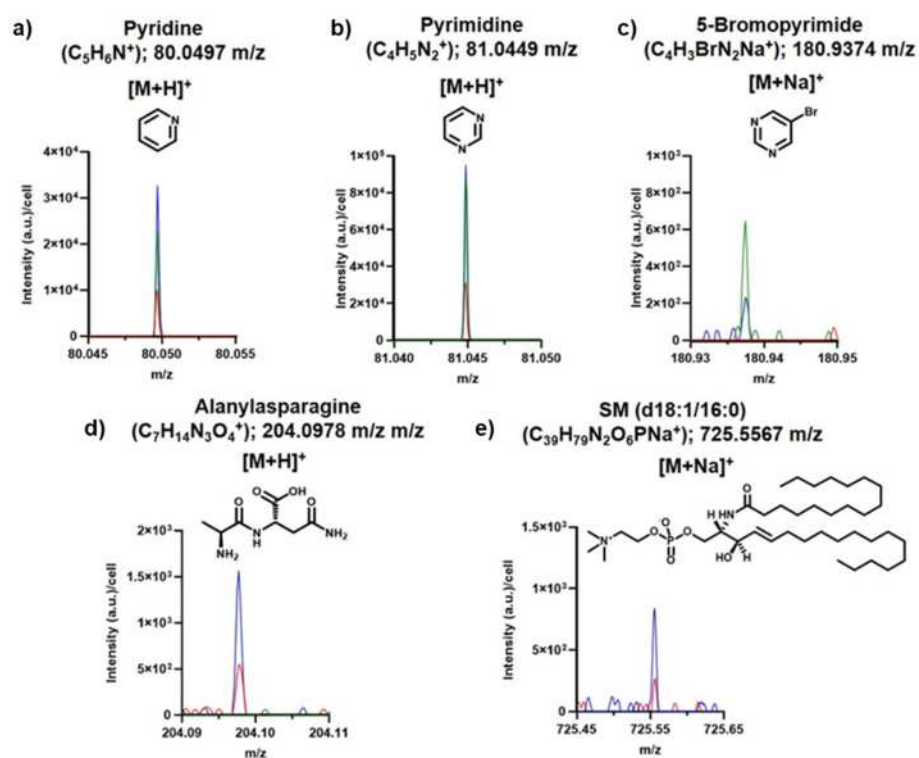


Figure A4.9. 3D OrbiSIMS spectrum of metabolite from a single cell macrophage each cell type in positive polarity. a) Pyridine $[M+H]^+$ at m/z 80.0497, b) Pyrimidine $[M+H]^+$ at m/z 81.0449, c) 5-bromopyrimidine $[M+Na]^+$ at m/z 180.9374, d) Alanylparagine $[M+H]^+$ at m/z 204.0978, e) SM(*d18:1/16:0*) $[M+Na]^+$ at m/z 725.5567.

Appendix 5:

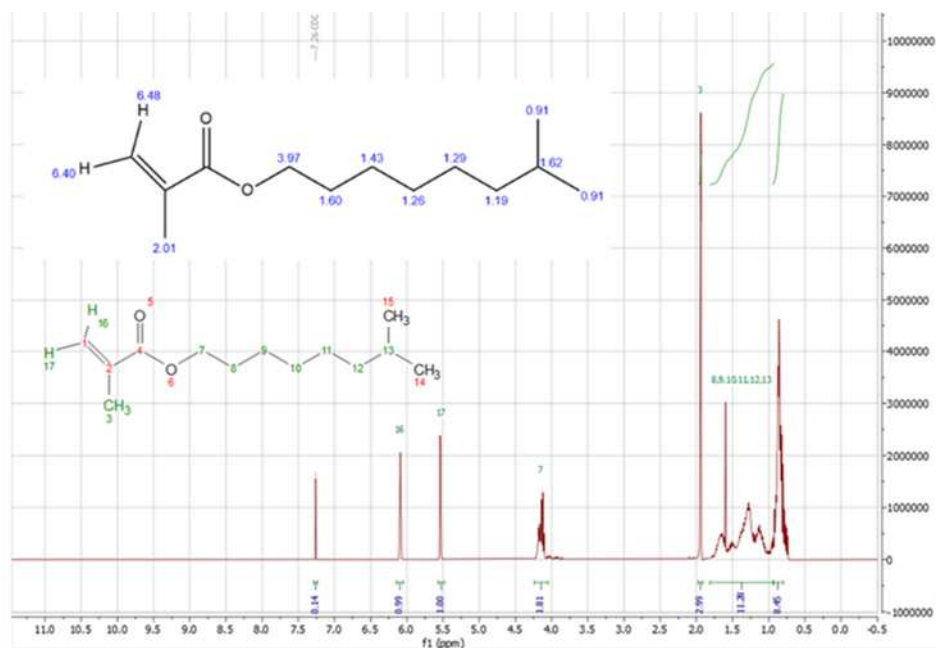


Figure A5.1. The NMR spectra of iDMA monomer.

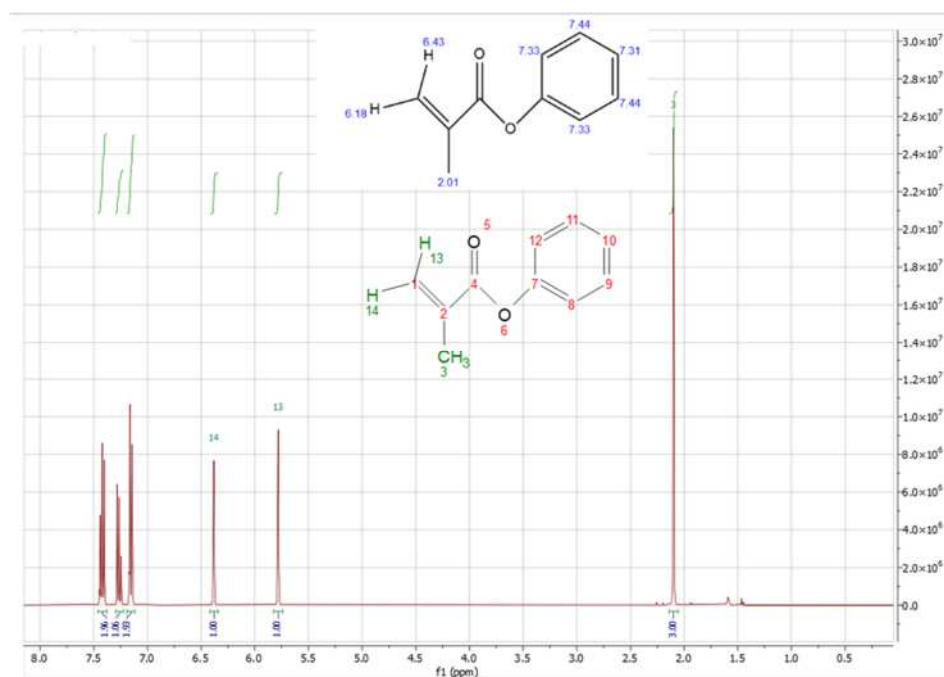


Figure A5.2. The NMR spectra of PhMA monomer.

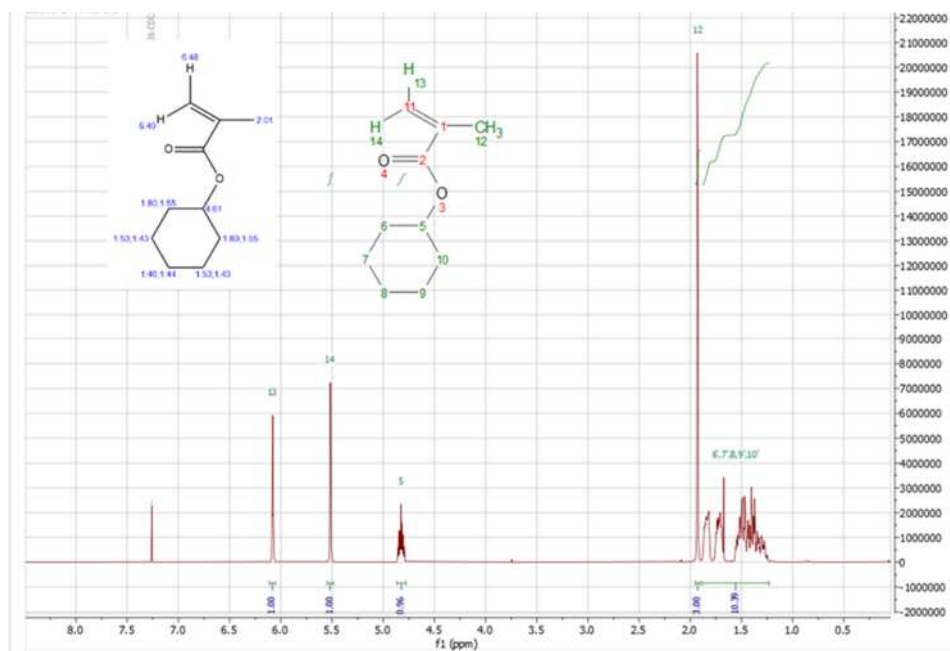


Figure A5.3. The NMR spectra of CHMA monomer

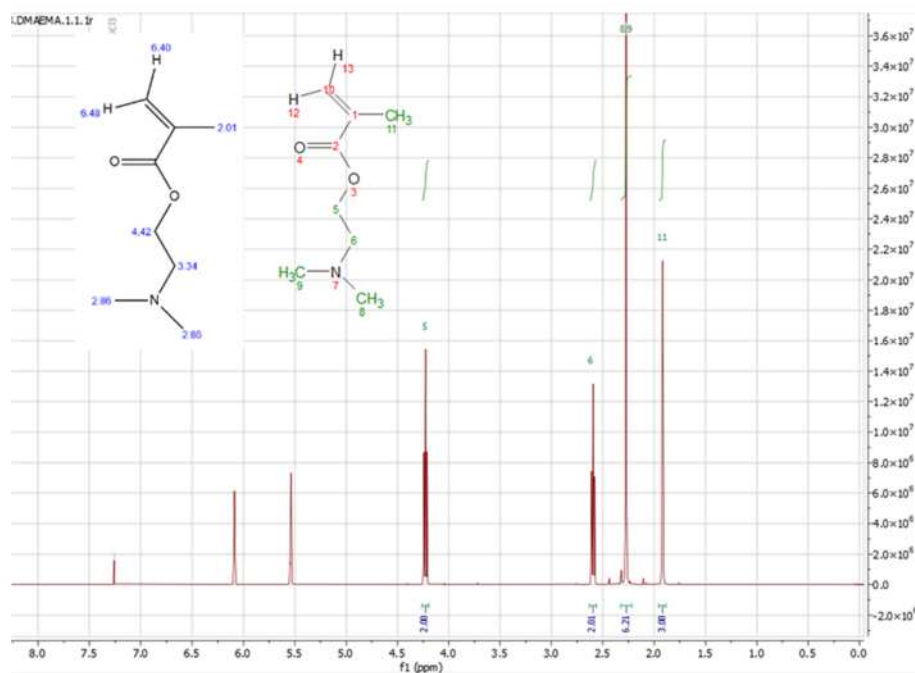


Figure A5.4. The NMR spectra of DMAEMA monomer.

Sample Information

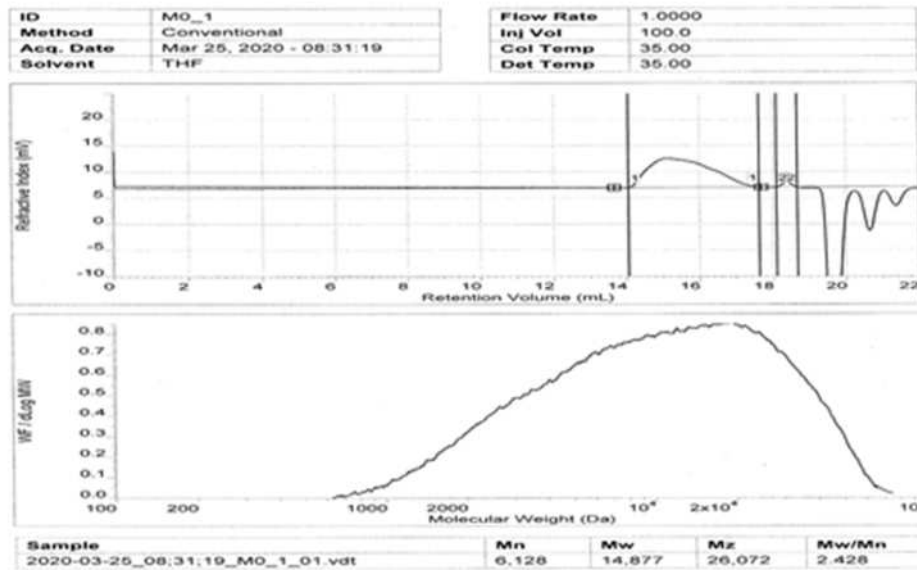


Figure A5.5. GPC result of copolymer EGDMA-co-HDFDMA

Sample Information

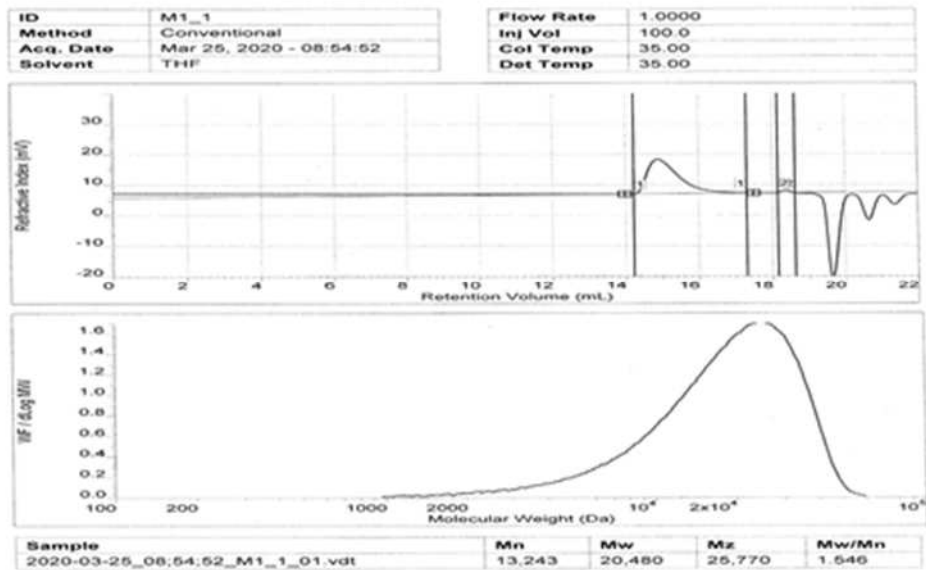


Figure A5.6. GPC result of copolymer CHMA-co-DMAEMA

Sample Information

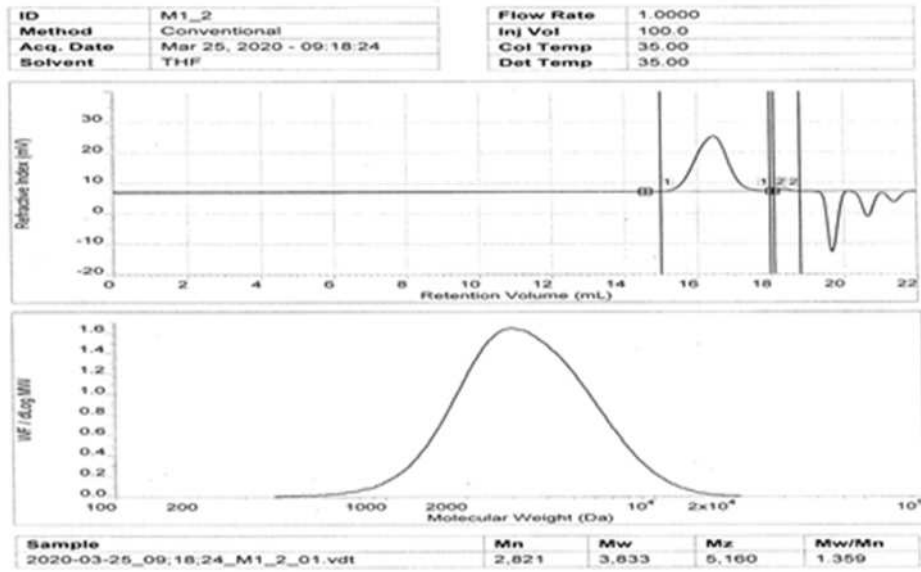


Figure A5.7. GPC result of copolymer tBCHMA

Sample Information

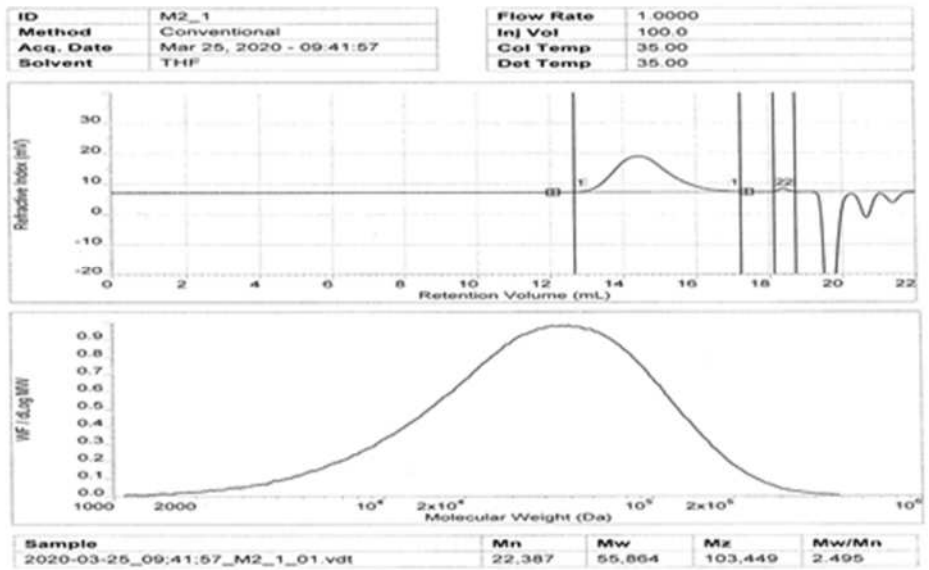


Figure A5.8. GPC result of copolymer CHMA-co-iDMA

Sample Information

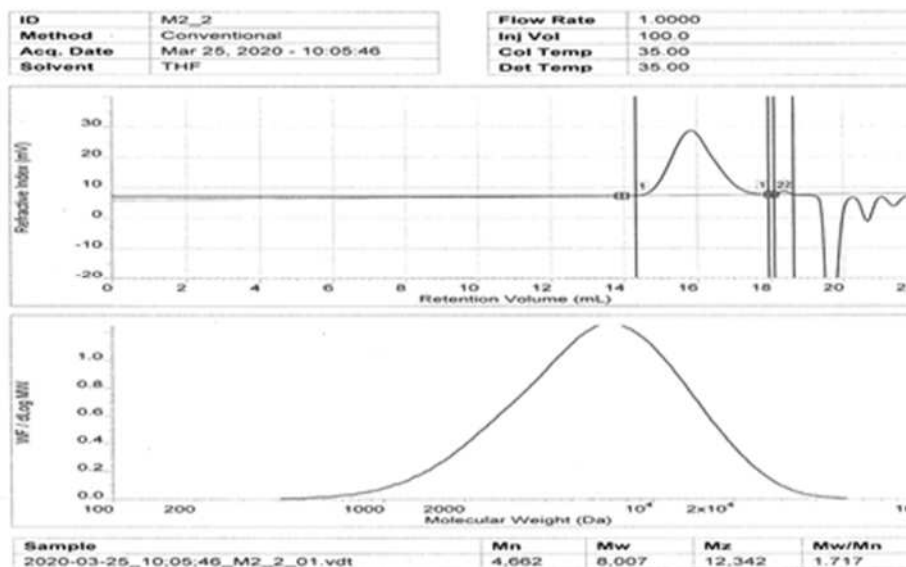


Figure A5.9. GPC result of copolymer PhMA-co-iDMA

Appendix6:

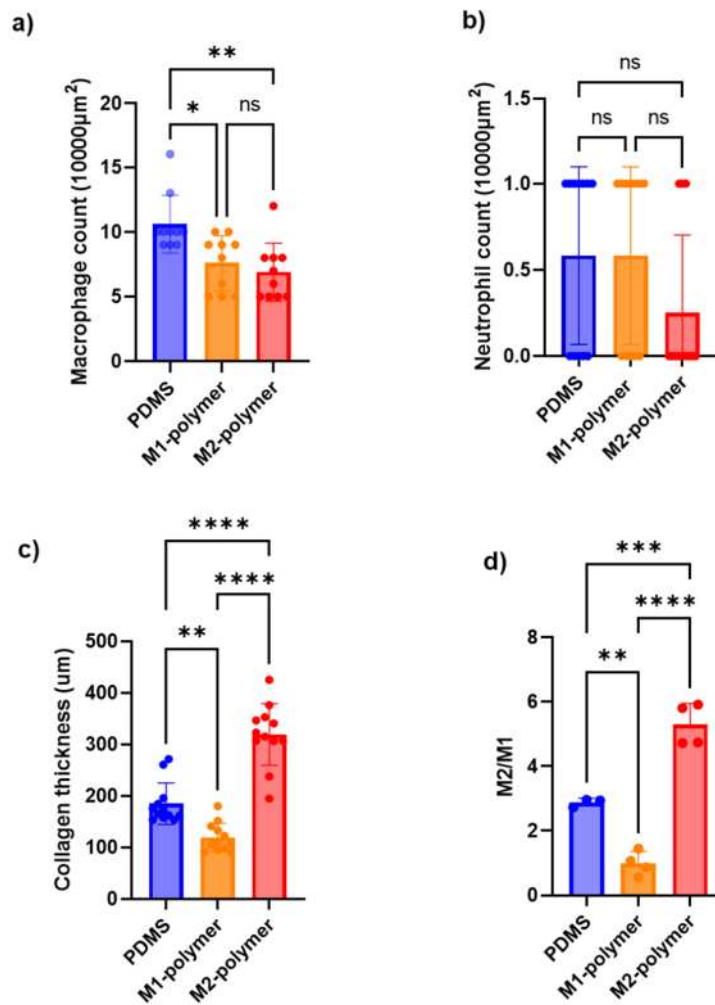
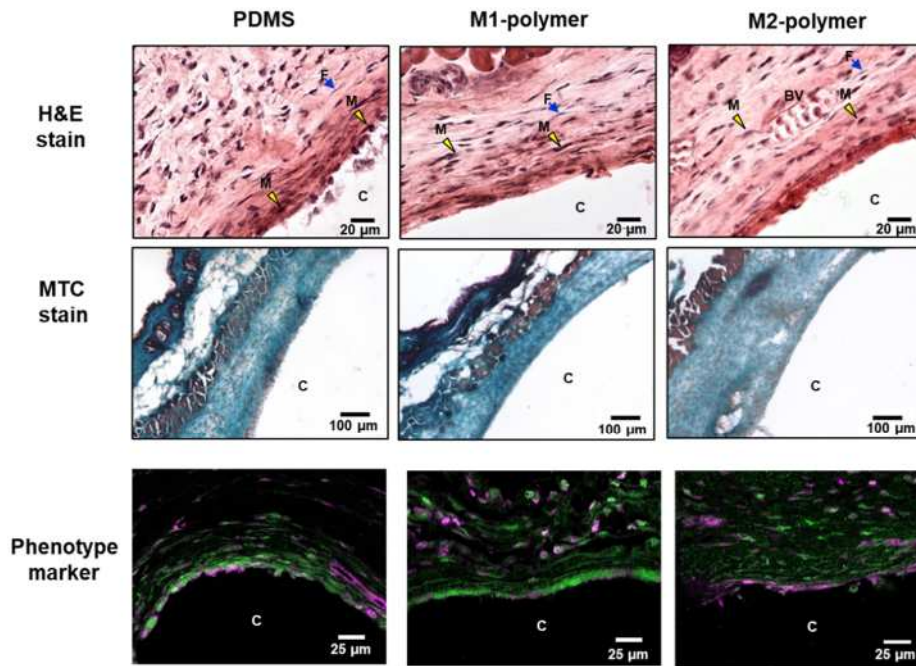


Figure A6.1. *Histological analysis of tissue sections following 28 days implantation of polymer coated catheter sections in a murine model of foreign body response. Representative H&E staining images, showing a well-defined inflammatory reaction fibroblast (F), blood vessels (BV), macrophage (M) and catheter (C) captured at $\times 40$ magnification the scale bar = $20\ \mu\text{m}$. MTC staining image of each tissue section slide for identifying collagen thickness, captured at $\times 10$ magnification. Scale bar = $100\ \mu\text{m}$. (a-c) show the infiltration count of macrophages, neutrophils and collagen thickness from the site surrounding the foreign body. All data are presented as the mean with \pm s.d ($N=2$, $n=3$). Significance was calculated by one-way ANOVA with Tukey's post-hoc analysis: * $p<0.05$, ** $p<0.01$, *** $p<0.001$. d). Representative, phenotype marker images show tissue section stained for the M1 marker iNOS in green and M2 marker arginase1 in magenta and C represents the catheter site. (Images were acquired on confocal). Scale bar = $25\ \mu\text{m}$. d) The ratio of M2-like macrophages to M1-like macrophages for each polymer. All data are presented as the mean with \pm s.d ($N = 2$ and $n = 5$). Significance was calculated by one-way ANOVA with Tukey's post-hoc analysis: *** <0.0001*

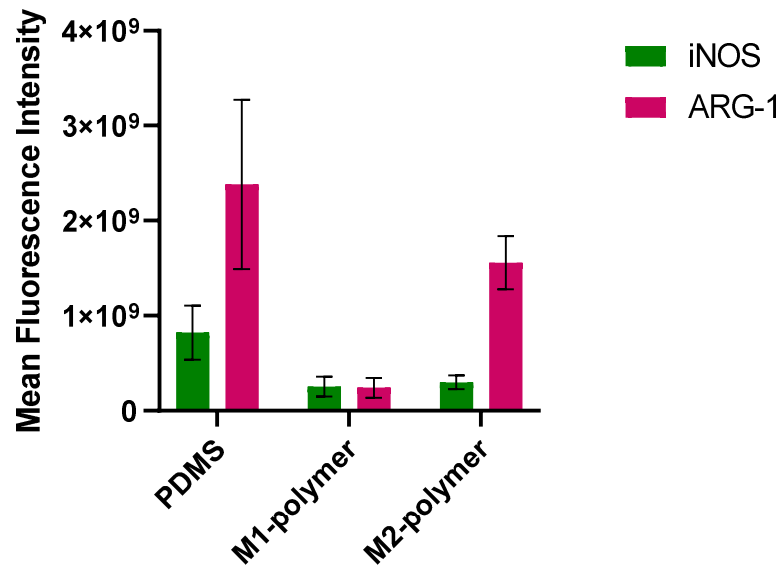


Figure A6.2. The mean fluorescence intensity of iNOS and ARG-1 expression in tissue images. M2-polymer shown high level of the Arg-1 expression.

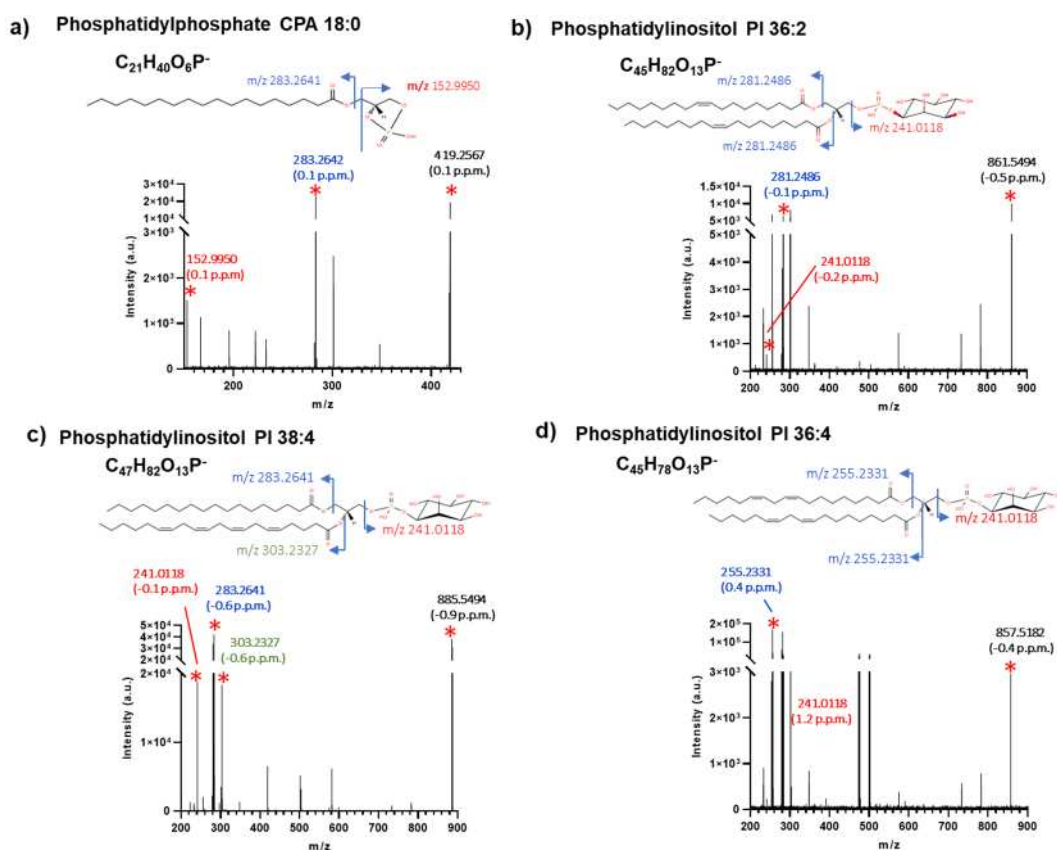


Figure A6.3. MS/MS product spectrum of lipids $[M-H]^-$. a) The structure of CPA (18:0) at m/z 419.2517 was confirmed based on the detection of the PA head-group ions, $[C_6H_{10}PO_8]^-$ at m/z 241.0, and fatty acid moieties from these lipids are F18:0, $[C_{18}H_{35}O_2]^-$ at m/z 283.2642. b) The precursor PI (36:2) ion is the signature fragments of PI headgroup, $[C_6H_{10}PO_8]^-$ and two FA18:1 fatty acid moieties are represented by $[C_{18}H_{33}O_2]^-$. and other MS/MS of PI (38:4) and (36:4) lipids are reported in Figure c and d).

Table A6.1. Chemical structure of the monomers and synthesis of copolymers, CHMA-co-DMAEMA and CHMA-co-iDMA.

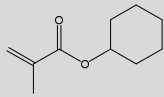
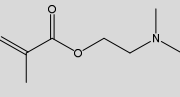
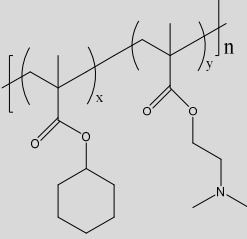
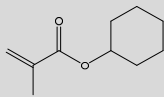
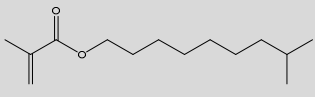
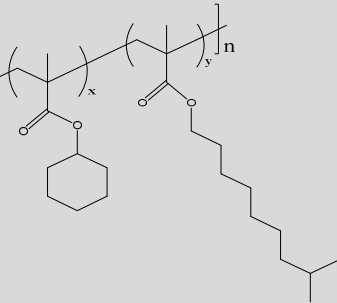
Code	Monomer 1 name/structure (66%)	Monomer 2 name/structure (33%)	Copolymers
M1-like	 Cyclohexyl methacrylate (CHMA)	 Dimethylamino- ethylmethacrylate (DMAEMA)	 CHMA-co-DMAEMA
M2-like	 Cyclohexyl methacrylate (CHMA)	 Isodecyl methacrylate (iDMA)	 CHMA-co-iDMA

Table A6.2 Hematoxylin and Eosin (H&E) staining schedule

1.	Water rinse to remove OCT	5 min
2.	Haematoxylin solution	5 min
3.	Water rinse	1 min
4.	1 % acetic acid in alcohol	30 s
5.	Water rinse	1 min
6.	Alkine Scott's	1 min
7.	Water rinse	1 min
8.	Eosin	2 min
9.	Water rinse	1 min
10.	50 % alcohol	30 s
11.	70 % alcohol	30 s
12.	90 % alcohol	30 s
13.	100 % alcohol × 2	30 s each
14.	Xylene × 2	2 min each
15.	Mounting media onto tissue slide and covered with a thin coverslip	

Table A6.3. Masson Trichrome Stain Kit (Light Green) Masson 1929 schedule.

1.	Fixing, 4 %PFA	1 h
2.	Water rinse	5 min
3.	Haematoxyling, mixing equal volumes of Weigerts solution A & B (1:1) as required	20 min
4.	Water rinse	1 min
5.	1 % acetic acid in alcohol	30 s
6.	Water rinse	1 min
7.	Ponceau fuchsin Masson solution for	5 min
8.	Rinse in distilled water	2 min
9.	The light green solution	3 min
10.	Water rinse	30 s
11.	50 % alcohol	30 s
12.	70 % alcohol	30 s
13.	90 % alcohol	30 s
14.	100 % alcohol × 2	30 s each
15.	Xylene × 2	2 min each
16.	Mounting media onto tissue slide and covered with a thin coverslip	

Table A6.4. Sequential antibody staining for macrophage marker schedule.

1.	Washing in 0.2% Tween 20 in PBS × 3	5 min
2.	0.1% Triton X-100 in PBS	10 min
3.	Washing in 0.2% Tween 20 in PBS × 3	5 min
4.	5% BSA and plus 5% donkey serum in PBS	1 h
5.	0.2% PBS-Tween 20 rinse × 3	5 min
6.	Add diluted primary antibody with 1:50 of rabbit anti-mouse iNOS (Abcam) and 1:50 of goat anti-mouse Arg-1 (Thermo Fisher Scientific) in 5% goat serum at 4°C	Overnight
7.	Washing in 0.2% Tween 20 in PBS × 3	5 min
8.	Add diluted secondary antibodies, donkey anti-goat IgG (H + L), and donkey anti-rabbit IgG (H + L) labeled with Alexa Fluor-594 and -488 (1:200; A11058 and A21206, Thermo Fisher Scientific),	1 h
9.	Washing in 0.2% Tween 20 in PBS × 3	5 min
10.	4',6 Diamidino-2-Phenylindole (DAPI, 20000 ng/ml)	5 min
11.	Washing in 0.2% Tween 20 in PBS × 2	5 min
12.	Final, washing in distilled water	5 min
13.	Mounting media onto tissue slide and covered with a thin coverslip	

Table A6.5. Glycerolipid fragments in 3D OrbiSIMS at surrounding implants in each sample. PDMS, M1-polymer and M2-polymer. Monoglycerides (MG), diglycerides (DG)

Mass m/z	Assignment	Glycerolipid	Average normalises Intensity (4 areas)	Average p.p.m (4 areas)
PDMS				
551.504	C ₃₅ H ₆₇ O ₄ ⁺	MG 32:2	1.18×10 ⁻²	1
575.5038	C ₃₇ H ₆₇ O ₄ ⁺	MG 34:4	5.79×10 ⁻²	0.6
577.5193	C ₃₇ H ₆₉ O ₄ ⁺	MG 34:3	3.92×10 ⁻²	0.4
601.5195	C ₃₉ H ₆₉ O ₄ ⁺	DG 0-36:5	4.94×10 ⁻²	0.6
M1-polymer				
551.504	C ₃₅ H ₆₇ O ₄ ⁺	MG 32:2	1.42×10 ⁻²	0.9
575.5038	C ₃₇ H ₆₇ O ₄ ⁺	MG 34:4	6.53×10 ⁻²	0.8
577.5193	C ₃₇ H ₆₉ O ₄ ⁺	MG 34:3	4.53×10 ⁻²	0.7
601.5195	C ₃₉ H ₆₉ O ₄ ⁺	DG 0-36:5	5.35×10 ⁻²	0.8
M2-polymer				
551.504	C ₃₅ H ₆₇ O ₄ ⁺	MG 32:2	7.50×10 ⁻³	0.6
575.5038	C ₃₇ H ₆₇ O ₄ ⁺	MG 34:4	3.83×10 ⁻²	0.3
577.5193	C ₃₇ H ₆₉ O ₄ ⁺	MG 34:3	2.93×10 ⁻²	0.1
601.5195	C ₃₉ H ₆₉ O ₄ ⁺	DG 0-36:5	3.75×10 ⁻²	0.3

Table A6.6. Show unique lipids signature for each phenotype; 8 unique for PDMS, 16 unique for M1-polymer and 4 unique for M2-polymer.

Mass <i>m/z</i>	Formula [M-H] ⁻	Name
PDMS		
467.2567	C ₂₅ H ₄₁ O ₆ P ⁻	LPA O-22:6
476.2784	C ₂₃ H ₄₄ NO ₇ P ⁻	LPA 15:2
655.4709	C ₃₇ H ₆₉ O ₇ P ⁻	LPA 34:3
679.4712	C ₃₉ H ₆₉ O ₇ P ⁻	PA O-36:5
681.4867	C ₃₉ H ₇₁ O ₇ P ⁻	PA O-36:4
719.4662	C ₄₁ H ₆₉ O ₈ P ⁻	PA 38:6
738.5083	C ₄₁ H ₇₄ NO ₈ P ⁻	PE 36:4
745.4819	C ₄₃ H ₇₁ O ₈ P ⁻	PA 40:7
M2-polymer		
795.5743	C ₄₅ H ₈₅ NO ₈ P ⁻	LPI O-33:0
795.6271	C ₄₇ H ₈₉ O ₇ P ⁻	PA O-44:3
836.5446	C ₄₆ H ₈₀ NO ₁₀ P ⁻	PS O-40:6;O
859.534	C ₄₅ H ₈₁ O ₁₃ P ⁻	PI O-36:4;O
M1-polymer		
421.2728	C ₂₁ H ₄₃ O ₆ P ⁻	LPA O-18:1
475.3195	C ₂₅ H ₄₉ O ₆ P ⁻	LPA O-22:2
537.32	C ₂₆ H ₅₁ O ₉ P ⁻	LPG 20:1
571.2891	C ₂₅ H ₄₉ O ₁₂ P ⁻	LPI 16:0
577.2787	C ₂₇ H ₄₇ O ₁₁ P ⁻	LPI O-18:4
585.3048	C ₂₆ H ₅₁ O ₁₂ P ⁻	PG 21:0;O
670.5186	C ₃₈ H ₇₄ NO ₆ P ⁻	LPC O-30:3
729.5445	C ₄₁ H ₇₉ O ₈ P ⁻	PA 38:1
730.5395	C ₄₀ H ₇₈ NO ₈ P ⁻	PE 35:1
736.5294	C ₄₂ H ₇₆ NO ₇ P ⁻	LPC 34:5
747.5172	C ₄₀ H ₇₇ O ₁₀ P ⁻	PG 34:1
758.4981	C ₄₀ H ₇₄ NO ₁₀ P ⁻	PS 34:2

773.533	$C_{42}H_{79}O_{10}P^-$	PG 36:2
791.5433	$C_{42}H_{81}O_{11}P^-$	LPI O-33:2
793.559	$C_{42}H_{83}O_{11}P^-$	LPI O-33:1
833.5917	$C_{45}H_{87}O_{11}P^-$	PG 39:1;O
837.5489	$C_{43}H_{83}O_{13}P^-$	PI 34:0
839.5643	$C_{43}H_{85}O_{13}P^-$	LPI 34:0;O
868.608	$C_{48}H_{88}NO_{10}P^-$	PS 42:3

Table A6.7. Targeted phospholipid analysis in 3D OrbiSIMS spectra.

Mass m/z	Assignment [M-H] ⁻	Phospholipids	Area1		Area 2		Area 3		Area4	
			Mass error p.p.m	Norm. intensity	Mass error p.p.m	Norm. intensity	Mass error p.p.m	Norm. intensity	Mass error p.p.m	Norm. intensity
PDMS										
673.4821	C ₃₇ H ₇₁ O ₈ P	PA 34:1	0.3	1.54×10 ⁻⁴	-0.1	5.52×10 ⁻⁵	0.8	5.66×10 ⁻⁰⁵	1.0	5.79×10 ⁻⁰⁵
747.498	C ₄₃ H ₇₃ O ₈ P	PA 40:6	0.7	4.57×10 ⁻⁴	0.3	7.92×10 ⁻⁵	1.2	9.79×10 ⁻⁰⁵	0.8	1.10×10 ⁻⁰⁴
751.5291	C ₄₃ H ₇₇ O ₈ P	PA 40:4	0.3	2.57×10 ⁻⁴	0	4.07×10 ⁻⁵	0.9	5.80×10 ⁻⁰⁵	0.7	7.03×10 ⁻⁰⁵
786.5294	C ₄₂ H ₇₈ NO ₁₀ P	PS 36:2	0.4	5.42×10 ⁻⁴	-0.2	1.18×10 ⁻⁴	0.9	1.40×10 ⁻⁰⁴	0.8	1.65×10 ⁻⁰⁴
788.5451	C ₄₂ H ₈₀ NO ₁₀ P	PS 36:1	0.5	6.03×10 ⁻⁴	-0.1	1.37×10 ⁻⁴	1.3	1.55×10 ⁻⁰⁴	1.0	1.69×10 ⁻⁰⁴
838.5609	C ₄₆ H ₈₂ NO ₁₀ P	PS 40:4	0.6	3.10×10 ⁻⁴	0.2	5.82×10 ⁻⁵	1.2	7.27×10 ⁻⁰⁵	1.0	8.50×10 ⁻⁰⁵
764.5244	C ₄₃ H ₇₆ NO ₈ P	PE 38:5	0.4	2.47×10 ⁻⁴	0	4.27×10 ⁻⁵	1.1	5.37×10 ⁻⁰⁵	0.8	5.98×10 ⁻⁰⁵
766.5401	C ₄₃ H ₇₈ NO ₈ P	PE 38:4	0.4	8.32×10 ⁻⁴	0.1	1.81×10 ⁻⁴	1.1	2.31×10 ⁻⁰⁴	0.7	2.49×10 ⁻⁰⁴
790.5402	C ₄₅ H ₇₈ NO ₈ P	PE 40:6	0.4	4.20×10 ⁻⁴	0	7.67×10 ⁻⁵	0.9	8.64×10 ⁻⁰⁵	0.7	9.93×10 ⁻⁰⁵
857.5196	C ₄₅ H ₇₉ O ₁₃ P	PI 36:4	0.5	0.87×10 ⁻⁴	0.2	1.79×10 ⁻⁴	1.2	2.28×10 ⁻⁰⁴	1.0	2.66×10 ⁻⁰⁴
861.5511	C ₄₅ H ₈₃ O ₁₃ P	PI 36:2	0.5	1.10×10 ⁻³	0.3	2.11×10 ⁻⁴	1.3	2.37×10 ⁻⁰⁴	1.0	2.87×10 ⁻⁰⁴
885.5508	C ₄₇ H ₈₃ O ₁₃ P	PI 38:4	0.3	8.80×10 ⁻³	0.2	1.54×10 ⁻³	1.1	1.89×10 ⁻⁰³	0.9	2.04×10 ⁻⁰³

M1-polymer										
673.4821	C ₃₇ H ₇₁ O ₈ P	PA 34:1	0.7	8.89×10 ⁻⁰⁵	0.3	2.82×10 ⁻⁰⁵	0.7	5.38×10 ⁻⁰⁵	0.6	5.68×10 ⁻⁰⁵
747.498	C ₄₃ H ₇₃ O ₈ P	PA 40:6	0.9	9.41×10 ⁻⁰⁵	0.9	3.33×10 ⁻⁰⁵	1.0	5.92×10 ⁻⁰⁵	1.1	6.99×10 ⁻⁰⁵
751.5291	C ₄₃ H ₇₇ O ₈ P	PA 40:4	0.7	1.23×10 ⁻⁰⁴	0.6	4.20×10 ⁻⁰⁵	0.6	6.79×10 ⁻⁰⁵	0.8	7.18×10 ⁻⁰⁵
786.5294	C ₄₂ H ₇₈ NO ₁₀ P	PS 36:2	0.7	3.88×10 ⁻⁰⁴	0.6	1.68×10 ⁻⁰⁴	0.9	2.59×10 ⁻⁰⁴	0.8	2.88×10 ⁻⁰⁴
788.5451	C ₄₂ H ₈₀ NO ₁₀ P	PS 36:1	0.7	4.45×10 ⁻⁰⁴	0.8	1.87×10 ⁻⁰⁴	1.0	2.91×10 ⁻⁰⁴	0.9	3.26×10 ⁻⁰⁴
838.5609	C ₄₆ H ₈₂ NO ₁₀ P	PS 40:4	1.0	1.55×10 ⁻⁰⁴	1.0	6.06×10 ⁻⁰⁵	1.1	9.17×10 ⁻⁰⁵	1.1	1.05×10 ⁻⁰⁴
764.5244	C ₄₃ H ₇₆ NO ₈ P	PE 38:5	0.6	1.64×10 ⁻⁰⁴	0.7	7.38×10 ⁻⁰⁵	0.9	1.26×10 ⁻⁰⁴	0.8	1.47×10 ⁻⁰⁴
766.5401	C ₄₃ H ₇₈ NO ₈ P	PE 38:4	0.6	4.80×10 ⁻⁰⁴	0.6	2.41×10 ⁻⁰⁴	0.9	3.54×10 ⁻⁰⁴	0.8	4.04×10 ⁻⁰⁴
790.5402	C ₄₅ H ₇₈ NO ₈ P	PE 40:6	0.5	1.64×10 ⁻⁰⁴	0.7	7.06×10 ⁻⁰⁵	0.7	1.07×10 ⁻⁰⁴	0.7	1.22×10 ⁻⁰⁴
857.5196	C ₄₅ H ₇₉ O ₁₃ P	PI 36:4	0.8	5.39×10 ⁻⁰⁴	0.7	2.49×10 ⁻⁰⁴	1.0	3.66×10 ⁻⁰⁴	1.1	4.02×10 ⁻⁰⁴
861.5511	C ₄₅ H ₈₃ O ₁₃ P	PI 36:2	0.8	7.32×10 ⁻⁰⁴	0.9	3.43×10 ⁻⁰⁴	1.0	5.06×10 ⁻⁰⁴	1.0	5.52×10 ⁻⁰⁴
885.5508	C ₄₇ H ₈₃ O ₁₃ P	PI 38:4	0.5	4.77×10 ⁻⁰³	0.6	2.11×10 ⁻⁰³	0.7	3.18×10 ⁻⁰³	0.7	3.42×10 ⁻⁰³
M2-polymer										
673.4821	C ₃₇ H ₇₁ O ₈ P	PA 34:1	0.2	5.44×10 ⁻⁰⁵	0.2	8.07×10 ⁻⁰⁵	0	8.54×10 ⁻⁰⁵	0.3	9.54×10 ⁻⁰⁵
747.498	C ₄₃ H ₇₃ O ₈ P	PA 40:6	0.4	9.36×10 ⁻⁰⁵	0.6	1.54×10 ⁻⁰⁴	0.3	1.70×10 ⁻⁰⁴	0.6	2.70×10 ⁻⁰⁴
751.5291	C ₄₃ H ₇₇ O ₈ P	PA 40:4	0.1	1.04×10 ⁻⁰⁴	0.2	1.72×10 ⁻⁰⁴	0	1.77×10 ⁻⁰⁴	0.2	2.22×10 ⁻⁰⁴

786.5294	C ₄₂ H ₇₈ NO ₁₀ P	PS 36:2	0.1	1.36×10 ⁻⁰⁴	0.3	2.39×10 ⁻⁰⁴	0.2	2.32×10 ⁻⁰⁴	0.3	3.36×10 ⁻⁰⁴
788.5451	C ₄₂ H ₈₀ NO ₁₀ P	PS 36:1	0.3	7.07×10 ⁻⁰⁵	0.5	1.26×10 ⁻⁰⁴	0.3	1.11×10 ⁻⁰⁴	0.4	1.65×10 ⁻⁰⁴
838.5609	C ₄₆ H ₈₂ NO ₁₀ P	PS 40:4	0.3	1.42×10 ⁻⁰⁴	0.4	2.05×10 ⁻⁰⁴	0.4	2.08×10 ⁻⁰⁴	0.5	2.61×10 ⁻⁰⁴
764.5244	C ₄₃ H ₇₆ NO ₈ P	PE 38:5	0.2	2.29×10 ⁻⁰⁵	0.1	4.06×10 ⁻⁰⁵	0	4.36×10 ⁻⁰⁵	0.2	7.48×10 ⁻⁰⁵
766.5401	C ₄₃ H ₇₈ NO ₈ P	PE 38:4	0.3	2.31×10 ⁻⁰⁴	0.3	3.72×10 ⁻⁰⁴	0.1	3.65×10 ⁻⁰⁴	0.3	5.03×10 ⁻⁰⁴
790.5402	C ₄₅ H ₇₈ NO ₈ P	PE 40:6	0.3	9.42×10 ⁻⁰⁵	0.3	1.62×10 ⁻⁰⁴	0.1	1.65×10 ⁻⁰⁴	0.3	2.10×10 ⁻⁰⁴
857.5196	C ₄₅ H ₇₉ O ₁₃ P	PI 36:4	0.3	1.33×10 ⁻⁰⁴	0.3	2.31×10 ⁻⁰⁴	0.1	2.52×10 ⁻⁰⁴	0.4	4.50×10 ⁻⁰⁴
861.5511	C ₄₅ H ₈₃ O ₁₃ P	PI 36:2	0.4	1.80×10 ⁻⁰⁴	0.4	3.33×10 ⁻⁰⁴	0.2	3.45×10 ⁻⁰⁴	0.5	4.93×10 ⁻⁰⁴
885.5508	C ₄₇ H ₈₃ O ₁₃ P	PI 38:4	0.4	1.76×10 ⁻⁰³	0.3	2.97×10 ⁻⁰³	0.1	3.04×10 ⁻⁰³	0.3	4.78×10 ⁻⁰³

Table A6.8. Characteristic molecular ion and fragments of amino acid in 3D OrbiSIMS spectra (positive polarity)

Mass m/z	Assignment	Amino acids
80.0498	C ₅ H ₆ N ⁺	Leucine
86.0967	C ₅ H ₁₂ N ⁺	Isoleucine
81.045	C ₄ H ₅ N ₂ ⁺	Histidine
82.0528	C ₄ H ₆ N ₂ ⁺	Histidine
93.0449	C ₅ H ₅ N ₂ ⁺	Histidine
94.0527	C ₅ H ₆ N ₂ ⁺	Histidine
95.0605	C ₅ H ₇ N ₂ ⁺	Histidine
110.0713	C ₅ H ₈ N ₃ ⁺	Histidine
156.0768	C ₆ H ₁₀ N ₃ O ₂ ⁺	Histidine
100.087	C ₄ H ₁₀ N ₃ ⁺	Arginine
112.0869	C ₅ H ₁₀ N ₃ ⁺	Arginine
114.1026	C ₅ H ₁₂ N ₃ ⁺	Arginine
120.0444	C ₇ H ₆ NO ⁺	Tryptophan
130.0652	C ₉ H ₈ N ⁺	Tryptophan
131.073	C ₉ H ₉ N ⁺	Tryptophan
132.0808	C ₉ H ₁₀ N ⁺	Tryptophan
143.073	C ₁₀ H ₉ N ⁺	Tryptophan
157.0761	C ₁₀ H ₉ N ₂ ⁺	Tryptophan
158.0839	C ₁₀ H ₁₀ N ₂ ⁺	Tryptophan
159.0917	C ₁₀ H ₁₁ N ₂ ⁺	Tryptophan
84.0447	C ₄ H ₆ NO ⁺	Glutamic acid
84.0811	C ₅ H ₁₀ N ⁺	Lysine
86.0603	C ₄ H ₈ NO ⁺	Hydroxyproline
87.0555	C ₃ H ₇ N ₂ O ⁺	Asparagine
120.0808	C ₈ H ₁₀ N ⁺	Phenylalanine
166.0863	C ₉ H ₁₂ NO ₂ ⁺	Phenylalanine
101.071	C ₄ H ₉ N ₂ O ⁺	Glutamine
130.0499	C ₅ H ₈ NO ₃ ⁺	Glutamine
136.0758	C ₈ H ₁₀ NO ⁺	Tyrosine
104.053	C ₄ H ₁₀ NS ⁺	Methionine
116.0706	C ₅ H ₁₀ NO ₂ ⁺	Proline
82.0654	C ₅ H ₈ N ⁺	Multiple amino acids
83.0607	C ₄ H ₇ N ₂ ⁺	Multiple amino acids
88.0396	C ₃ H ₆ NO ₂ ⁺	Multiple amino acids
96.0809	C ₆ H ₁₀ N ⁺	Multiple amino acids
98.0966	C ₆ H ₁₂ N ⁺	Multiple amino acids
100.0394	C ₄ H ₆ NO ₂ ⁺	Multiple amino acids
102.055	C ₄ H ₈ NO ₂ ⁺	Multiple amino acids
107.0492	C ₇ H ₇ O ⁺	Multiple amino acids
114.055	C ₅ H ₈ NO ₂ ⁺	Multiple amino acids
117.0573	C ₈ H ₇ N ⁺	Multiple amino acids
118.0651	C ₈ H ₈ N ⁺	Multiple amino acids
119.0492	C ₈ H ₇ O ⁺	Multiple amino acids

128.0706	$C_6H_{10}NO_2^+$	Multiple amino acids
121.0648	$C_8H_9O^+$	Multiple amino acids
77.0389	$C_6H_5^+$	Generic fragment
80.0624	$C_6H_8^+$	Generic fragment
89.0388	$C_7H_5^+$	Generic fragment
91.0545	$C_7H_7^+$	Generic fragment
102.0465	$C_8H_6^+$	Generic fragment
103.0543	$C_8H_7^+$	Generic fragment
105.0699	$C_8H_9^+$	Generic fragment

Table A6.9. Peak exported from SurfaceLab positive mode from each tissue sample, consisting of ions detected in the spectrum and assigned as RG sequences of lysozyme [M-H]⁺ C₈H₁₆N₅O₂⁺, m/z 124.1298

Sample	Area1		Area 2		Area 3		Area4	
	Mass error p.p.m	Norm. intensity	Mass error p.p.m	Norm. intensity	Mass error p.p.m	Norm. intensity	Mass error p.p.m	Norm. intensity
PDMS	0.4	2.51×10 ⁻⁰⁵	0.6	4.09×10 ⁻⁰⁶	-0.1	2.30×10 ⁻⁰⁶	0.2	2.67×10 ⁻⁰⁵
M1-polymer	0.2	1.42×10 ⁻⁰⁶	0.3	5.59×10 ⁻⁰⁵	8.7	0	-6	0
M2-polymer	0.2	1.03×10 ⁻⁰⁴	-0.3	8.89×10 ⁻⁰⁵	-0.1	1.03×10 ⁻⁰⁴	0.2	1.43×10 ⁻⁰⁴

Table A6.10. Other small molecules in each sample and search by human metabolome data base

Mass <i>m/z</i>	Assignment [M-H] ⁻	Metabolites	Area1		Area 2		Area 3		Area4	
			Mass error p.p.m	Norm. intensity	Mass error p.p.m	Norm. intensity	Mass error p.p.m	Norm. intensity	Mass error p.p.m	Norm. intensity
PDMS										
80.0497	C ₅ H ₆ N ⁺	Pyridine	4.1	9.77×10 ⁻⁰⁵	4.1	1.46×10 ⁻⁰⁵	3.9	2.67×10 ⁻⁰⁵	3.7	9.44×10 ⁻⁰⁵
81.0449	C ₄ H ₅ N ₂ ⁺	Pyrimidine	3.9	1.20×10 ⁻⁰⁴	4.2	2.19×10 ⁻⁰⁵	3.9	5.30×10 ⁻⁰⁵	3.6	1.22×10 ⁻⁰⁵
112.0869	C ₅ H ₁₀ N ₃ ⁺	Histamine	-0.1	5.95×10 ⁻⁰⁴	-0.2	1.90×10 ⁻⁰⁴	-0.2	1.96×10 ⁻⁰⁴	-0.4	5.76×10 ⁻⁰⁴
121.051	C ₅ H ₅ N ₄ ⁺	Purine	0.2	4.49×10 ⁻⁰⁵	0.4	5.31×10 ⁻⁰⁶	0.0	2.26×10 ⁻⁰⁵	-0.1	6.79×10 ⁻⁰⁵
M1-polymer										
80.0497	C ₅ H ₆ N ⁺	Pyridine	4.5	5.89×10 ⁻⁰⁵	4.5	2.57×10 ⁻⁰⁵	4.0	5.71×10 ⁻⁰⁵	3.5	1.08×10 ⁻⁰⁵
81.0449	C ₄ H ₅ N ₂ ⁺	Pyrimidine	4.0	5.87×10 ⁻⁰⁵	3.7	6.67×10 ⁻⁰⁵	4.1	5.03×10 ⁻⁰⁵	3.9	1.27×10 ⁻⁰⁵
112.0869	C ₅ H ₁₀ N ₃ ⁺	Histamine	0.0	1.70×10 ⁻⁰⁴	-0.1	7.32×10 ⁻⁰⁵	4.2	6.78×10 ⁻⁰⁵	4.0	3.03×10 ⁻⁰⁵
121.051	C ₅ H ₅ N ₄ ⁺	Purine	-0.1	2.13×10 ⁻⁰⁶	0.2	3.34×10 ⁻⁰⁶	-	0	-	0
M2-polymer										
80.0497	C ₅ H ₆ N ⁺	Pyridine	3.4	1.75×10 ⁻⁰⁴	3.2	9.20×10 ⁻⁰⁵	0	1.80×10 ⁻⁰⁴	0.3	2.61×10 ⁻⁰⁴

81.0449	$C_4H_5N_2^+$	Pyrimidine	3.1	2.39×10^{-05}	3.2	1.35×10^{-04}	3.3	3.36×10^{-04}	3.3	3.67×10^{-04}
112.0869	$C_5H_{10}N_3^+$	Histamine	-0.9	1.54×10^{-03}	-0.9	1.14×10^{-03}	-0.7	1.79×10^{-03}	-0.8	2.07×10^{-03}
121.051	$C_5H_5N_4^+$	Purine	-0.5	6.25×10^{-05}	-0.6	7.19×10^{-05}	-0.4	1.67×10^{-04}	-0.4	1.09×10^{-04}